


Winter 2003

Shock Wave Dispersion in Weakly Ionized Gas

Prasong Kessaratikoon
Old Dominion University

Follow this and additional works at: https://digitalcommons.odu.edu/physics_etds

 Part of the [Atomic, Molecular and Optical Physics Commons](#), and the [Fluid Dynamics Commons](#)

Recommended Citation

Kessaratikoon, Prasong. "Shock Wave Dispersion in Weakly Ionized Gas" (2003). Doctor of Philosophy (PhD), dissertation, Physics, Old Dominion University, DOI: 10.25777/gfdm-m122
https://digitalcommons.odu.edu/physics_etds/60

This Dissertation is brought to you for free and open access by the Physics at ODU Digital Commons. It has been accepted for inclusion in Physics Theses & Dissertations by an authorized administrator of ODU Digital Commons. For more information, please contact digitalcommons@odu.edu.

**SHOCK WAVE DISPERSION
IN
WEAKLY IONIZED GAS**

by

Prasong Kessaratikoon
M.S. May 1999, Old Dominion University

A Dissertation Submitted to the Faculty of
Old Dominion University in Partial Fulfillment of the
Requirement for the Degree of

DOCTOR OF PHILOSOPHY
PHYSICS
OLD DOMINION UNIVERSITY

December 2003

Approved by:

.....
Leposava Vušković (Director)

.....
Charles I. Sukenik (Member)

.....
Gail E. Dodge (Member)

.....
James L. Cox, Jr. (Member)

.....
Hani E. Elsayed-Ali (Member)

ABSTRACT

SHOCK WAVE DISPERSION IN WEAKLY IONIZED GAS

Prasong Kessaratikoon
Old Dominion University, 2003
Director: Dr. Leposava Vušković

Electrodeless microwave (MW) discharge in two straight, circular cylindrical resonant cavities in $TE_{1,1,1}$ and $TM_{0,1,2}$ modes were introduced to perform additional experimental studies on shock wave modification in non-equilibrium weakly ionized gases and to clarify the physical mechanisms of the shock wave modification process. The discharge was generated in 99.99% Ar at a gas pressure between 20 and 100 Torr and at a discharge power density less than 10.0 Watts/cm^3 . Power density used for operating the discharge was rather low in the present work, which was determined by evaluating the power loss inside the resonant cavity. It was found that the shock wave deflection signal amplitude was decreased while the shock wave local velocity was increased in the presence of the discharge. However, there was no apparent evidence of the multiple shock structure or the widening of the shock wave deflection signal, as observed in the d.c. glow discharge [3,5]. The shock wave always retained a more compact structure even in the case of strong dispersion in both the TE and the TM mode. The shock wave propagated faster through the discharge in the TE mode than in the TM mode. Discharge characteristics and local parameters such as gas temperature T_g , electron density N_e , local electric field E , and average power density, were determined by using the MW discharge generated from an Argon gas mixture that contains 95% Ar, 5% H_2 , and traces of N_2 . The gas temperature was evaluated by using the amplitude reduction technique and the emission

spectroscopy of Nitrogen. The gas temperature distribution was flat in the central region of the cavity. By comparing the gas temperature calculated from the shock wave local velocity and from the amplitude reduction technique, the present work was sufficiently accurate to indicate that the thermal effect is dominant. The electron density was obtained from measured line shapes of hydrogen Balmer lines by using the gas temperature and the well-tested approximate formula for deconvolution of Stark and Doppler broadening. The local electric field inside the MW discharge was evaluated by using a simplified kinetic model. Dispersion of a shock wave in a MW discharge will most likely be applied in future technical solutions in aircraft design, or rocket shock wave modification systems. We hope that the present study will contribute to a better understanding of the physical mechanism leading to shock wave dispersion in weakly ionized gas.

Copyright, 2003, by Prasong Kessaratikoon, All Rights Reserved.

*This thesis is dedicated to my wife, Sirinporn Kessaratikoon,
and my two lovely daughters,
Tanika (Mimi) Kessaratikoon and Yanisa (Gamma) Kessaratikoon.*

ACKNOWLEDGMENTS

It was a great opportunity to work with so many incredible people in the last six years. I am lucky to have had a chance to study here and learn more knowledge, research skills, and wonderful experiences at a high level. I am very thankful to all of those people who have contributed to the successful completion of this dissertation.

I was privileged to be awarded a scholarship from the Government of Thailand and the leave of absence from the Thaksin University to study toward my doctoral degree. I would like to thank the Government of Thailand and the President, the Dean of Faculty of Science, the Chairman of Physics Department, and my colleagues of Thaksin University who gave me infinite assistance and support. I would also like to thank all of officers of the Office of Educational Affairs in Washington, DC and in Bangkok for helping me to get through all difficult procedures and situations while I was studying in the United States.

The untiring efforts of my major advisor deserve special recognition. I would like to thank my advisor, Dr. Leposava Vušković, who always helped and supported me not only with knowledge of Physics and research, but also about life. Her dedication, leadership, focus, efficiency, generosity, and kindness made her not only an outstanding professor but also a great advisor.

I am particularly grateful to Dr. Svetozar Popović, who has great experience in Discharge Physics and who transferred a great deal of Discharge Physics knowledge to me. His cleverness, steady assistance, patience, and kindness helped me to complete my work. I would also like to thank him for all of his corrections, ideas, and guidance in writing this dissertation.

I extend many, many thanks to my committee members: Dr. Charles Sukenik, Dr. Gail Dodge, Dr. James Cox, and Dr. Hani Elsayed-Ali for accepting to review my thesis, suggestions on my research, and also editing of this manuscript.

I would like to thank all staff members of the Physics Department of Old Dominion University for assistance and for supporting me. Especially, Mr. Walt Hooks who was always ready to help and enjoyed discussing Thai food with me.

I would also like to thank Mr. Bobby Powell for his excellent assistance to build, buy, and fix some parts of the experiment. A special thank goes to Mr. Bob Evans who helped me to set up computers in the lab and my office.

It was a wonderful time to work with my fellow graduate students, in particular George Brooke, Thao Dinh, Hugh Thurman, and Minarni Shiddiq. I am thankful to them for sharing and discussing Physics, research problems, homework and exams.

A particular and very special thanks “*Kuab Khun Mak Mak.....Krub*” (thank you very much) to my wife, *Sirinporn*, and my two lovely daughters, *Tanika* and *Yanisa*, who always supported and inspired me to get through all the years of hard work. I would also like to send my special thanks to my father, *Som*, my mother, *Pisawong*, my sisters and brothers, and my wife’s family in Thailand, for their infinite support, love, care, and concern in many ways.

TABLE OF CONTENTS

	Page
LIST OF TABLES.....	x
LIST OF FIGURES.....	xi
 Section	
1. INTRODUCTION.....	1
2. SHOCK WAVE AND MICROWAVE DISCHARGE.....	4
2.1 Introduction.....	4
2.2 Shock Wave Generation.....	6
2.2.1 Normal Shock Wave.....	8
2.2.2 Normal Shock Wave in Ideal Gases.....	12
2.2.3 Shock Tube.....	16
2.3 Shock Wave Generation Using a Spark Discharge.....	17
2.3.1 Spark Gap.....	18
2.3.2 Shock Wave Generation.....	20
2.4 Microwave Discharge.....	21
2.4.1 Magnetron Power Supply.....	23
2.4.2 Design of a Cylindrical Resonant Cavity.....	25
2.4.3 TE Mode and TM Mode.....	28
2.4.4 Detuning of Resonant Cavity.....	31
3. EXPERIMENT.....	33
3.1 Experimental Apparatus.....	33
3.2 Determination of Shock Wave Characteristics	35
3.2.1 Schlieren Measurement Technique.....	35
3.2.2 Laser Schlieren System.....	40
3.2.3 Experiment Set-up.....	42
3.2.4 Laser Schlieren Technique Results and Discussion.....	44
3.2.5 Local Velocity of Shock Wave in Argon MW Discharge.....	63
3.3 Determination of Shock Wave Dispersion in MW Discharge.....	68
3.3.1 Shock Wave Dispersion in Ar MW Discharge (TE Mode).....	70
3.3.2 Shock Wave Dispersion in Ar MW Discharge (TM Mode).....	84
3.4 Determination of Gas Temperature.....	99
3.4.1 Amplitude Reduction Technique.....	100
3.4.2 Emission Spectroscopy of Nitrogen.....	112

3.5	Determination of Electron Density.....	135
3.5.1	Experimental Set-up.....	136
3.5.2	Electron Density Evaluation.....	137
3.6	Evaluation of the Local Electric Field.....	140
3.6.1	Measurement of Initial Electric Field.....	142
3.6.2	Measurement of Time Dependence of the Intensity of H_{β} Line.....	143
3.6.3	Evaluation of the Time Evolution of the Local Electric Field.....	147
3.7	Evaluation of the Average Power Density.....	150
4.	RESULTS AND DISCUSSION.....	154
4.1	Introduction.....	154
4.2	Shock Wave Dispersion in Weakly Ionized Gas.....	156
4.3	Characterization of MW Discharge.....	161
4.3.1	Gas Temperature.....	161
4.3.2	Electron Density.....	166
4.3.3	Local Electric Field.....	166
4.3.4	Power Density.....	167
4.4	Conclusion.....	167
5.	CONCLUSION.....	169
	REFERENCES.....	172
	APPENDIX.....	175
	VITA.....	176

LIST OF TABLES

Table	Page
I. Roots of the Bessel Function $J_m(x) = 0$	26
II. Roots of the Bessel Function $J'_m(x) = 0$	27
III. Values of constants for the evaluation of rotational term values of the Nitrogen Positive System, $C^3\Pi_u$ and $B^3\Pi_g$, from Ref. [45].....	119

LIST OF FIGURES

Figure	Page
1. Scheme of normal shock wave.....	8
2. Model of normal shock wave. (a) Moving normal shock wave. (b) Stationary normal shock wave.....	10
3. Control volume for a normal shock wave.....	10
4. Mach number behind normal shock wave for $\gamma = 1.4$	14
5. Limiting values of the Mach number behind the normal shock wave as a function of γ	15
6. Scheme of shock tube.....	16
7. High voltage DC power supply circuit to create a spark discharge and generate a shock wave.....	19
8. Electron oscillation in MW discharge.....	21
9. Magnetron tube circuit.....	24
10. Right circular cylinder cavity.....	25
11. Scheme of microwave discharge experiment.....	29
12. Right circular cylinder resonant cavity of $TE_{1,1,1}$ and $TM_{0,1,2}$	30
13. Detuning of resonant cavity.....	32
14. Schematic of the shock tube/discharge tube and the experiment apparatus.....	36
15. Schematic of Schlieren photography arrangement.....	38
16. Schematic of the laser Schlieren set-up.....	40
17. Voltage signal (density gradient profile) across a shock wave.....	41
18. Shock wave characteristic experimental set-up.....	43

19. Shock wave deflection waveform signal in neutral N ₂ at 20 Torr and 10 kV d.c. high voltage to spark gap.....	44
20. Shock wave deflection waveform signal in neutral Ar at 20 Torr and 10 kV d.c. high voltage to spark gap.....	45
21. Shock wave profile in neutral N ₂	46
22. Shock wave profile in neutral Ar	47
23. Shock wave deflection waveform signal from two laser beams in neutral Ar at 20 Torr and 10 kV d.c. high voltage to spark gap.....	48
24. Calculation of average velocity and local velocity in neutral gas.....	49
25. Average and local velocity of shock wave in neutral N ₂ and d = 0.38 cm.....	51
26. Average and local velocity of shock wave in neutral Ne and d = 0.38 cm.....	52
27. Average and local velocity of shock wave in neutral Ar and d = 0.38 cm.....	53
28. Relative temperature of shock wave in neutral Ar, N ₂ and Ne.....	55
29. Relative pressure of shock wave in neutral Ar, N ₂ and Ne.....	56
30. Relative density of shock wave in neutral Ar, N ₂ and Ne.....	57
31. Total energy per unit volume of shock wave in neutral Ar, N ₂ , and Ne.....	58
32. Mach number behind shock wave in neutral Ar, N ₂ , and Ne.....	59
33. Relative number density in neutral Ar, N ₂ , and Ne.....	60
34. Voltage dependence of the average velocity of a shock wave generated by a spark gap (d ~ 0.5 cm), in neutral N ₂ at 30 Torr.....	61
35. Pressure dependence of average velocity of shock wave in neutral N ₂ at V = 10 kV with some distances between the spark gap.....	62
36. Laser deflection waveform signal in Ar MW discharge and Ar at 15 Torr and d = 0.38 cm.....	64
37. Local velocities of shock wave in Ar MW discharge at 10 kV high voltage power supply to spark gap and d = 0.38 cm.....	66
38. Resonant cavity for the shock wave dispersion study in Ar MW discharge.....	69

39.	Shock wave deflection waveform signal in neutral Ar and Ar MW discharge at the 1 st position and 7 th position; Pressure 60Torr; Spark gap voltage 8 kV.....	73
40.	Shock wave deflection waveform signal in neutral Ar and Ar MW discharge at the 1 st position and 7 th position ; Pressure 70 Torr; Spark gap voltage 8 kV.....	74
41.	Shock wave deflection waveform signal in neutral Ar and Ar MW discharge at the 3 rd position and 9 th position ; Pressure 50 Torr; Spark gap voltage 8 kV.....	75
42.	Shock wave deflection waveform signal in neutral Ar and Ar MW discharge at the 5 th position and 11 th position; Pressure 40 Torr; Spark gap voltage 8 kV.....	76
43.	Shock wave deflection waveform signal in neutral Ar and Ar MW discharge at the 5 th , 6 th , 7 th , and 8 th position; Pressure 30 Torr; Spark gap voltage 8 kV.....	77
44.	Propagation of shock wave through neutral Ar and Ar MW discharge at 50 Torr; Spark gap voltage 8 kV.....	78
45.	Propagation of shock wave through neutral Ar and Ar MW discharge at 70 Torr; Spark gap voltage 8 kV.....	79
46.	Shock wave local velocity in neutral Ar and in Ar MW discharge at 6 th position.....	80
47.	Shock wave local velocity in neutral Ar and in Ar MW discharge at 7 th position.....	81
48.	Shock wave local velocity in neutral Ar and in Ar MW discharge at 50 Torr in TE mode.....	82
49.	Shock wave local velocity in neutral Ar and in Ar MW discharge at 70 Torr in TE mode.....	83
50.	Shock wave deflection waveform signal in neutral Ar and Ar MW discharge at the 1 st position and 7 th position (TM mode); Pressure 40Torr; Spark gap voltage 8 kV.....	88
51.	Shock wave deflection waveform signal in neutral Ar and Ar MW discharge at the 1 st position and 7 th position (TM mode); Pressure 100Torr; Spark gap voltage 8 kV.....	89
52.	Shock wave deflection waveform signal in neutral Ar and Ar MW discharge at the 5 th position and 11 th position (TM mode); Pressure 70Torr; Spark gap voltage 8 kV.....	90

53.	Shock wave deflection waveform signal in neutral Ar and Ar MW discharge at the 6 th position and 12 th position (TM mode); Pressure 60Torr; Spark gap voltage 8 kV.....	91
54.	Shock wave deflection waveform signal in neutral Ar and Ar MW discharge at the 4 th , 5 th , 6 th , and 7 th position (TM mode); Pressure 30Torr; Spark gap voltage 8 kV.....	92
55.	Propagation of shock wave through neutral Ar and Ar MW discharge at 50 Torr (TM mode); Spark gap voltage 8 kV.....	93
56.	Propagation of shock wave through Ar neutral gas and Ar MW discharge at 80 Torr (TM mode); Spark gap voltage 8 kV.....	94
57.	Shock wave local velocity in neutral Ar and in Ar MW discharge at 4 th position in TM mode.....	95
58.	Shock wave local velocity in Ar neutral gas and in Ar MW discharge at 5 th position in TM mode.....	96
59.	Shock wave local velocity in neutral Ar and in Ar MW discharge at 50 Torr in TM mode.....	97
60.	Shock wave local velocity in neutral Ar and in Ar MW discharge at 70 Torr in TM mode.....	98
61.	Amplitude reduction of shock wave in neutral Ar and Ar MW discharge at 8 th position, 30 Torr and TE Mode.....	102
62.	Amplitude reduction of shock wave in neutral Ar and Ar MW discharge at 6 th position, 70 Torr and TM Mode.....	103
63.	Gas temperature distribution in Ar MW discharge at 30 Torr in TE mode.....	106
64.	Gas temperature Distribution in Ar MW discharge at 50 Torr in TE mode.....	107
65.	Gas temperature Distribution in Ar MW discharge at 70 Torr in TE mode.....	108
66.	Gas temperature Distribution in Ar MW discharge at 40 Torr in TM mode.....	109
67.	Gas temperature Distribution in Ar MW discharge at 50 Torr in TM mode.....	110
68.	Gas temperature Distribution in Ar MW discharge at 70 Torr in TM mode.....	111
69.	Schematic of the experimental set-up for N ₂ emission spectroscopy.....	114
70.	Energy level diagram of the N ₂ molecule reproduced from Ref. [44].....	115

71. Example of five rotational transitions of the ${}^3\Pi_1 - {}^3\Pi_1$ transition belonging to the P , Q , or R branches in $(0-2)$ vibrational band of the $C^3\Pi_u - B^3\Pi_g$ electronic excitation.....	117
72. Fortrat diagram of $N_2 (0-2)$ band in $C^3\Pi_u - B^3\Pi_g$ system.....	120
73. Rotational spectrum of the $(0-2)$ band at 380.5 nm, of the Nitrogen Second Positive System recorded at 8 th position in TM mode discharge at 70 Torr.....	121
74. Intensity distribution of rotational branches in $(0-2)$ band of the second positive system, $C^3\Pi_u - B^3\Pi_g$ in Nitrogen emission spectrum as a function of wavelength variation from the band head (380.5 nm) at $T_r = 1200$ K.....	126
75. Rotational temperature from the R_0 branch of the $N_2 (0-2)$ band in Second Positive System from TE mode at 8 th position and 30 Torr.....	127
76. Rotational temperature from the R_0 branch of the $N_2 (0-2)$ band in Second Positive System from TE mode at 8 th position and 75 Torr.....	128
77. Rotational temperature from the R_0 branch of the $N_2 (0-2)$ band in second positive system from TM mode at 7 th position and 50 Torr.....	129
78. Rotational temperature from the R_0 branch of the $N_2 (0-2)$ band in second positive system from TM mode at 9 th position and 70 Torr.....	130
79. Rotational temperature in TE mode.....	132
80. Rotational temperature in TM mode.....	133
81. Comparison of the rotational temperature evaluated from $(0-2)$ and $(0-3)$ bands in TM mode.....	134
82. H_β profiles in Ar (5% of hydrogen) MW discharge (TM mode) at 7 th position; 30 Torr.....	137
83. Electron density in Ar MW discharge (TM mode).....	139
84. Simplified kinetic scheme in calculating balance of the excited state C of the Second Positive System of Nitrogen.....	141
85. Initial electric field (E_0) in Ar MW discharge.....	144
86. Schematic of time dependence of the intensity of H_β line measurement.....	145

87.	Time dependence of the intensity of H_{β} line and time- dependent electron density , $N_e(t)$, at 7 th position; p = 30 Torr.....	146
88.	Measured normalized waveform, $I_C(t)/I_{Cmax}$, at 7 th position; p = 30 Torr and calculated normalized waveform, $N_C(t)/N_{Cmax}$	148
89.	Time evolution of the local electric field at 7 th position; p = 30 Torr.....	149
90.	A cylindrical coaxial cavity in Ar MW discharge.....	150
91.	Comparison of shock wave deflection signal in neutral gas, MW discharge and d.c. glow discharge.....	157
92.	Comparison between the gas temperature corresponding to the observed local propagation velocity and the measured gas temperature evaluated from shock wave amplitude reduction technique at 70 Torr in TE mode.....	159
93.	Comparison between the gas temperature corresponding to the observed local propagation velocity and the measured gas temperature evaluated from shock wave amplitude reduction technique at 70 Torr in TM mode.....	160
94.	Gas temperature and rotational temperature in TE mode.....	164
95.	Gas temperature and rotational temperature in TM mode.....	165

Section 1

INTRODUCTION

Shock wave dispersion and propagation in non-equilibrium weakly ionized gases have been the subject of many recent experimental studies (see, for example, [1-3]). Most of the studies were performed in positive columns of d.c. glow discharges. The most important observed effects of non-equilibrium plasma on the shock wave are the decrease of shock amplitude combined with the widening of the shock width (dispersion) and the increase of the propagation velocity of the shock. However, there are some ambiguities related to the presence of electrodes in this type of discharge and also their impact on the local values of plasma and gas parameters. In order to eliminate a possible influence of the electrodes on shock modification, a microwave (MW) discharge in a straight circular cylindrical resonant cavity was introduced in the present work. The aim of these experimental studies on shock wave modification in non-equilibrium weakly ionized gases was to clarify the physical mechanisms of the shock wave modification process.

An apparatus to study the dispersion and the propagation of a shock wave in MW discharge was set up in the Atomic Beams Laboratory at ODU. This facility was used to implement and test the proposed electrodeless MW large volume "near" atmospheric pressure plasma generator. The proposed experimental set-up is the combination of a shock tube and a microwave discharge, integrated in a single tube in a manner similar to that previously described in [4-6], which used a d.c. glow discharge

This dissertation follows the style of *Physical Review*

to generate the plasma. Moreover, this type of discharge is the most likely future technical solution for use in an aircraft, or rocket shock wave modification system.

MW discharges initiated by high frequency or MW fields differ significantly from d.c. or low frequency discharges in many ways. For example, this type of discharge requires sufficient size of the container walls. The direction of electron motion inside the discharge changes and oscillates inside the container in the rhythm of the external high frequency electric field all the time. Further differences include the initiation of the discharge and the conditions required to keep it operating. There are many basic processes which go on in a gas subjected to MW electric field. These processes, involving the interaction of the field, electrons, atoms or molecules, ions and walls of the container, determine the values of the experimental parameters by which we describe the phenomenon. We can see that these considerations lead us directly to one of the great difficulties in describing this kind of discharge, namely the large number of independent variables which must be taken into account. In order to describe the phenomena, I performed auxiliary experiments in order to determine the power density, the reduced electric field, the electron density, and the gas temperature during the discharge in the range of gas pressure between 20 and 100 Torr. Also I calculated, designed, and constructed several resonant cavities capable of sustaining particular modes of MW field distribution. The cavities were used for studies of the effect of MW mode structure on the dispersive properties of the MW cavity discharge.

The first objective of the study was to generate an acoustic shock wave by using a spark gap and to investigate the influence on shock wave parameters of macroscopic parameters such as distance between a spark gap, gas pressure, and applied power. It

included evaluation of the propagation velocity and Mach number of the shock wave in the absence and in the presence of a MW discharge in Ar. The second objective was to generate and characterize a MW discharge in Ar. The third objective was to study the equilibrium and non-equilibrium conditions of a MW discharge in Ar. The fourth objective was to evaluate the propagation and dispersion of a shock wave in weakly ionized argon generated by the MW discharge. The task was to examine the effect of microscopic parameters such as electron density, gas temperature, and electric field during the MW discharge in Ar. Finally, the fifth objective was to study the mode dependence of the shock wave propagation and dispersion in the MW discharge in Ar. Cylindrical resonant cavities in TE and TM mode were designed, constructed, and used in this study.

This dissertation is organized as follows: In Section 2, I describe the method of generating the shock wave by using a spark gap. In addition, I describe the generation of a MW discharge and design of a resonant cavity, as well as detuning of the resonant cavity. In Section 3, I discuss the experimental apparatus and diagnostic techniques to determine the discharge characteristics such as electron density, gas temperature, and local electric field. I also discuss the methods for measuring the shock wave propagation and dispersion. In Section 4, I present and discuss the experimental results, and also I outline a direct application of this work. Finally, the conclusion will be given in Section 5.

Section 2

SHOCK WAVE AND MICROWAVE DISCHARGE

2.1 Introduction

Shock wave propagation in plasmas has been the subject of extensive investigations in recent years [7-9]. This work is devoted to a separate group of phenomena associated with the interaction of the shock wave with weakly ionized gas at atmospheric or near-atmospheric pressure. Recent experimental and modeling work in Russia [10-14] and in the U.S. [15-18] has been extensively focused on shock wave propagation in weakly ionized glow discharge plasmas (with an ionized fraction of $n_e/N \sim 10^{-8} - 10^{-6}$). At these conditions, a number of "anomalous" effects were observed, including the shock wave acceleration, weakening, and dispersion. These effects were studied in discharges in different kind of gases (i.e., air, N₂, Ar) at moderate pressure, typically $P = 30$ Torr, and Mach number $M = 1.1 - 10$. This "anomalous" shock wave behavior in non-equilibrium weakly ionized gas was originally suggested to be due to the effect of the flow field modification by the charged species (ion-acoustic wave) [19] or by the metastable species present in the discharge [20-22]. However, there were difficulties related to the presence of electrodes and their influence on the dispersion of the shock wave, which were reported in some works [16, 18, 23-24]. One of the objectives of the present thesis is to perform a new experiment avoiding these ambiguities by introducing the MW electrodeless discharge in this type of research.

MW electrodeless discharges have played an important role for several decades in plasma sources for industrial applications, such as solid surface modification and thin film deposition. In recent years, there has been a great interest in MW discharges as primary light sources in analytical atomic emission spectrometry [25-26] and also as discharge sources in plasma physics [27-29]. We will apply this kind of discharge to review the study of the "anomalous" behavior of shock waves that has been mostly investigated in dc glow discharges.

The non-equilibrium state is a very important property of the MW discharge. Electrons start to accelerate and consequently increase their kinetic energy under the applied MW electric field. In the course of acceleration from an electric field, the electrons mainly collide elastically with much heavier neutral particles. Most scattered electrons continue to increase their kinetic energy due to the effect of the applied electric field. Due to collisions and the effect of the external field, the average energy of electrons becomes remarkably higher than the energy of the heavy particles. Therefore, the non-equilibrium state of the discharge plasma is observed to have different average kinetic energies for electrons and heavy particles. Furthermore, a fraction of electrons keeps gaining more energy from the field until they reach the threshold for inelastic collisions. When inelastic collisions occur, electrons transfer most of their energy to the gas molecules and excite, ionize or dissociate the molecule. As a result, the population of electrons in the high-energy tail of the energy distribution decreases quickly as the energy increases. For this reason, the electron energy distribution function (EEDF) is far from a Maxwellian distribution, due to the combined effect of all elastic and inelastic collision processes leading to a highly non-equilibrium electron energy distribution.

According to this result, the non-equilibrium state of the MW discharge directly affects the discharge characteristic (i.e., electron density, electron average kinetic energy, and gas average kinetic energy). Consequently, the interaction between the shock wave and the MW discharge depending on the characterization of the discharge will also be affected by this result. In this work, the degree of ionization in the MW discharge was about 10^{-5} - 10^{-4} , which is greater than in the dc glow discharge ($\sim 10^{-8}$ - 10^{-6}).

This chapter is devoted to a detailed description of the shock wave and the MW electrodeless discharge. The shock wave generation technique will be discussed in Section 2.2. We will describe the spark gap shock wave generator in Section 2.3. The description of MW electrodeless discharge will be given in Section 2.4. Designation and detuning of the resonance MW cavity will be discussed in detail. We will also discuss the generation of transversal electric (TE) and transversal magnetic (TM) mode of generation of a MW.

2.2 Shock Wave Generation

The propagation of an ordinary sound or acoustic wave in gas is accomplished through small amplitude longitudinal displacements of molecules. There is no net flow of gas, and any physical changes in the gas are small and reversible. The velocity of such a wave, termed the local sound speed of the gas, is determined by the collision rate between gas molecules. It is therefore approximately equal to the mean kinetic velocity of the molecules and is primarily determined by the temperature of the gas.

A totally different situation arises when a disturbance is forced through the gas at a speed greater than the speed of sound. In this case it is evident that a wave of a very different nature is established in the gas. Since the molecules can only move away from

the supersonic (i.e. greater than the sound speed) disturbance at the sound speed, the pressure, density, and temperature must change due to this disturbance. Familiar examples are the phenomena associated with detonation waves, explosions, and the wave system formed at the nose of a projectile moving with a supersonic speed. In all those cases the wave front is very steep, and there is a large pressure rise in transversing the wave, which is termed a *shock wave*. Because of the large pressure gradient in the shock wave, the gas experiences a large increase in its density with a corresponding change in its refractive index. Since the shock wave is more or less an instantaneous compression of the gas, it cannot be a reversible process. The energy for compressing the gas flowing through the shock wave is derived from the kinetic energy it possessed upstream of the shock wave. Because of the irreversibility of the shock process, the kinetic energy of the gas leaving the shock wave is smaller than that for an isentropic flow compression (no heat transferred to or from the system) between the same pressure limits. The reduction in the kinetic energy because of the shock wave appears as a heating of the gas to a static temperature above that corresponding to the isentropic compression value.

By definition, the shock wave is a front across which there is a linearly discontinuous, finite jump in pressure with corresponding jump in temperature, density, and other fluid properties. Because shock waves are nonlinear, analysis of their behavior is complex; e.g., its reflection does not obey any simple wave laws such as equality of the incident and reflected angles. We can study a shock wave using the *Mach number* that is the ratio of the local speed of a shock wave to its sound speed in a medium.

The basic equations describing the properties of shock waves are derived for the *normal shock wave* as described in next section, and it is applied to the flow of perfect or

ideal gas and also in weakly ionized gas.

2.2.1 Normal Shock Wave

There are several types of shock waves, each having specific characteristics. In some cases, the shock wave is stationary with respect to the body in which it is formed, signifying that the speed of propagation of the shock wave is equal to that of the body itself; otherwise the shock would not be attached to the body. When the shock wave front is perpendicular to the direction of the flow, as illustrated in Figure 1, it is termed a *normal shock*.

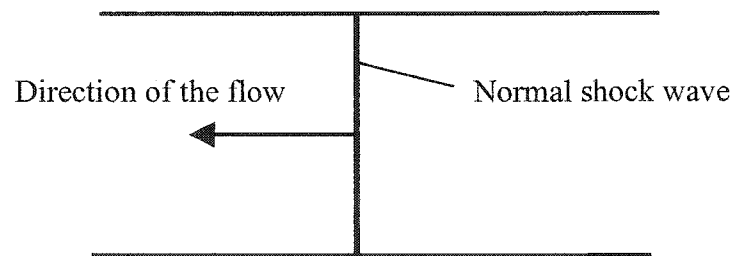


FIG. 1. Scheme of normal shock wave.

The theory describing the effects produced by a shock wave is fairly well developed. Equations have been derived relating the velocities and the thermodynamic properties of the gas immediately in front of and in back of the shock wave. However, the theory does not give complete information regarding the causes leading to the formation of the compression shock wave. Undoubtedly, the more or less spontaneous manner in which the shock process occurs makes it difficult to derive a complete theoretical explanation for the shock wave phenomena. In recent years considerable experimental work has been devoted to the accumulation of data regarding shock waves.

Those data are being correlated with the results of theoretical studies to evolve a working theory for the shock wave phenomena. In this section, we will discuss the general characteristics of the *normal shock wave*.

The flow through a normal shock wave may be analyzed by considering the one dimensional flow through a stream tube created by the streamlines. In the analysis, the following assumptions are made.

1. The boundary surface forming the stream tube is far removed from the boundary layers adjacent to any solid surface. Since all friction forces may be assumed to be confined to the shearing stresses in the boundary layer, the configuration under discussion is a *frictionless duct*.
2. The shock process takes place at *constant area*; that is, the streamlines forming the boundary of the stream tube are parallel.
3. The shock wave front is perpendicular to the streamlines.
4. The flow process, including the shock wave, is adiabatic, no external work is performed, and the effects of body forces are negligible.

Figure 2a illustrates a model of a shock wave moving to the right, with a velocity V_{shock} measured with respect to a stationary observer. It is demonstrated in the investigation of the speed of propagation of small disturbances that a moving wave problem may be transformed into a stationary wave problem by superimposing the wave velocity on all of the flow velocities, as is illustrated schematically in Figure 2b. In effect, the observer in Figure 2b moves at the same speed as the shock wave. The control volume enclosing the stationary normal shock wave is illustrated in Figure 3.

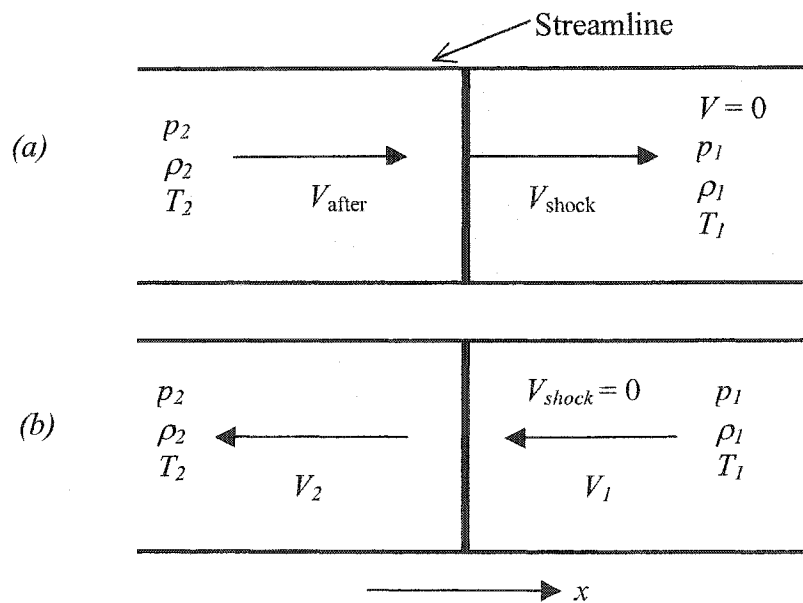


FIG. 2. Model of normal shock wave. (a) Moving normal shock wave. (b) Stationary normal shock wave.

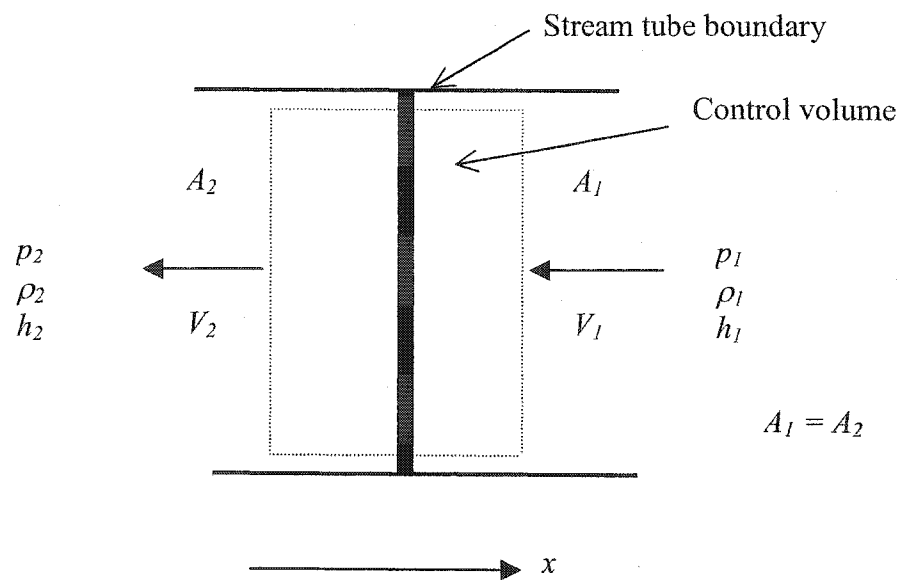


FIG. 3. Control volume for a normal shock wave.

The pressure p , density ρ , temperature T , specific enthalpy h , cross sectional area A , and velocity V are all listed in Figure 2 and Figure 3. Subscripts 1 and 2 refer to the regions in front of (upstream) and behind a shock wave, respectively.

The analysis of the normal shock wave involves, as for any other flow problem, determining the pressure, density, and speed of the fluid at the location under consideration. In general, there are four unknown properties: p_2 , ρ_2 , h_2 , and V_2 ; for their determination there are available the continuity equation, the momentum or dynamic equation, the energy equation, and the equation of state for the fluid.

Continuity equation

$$\rho_1 V_1 = \rho_2 V_2 \quad (1)$$

Momentum equation

$$p_1 + \rho_1 V_1^2 = p_2 + \rho_2 V_2^2 \quad (2)$$

Energy equation

$$h_1 + \frac{1}{2} V_1^2 = h_2 + \frac{1}{2} V_2^2 \quad (3)$$

Equation of state

$$u = u(p, \rho) \quad \text{and} \quad h = h(p, \rho). \quad (4)$$

For a simple thermodynamic system, each of the properties p , ρ , T , h , the gas specific internal energy (u), and entropy (s) is uniquely related to any two of the other properties.

Eqs. (1), (2), (3), and (4) comprise a set of four equations involving the four flow properties p , ρ , u , and V . Those equations are quite general, and they govern the behavior of a normal shock wave for a simple thermodynamic system. The specific enthalpy h is defined by

$$h = u + RT, \quad (5)$$

where R is the gas constant for unit mass.

2.2.2 Normal Shock Wave in Ideal Gases

For an ideal gas, the equations of state are

$$p = \rho RT, \quad (6)$$

$$h = c_p T, \quad (7)$$

$$c_p - c_v = R, \quad (8)$$

and

$$\gamma = \frac{c_p}{c_v}, \quad (9)$$

where c_p and c_v are the specific heats at constant pressure and volume, respectively.

By using Eqs. (1) through (9), the following relations for the changes in pressure, density, and temperature across the shock can be derived:

$$\frac{p_2}{p_1} = \frac{2\gamma M_1^2 - (\gamma - 1)}{\gamma + 1}, \quad (10)$$

$$\frac{\rho_2}{\rho_1} = \frac{V_1}{V_2} = \frac{(\gamma + 1)M_1^2}{(\gamma - 1)M_1^2 + 2}, \quad (11)$$

and

$$\frac{T_2}{T_1} = \left[\frac{p_2/p_1}{\rho_2/\rho_1} \right] = \frac{[2\gamma M_1^2 - (\gamma - 1)][(\gamma - 1)M_1^2 + 2]}{(\gamma + 1)^2 M_1^2}. \quad (12)$$

We also obtain the shock Mach number after a normal shock (M_2)

$$M_2 = \left(\frac{M_1^2 + \frac{2}{\gamma - 1}}{\frac{2\gamma}{\gamma - 1} M_1^2 - 1} \right)^{\frac{1}{2}}, \quad (13)$$

where M_1 is the shock Mach number before a normal shock, defined as

$$M_1 = \frac{V_1}{a_1}, \quad (14)$$

and a_1 is the sound speed in the un-shocked gas, given by

$$a_1^2 = \frac{\gamma p_1}{\rho_1}. \quad (15)$$

Figure 4 presents the Mach number after a normal shock wave M_2 as a function of M_1 , for an ideal gas ($\gamma = 1.4$). This picture shows that as M_1 in front of the normal shock wave is increased indefinitely, the Mach number M_2 in back of the normal shock wave continually decreases, but approaches the limiting value $\sqrt{(\gamma - 1)/2\gamma}$. The limiting value of M_2 depends only on the specific heat ratio for the gas. Figure 5 presents the limiting value of M_2 as a function of γ .

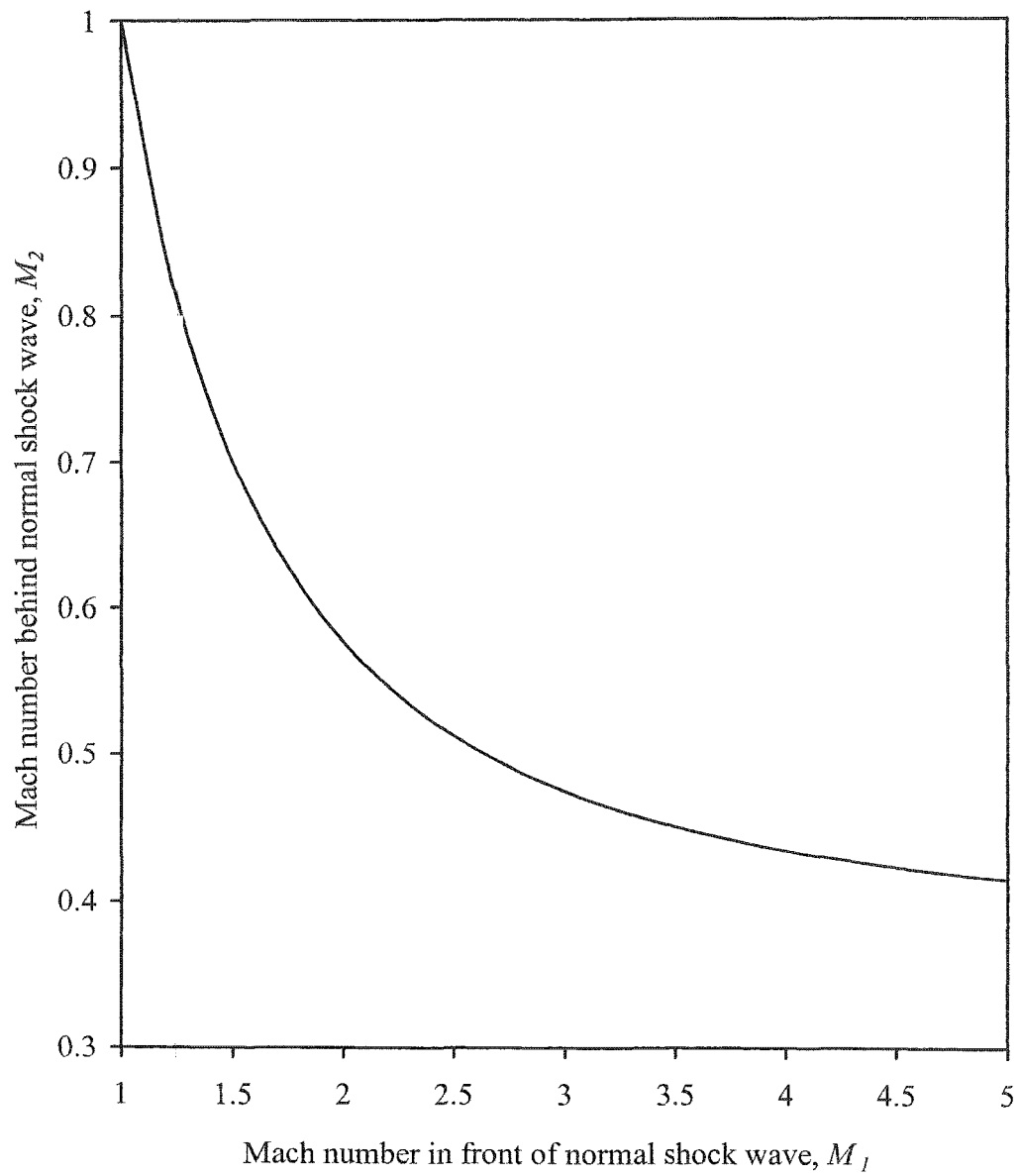


FIG. 4. Mach number behind normal shock wave for $\gamma = 1.4$.

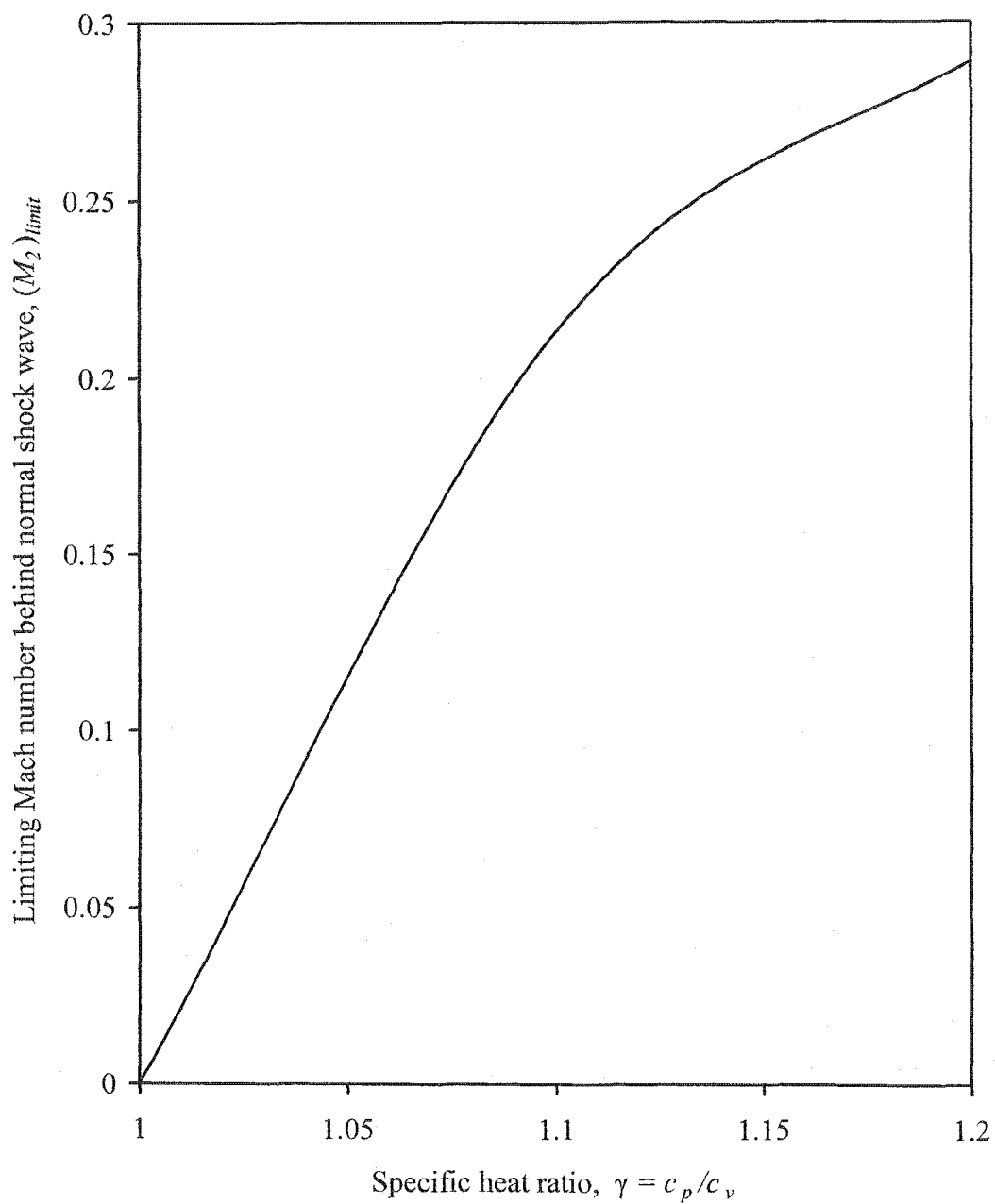


FIG. 5. Limiting values of the Mach number behind the normal shock wave as a function of γ .

2.2.3 Shock Tube

The shock tube used in the present work is a device in which normal shock waves generated by the discharge of a spark gap (see also Section 2.3) are launched into a weakly ionized gas. The tube, itself, was a quartz tube; the discharge was generated in a spark gap via the d.c. high voltage power supply circuit (see Figure 7). The normal shock wave would then propagate to the other end of the tube, as shown in Figure 6. A discharge region could be produced at the center of the tube at the same time, which could cover $1/3$ to $1/4$ of the tube length. During the experiment, a shock wave was propagated through the shock tube either when the discharge was turned on or when it was turned off. Thus, this specific shock tube/discharge tube was very useful for studying shock wave propagation and dispersion in a neutral gas or a gas discharge.

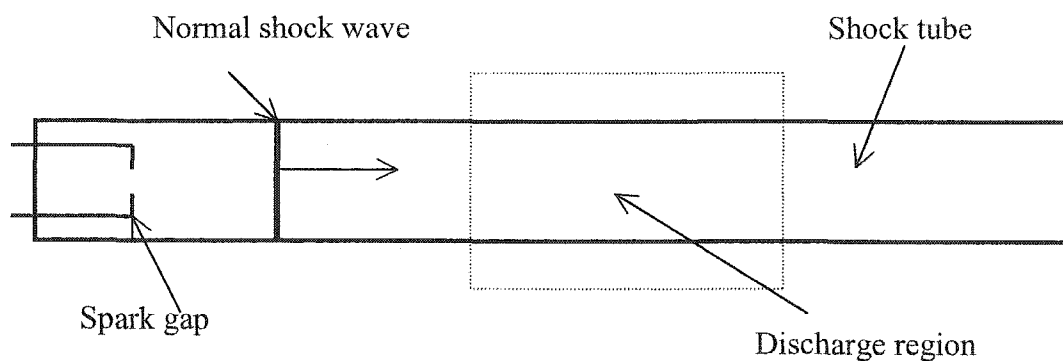


FIG. 6. Scheme of shock tube.

In our experiment, an Ar MW discharge in two different modes were generated in the central region ($\sim 1/4$ of the shock tube/discharge tube) at various values of gas pressure by using the magnetron tube and the magnetron tube circuit (see Section 2.4.1). The normal shock wave generated by a spark gap that was always fired at the same discharge voltage would propagate along the tube through the Ar neutral gas region (discharge off) or through the Ar MW discharge region (discharge on). By using the laser Schlieren measurement technique (see Section 3.2.2), we were able to study the propagation and dispersion of the shock wave in both the Ar neutral gas and the Ar MW discharge.

2.3 Shock Wave Generation Using a Spark Discharge

The spark discharge in a gas is a very well-known phenomenon. The ability of a spark to convert electrical energy into highly concentrated thermal energy is an extremely useful process. In the spark discharge process, after initial breakdown, the gas is electrically conductive. The electric current heats up the gas, changing it into a plasma and forcing the plasma to expand. The evolution of spark gap discharges in gases was studied by Akram and Lundgren [33, 34].

We can assume that a spark discharge process in a chemically inert gas mixture occurs in the following four stages:

- 1) Breakdown of the gas mixture and the formation of the breakdown channel
- 2) Dissociation and ionization of the gas and heating of the neutral gas by fast electron (thermalization)
- 3) Expansion of the plasma channel and the formation of a shock wave

- 4) Recombination, cooling of the plasma, and attenuation of the shock wave to a sound wave

In this section, we will focus only on the last two stages, termed the thermodynamic phase of a spark discharge process. In the following, we describe the *spark gap* which was used to create a shock wave in our experiment.

2.3.1 Spark Gap

This section presents the spark gap that is used for generating a normal shock wave in a shock tube. The spark gap technique is one of several methods used to generate a shock wave. The spark discharge is generated between two coaxial pins made of conductive material. These two pins will be used as electrodes of the high voltage power supply and will be used to create a shock wave, as shown in Figure 7.

Our design of the spark generator is shown in Figure 7. We recommend the use of a 1.865 $\mu\text{F}/25\text{kV}$ capacitor or any other with specifications close to this value. After the capacitor is charged, the high voltage spark gap 1 is closed, and the capacitor current begins to flow through the gap and the 150 Ω resistor. The voltage across the 150 Ω resistor appears across the tungsten or copper electrodes in spark gap 2, which are inside the pressurized shock tube, and this produces a spark discharge. It is this discharge that produces the normal shock wave inside the shock tube.

Usually, the high voltage spark gap 1 is closed via a pulse generator. However, we used an electrically controlled opening valve. This scheme works as follows:

- 1) The high voltage spark gap 1 is pressurized (usually with dry air) to a few atmospheres.
- 2) The capacitor is charged and the voltage is monitored with a voltmeter.
- 3) The normally closed pneumatic valve is then energized and opened.
- 4) The pressure in the spark gap falls quickly to atmospheric pressure, and breakdown occurs across spark gap 1.
- 5) The capacitor voltage is transferred to spark gap 2, and the spark discharge is generated.

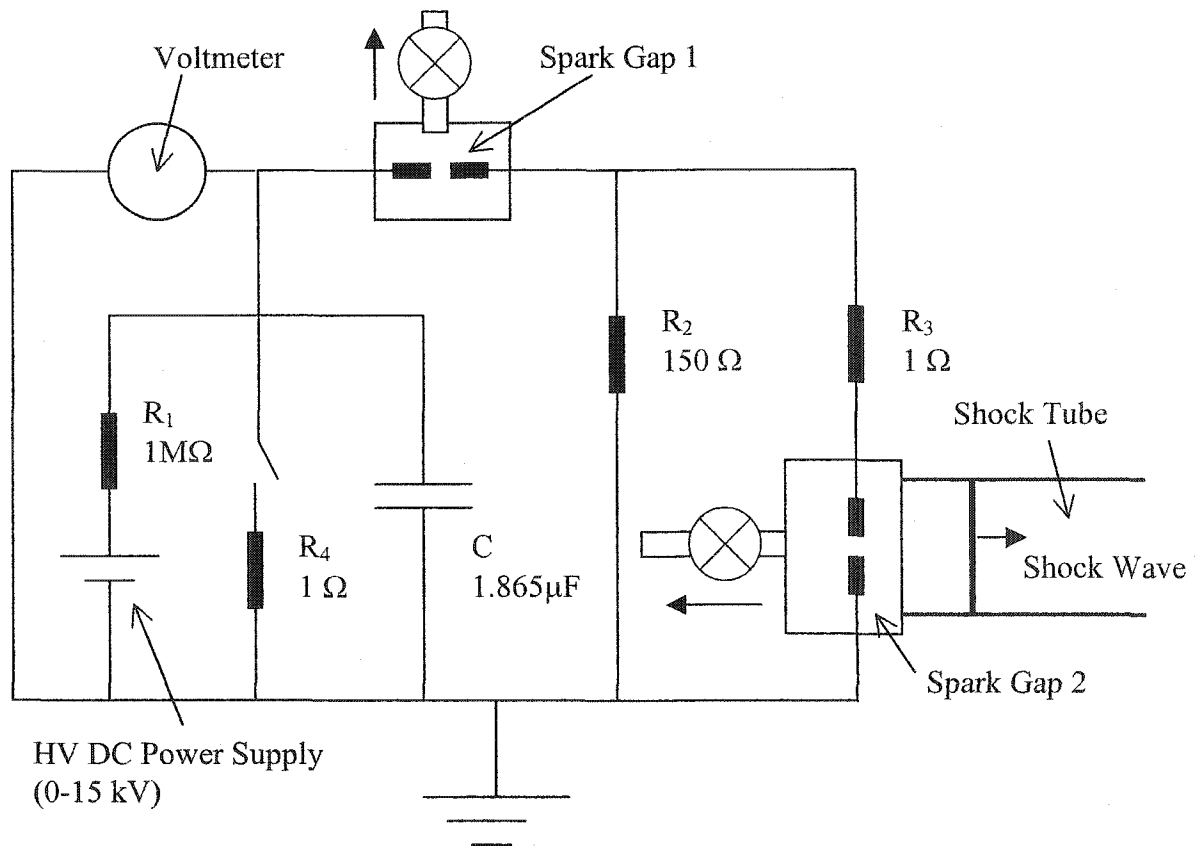


FIG. 7. High voltage d.c. power supply circuit to create a spark discharge and generate a shock wave.

This scheme has two major advantages: (a) an expensive high voltage pulser is not required as a triggering mechanism, and (b) the electromagnetic impulse (EMI) produced by the trigger source (which is significant) is avoided.

2.3.2 Shock Wave Generation

During the discharge process, the energy in the gas is stored in highly excited molecules, which may even be dissociated and ionized. However, a few milliseconds after the inception of the discharge, relaxation and recombination process will have returned the molecules to low-energy states, with all the energy in the form of translational, rotational, and vibrational modes. The energy in the gas can then be determined from the measured pressure rise and the heat capacity of the gas at constant volume. Reinmann and Akram [35] used this technique to measure the energy delivered to the gas by a spark discharge. The time history of the energy balances in the spark gap for the three cases have also been studied and reported by these authors. Their conclusion was that *increasing the spark gap distance as well as increasing the pressure will deposit more energy into the gas under the same electrical conditions of the ignition system*. Basically, we can say that *we can make a stronger shock wave if we increase the distance of the spark gap and the pressure of the system*. In section 3, we have some data to confirm this conclusion.

2.4 Microwave Discharge

Discharges driven by high frequency or MW fields differ significantly from dc or low frequency discharges in many ways. Electrons and charged particles will be accelerated when a high frequency or MW electric field is applied across a volume of gas. The energy will be transferred to these electrons much more than to the ions, and the electrons are accelerated so much more than the ions because of the difference in mass between them. The direction of the force on the electron changes when the direction of the field changes, so the electron will oscillate inside the container. For this reason, the walls of the container of the gas must be sufficiently far apart (see Figure 8). This is the characteristic that distinguishes high frequency or MW discharges from low frequency or d.c. discharges. For a low frequency, the electron will strike the walls of the container before changing the direction of acceleration. The impact of electrons on the wall is likely to create other electrons or impurity atoms from the walls, thus introducing complicating factors into the discharge.

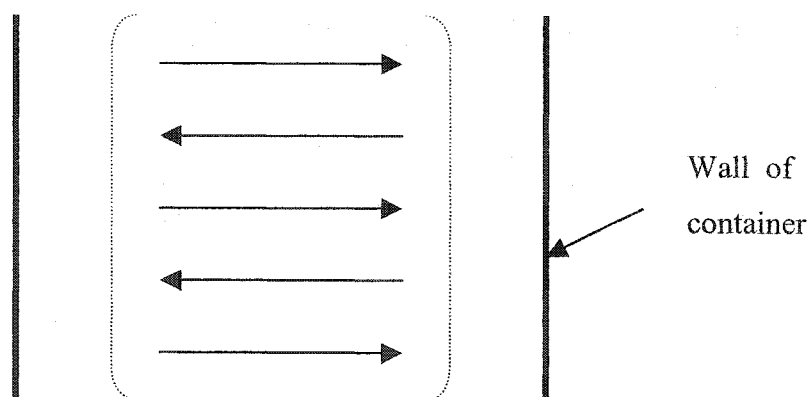


FIG. 8. Electron oscillation in MW discharge.

At high frequencies, the electrons are accelerated by the field each time they collide with an atom. Sometimes, they may lose energy, and sometimes they may gain energy, but on the average energy transfer from the field to the electrons will occur. An electron may gain sufficient energy to exceed the excitation energy level of the atom, if the field is large enough. In the next collision, the electron may excite the atom and lose most of its energy. Subsequently, the excitation energy is transferred into radiation when the atom de-excites to its ground state. Hence, the electron energy losses by elastic collisions and by inelastic collisions must be taken into account in the energy balance. Furthermore, some electrons may acquire sufficient kinetic energy to ionize the atoms. We gain more electrons by this process while, at the same time, electrons are being lost by diffusion to the walls, by recombination with positive ions, or by attachment to neutral atoms or molecules. The value of the electron concentration in the microwave discharge will be determined by the relative values of these production and loss rates. The production and loss rates are complicated functions of the gas species, the gas density, the electric field magnitude and frequency, and the geometry of the container. We should now consider in detail how to make our own microwave discharge for studying the dispersion of a shock wave inside this type of discharge.

The magnetron power supply used in generating microwave radiation in this work is described in Section 2.4.1. The geometry and design of the cylindrical resonant cavity is discussed in Section 2.4.2. In Section 2.4.3, I will describe the resonant cavities sustaining the transverse electric (TE) mode and transverse magnetic (TM) mode, which are used in the experiment. The important phenomena of detuning a resonant cavity is discussed in Section 2.4.4.

2.4.1 Magnetron Power Supply

In our experiment, we used the magnetron tube from a commercial MW oven to generate the required 2.45 GHz of MW energy. Magnetron tube operation is based on the motion of electrons under the combined influence of electric and magnetic fields. Basically, the magnetron tube required a *low-voltage-high-current ac filament supply* and a *high-voltage-low-current dc cathode supply*. The microwave output power is directly related to the dc input power. We can measure and adjust the dc input power by employing the circuit of Meiners and Alford [38] in our experiment, as shown in Figure 9.

We bought a small portable MW oven providing 700 Watt of MW power at 2.45 GHz and an extra transformer for the magnetron power supply. We used a variable autotransformer (120 V, 5 A) to supply current for this transformer. To monitor the power input to the cathode d.c. supply, we did not use an ac wattmeter such as described in Ref. [38], but we developed other experimental techniques to measure the input power to the discharge. This topic will be discussed in Section 3. This circuit is very useful because we can supply a constant current to the magnetron filament while allowing for an adjustable level of the d.c. voltage applied to the magnetron cathode.

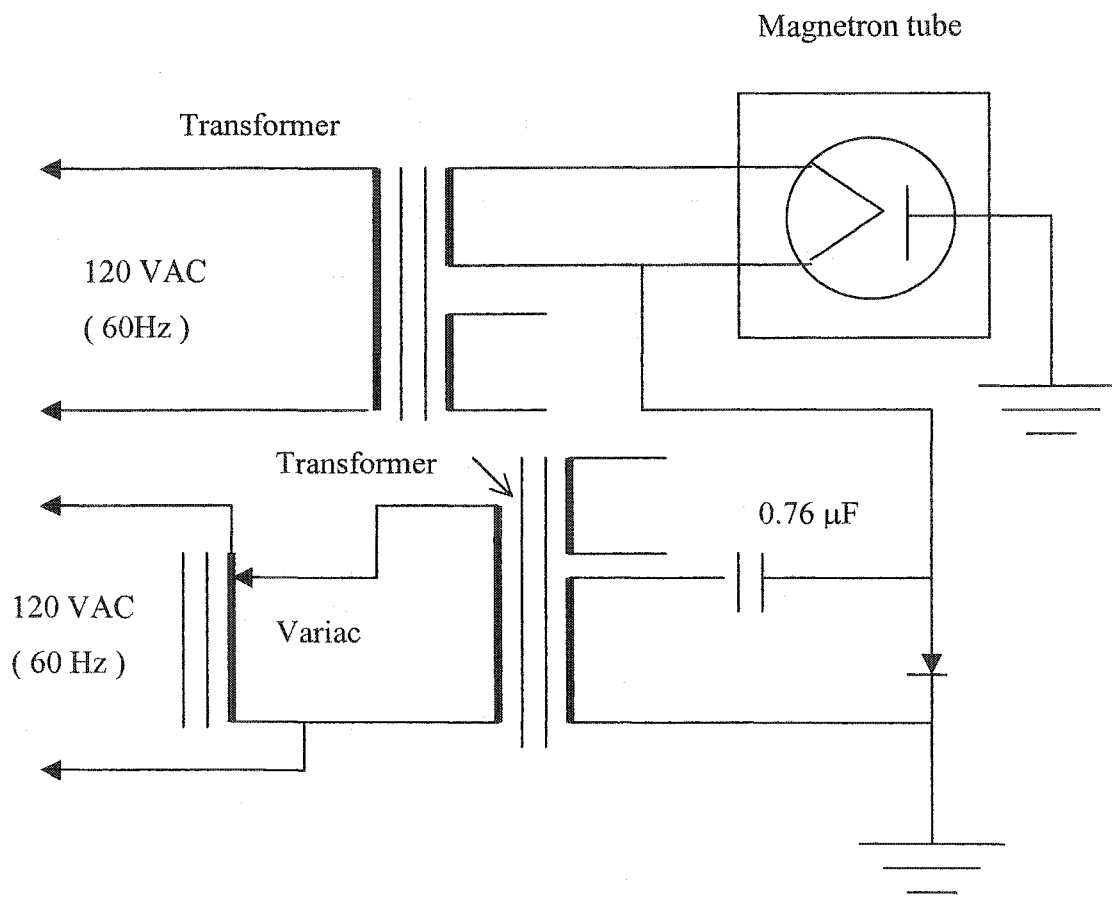


FIG. 9. Magnetron tube circuit.

2.4.2 Design of a Cylindrical Resonant Cavity

In order to generate a MW discharge by using MW energy from a magnetron tube, we had to make a resonant cavity which was designed to correspond to 2.45 GHz. We used a the right circular cylinder resonant cavity (as shown in Figure 10) in our experiment.

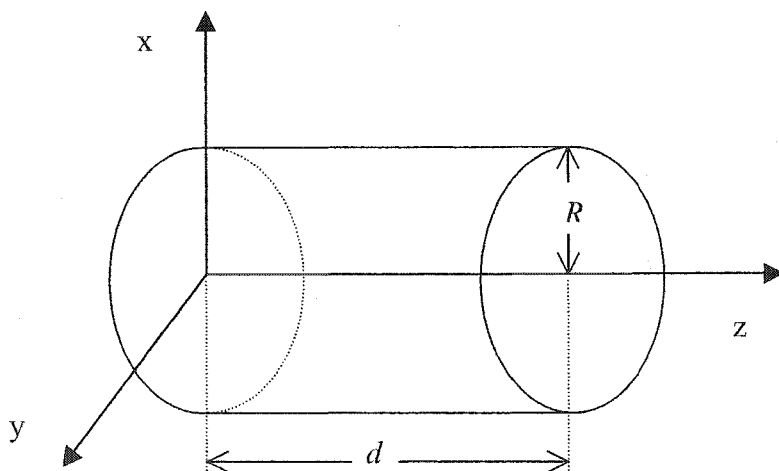


FIG. 10. Right circular cylinder cavity.

We assume that the end surfaces are planar and perpendicular to the axis of the cylinder. Generally, the walls of the cavity are taken to have infinite conductivity, while the cavity is filled with a lossless dielectric with permeability μ and permittivity ϵ .

The relationship between the resonance frequencies and the dimensions of the right circular cylinder resonant cavity with inner radius R and length d can be derived from the propagation of electromagnetic waves in a hollow metallic cylinder. The

detailed theory given, for example, in Ref. [39]. The equations that were used to design the cavities used in our experiment are as follows:

For a TM mode, we have the equation

$$W_{mnp} = \frac{l}{\sqrt{\mu\epsilon}} \sqrt{\frac{x_{mn}^2}{R^2} + \frac{p^2 \pi^2}{d^2}}, \quad (16)$$

where x_{mn} is the n th root of the equation, $J_m(x) = 0$. $J_m(x)$ is the m^{th} order Bessel function. These roots are given in Table I. The integers m , p , and n take on the values $m, p = 0, 1, 2, \dots$, and $n = 1, 2, 3, \dots$; μ is the permeability of the material, ϵ is the permittivity of the material, R is the cavity radius, and d is the cavity length, as shown in Figure 10.

TABLE I. Roots of the Bessel Function $J_m(x) = 0$

$m = 0,$	$x_{0n} = 2.405, 5.520, 8.654, \dots$
$m = 1,$	$x_{1n} = 3.802, 7.016, 10.173, \dots$
$m = 2,$	$x_{2n} = 5.136, 8.417, 11.520, \dots$
\cdot	\cdot
\cdot	\cdot
\cdot	\cdot

For example, for a TM mode corresponding to $m = 0$, $n = 1$, and $p = 2$, designated as $TM_{0,1,2}$, we can rewrite Eq. (16) as follows:

$$w_{012} = \frac{2.405}{\sqrt{\mu\epsilon} R} \left(1 + 6.8309 \frac{R^2}{d^2} \right)^{\frac{1}{2}}. \quad (17)$$

Similarly, for a TE mode, we can write the equation as follows:

$$w_{mnp} = \frac{1}{\sqrt{\mu\epsilon}} \sqrt{\frac{x'_{mn}{}^2}{R^2} + \frac{p^2 \pi^2}{d^2}}, \quad (18)$$

where x'_{mn} is the n th root of $J'_m(x) = 0$. $J'_m(x)$ is the m^{th} order Bessel function that satisfies the boundary condition for this cavity mode. These roots, for a few values of m and n , are shown in Table II. The integer $m = 0, 1, 2, \dots$, but the integers $n, p = 1, 2, 3, \dots$

TABLE II. Roots of the Bessel Function $J'_m(x) = 0$

$m = 0,$	$x'_{0n} = 3.832, 7.016, 10.173, \dots$
$m = 1,$	$x'_{1n} = 1.841, 5.331, 8.536, \dots$
$m = 2,$	$x'_{2n} = 3.054, 6.706, 9.970, \dots$
\cdot	\cdot
\cdot	\cdot
\cdot	\cdot

For example, for the TE mode with $m = n = p = 1$, denoted as TE_{1,1,1}, we can rewrite Eq. (18) as

$$w_{III} = \frac{1.841}{\sqrt{\mu\epsilon} R} \left(1 + 2.912 \frac{R^2}{d^2} \right)^{\frac{1}{2}}. \quad (19)$$

By using these equations, we can design our cavities by calculating the dimensions (d and R) that correspond to our microwave energy (2.45 GHz) and our chosen mode of operation. In the next section, we will discuss in detail how to design and choose suitable resonant cavities in the TE and TM modes of operation for our experiments.

2.4.3 TE Mode and TM Mode

In our experiment, we directly connect a magnetron tube antenna to a resonant cavity in order to generate a MW discharge (as shown in Figure 11). We actually need a cavity with a radius (R) that is approximately 2 times longer than the length of the magnetron tube antenna and with a length (d) that is about 1 foot (~ 0.24 m) long to perform our measurement. We also need both TE and TM modes to compare our data. For this purpose, we wrote a computer program for calculating the size of the cavity using Eqs. (17) and (19), and the result is shown in Figure 12.

We can see from Figure 12 that we chose TE_{1,1,1} and TM_{0,1,2} modes because they can be created in cavities with radii and lengths that satisfy our requirements. We need to fix $d = 0.24$ m, and this corresponds to the cavity $R = 0.037$ m for the TE_{1,1,1} mode and to $R = 0.054$ m for TM_{0,1,2} mode.

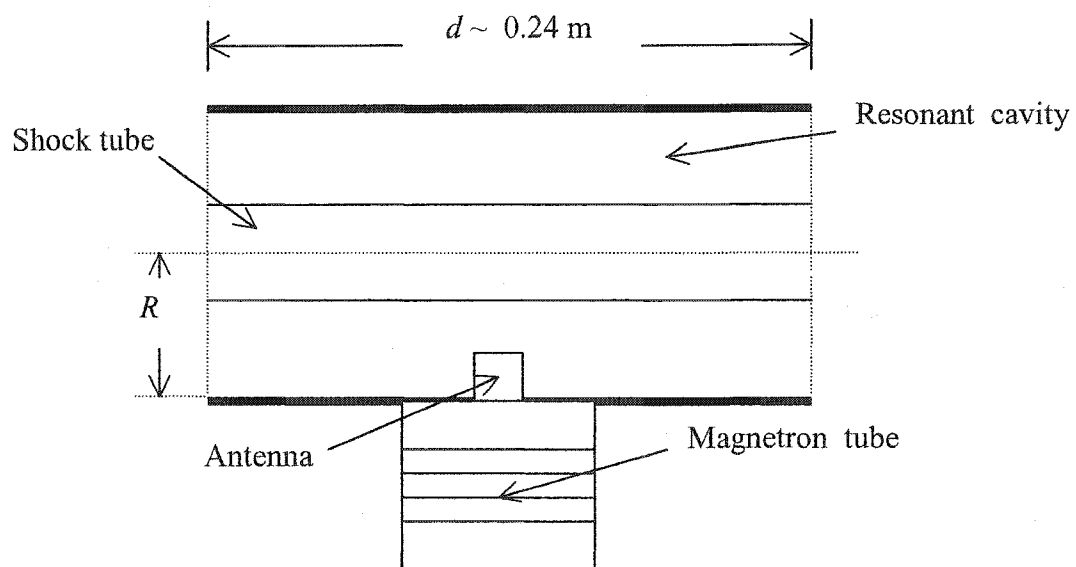


FIG. 11. Scheme of microwave discharge experiment.

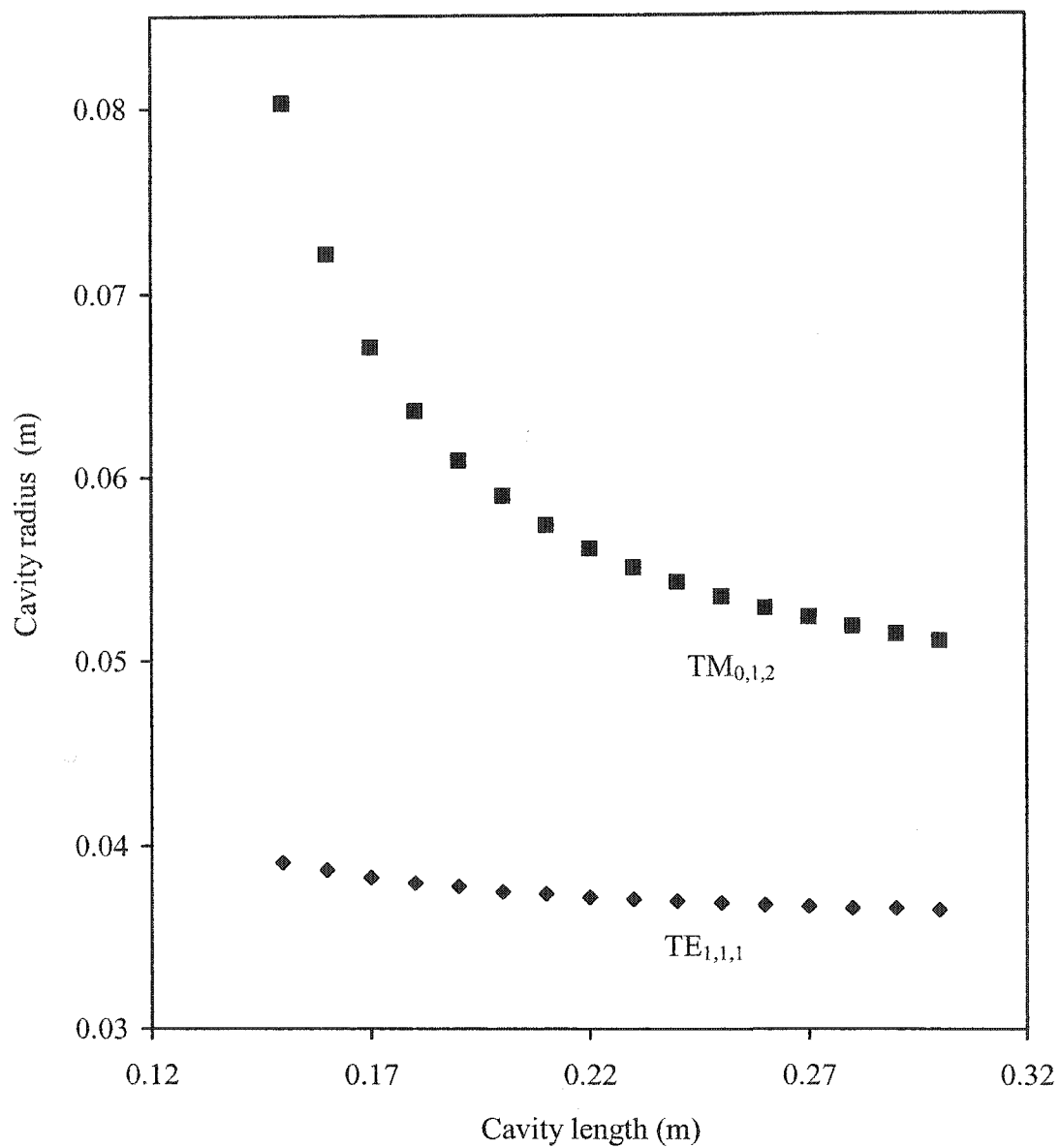


FIG. 12. Right circular cylinder resonant cavity of $TE_{1,1,1}$ and $TM_{0,1,2}$.

For our experiment, we built two resonant cavities that have the same length ($d = 0.24$ m) but have different radii, as discussed above. For diagnostic purposes, we drilled holes along the lengths of the cavities. We will describe this topic in detail in the section on the experimental set-up in Section 3.

2.4.4 Detuning of Resonant Cavity

In Section 2.4.2 and 2.4.3, we assumed that the cavity is an ideal, lossless cavity. In this case, the wall of the cavity has an infinite conductivity, and the cavity is filled with a lossless dielectric material. However, we have to recognize that our cavity is made of an imperfect conductor and filled with an ordinary dielectric material. The MW energy may be lost in a cavity in many ways as shown in Ref. [40]. Furthermore, when we have a MW discharge inside a cavity that has been used in a previous experiment, the conductivity and dielectric constant of the gas in the discharge column will be different in the new experiment. The MW energy, generated by a magnetron tube, will be absorbed inside the cavity, but the absorbed energy will be less than for an ideal cavity. To evaluate this difference, either by experiment or by theory, is a complicated problem. We reduced the degree of complexity of this problem by designing our resonant cavity to be a piston-like cavity, as shown in Figure 13. We can adjust the length of the cavity and tune the size of the cavity to correspond with the MW energy within in the cavity. It was found that the resonant cavity can be built in the same shape as the cavities discussed above (right circular cylinder cavity with radius R), but it should be longer than 0.24 m to allow for precision tuning.

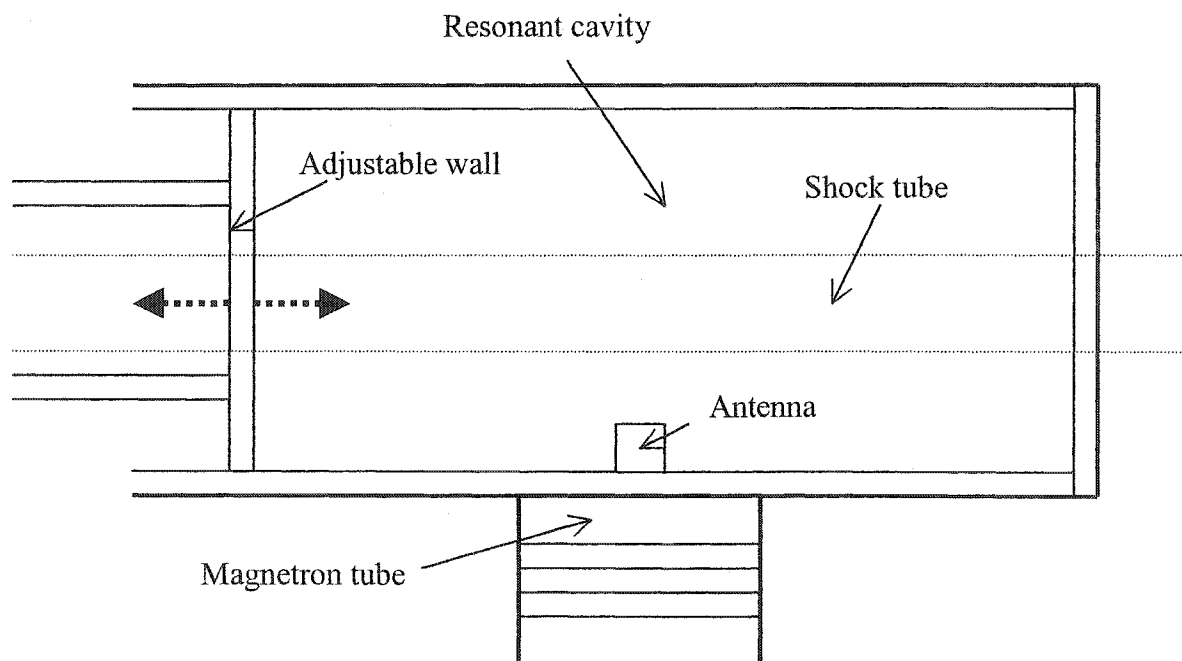


FIG. 13. Detuning of resonant cavity.

Section 3

EXPERIMENT

3.1 Experimental Apparatus

The shock wave generation system consists of the high voltage power supply with a voltage range of 0 kV to 30 kV and a current range of 0 mA to 2.0 mA (Spellman), a spark gap circuit created by Accurate Automation Corporation in Chattanooga Tennessee, [shown in Figure 7 in Section 2.3.1 (not included the spark gap 2)], and the spark gap 2 that was made in our own laboratory. The two copper wires (each with 0.254 cm diameter and 25.4 cm length) covered with a rubber insulator and connected with an electrical feedthrough, were used as two electrodes in the spark gap 2. This system was connected to the shock tube/discharge tube and to the vacuum chamber.

The shock tube/discharge tube is made of quartz and is 1.22 m long, has a 3.3 cm outer diameter (OD), and has a 3.0 cm inner diameter (ID). One end of the tube was connected to a vacuum chamber containing the shock wave generation system via the spark gap 2. Therefore, we call it *the spark gap chamber*. On the other end, the tube was connected to an expansion chamber to avoid complications with the reflected shock wave. Two ports, one in the spark gap chamber and the other at the end of the expansion chamber, allowed for evacuation, filling, and gas flow. The vacuum chamber was evacuated by a mechanical pump (Sargent-Welch), with a pumping speed of about 25-30 l/min, to a background pressure of 10^{-3} Torr. About a quarter of the shock tube/discharge tube's length was covered by the MW discharge.

The MW source was a magnetron tube taken from a 700 Watt commercial MW oven (General Electric JES739WD). It was connected with one of the right circular cylindrical resonant cavities, either in TM or TE modes, and the special magnetron tube operating circuit, as shown in Figure 9 in Section 2.4.1. The shock tube passed through the cavity along its axis. This design allowed us to couple the microwaves into the gas in the shock tube/discharge tube without passing probes through the vacuum wall. In this way, we created a MW discharge that covered about 0.30 m of the tube's length. During the discharge operation, we used a digital multimeter (BK Precision, Model 2704B) to monitor the approximate temperature of the magnetron tube. By doing this, we found that the magnetron tube could be operated, with the temperature of its cooler fins as high as 130 °C.

In our experiments we used Argon (Ar) gas mixture at a research grade purity of (99.99%) for shock wave velocity measurements and a mixture of Ar + H₂ at a research grade purity of 95.0% Ar and 5.0% H₂¹ for MW discharge diagnosis. The gas was filled with a sealed valve (Hoke) from a gas tank. Two capacitance manometer gauges were used to monitor chamber pressure (covering the pressure range 10⁻³ – 10³ Torr) (MKS 122A) via a pressure read-out (MKS PDR-C-2C). We performed our experiment first in the absence and then in the presence of the MW discharge in Ar. The gas exhaust from the experiment was pumped out by a mechanical pump connected to the chamber near the spark gap region, via a controlling valve (Veeco).

¹ 0.01% of N₂ was examined in the MW discharge of Ar gas

A ceramic vacuum-sealed feedthrough to spark gap 2 electrically insulated the shock tube/discharge tube and the vacuum chamber from the shock wave generation system. At the same time, the vacuum chamber had to be insulated from the MW discharge system. A weak gas flow was regulated inside the chamber both during and in the absence of the discharge. Furthermore, we applied a strong flush of fresh Ar through the discharge tube for the purpose of cleaning the chamber walls after every measurement. This procedure was introduced after the gas exhaust was pumped out of the chamber. A general schematic of the experimental apparatus is shown in Figure 14. In this figure, the specific plasma diagnostics, such as the laser deflection technique (Section 3.2) and the imaging monochromator measurement technique (Section 3.3) are not shown. The lay-outs for the specific diagnostic techniques will be described separately in the corresponding sections.

3.2 Determination of Shock Wave Characteristics

3.2.1 Schlieren Measurement Technique

We used the Schlieren technique to study shock wave propagation through the MW discharge. The Schlieren technique is based on the angular deflection experienced by a light ray when passing through a fluid region characterized by refractive index inhomogeneities. Basically, these inhomogeneities are generated by density and temperature variations. Because of its simplicity (simple alignment of the equipment), ease of application, low cost (expensive laser sources are not required), and satisfactory accuracy of results, the Schlieren technique has found extensive use in the study of compressible gas flow and deserves attention in many applications in Physics.

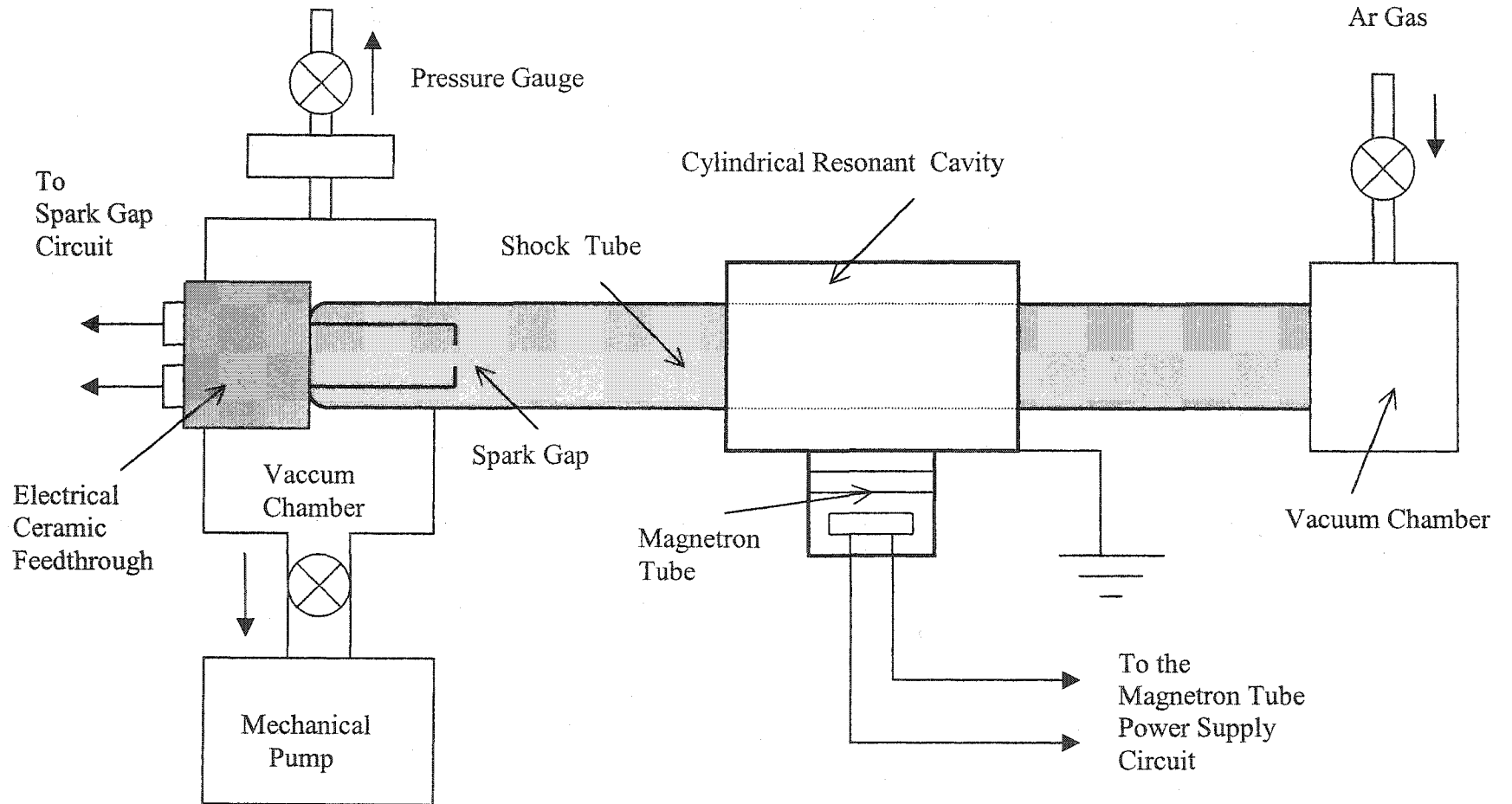


FIG. 14. Schematic of the shock tube/discharge tube and the experiment apparatus.

Hook and Huygens reported their first observations on the Schlieren effect in the 17th century. Schlieren measurement was applied in the manufacture of optical instruments for astronomic studies. August Töepler (1864), who gave it the name *Schlieren*, the German term for striations or inhomogeneities in transparent solids, used this technique in fluid and heat transfer investigations. Töepler also developed a *knife-edge*, which is the first basic tool for flow visualizations, to produce a black and white image in which the intensity of the light is related to the density and temperature gradients in the optical field. Many applications and modifications have been introduced to the original system, including different arrangements of the optical components and the use of special filters to produce color images in lieu of black and white pictures.

Recently, the Schlieren technique has been routinely applied in shock wave and plasma physics. This technique is very useful and well-known in many successful and illuminating applications in these fields [41]. A detailed discussion of the Schlieren technique will not be given here because we can find a complete account in Ref. [42]. However, a brief description will be presented below.

A schematic arrangement used to employ the Schlieren measurement technique is shown in Figure 15.

In order to produce a collimated light beam through the test section, a point light source S is placed at the focal point of a lens L_1 . In the case that no deviation of light rays occurs in the test section, the light rays from the source pass with essentially equal intensity through all parts of the test section and are reunited at a point in the image I of the light source. This image is formed by the lens L_2 . Thus, if we put a knife edge at

the position of the image I , intercepting some of the rays through I , we should get the uniform darkened image of the test section on the screen. However, if we have some of the light rays deflected by the inhomogeneities of the refractive index at some locations in the test section, the image on the screen of those points will be lighter or darker than the rest of the field, depending on the direction of deviation.

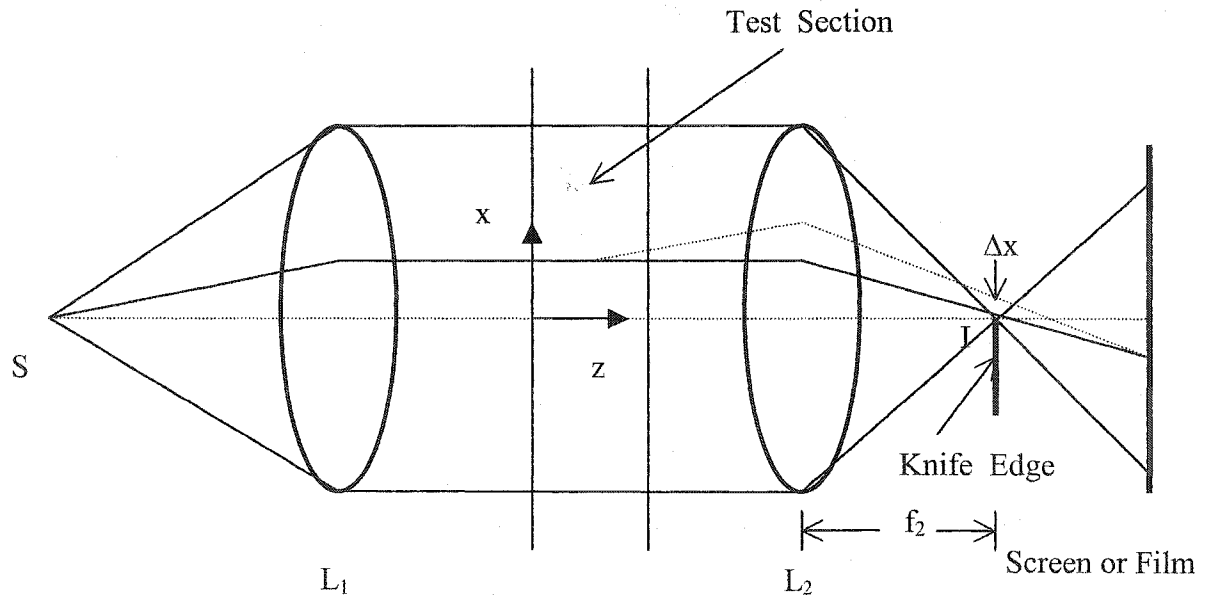


FIG. 15. Schematic of Schlieren photography arrangement.

From the Schlieren measurement technique shown in Figure 15, the relationship between the component of the angular deviation that is perpendicular to the knife edge and the relative change in light intensity on the screen is approximately

$$\frac{\Delta I}{I} = \frac{\alpha_x f_2}{\Delta x}, \quad (20)$$

where a coordinate system has been chosen, as shown in Figure 15, in which x is the direction perpendicular to the knife edge and the z -axis is the direction of the

undeviated ray. In this equation, α_x is the x -component of the total angular deviation, f_2 is the focal length of lens L_2 , I is the intensity at the screen, and Δx is the unobscured width (in the x direction) of the image of the source. We can calculate the x -component of the total angular deviation that is related to the x -component of the gradient of the refraction index by using the expression

$$\alpha_x = \int \frac{\partial}{\partial x} \ln n(x, y, z) dz = \int_0^L \frac{1}{n} \frac{\partial n}{\partial x} dz, \quad (21)$$

where n is the refractive index, and the limits of integration range over the length of the test section in the z direction.

For a plasma, n (the phase index of refraction) is given by

$$n - 1 = K_1 N_a - K_2 \lambda^2 N_e, \quad (22)$$

where N_a and N_e are atom and electron number densities, respectively, K_1 and K_2 are positive constants, and λ is the wavelength of the light.

We can also use this technique to apply to the study of shock fronts and other regions of large density gradient. Their Schlieren photographs, positions, and motions are conveniently studied and observed by this technique. However, if the plasma is only partially or weakly ionized, the atomic contributions to the refractive index may dominate, and the gradients observed will be the gradients in atom and ion number density.

We may also choose a laser to be the light source in the Schlieren system. We will discuss the laser Schlieren system in the following section.

3.2.2 Laser Schlieren System

Figure.16 shows the schematic of the laser Schlieren set-up and the experimental procedure followed for shock wave propagation analysis. A low powered ($< 5\text{mW}$) laser is passed through the test section and received by an array of very high response ($\sim 1\text{-}20\text{ ns}$) photodiodes placed on the opposite side of the test section. The principle of operation of a laser Schlieren system is the same as that of the ordinary Schlieren technique, except that the voltage signals are obtained from photodiodes instead of the image on the screen or film. These voltage signals relate to the density gradient fluctuations of the flow field.

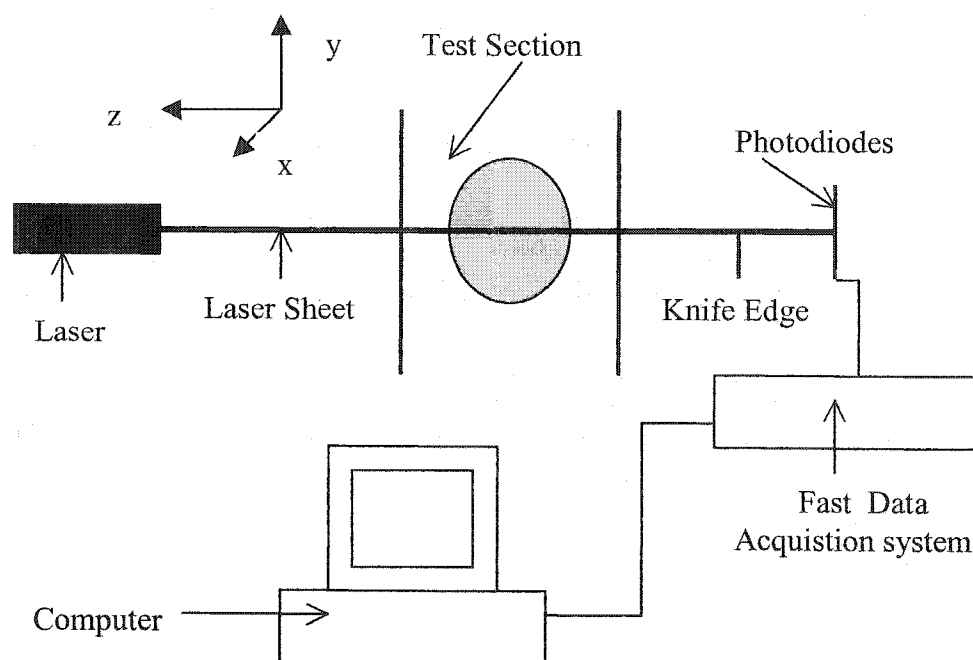


FIG. 16. Schematic of the laser Schlieren set-up.

Shock wave characteristics can be observed and studied by applying this technique. A laser sheet was generated using a cylindrical lens. When the laser sheet passes through a shock front, it is deflected and a time trace obtained from the array of photodiodes shows unsteady voltage signals as shown in Figure 17.

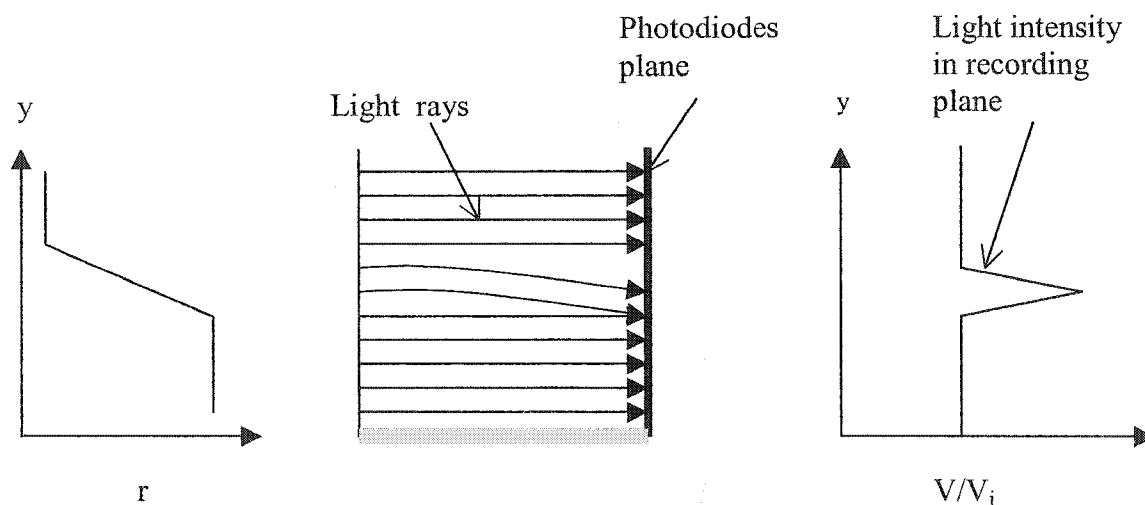


FIG. 17. Voltage signal (density gradient profile) across a shock wave.

This arrangement can produce the information on the existing density gradient fluctuations in the flow and the fluctuating nature of the flow. However, this arrangement should be free from its structural vibrations and initially required very careful alignment of the laser sheet itself. Therefore, a more rigid Schlieren set-up was later used. It is described in the following section.

3.2.3 Experiment Set-up

We applied the laser Schlieren technique in our experiment for studying shock wave characteristics. Two Helium-Neon laser heads (JDS Uniphase, Model 1101) compatible with the Model 1200 power supply, available in either 100/120 or 220 V AC configurations, were introduced to our experiment arrangement. These two laser heads have 1.5 mW minimum rated output power, 633 nm wavelength light, and 0.48 to 0.81 mm laser beam diameter. We also used two high response (~ 20 ns) photomultiplier tubes (PMT) from Hamamatsu (Model R1527) to detect a laser beam at the opposite side of the shock tube test section. These two photomultiplier tubes were supplied by a DC high voltage power supply (Keithley, Model 247) and connected to a two-channel oscilloscope (Tektronix, Model TDS 340A) for displaying signals. The right circular cylindrical resonant cavity designed to have two circular holes on the envelope was attached to our experiment, as shown in Figure 18. These two holes were separated by about 3.15 inches, or 8.0 cm, and were used to observe and study the characteristics of the shock wave created by a spark gap in neutral gas.

The gas pressure was varied from 20 to 100 Torr. The acoustic shock wave was generated by a spark gap driven by a triggered spark gap switch and high voltage capacitor. The stored pulse energy could be varied by changing the spark gap distance, as shown in Section 2.3.2. The change of acoustic shock wave propagation velocity at two different positions along the propagation path inside the shock tube was measured by this technique. The laser photo deflection amplitude is proportional to the shock density gradient. Thus, this technique provides an accurate measure of shock profiles and time-of-flight for the shock wave. The laser photo deflection waveform signals

were recorded by a two-channel oscilloscope. Two laser beams with a separation of about 8.0 cm were set perpendicular to the shock wave propagation path.

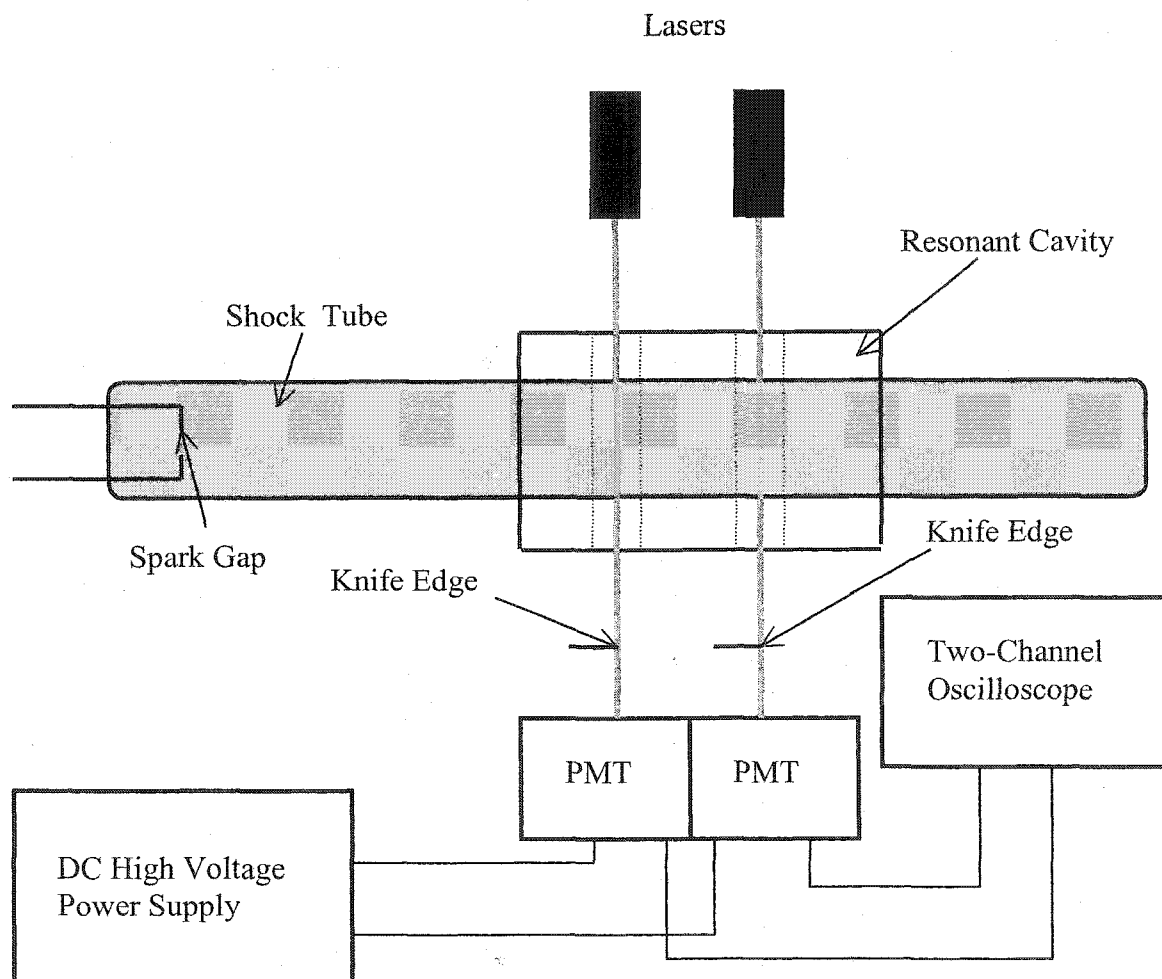


FIG. 18. Shock wave characteristic experimental set-up.

3.2.4 Laser Schlieren Technique Results and Discussion

The laser deflection waveform signals were detected in our first series of experiments by a two channel digital oscilloscope after a careful alignment of the experimental apparatus. The deflection waveform signals in Nitrogen (N_2), Neon (Ne), and Argon (Ar) were recorded at a variety of gas pressures. Typical characteristics of these signals for N_2 and for Ar are shown in Figures 19 and 20, respectively. The shock wave profiles can be derived from these signals, as shown in Figures 21 and 22. The data in Figures 19 and 20 can be collected by using only one laser beam at the 1st or 2nd holes on the resonant cavity.

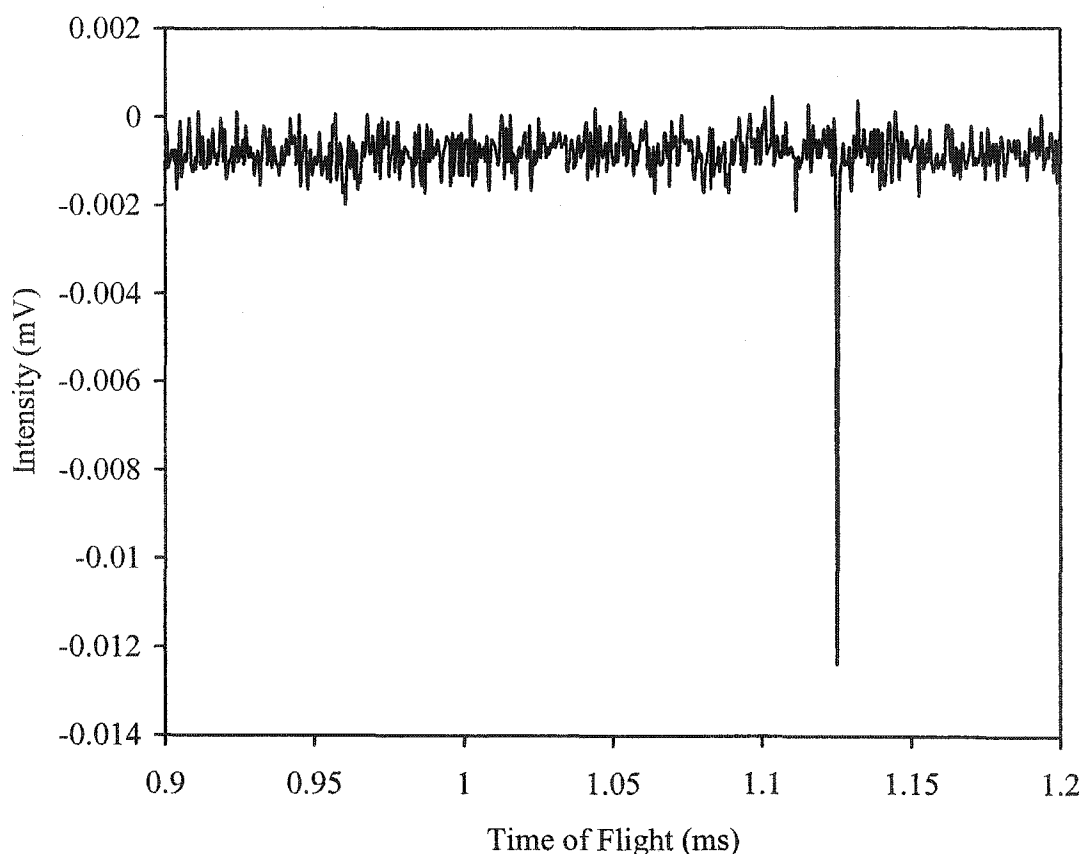


FIG. 19. Shock wave deflection waveform signal in neutral N_2 at 20 Torr and 10 kV d.c. high voltage to spark gap.

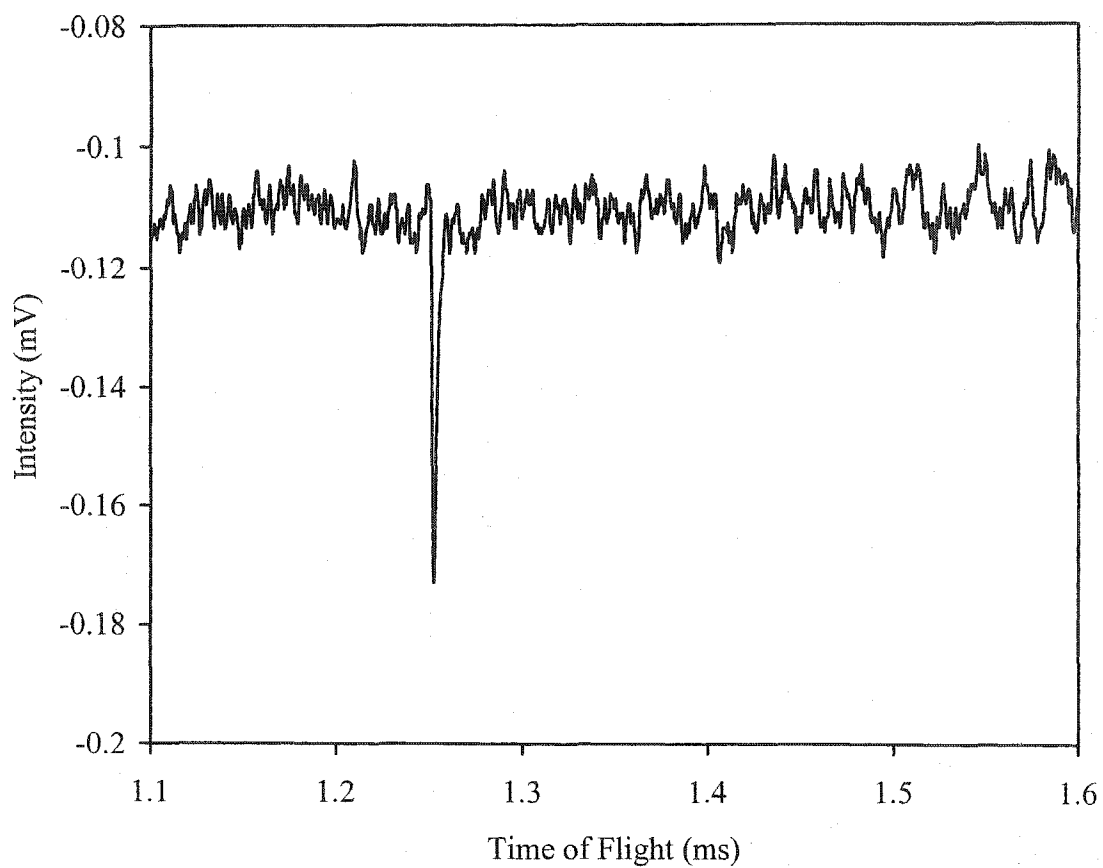


FIG. 20. Shock wave deflection waveform signal in neutral Ar at 20 Torr and 10 kV d.c. high voltage to spark gap.

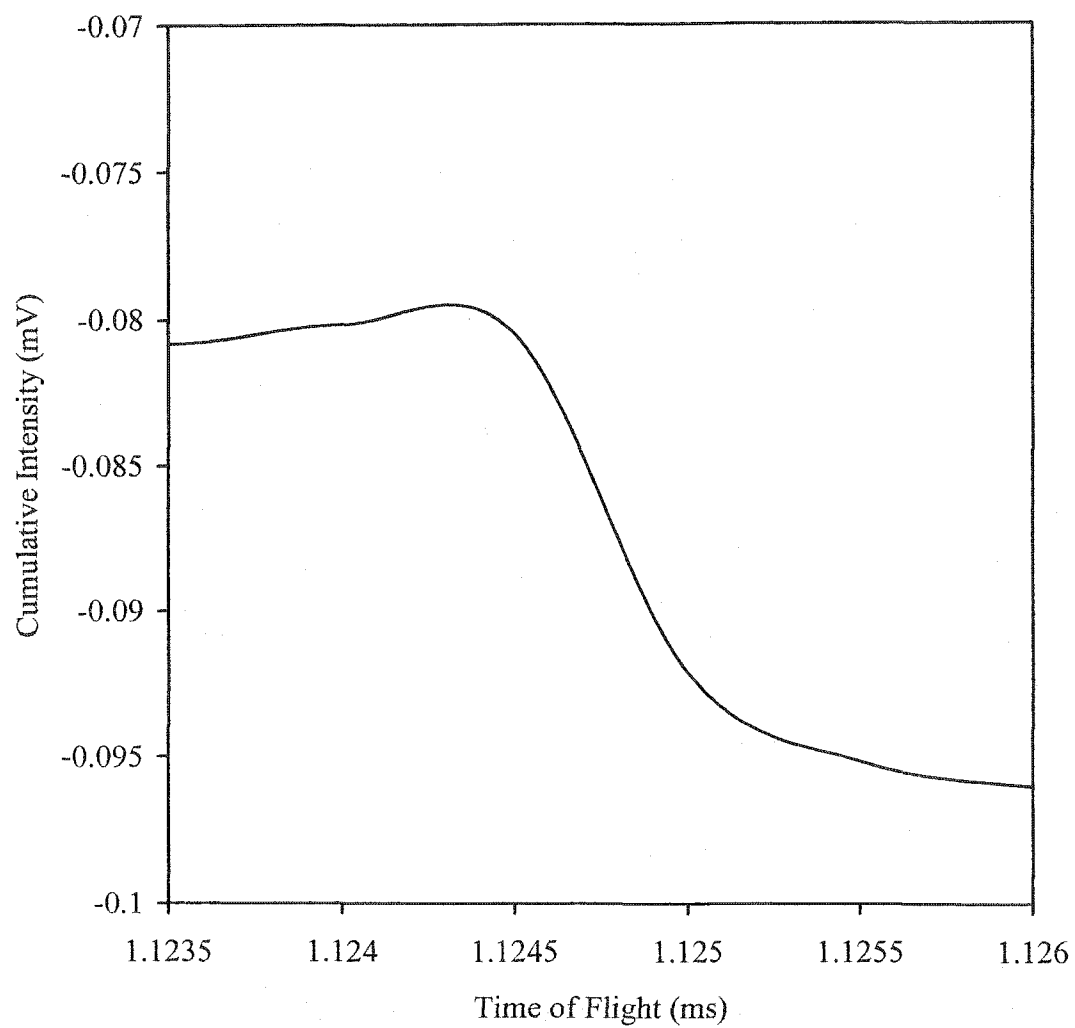


FIG. 21. Shock wave profile in neutral N₂.

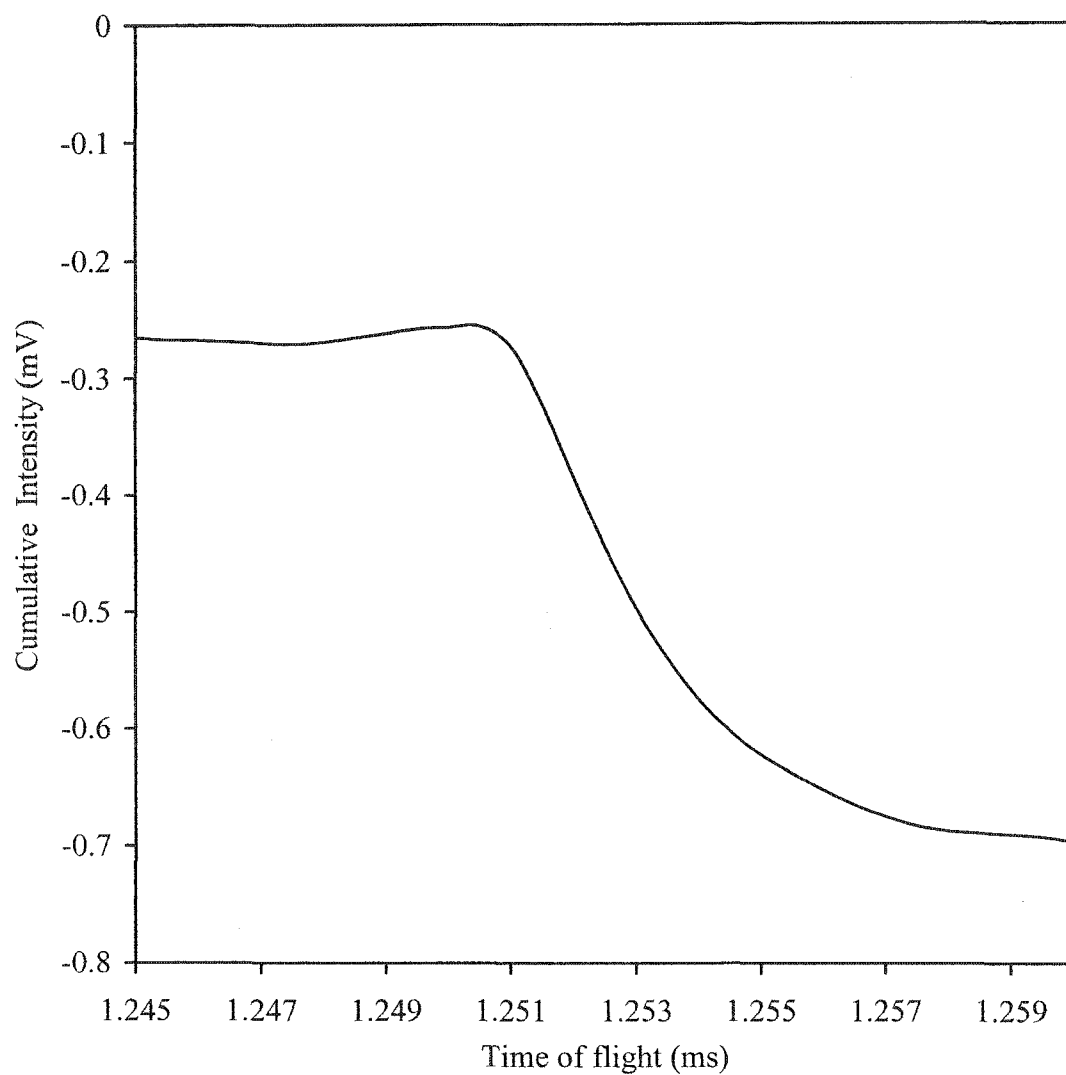


FIG. 22. Shock wave profile in neutral Ar.

The times-of-flight shown in Figures 19 to 22 are the differences between the times-of-arrival of the shock wave at a given position and the times of the shock wave generation. By using two laser beams at the same time, we can get the time-of-flight to two different position from the same shock wave, as shown in Figure 23.

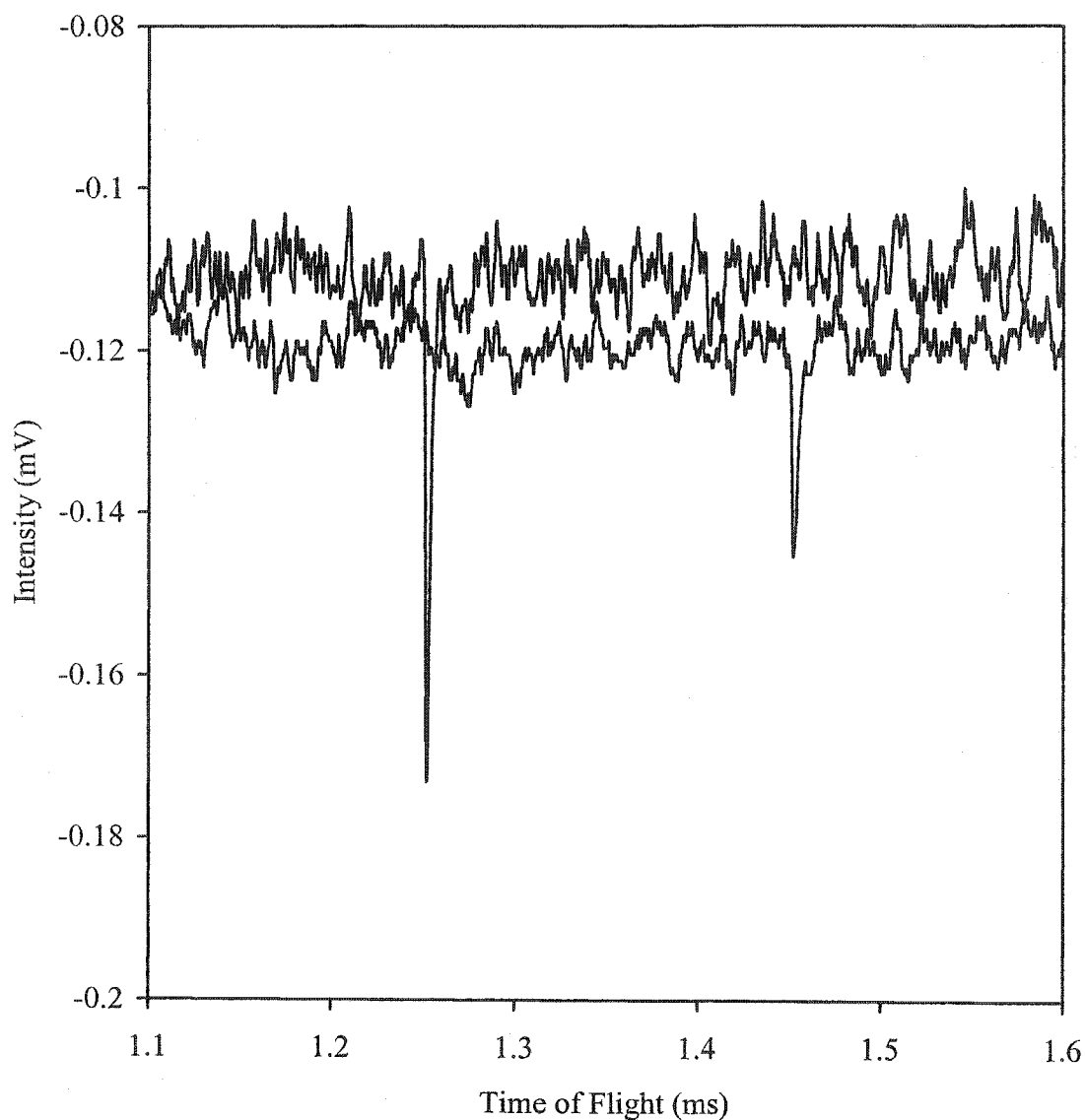


FIG. 23. Shock wave deflection waveform signal from two laser beams in neutral Ar at 20 Torr and 10 kV d.c. high voltage to spark gap.

We can determine the average velocity and the local velocity of a shock wave in neutral gas by using those sets of data and a simple method of calculation, as shown in Figure 24.

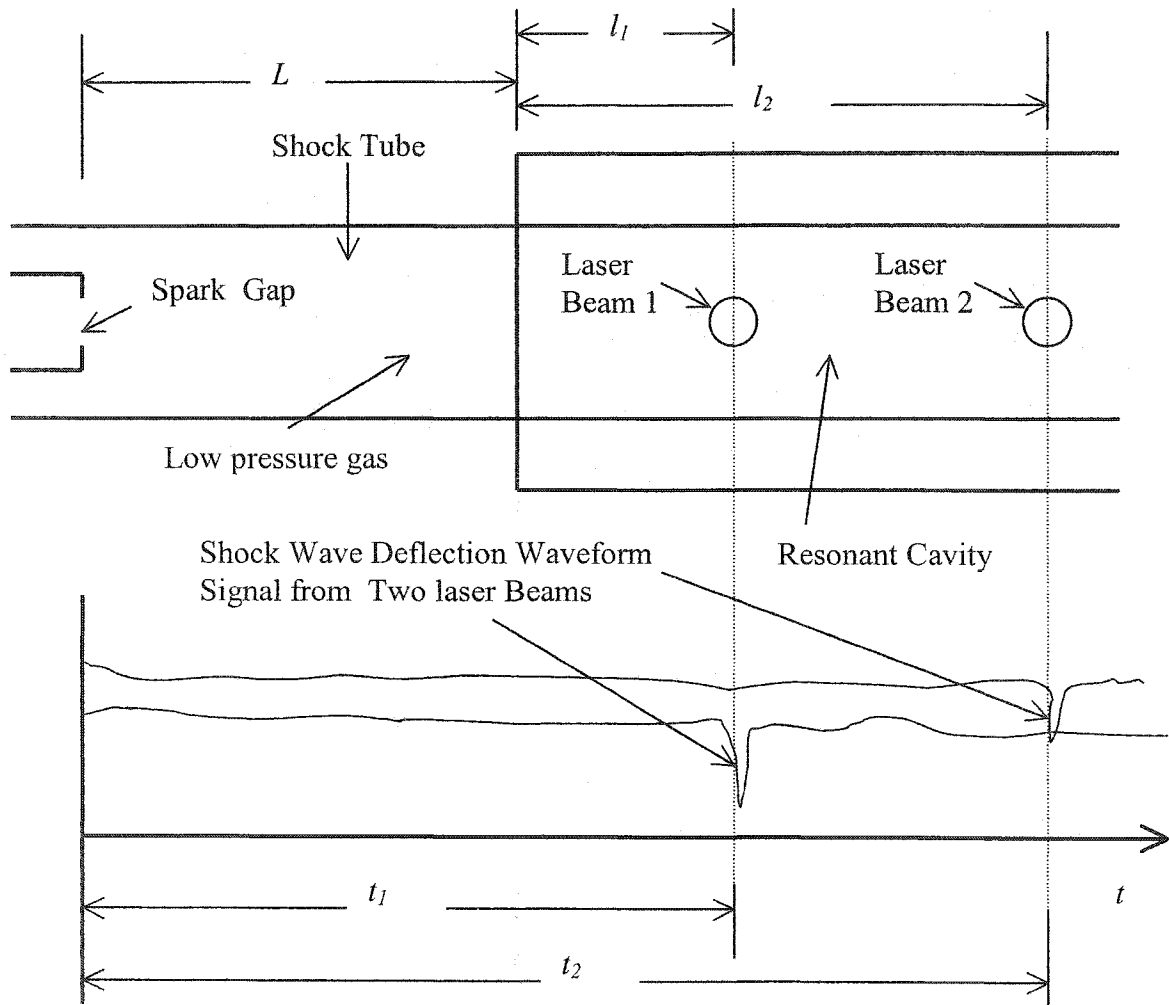


FIG. 24. Calculation of average velocity and local velocity in neutral gas.

We use data for neutral gases at different pressures and a certain value of d.c. high voltage applied to the spark gap (10 kV). We can then calculate an average velocity and a local velocity by using the following equations:

$$V_{1ng} = V[\text{spark}, 1^{st}] = (L + l_1)/t_1, \quad (23)$$

$$V_{12ng} = V[1^{st}, 2^{nd}] = (l_2 - l_1)/(t_2 - t_1), \quad (24)$$

and

$$V_{2ng} = V[\text{spark}, 2^{nd}] = (L + l_2)/t_2, \quad (25)$$

where V_{1ng} and V_{2ng} are the average velocities of a shock wave from the spark gap to the 1st and 2nd holes (or to the 1st or 2nd laser beam), respectively, V_{12ng} is the local velocity between the same two points, L , l_1 , and l_2 are the distances shown in Figure 24, and t_1 and t_2 are the times-of-flight of the shock wave measured by the two-channel oscilloscope at the 1st and 2nd holes, respectively.

We plot the two average velocities and the local velocity in neutral N_2 , Ne, and Ar as functions of gas pressure, as shown in Figures 25, 26, and 27, respectively. The spark gap distance (d) in those three set of experiments is approximately 0.38 cm. The increase of gas pressure in a shock tube reduces both the average and the local shock wave velocities. When we increase the gas pressure we increase the density of the gas, which affects directly the velocity of a shock wave. A shock wave cannot propagate very fast when the gas density is increased so that and the gas molecules or atoms pile up at the shock front. For this reason, the shock wave deflection waveform signal is very strong (very high intensity) when we increase the gas pressure. As the shock wave

propagates through the neutral gas, friction slows it down. This effect can be observed by noting that the local velocity is smaller than the average velocity, as shown in Figures 25 to 27. For the same reason, the average velocity V_{2ng} is smaller than the average velocity V_{1ng} .

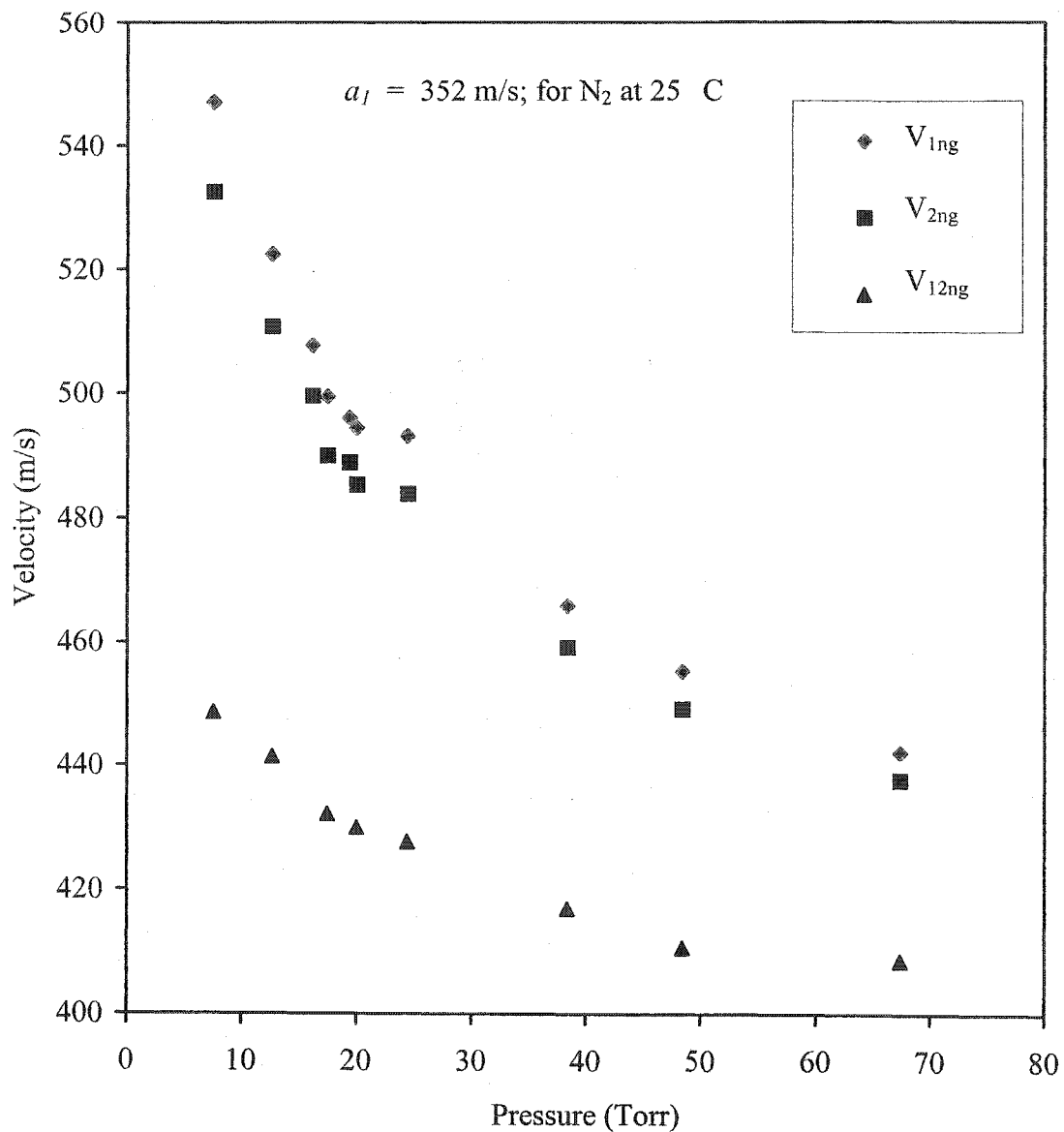


FIG. 25. Average and local velocity of shock wave in neutral N_2 and $d = 0.38 \text{ cm}$.

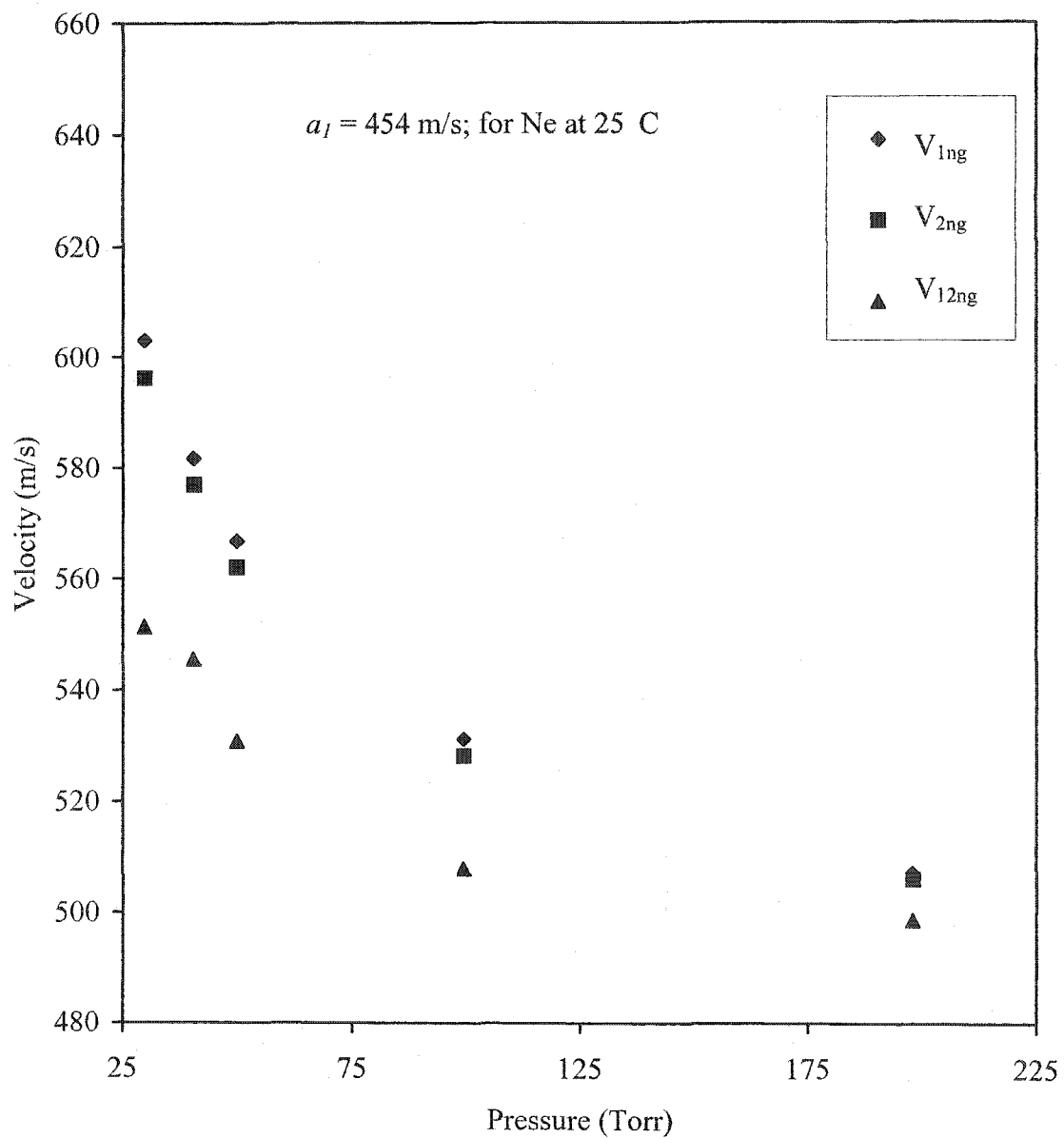


FIG. 26. Average and local velocity of shock wave in neutral Ne and $d = 0.38 \text{ cm}$.

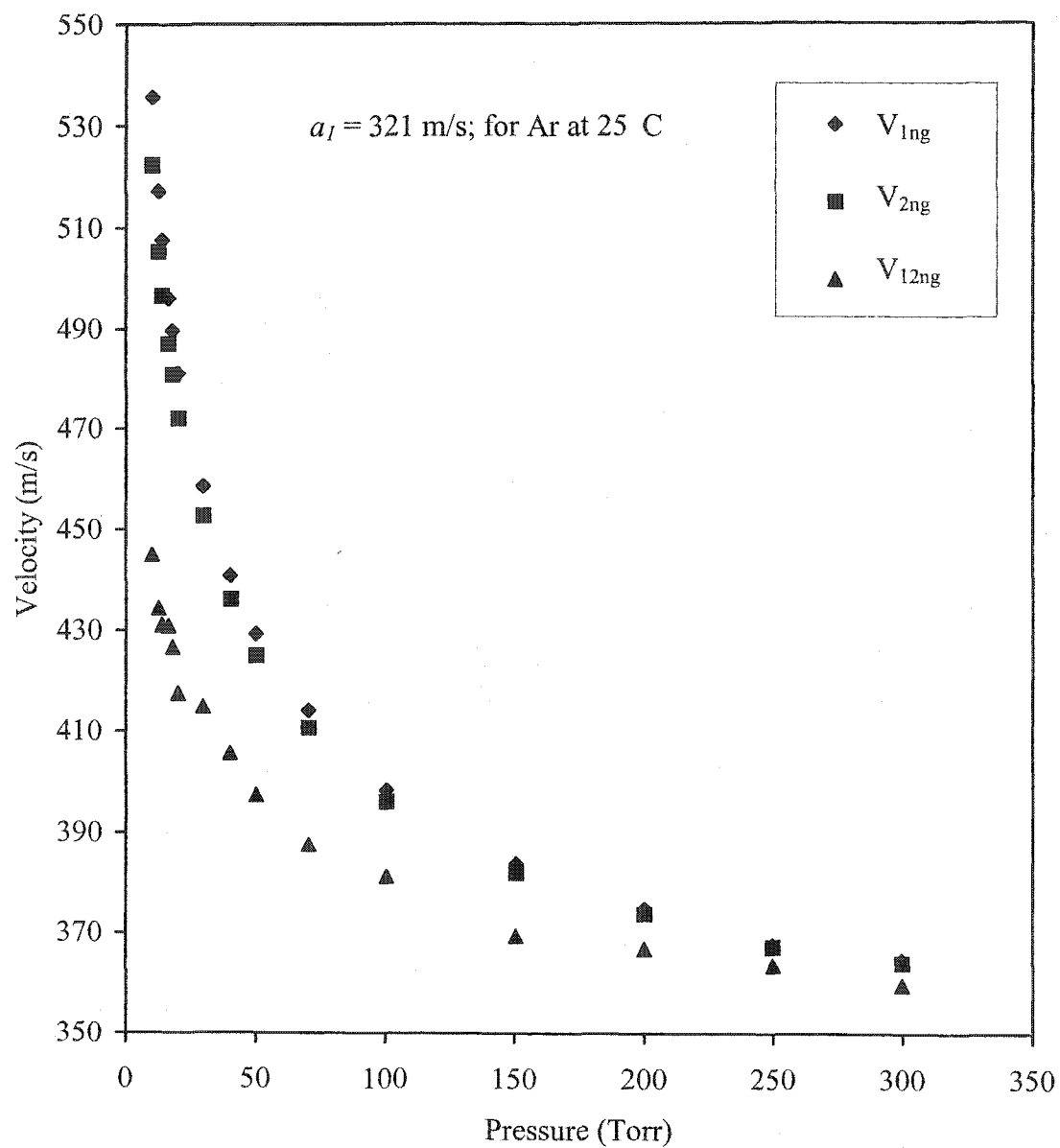


FIG. 27. Average and local velocity of shock wave in neutral Ar gas and $d = 0.38 \text{ cm}$.

From Figures 25 to 27, we can see that the average velocities of the shock wave in neutral N₂, Ne, and Ar (V_{1ng} and V_{2ng}) are not the best values to represent the shock wave velocity in our experiments. However, we can see that the local velocities of the shock wave (V_{l2ng}) can be used to describe the phenomena of the dispersion of a shock wave in neutral gas and maybe in a discharge. We will focus on the local velocity of a shock wave in both a neutral and in a MW discharge.

From those three sets of data, we can use those local velocities of the shock wave in three different gases to calculate three Mach numbers in front of the shock wave by using Eqs. (14) and (15) in Section 2.2.2. By doing this, we assume that *the temperature of the gas in front of the shock wave does not change much as the gas pressure changes, or in other words, the temperature in front of the shock wave remains constant while the gas pressure is changing.* The gas temperature in front of the shock wave is equal to the room temperature (~25 °C) during the experiment.

The ratio between the temperature behind and the temperature in front of the shock wave (relative temperature (T_2/T_1)) was calculated by using Eq. (12) in Section 2.2.2 and plotted as a function of gas pressure in Figure 28. We can also calculate the relative pressure (p_2/p_1), and relative density (ρ_2/ρ_1), as shown in Figures 29 and 30, by using Eqs. (10) and (11) from Section 2.2.2. According to this assumption, the temperature in front of the shock wave (T_1) in all gases is 298.15 K, and the density in front of the shock wave (ρ_1) can also be calculated. Thus, the total energy per unit volume, which is proportional to $\rho_1 (T_2 - T_1)$, was derived and plotted in Figure 31 as a function of the gas pressure. We calculated (by using Eq. (13) in Section 2.2.2) and plotted the Mach number behind of the shock wave (M_2) as a function of gas pressure in

Figure 32 for all three neutral gases. By using the set of data of the relative temperature and pressure, we also derived the relative number density (n_2/n_1) of the shock wave in all three neutral gases and plotted them against the gas pressure, as shown in Figure 33.

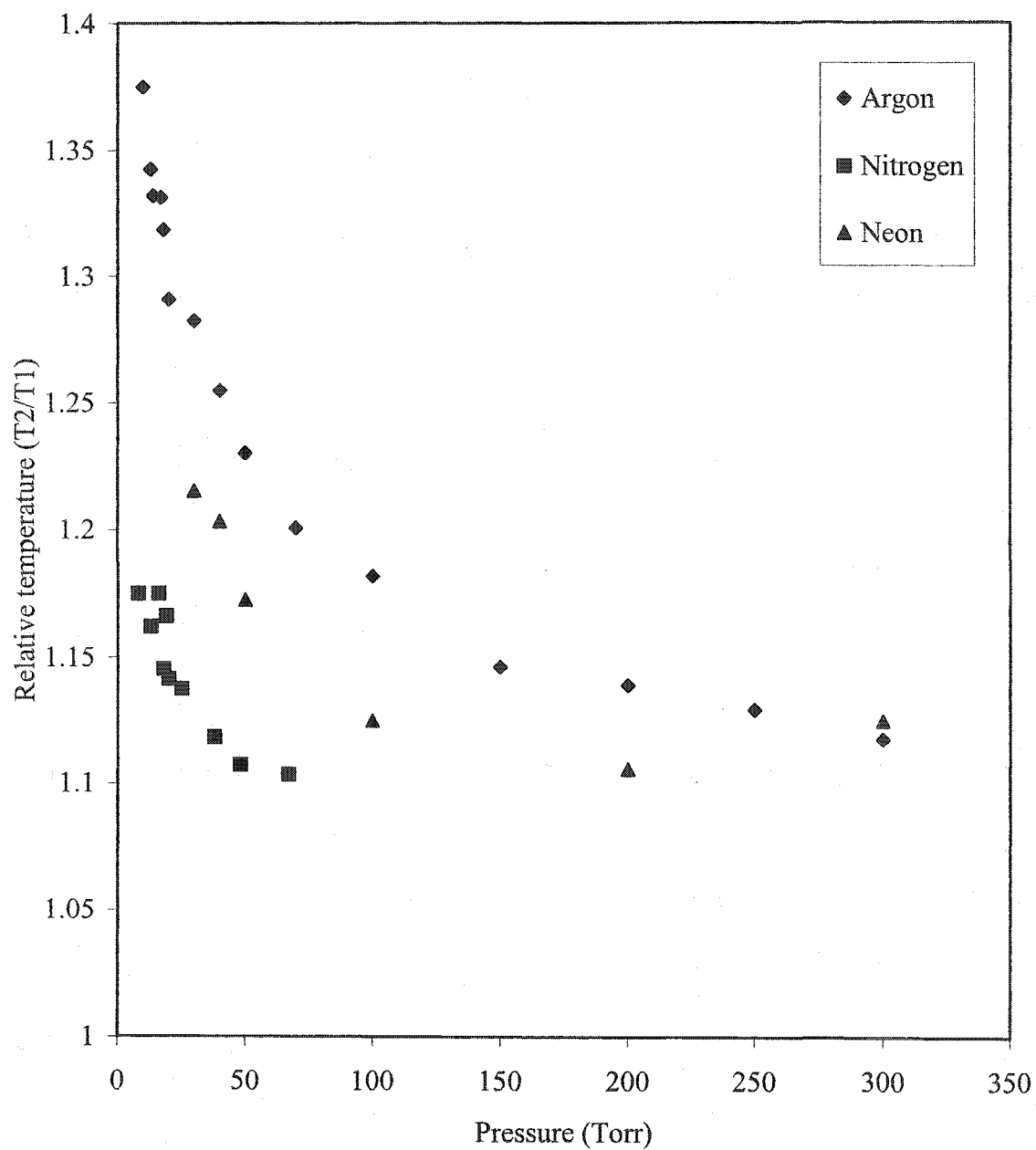


FIG. 28. Relative temperature of shock wave in neutral Ar, N₂, and Ne.

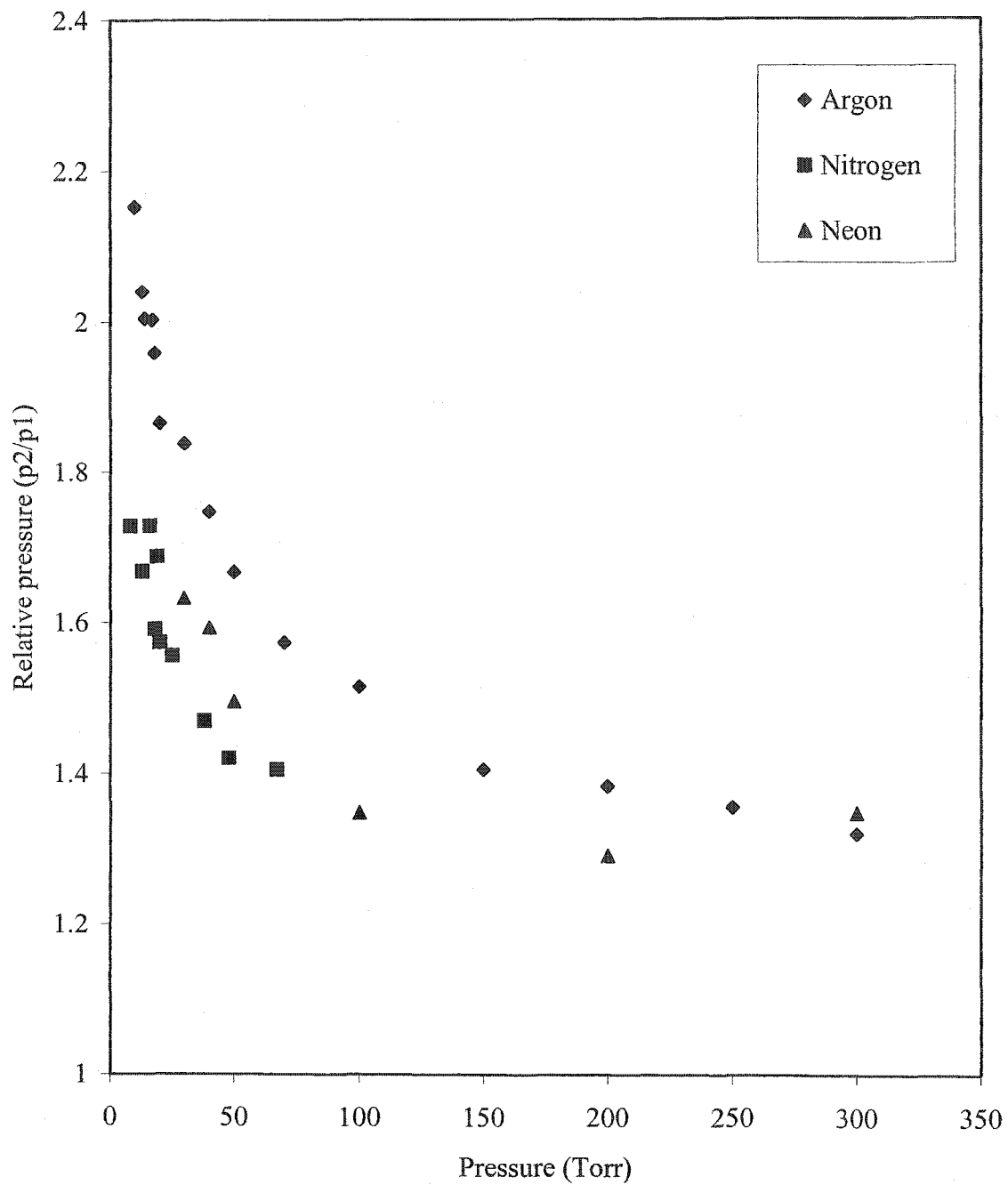


FIG. 29. Relative pressure of shock wave in neutral Ar, N₂, and Ne.

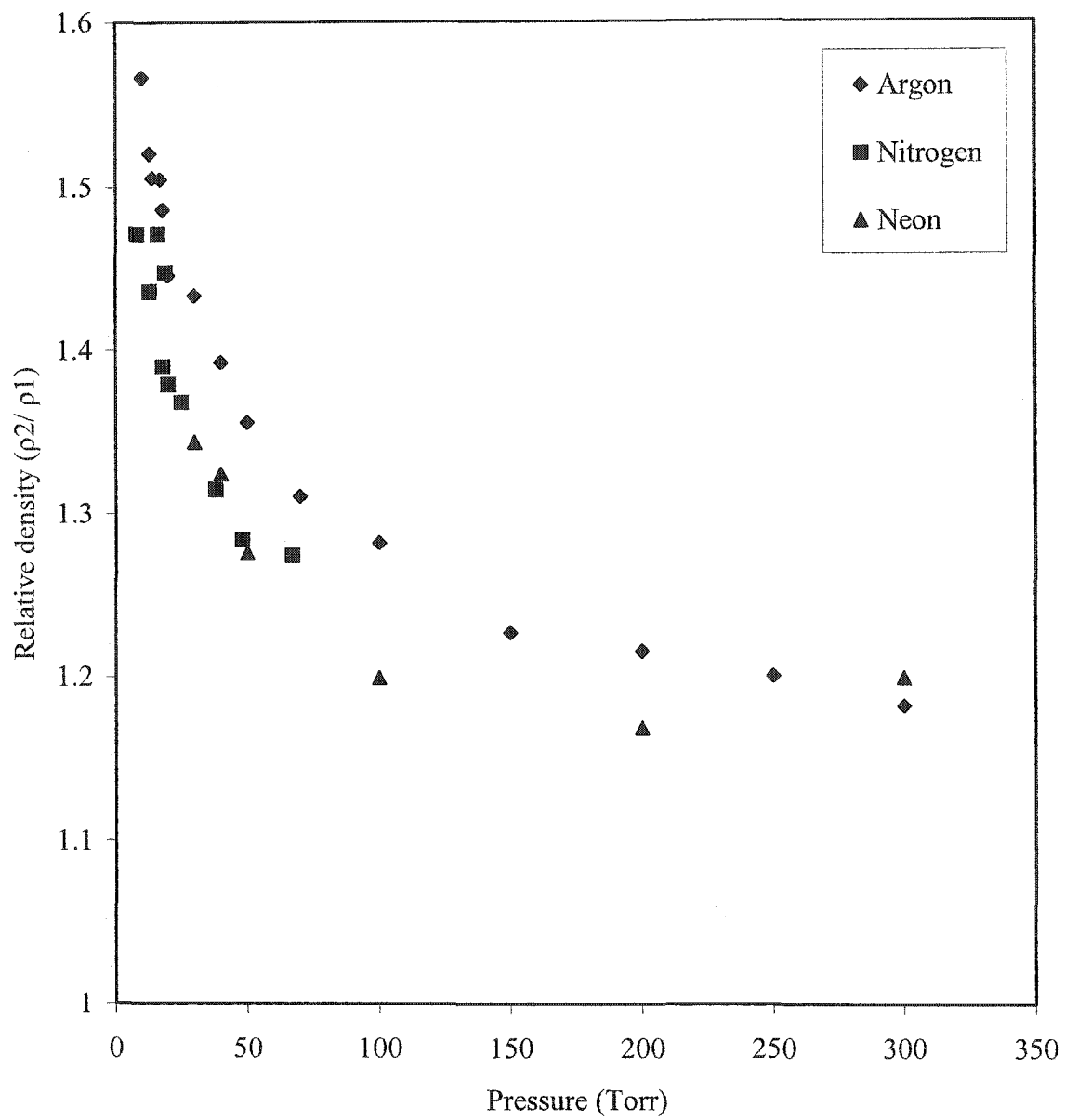


FIG. 30. Relative density of shock wave in neutral Ar, N₂, and Ne.

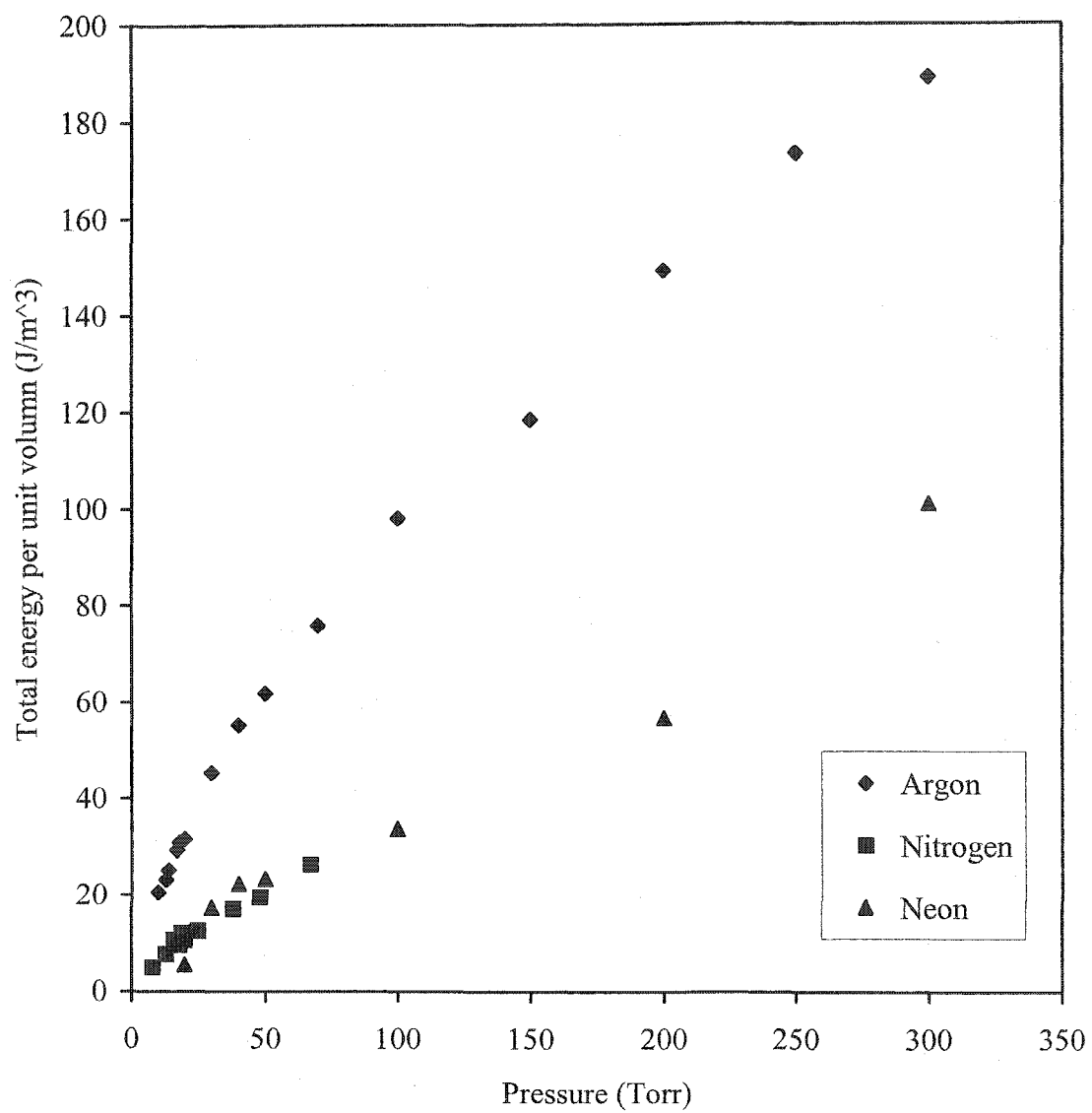


FIG. 31. Total energy per unit volume of shock wave in neutral Ar, N_2 , and Ne.

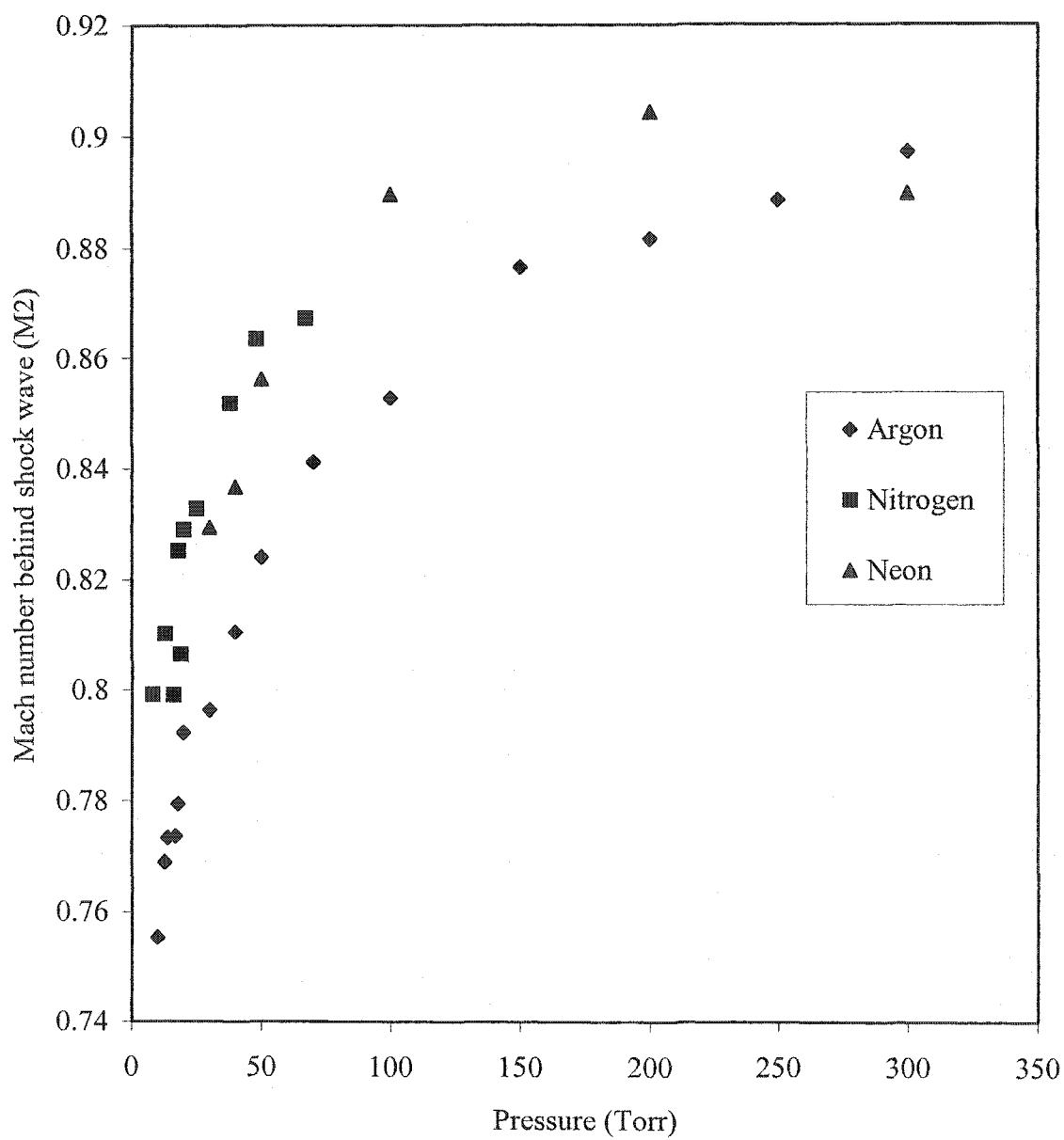


FIG. 32. Mach number behind shock wave in neutral Ar, N₂, and Ne.

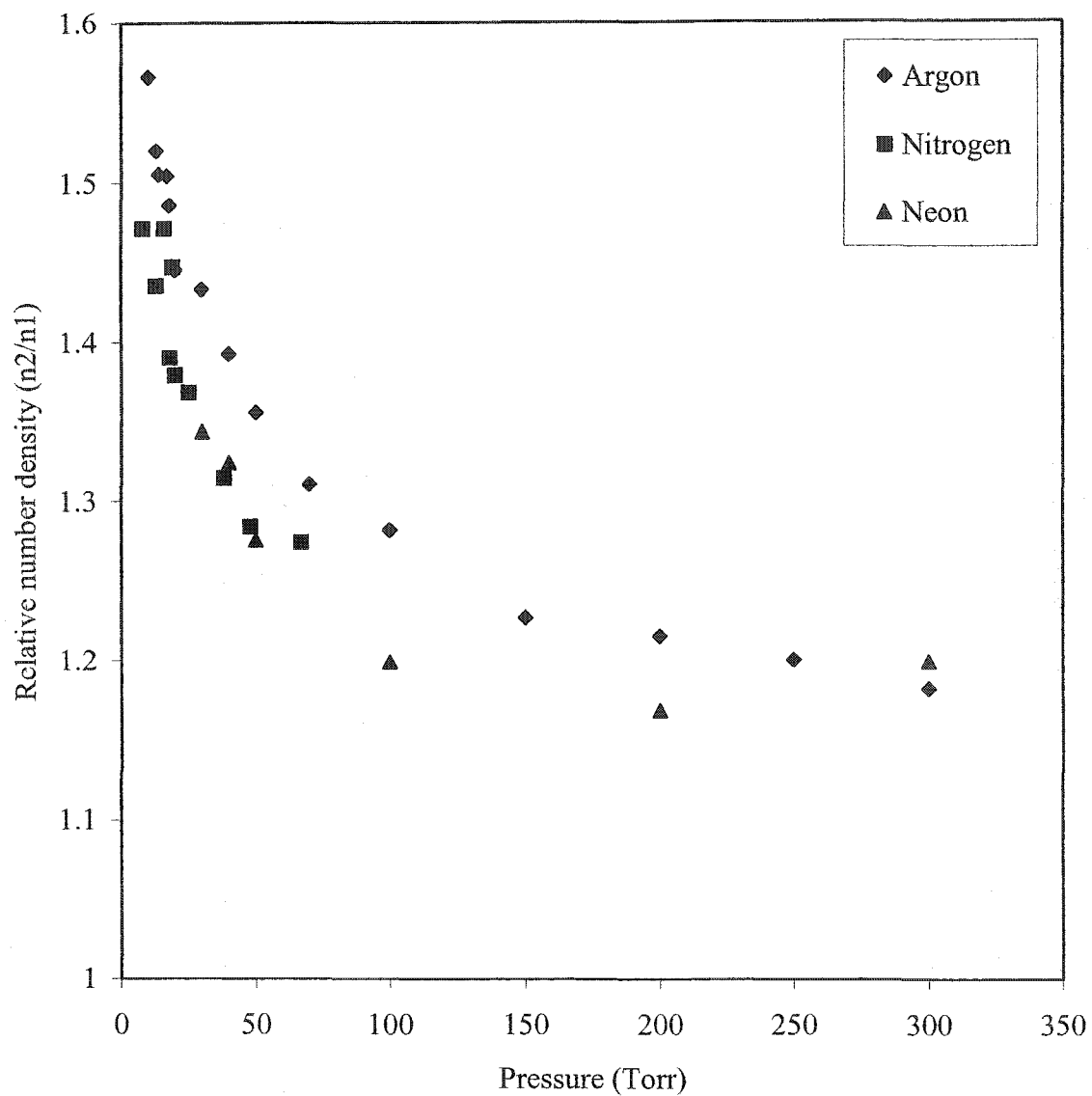


FIG. 33. Relative number density in neutral Ar, N₂, and Ne.

The voltage dependence of the average velocity of a shock wave in neutral N_2 gas was measured by using the 1st laser deflection waveform signal at 30 Torr and plotted in Figure 34. The average velocity of the shock wave produced at a spark gap distance (d) of about 0.50 cm increases when the d.c. high voltage power supply is increased from 5 to 12 kV, as shown in the Figure 34.

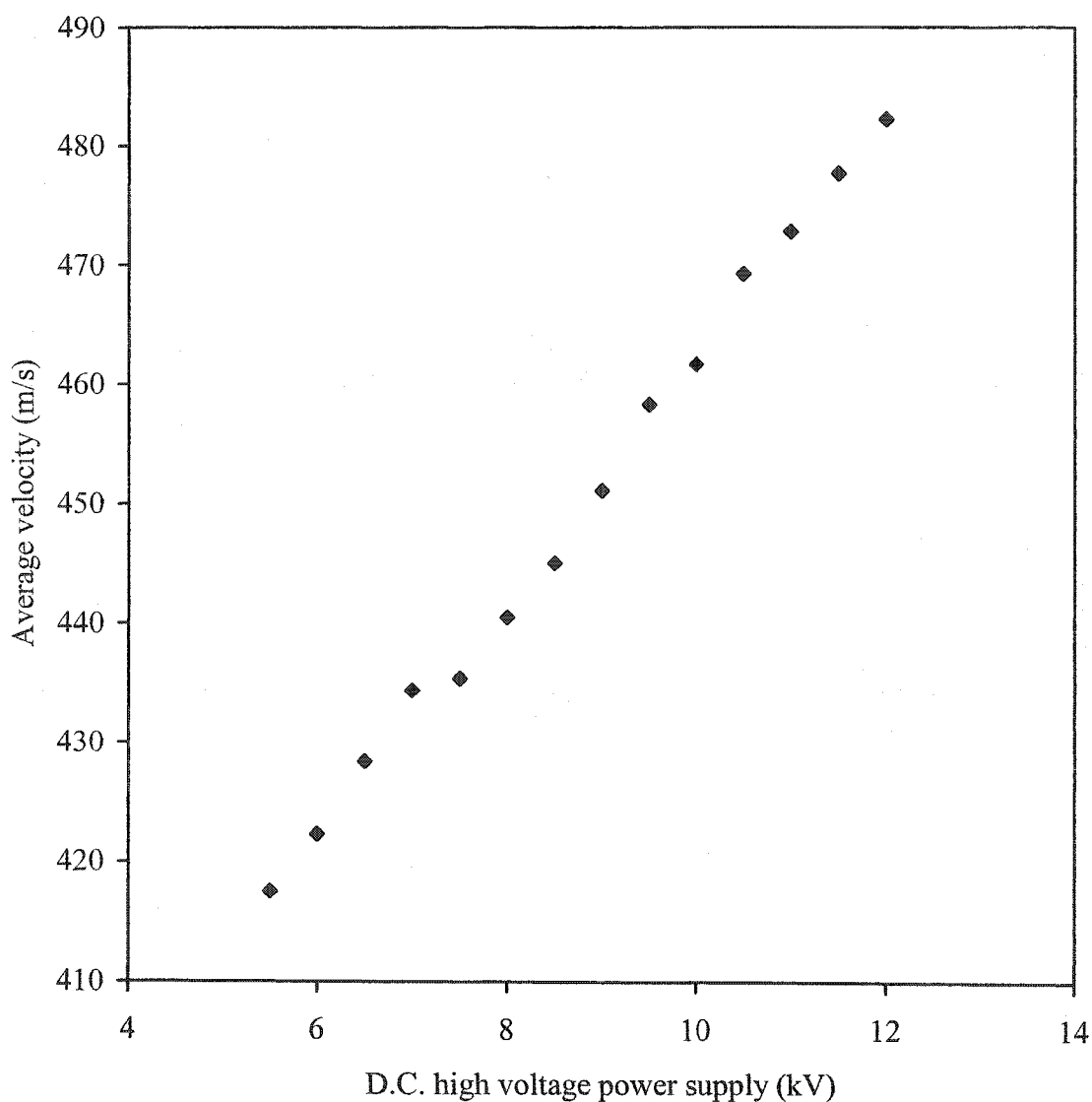


FIG. 34. Voltage dependence of the average velocity of a shock wave generated by a spark gap ($d \sim 0.5$ cm) in neutral N_2 at 30 Torr.

The experiment by Reinmann and Akram [35], described in Section 2.3.2, showed that changing a spark gap distance will give a strong shock wave. We repeated this experiment in neutral N_2 gas with 10 kV of d.c. high voltage supplied to the spark gap. The average velocity of the shock wave was plotted as a function of gas pressure, as shown in Figure 35.

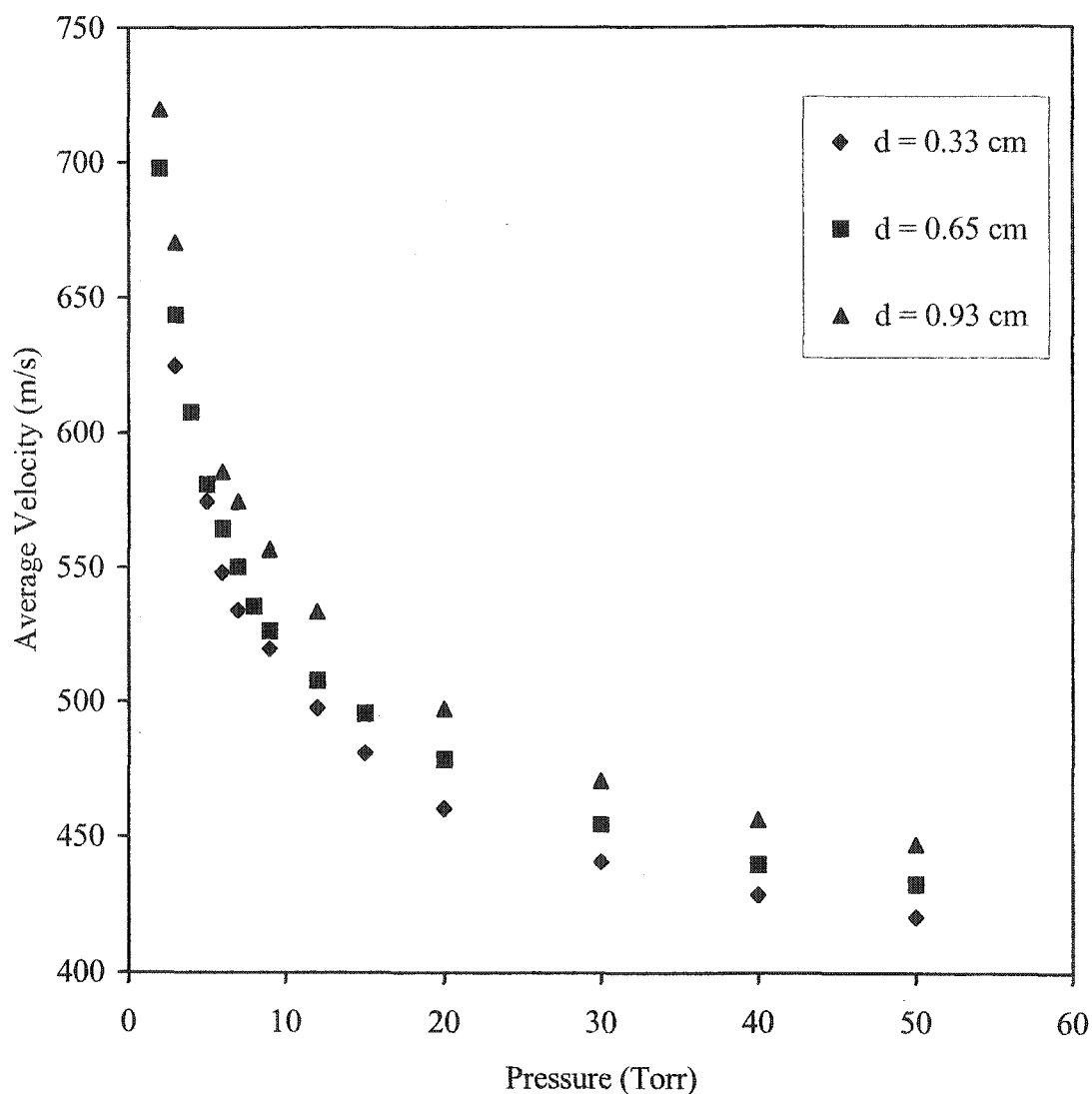


FIG. 35. Pressure dependence of average velocity of shock wave in neutral N_2 at $V = 10$ kV with some distances between the spark gap.

In this case, the distance of the spark gap was set successively to 0.33 cm, 0.65 cm, and 0.93 cm. From this figure, we can see that the shock wave can propagate faster when the spark gap has a larger distance, d .

3.2.5 Local Velocity of Shock Wave in Argon MW Discharge

By using the same set-up as shown in Figure 18, the deflection of the laser signals was measured when we have a MW discharge in all three gases. In this case, the resonant cavity was designed to generate a MW discharge in $TE_{1,1,1}$ mode, and the applied power to the magnetron tube was approximately 750 Watts. By increasing the gas pressure from 5 to 30 Torr, some waveform signals were detected in the Ar MW discharge, but it was very difficult to detect the signals in the Ne and N_2 MW discharges. In the case of the Ne MW discharge, it was easy to generate a Ne MW discharge and increase the gas pressure up to 30 Torr or more, but it was very difficult to get a waveform signal when a shock wave propagated through the discharge. The signals were very weak and hard to detect at the high end of the pressure range near 100 Torr. We have a strong waveform signal in the N_2 MW discharge, but it is very difficult to maintain the N_2 MW discharge at gas pressures from 20 to 30 Torr. In the case of the N_2 MW discharge, the magnetron tube and the resonant cavity were always heated up, and the variac in the magnetron power supply circuit would shut down the experiment. Ar gas was very convenient to work with in this experimental set-up; we could easily make a MW discharge and increase the gas pressure up to 100–200 Torr or more if we had a good cooling system for the magnetron tube and the resonant cavity. Furthermore, Ar gas is very well characterized in gas discharge physics. For this reason, we focus only on the experiment of the Ar gas and the Ar MW discharge.

Typical characteristics of laser deflection waveform signals in the Ar MW discharge and in pure Ar gas (no discharge) at a gas pressure of about 15 Torr are shown in Figure 36.

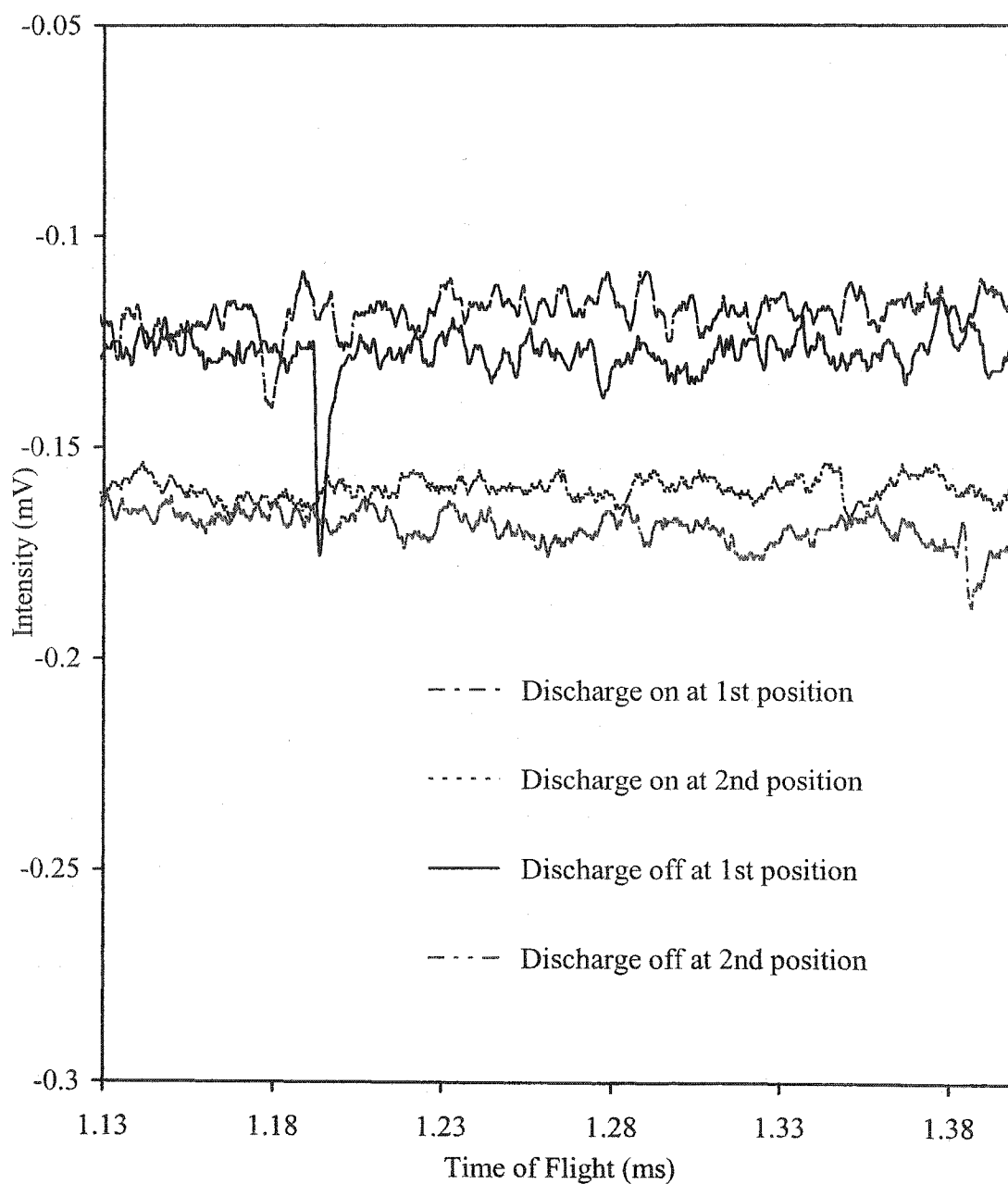


FIG. 36. Laser deflection waveform signal in Ar MW discharge and Ar gas at 15 Torr and $d = 0.38$ cm.

By using the picture in Figure 24 and Eqs. 23 and 25, we can calculate the local velocity of a shock wave at the 1st position (V_{1disc}) and at the 2nd position (V_{2disc}) for the Ar MW discharge from the following set of equations:

$$t_{1ng} = t_1 = (L + l_1) / V_{1ng}, \quad (26)$$

$$t_{1disc} = (L / V_{1ng}) + (l_1 / V_{1disc}), \quad (27)$$

$$t_{2ng} = t_2 = (L + l_2) / V_{2ng}, \quad (28)$$

and

$$t_{2disc} = (L / V_{1ng}) + (l_2 / V_{2disc}). \quad (29)$$

We can also directly calculate the local velocity of a shock wave between the 1st position and the 2nd position (V_{12disc}) by using the following equation:

$$V_{12disc} = (l_2 - l_1) / (t_{2disc} - t_{1disc}), \quad (30)$$

where V_{1disc} and V_{2disc} are the local velocities of a shock wave in the Ar MW discharge at the 1st position and at the 2nd position, respectively, and V_{12disc} is the local velocity of the shock wave in the Ar MW discharge between the two positions. In this case, the times-of-flight of a shock wave in neutral Ar gas, t_1 and t_2 , are equal to t_{1ng} and t_{2ng} , respectively. We plotted those three local velocities of the shock wave in the Ar MW discharge as a function of pressure, as shown in Figure 37. The spark gap distance (d) is the same as for those experiments in neutral Ar gas ($d \sim 0.38$ cm).

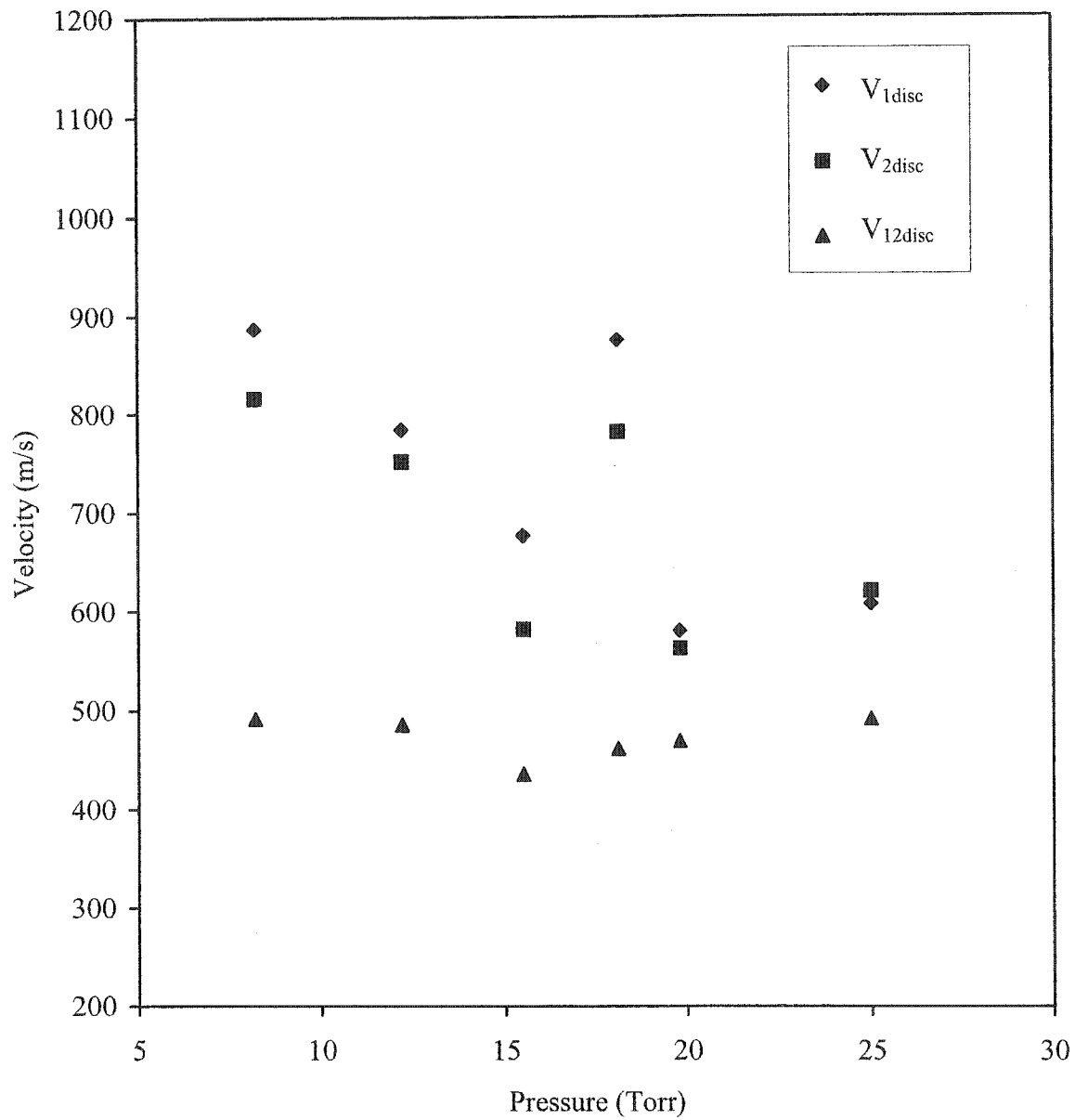


FIG. 37. Local velocities of shock wave in Ar MW discharge at 10 kV high voltage power supply to spark gap and $d = 0.38$ cm.

The result from Figure 37 shows that the local velocities of a shock wave in the Ar MW discharge calculated from Eq. (27) (V_{1disc}) and Eq. (29) (V_{2disc}) are higher than the local velocity calculated between the two positions from Eq. (30) (V_{12disc}) for pressures from 5 to 15 Torr. Furthermore, the local velocities of a shock wave in the Ar MW discharge (V_{1disc} and V_{2disc}) are still different (~20-30%) from the local velocity of the shock wave between the two positions (V_{12disc}) at pressures above 20 or 25 Torr. Our results suggest that for pressures above 20 Torr, calculation of the local velocity of a shock wave between two positions is the best way to study the dispersion and propagation of the shock wave in an Ar MW discharge.

If we measure the gas temperature in front of the shock wave in the Ar MW discharge, we can calculate the relative temperature, pressure, density, the total energy per unit volume, the Mach number behind a shock wave, and the relative number density of the shock wave propagating in the Ar MW discharge. The experiment by which we measured the gas temperature in the Ar MW discharge will be introduced in the next section, and the new resonant cavity that has a set of thirteen holes along its axis will also be introduced in the new experimental set-up. Thus, we can get a new set of data at 13 positions to study the dispersion and propagation of a shock wave in the weakly ionized Ar gas.

3.3 Determination of Shock Wave Dispersion in MW Discharge

In order to study the dispersion of a shock wave in the Ar MW discharge, we concluded that more than two data points were necessary. Therefore, we built another resonant cavity (for TE mode) in which we drilled a set of thirteen holes (instead of two holes) along the envelope of the cavity, as shown in Figure 38. The diameter of each hole is 0.5 cm. The holes are separated by about 0.75 inches (~ 1.9 cm) (see Appendix). The 4th, 7th, and 10th holes are elongated vertically to about 1.0 inch (~ 2.5 cm) (see Figure 38). We used these three special holes to measure the gas temperature distribution (described in Section 3.4) along the vertical axis. For the TM mode, we built a different resonant cavity to support the $TM_{0,1,2}$ mode according to the discussion outlined in Section 2.4.3.

Both new resonant cavities (TE and TM mode) were substituted for the two-hole resonant cavities, and essentially the same time-of-flight experiment was set up, as in Figures 14 and 18 in Sections 3.1 and 3.2.3, respectively. The two laser beams crossed two selected points at the same time. In this way, by turning the Ar MW discharge on and off, we could obtain two sets of shock wave time-of-flight data at thirteen different positions from the spark gap along the shock tube (or resonant cavity) axis. By plotting those two groups of data for the time-of-flight of the shock wave to these thirteen positions, we could obtain the information on dispersion of the shock wave in the Ar MW discharge. The results and analysis of the data for the TE mode and the TM mode will be shown in Sections 3.3.1 and 3.3.2, respectively.

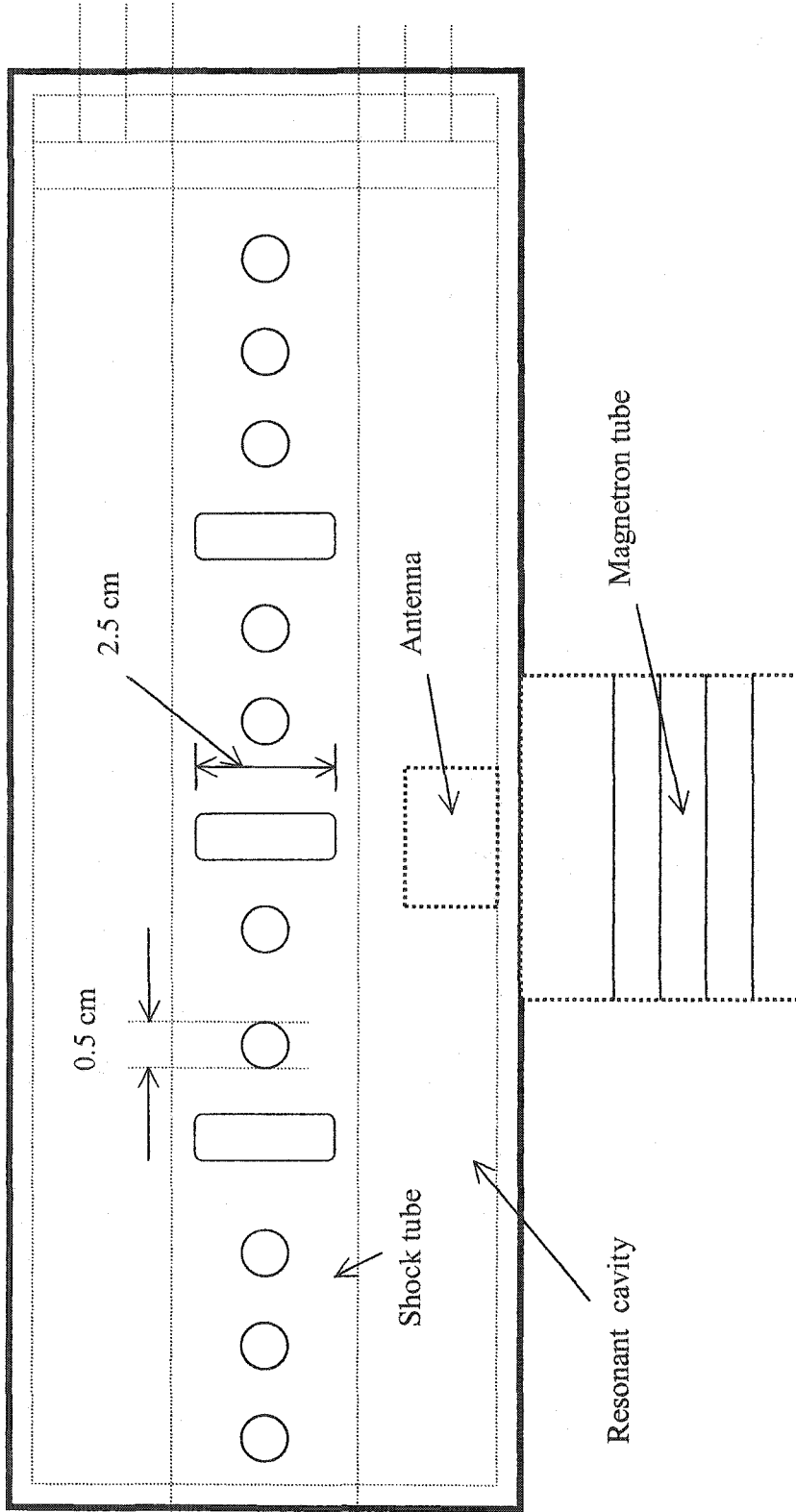


FIG. 38. Resonant cavity for the shock wave dispersion study in Ar MW discharge.

3.3.1 Shock Wave Dispersion in Ar MW Discharge (TE Mode)

The laser deflection waveform signals from the shock wave dispersion experiment in neutral Ar and in the Ar MW discharge by using the TE mode resonant cavity are shown in Figures 39 – 42 at several gas pressures. The shock wave waveform signals measured in the Ar MW discharge are obviously different from the shock wave waveform signals measured in neutral Ar in three ways. First, the waveform signal shape of a shock wave when the discharge was on at every observation position is the single peak signal. The double peak signal that occurs for a shock wave in a d.c. glow discharge can not be found in the Ar MW discharge (see Ref. [3,5]). Second, the time-of-flight for a shock wave in the discharge decreased at every observation position. In other words, a shock wave propagates faster in the Ar MW discharge than in neutral Ar. Thus, the shock wave propagation velocity both in the discharge and in the neutral gas could be calculated and compared, as shown at the end of this section. Third, the amplitude of the waveform signal for a shock wave propagating through the Ar MW discharge was reduced in comparison to the signal in neutral Ar gas. This effect is called "*amplitude reduction*." Its value was used to evaluate the gas temperature during the discharge, as discussed in Section 3.4.1.

The dynamics of shock wave dispersion during its propagation through the discharge is illustrated in Figure 43. Shown here is a sequence of time-of-flight data at the same pressure for several central locations in the cavity. One can see that the time-of-flight increases as the shock propagates from one observation point to another but that the increase is not uniform. The local velocity of the shock wave increases rapidly between the 6th and 7th positions.

Plots of the distance from the spark gap as a function of the shock wave time-of-flight at the thirteen positions at two values of gas pressure for both the Ar MW discharge and neutral Ar, are shown in Figures 44 - 45. Based on the uncertainty of our measurement results, the average errors in the time-of-flight measurements at a particular observation point when the discharge was first on and then off are about 0.14% and 0.1%, respectively. The uncertainty in the measurement of the distance from the spark gap is about 1 mm, or approximately 0.17%, obtained by averaging over all distance values. All values of uncertainty are too small to be seen in Figures 44 - 45, but we will use this value to evaluate the uncertainty of the local velocity of a shock wave.

From those sets of data shown in Figures 44 - 45, we can evaluate the local velocity of the shock wave in neutral Ar gas and in an Ar MW discharge by using the same technique that was used in Section 3.2.4 (see Eq. 24). In order to determine the velocity at the 2nd position, we used the time-of-flight between the 1st and the 3rd positions (see Eqs. (31) to (33)), etc.:

$$V_2 = \frac{l_3 - l_1}{t_3 - t_1}, \quad (31)$$

$$V_3 = \frac{l_4 - l_2}{t_4 - t_2}, \quad (32)$$

⋮
⋮
⋮

$$V_n = \frac{l_{n+1} - l_{n-1}}{t_{n+1} - t_{n-1}}, \quad (33)$$

where $n = 2, 3, 4, \dots, 12$.

By doing that, we obtained the sets of data for propagation of the shock wave in neutral Ar gas and in the Ar MW discharge at any local position from the spark gap for gas pressures between 20 and 100 Torr. The local velocities of the shock wave propagating through neutral Ar and the Ar MW discharge for pressures from 20 Torr to 100 Torr at the 6th and 7th position in TE mode are shown in Figures 46 – 47, respectively. The distribution of the shock wave local velocity along the resonant cavity in neutral Ar and the Ar MW discharge at 50 and 70 Torr are shown in Figures 48 – 49, respectively. According to Eqs. (31) to (33), by use of the average errors for the time-of-flight and for the distance from the spark gap, we found the average errors in the shock wave local velocities in neutral Ar and in the Ar MW discharge (as shown in Figures 46 - 49) to be 4.68% and 5.98%, respectively. Due to the statistical error shown in Figures 46 -49, the systematic error can be estimated to be the same order of the statistical error.

From these results in TE mode, we can conclude that shock wave deflection signal amplitudes in the Ar MW discharge are weaker than in neutral Ar. We have no sign of the broadening of the shock wave deflection signal (double peak) that is seen in d.c. glow discharges. The times-of-flight for a shock wave propagating in the Ar MW discharge are shorter than in neutral Ar (see Figures 39 - 45). A shock wave propagates in the Ar MW discharge faster than in neutral Ar (see Figures 46 - 49). A shock wave always propagates faster at the central region (5th to 8th positions) of the resonant cavity (see Figures 43 - 49).

Generally, the shock wave local velocity depends on the gas temperature in front of the shock. The calculation of the gas temperature in neutral Ar will be derived, and the result will be shown in Section 3.4; the measurements of the gas temperature in the

Ar MW discharge will be described in the same section. We will discuss these results in detail again in Section 4.

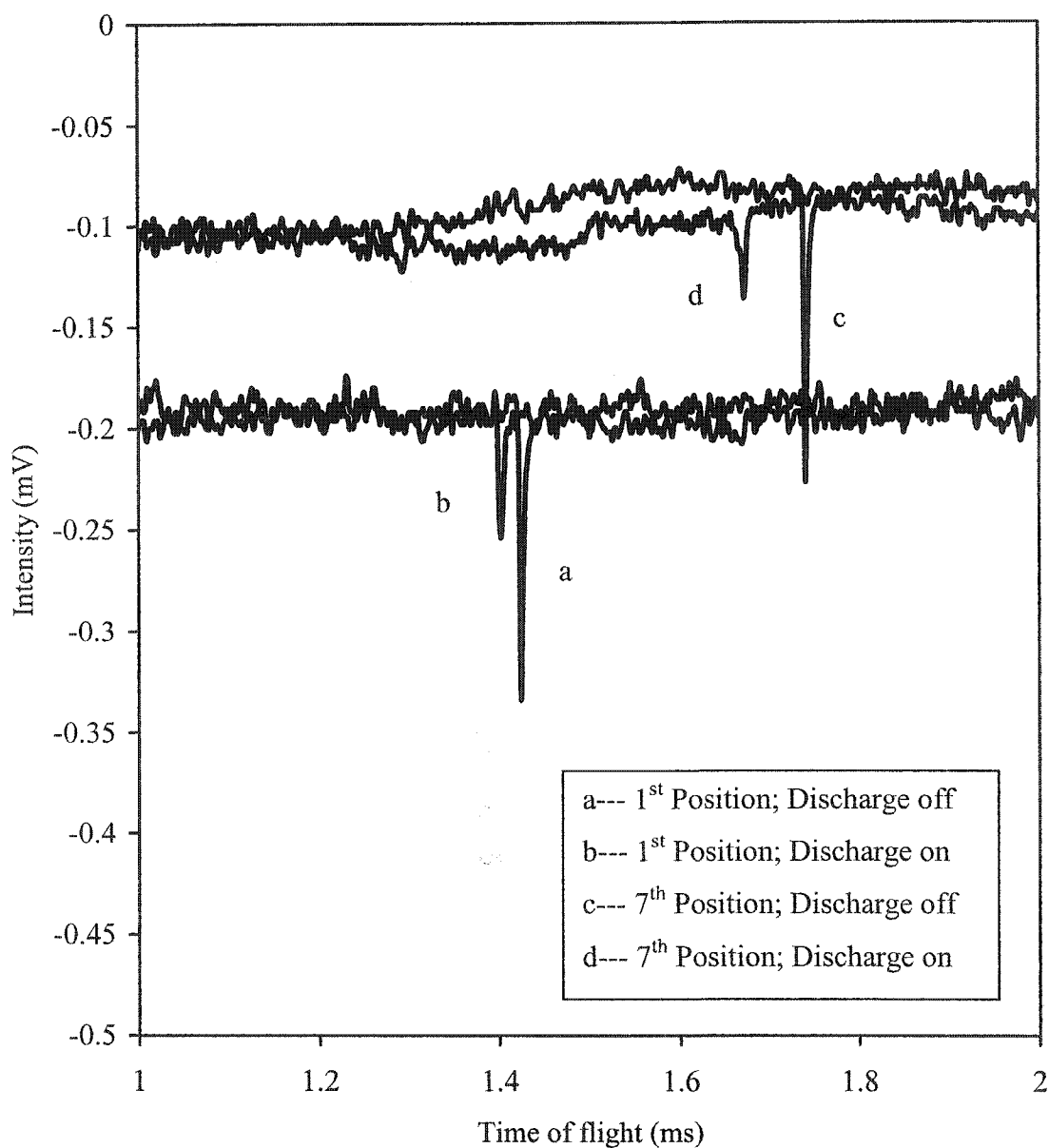


FIG. 39. Shock wave deflection waveform signal in neutral Ar and Ar MW discharge at the 1st position and 7th position; Pressure 60Torr ; Spark gap voltage 8 kV.

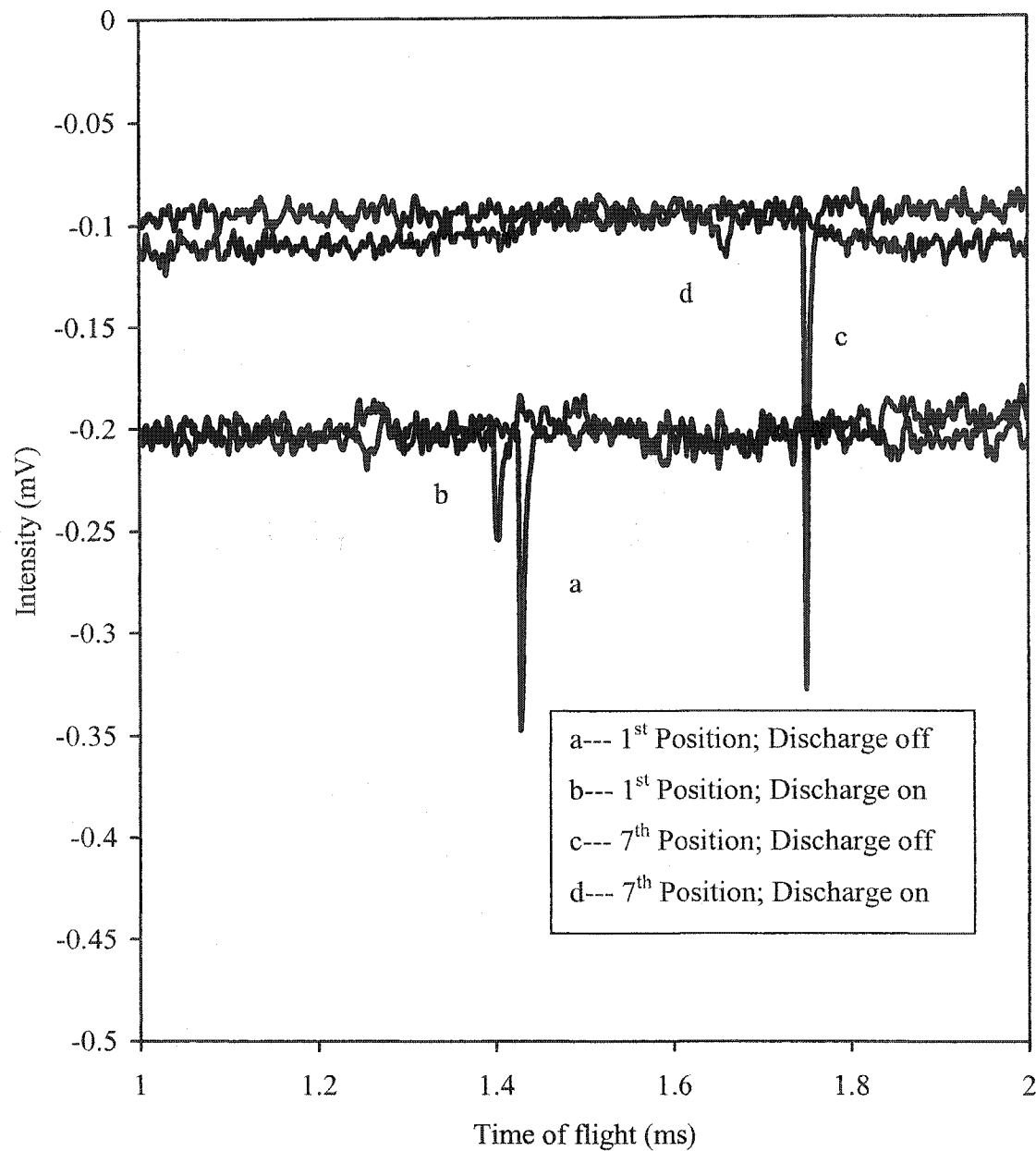


FIG. 40 Shock wave deflection waveform signal in neutral Ar and Ar MW discharge at the 1st position and 7th position; Pressure 70 Torr; Spark gap voltage 8 kV.

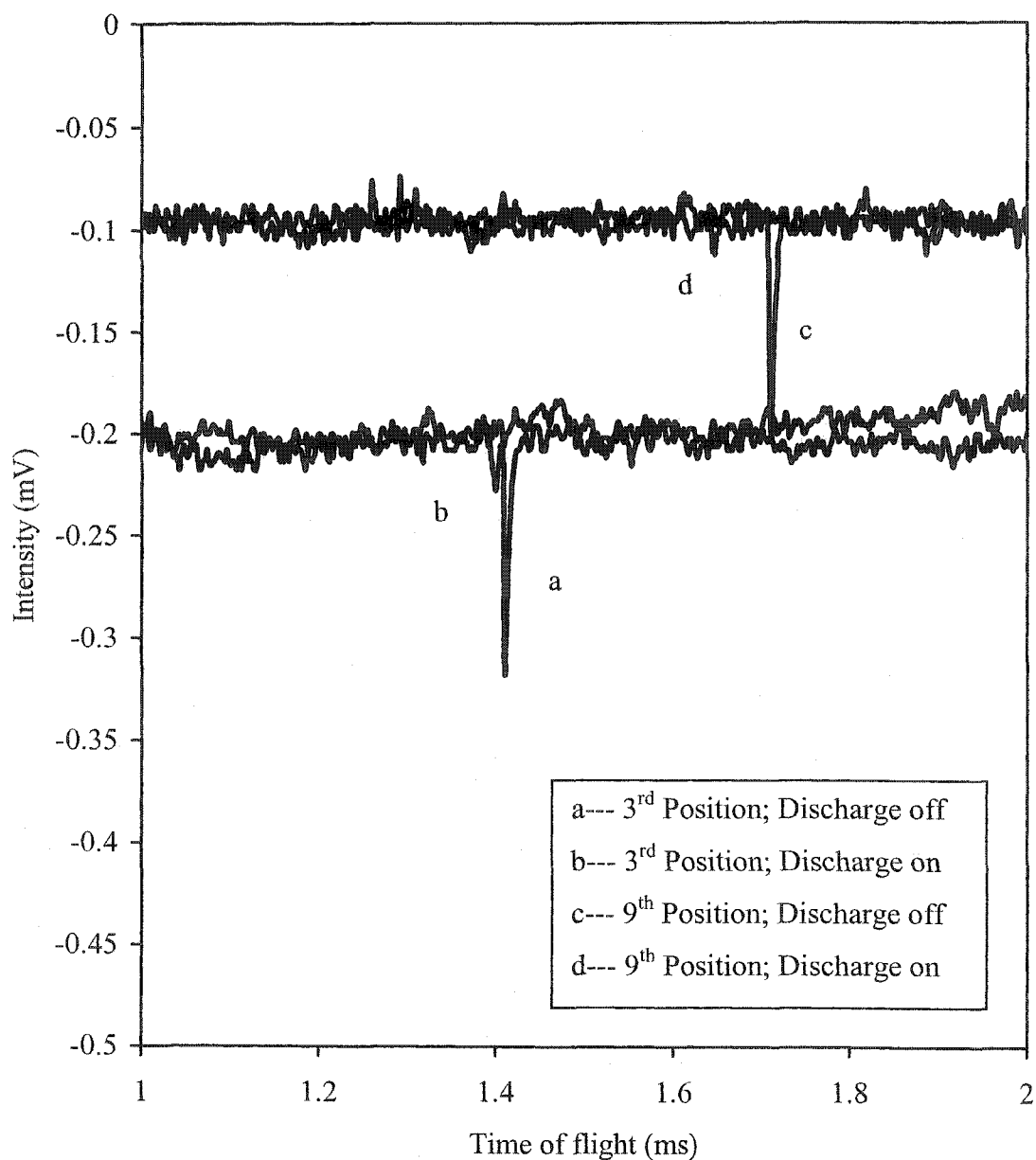


FIG. 41 Shock wave deflection waveform signal in neutral Ar and Ar MW discharge at the 3rd position and 9th position; Pressure 50 Torr; Spark gap voltage 8 kV.

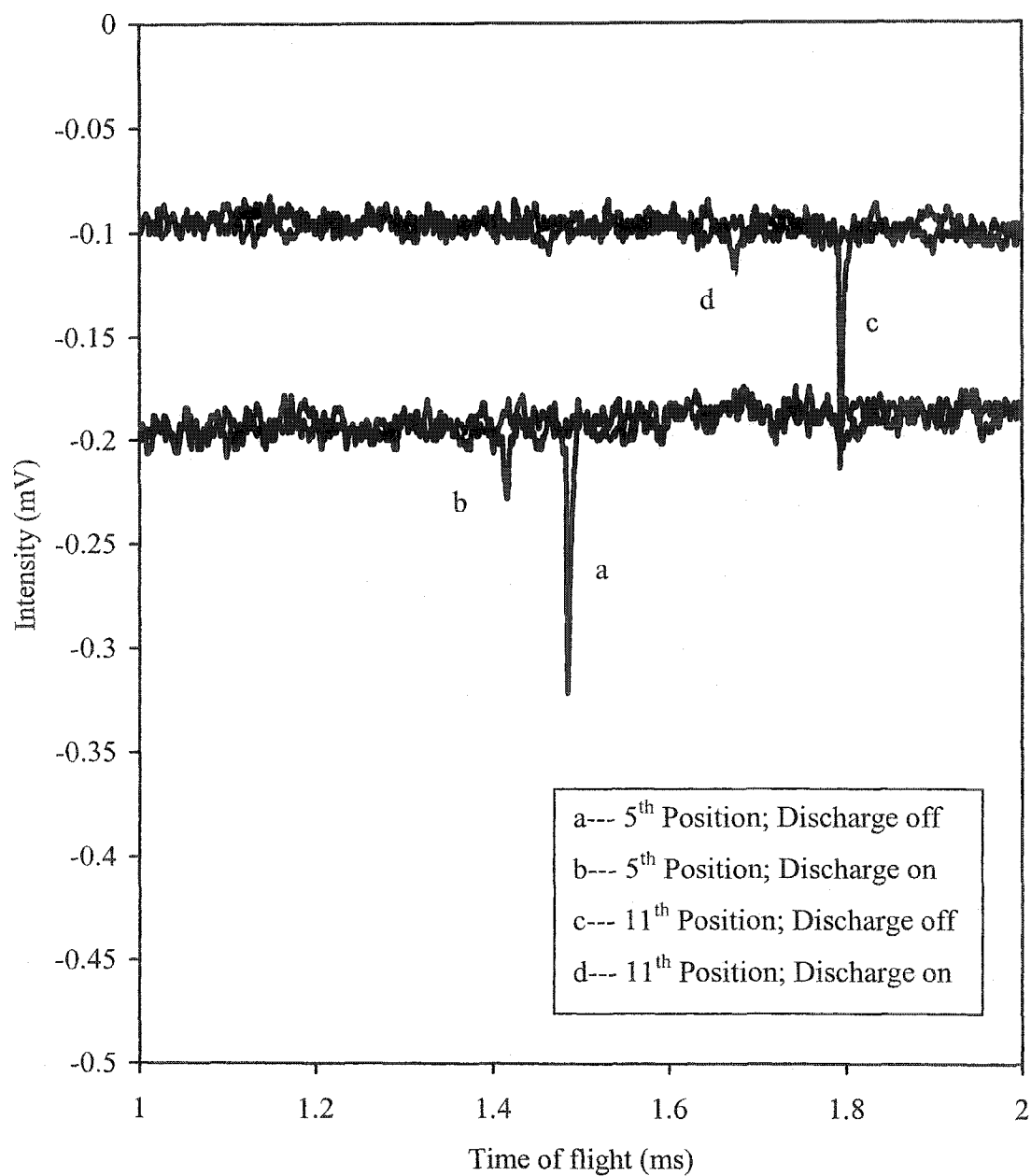


FIG. 42 Shock wave deflection waveform signal in neutral Ar and Ar MW discharge at the 5th position and 11th position; Pressure 40 Torr; Spark gap voltage 8 kV.

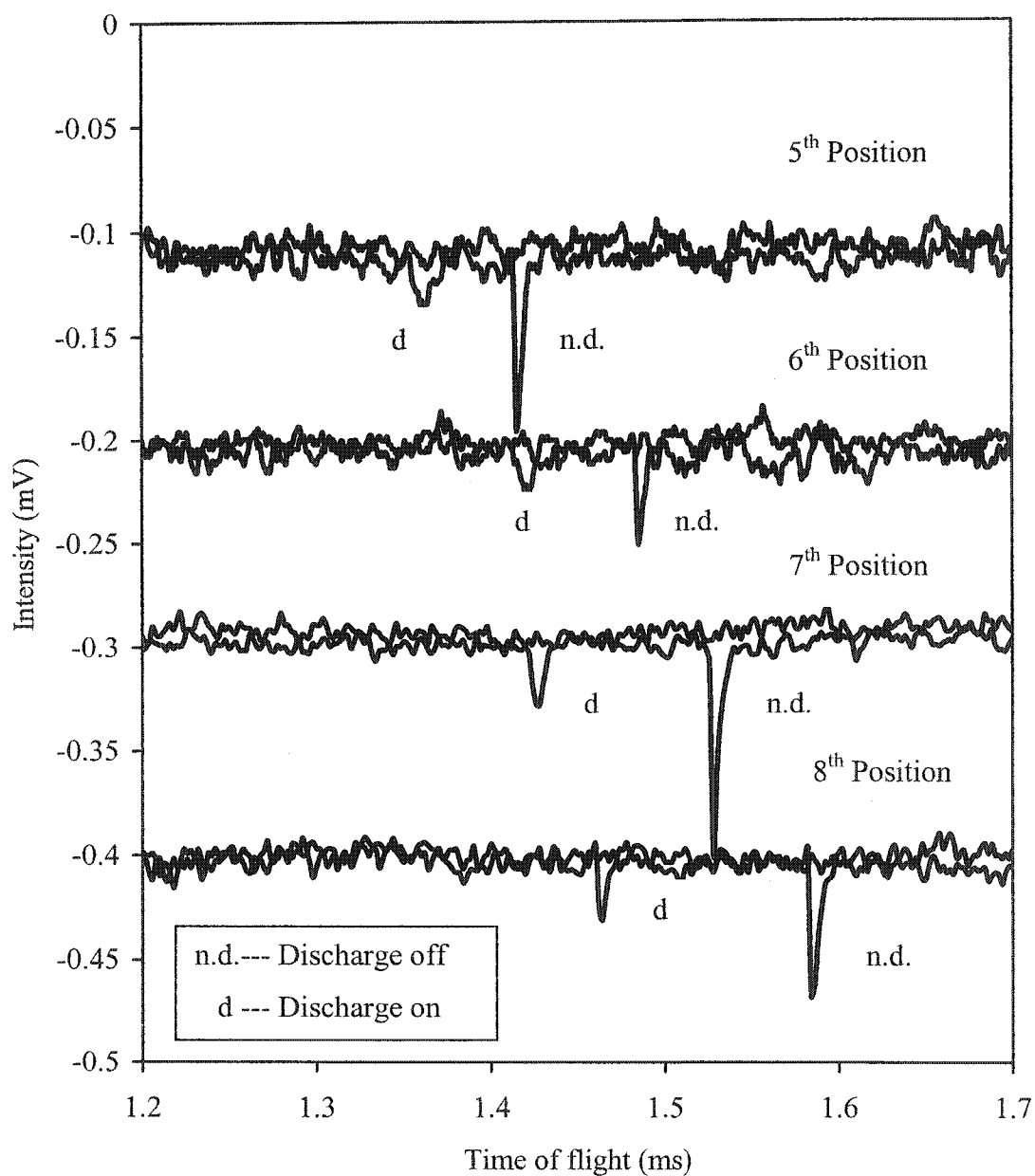


FIG. 43 Shock wave deflection waveform signal in neutral Ar and Ar MW discharge at the 5th, 6th, 7th, and 8th position; Pressure 30 Torr; Spark gap voltage 8 kV.

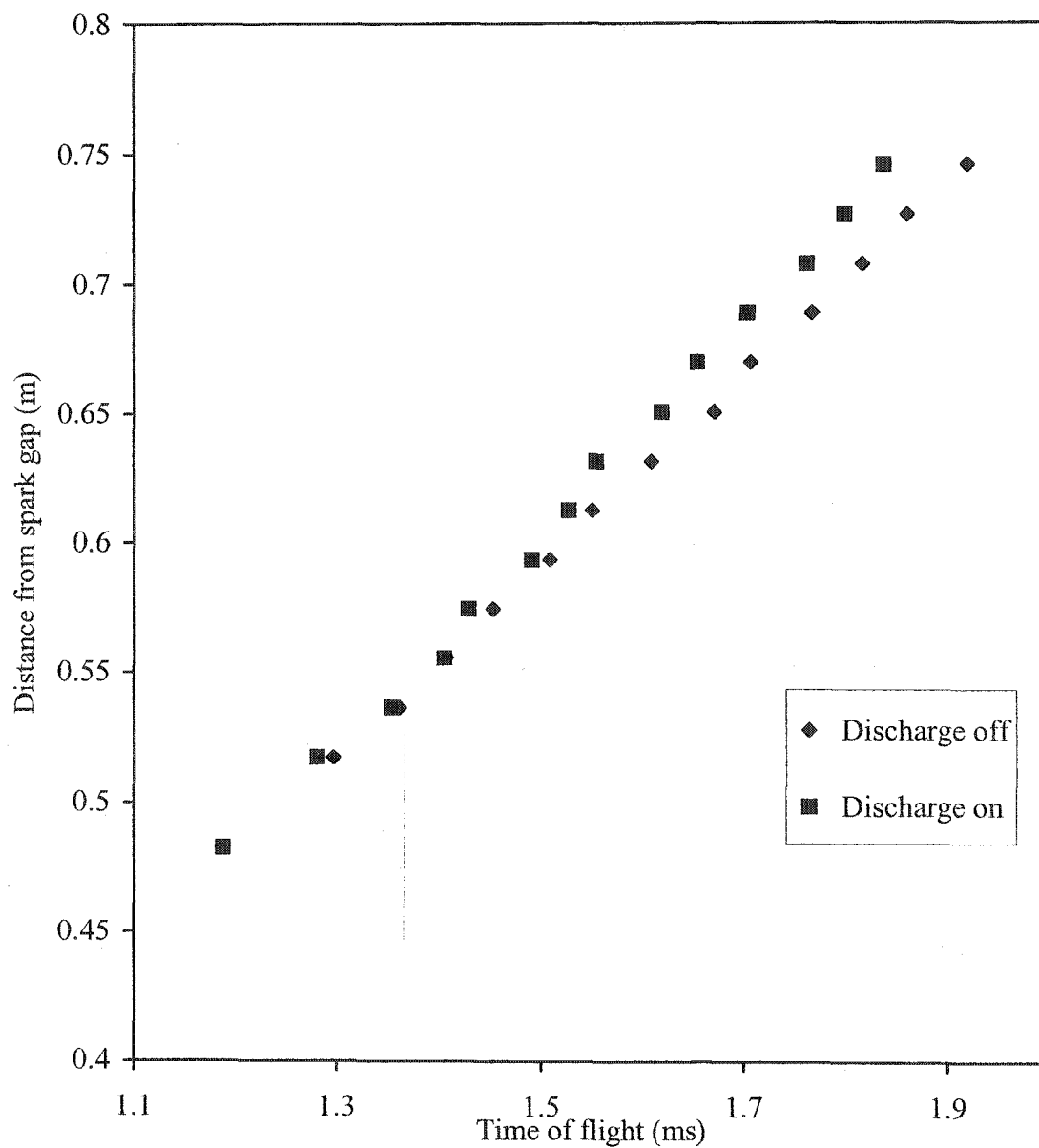


FIG. 44 Propagation of shock wave through neutral Ar and Ar MW discharge at 50 Torr; Spark gap voltage 8 kV.

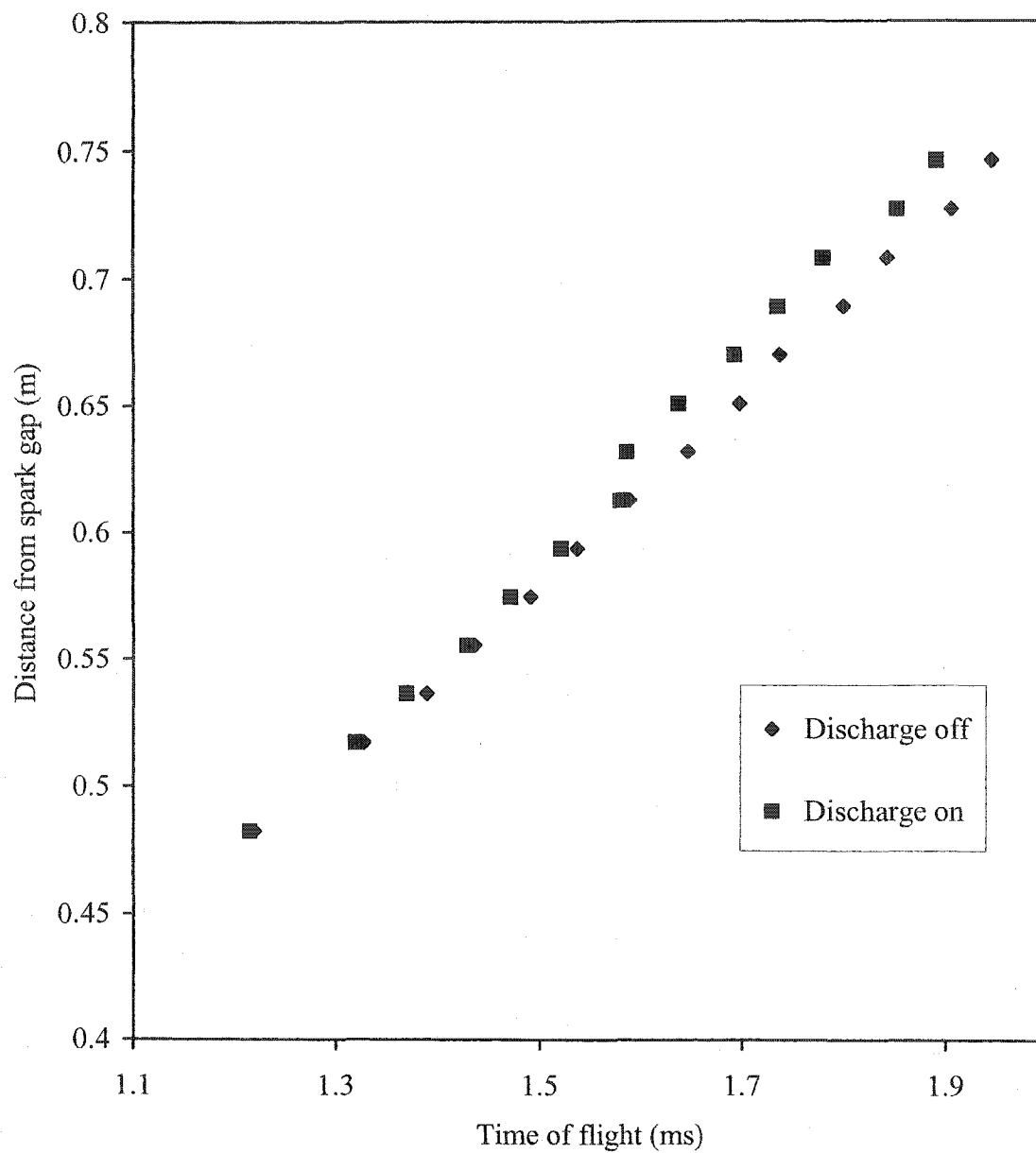


FIG. 45 Propagation of shock wave through neutral Ar and Ar MW discharge at 70 Torr; Spark gap voltage 8 kV.

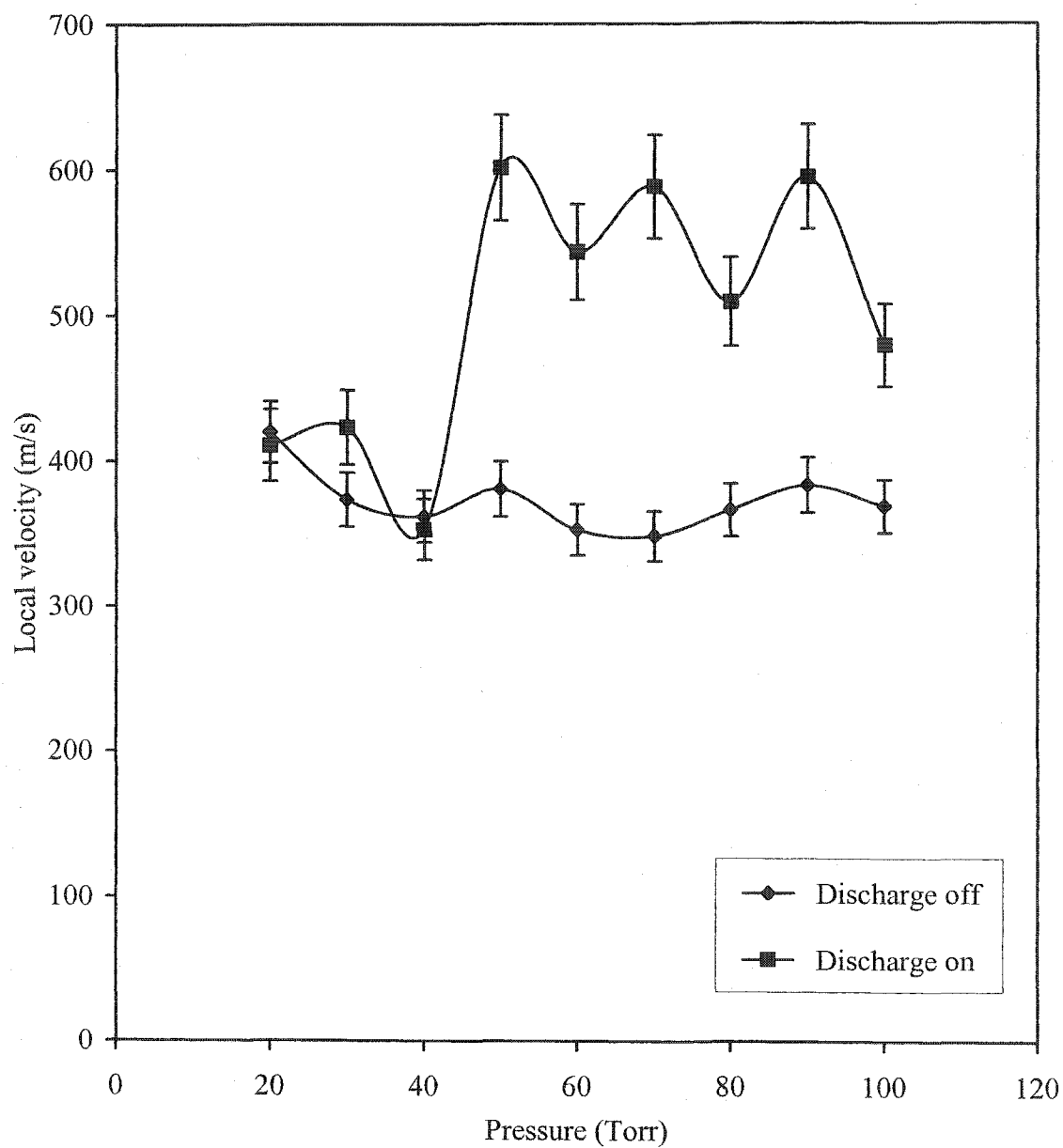


FIG. 46 Shock wave local velocity in neutral Ar and in Ar MW discharge at 6th position

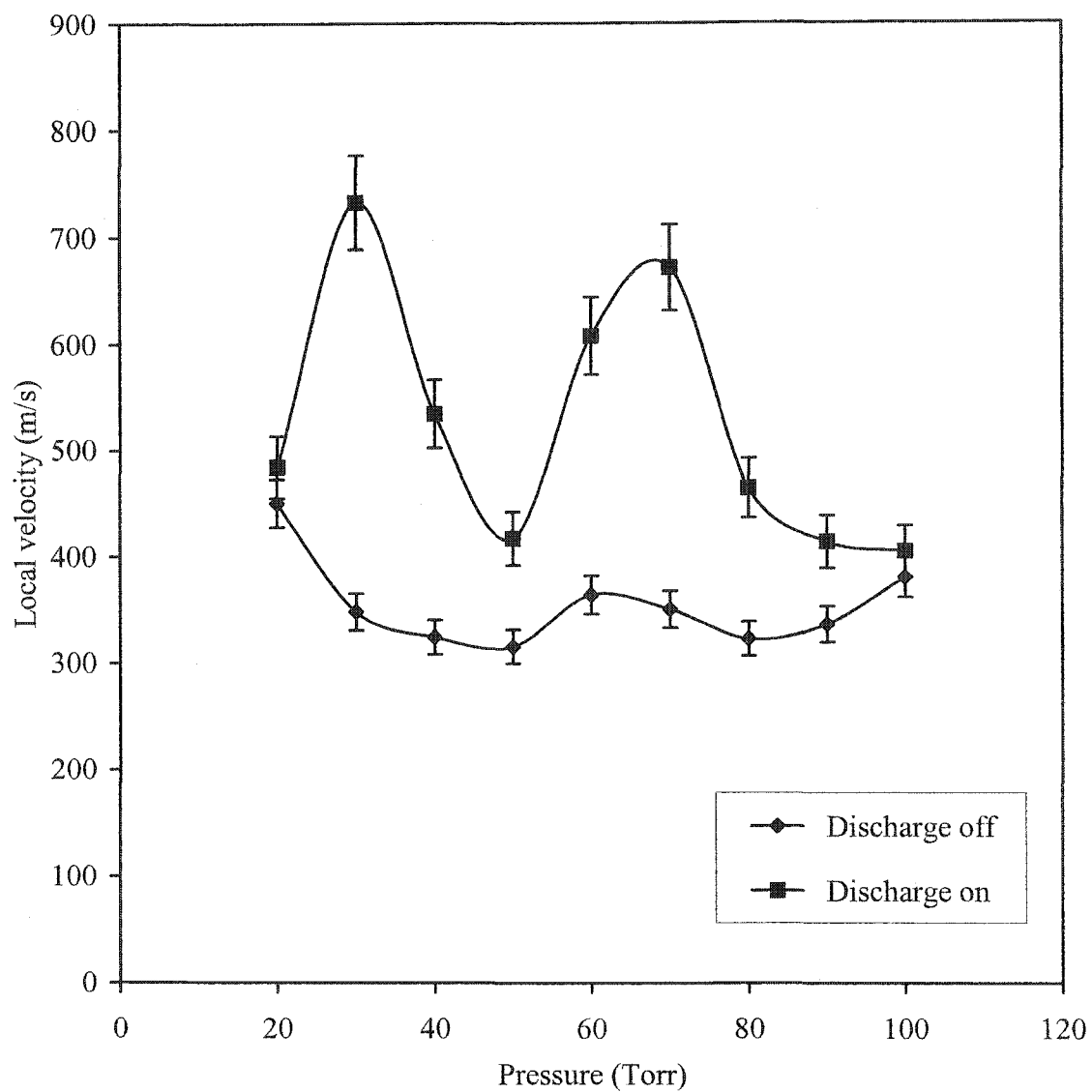


FIG. 47 Shock wave local velocity in neutral Ar and in Ar MW discharge at 7th position

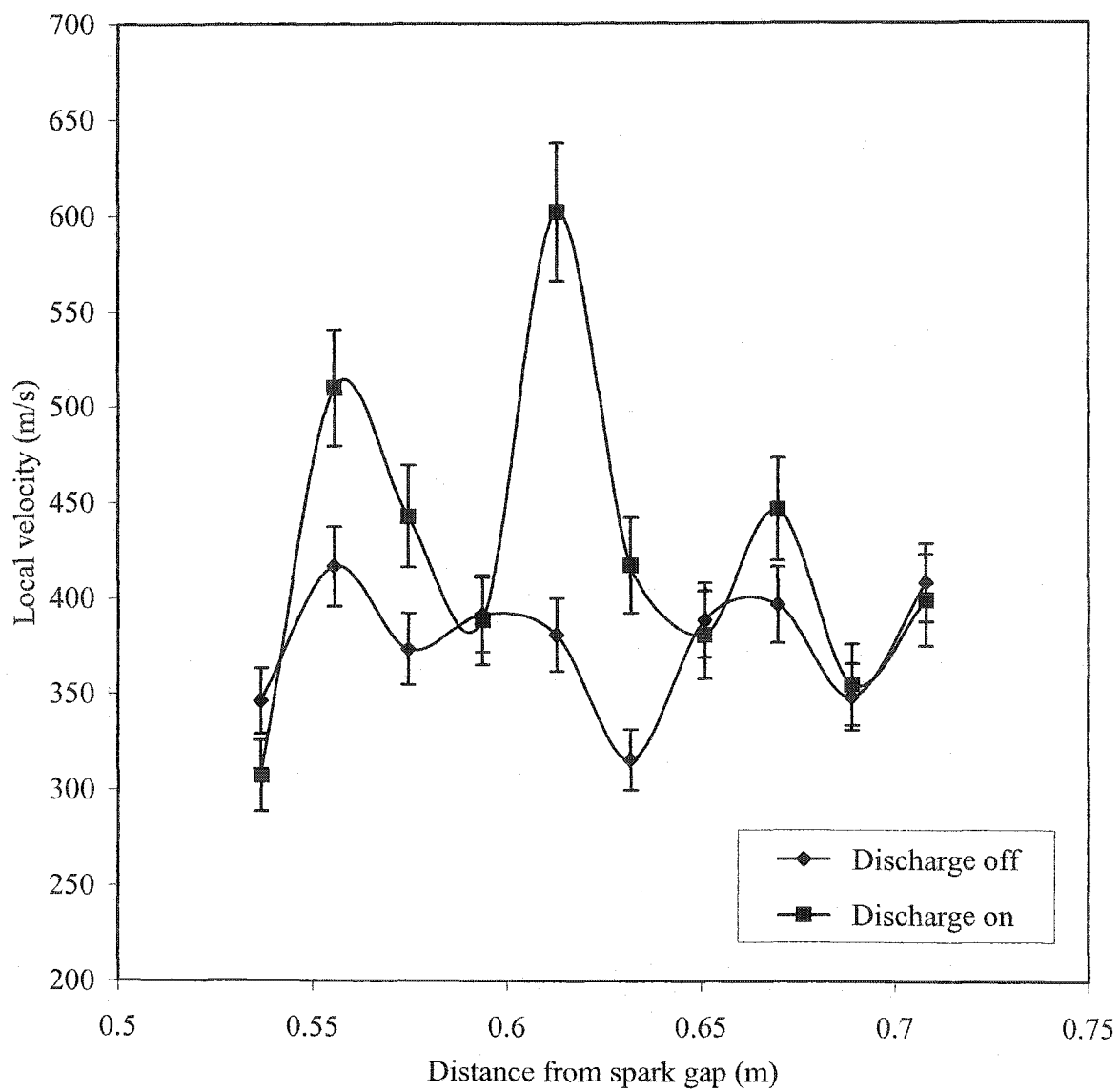


FIG. 48 Shock wave local velocity in neutral Ar and in Ar MW discharge at 50 Torr in TE mode

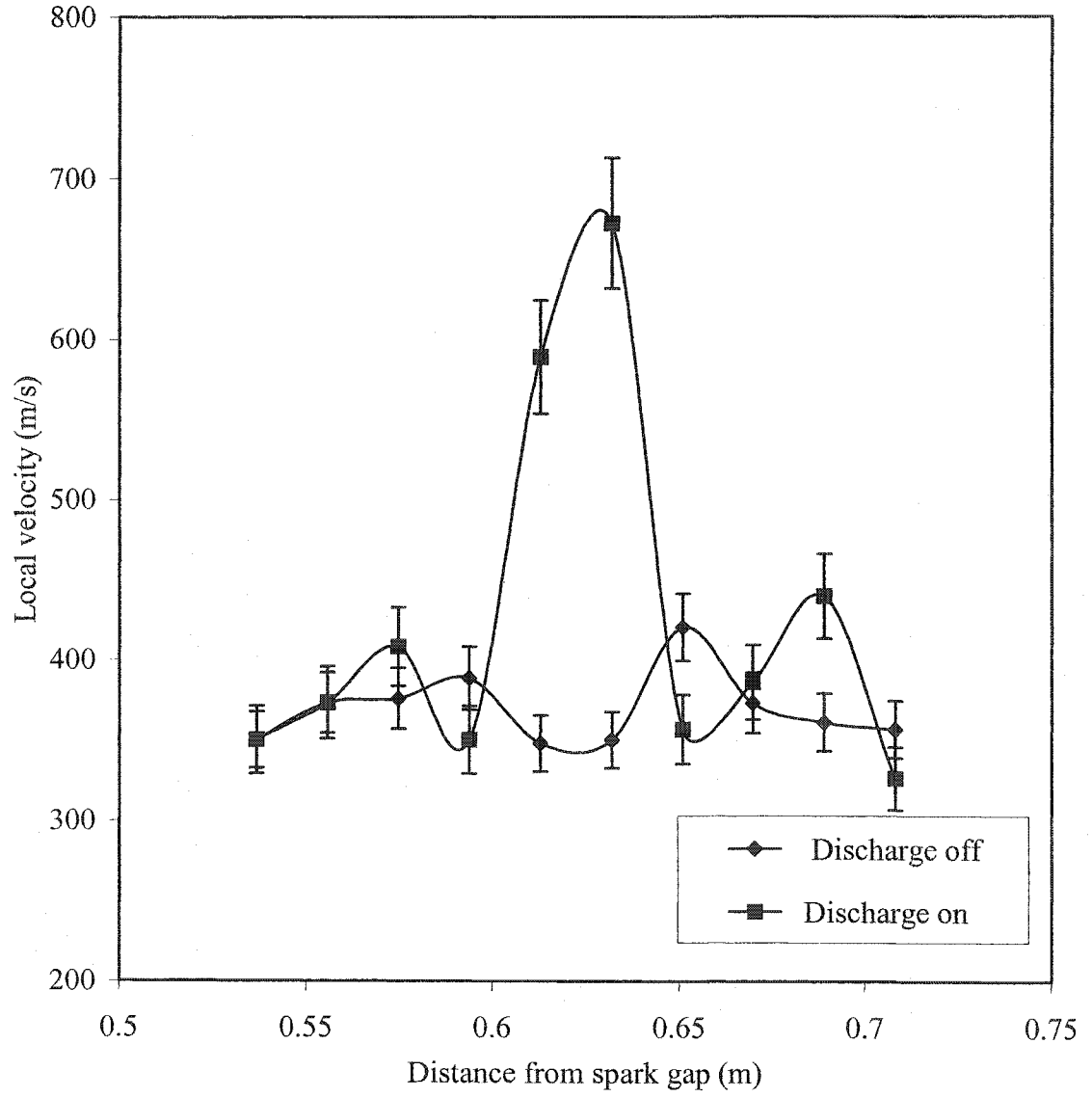


FIG. 49 Shock wave local velocity in neutral Ar and in Ar MW discharge at 70 Torr in TE mode

3.3.2 Shock Wave Dispersion in Ar MW Discharge (TM Mode)

Using the resonant cavity that supports the TM mode, we performed the same set of measurements of the laser deflection waveform signals as in the discharges generated in TE mode (Section 3.3.1) in neutral Ar and in the Ar MW discharge at several values of gas pressure. Typical waveforms are shown in Figures 50 to 53. We obtained almost the same results as in the TE mode. The reduction of shock wave amplitude, the decrease in time-of-flight, and the increase in shock wave propagating velocity in the discharge were apparent. Furthermore, we still could not see the double peak structure (broadening) of the shock waveform signal in the presence of the Ar MW discharge in the TM mode. Since this is a difference between the electric field polarization in TE mode (perpendicular to shock wave propagation direction) and the TM mode (parallel to shock wave propagation direction), we carefully examined these results in TM mode and then compared them with the results in TE mode. By doing this, we found that the time-of-flight for a shock wave in the Ar MW discharge in TM mode is relatively longer than in TE mode. This means that a shock wave propagates in the Ar MW discharge in TE mode faster than in TM mode. The amplitude reduction for a shock waveform signal in the Ar MW discharge in TM mode is relatively less than in TE mode at the same measurement point and gas pressure. Thus, the gas temperature (evaluated by using the amplitude reduction technique) in TM mode should be lower than in TE mode at the same position and gas pressure. This result will be shown and discussed in Section 3.4. Our interest in TM mode was due to the polarization of the electric field inside the resonant cavity, as mentioned above. This would be equivalent to the change of electrode polarity in the d.c. glow discharge (Bletzinger et. al.) [3]. The difference in the observed shock

dispersion in TE and TM modes would suggest that the different electric field polarization in these two modes has an effect on shock wave propagation through the Ar MW discharge.

A train of several deflection signals at the same pressure, but at different positions, is shown in Figure 54. The waveforms indicate strong amplitude dispersion but a smaller change in propagation velocity. The plot between the distance from the spark gap and the shock wave time-of-flight at the thirteen positions at several gas pressures, with and without the Ar MW discharge, are shown in Figures 55 and 56. For TM mode, we assumed that the average error of the time-of-flight measurements at these observation points, with the discharge both on and off, were the same values as for the TE mode (about 0.14% and 0.1% respectively), since the same experimental setup was identical. The uncertainty in the measurement of the distance from the spark gap in TM mode can be estimated to be the same as for the TE mode (about 1 mm, or approximately 0.17%, by averaging over all distance values) and will be used to evaluate the uncertainty of the local velocity of a shock wave at the end of this section.

The same technique used for the TE mode has been used to evaluate the local velocity of a shock wave in neutral Ar and in the Ar MW discharge in TM mode. Then, the local velocity of the shock wave in neutral Ar gas and in the Ar MW discharge in TM mode at any position from the spark gap at pressures from 30 to 100 Torr can be obtained as precisely as in TE mode by using Eqs. (31) to (33). The local velocity of the shock wave propagating through neutral Ar and through the Ar MW discharge for pressures from 30 to 100 Torr at the 4th and 5th positions in TM mode are shown in Figures 57 – 58, respectively. The distribution of the shock wave local velocity along the resonant cavity

in neutral Ar and in the Ar MW discharge at 50 and 70 Torr are shown in Figures 59 – 60, respectively. Calculated in the same way as for TE mode, the average errors in the shock wave local velocity in neutral Ar and in the Ar MW discharge in TM mode (as shown in Figures 57 - 60) are 4.68% and 5.98%, respectively. We can also estimate the systematic error that is in the same order of the statistic error for the TM mode.

From Figures 50-56, we can see obviously the same three results obtained in TE mode. First, shock wave deflection signal amplitudes in the Ar MW discharge are smaller than in neutral Ar in TM mode. Second, we still have no sign of the broadening of the shock wave deflection signal (double peak) seen in d.c. glow discharges. Third, the times-of-flight of a shock wave propagating in the Ar MW discharge are shorter than in neutral Ar. As in TE mode, we also see from Figures 57-60 that the shock wave local velocity propagates in the Ar MW discharge faster than in neutral Ar for TM mode. Furthermore, a shock wave always propagates faster at the central region (4th to 9th position) of the resonant cavity for TM mode (see Figures 54-60).

By comparison to the TE mode, we can see that the average local velocity of a shock wave in the Ar MW discharge in TM mode is lower than in TE mode at the same measurement point or gas pressure (see Figures 48, 49, 59, and 60). We have seen in Section 3.3.1 that the shock wave local velocity depends on the gas temperature in front of the shock. Therefore, we estimate that the gas temperature in the Ar MW discharge in TE mode should be higher than in TM mode. Furthermore, we found that the amplitude reduction of a shock waveform amplitude in TM mode is smaller than in TE mode. This result confirmed that the gas temperature in the Ar MW discharge in TE mode should be higher than in TM mode. Results and discussion of how the shock wave local velocity

depends on gas temperature in either TE and TM mode will be discussed in detail and results for these modes will be compared in Section 4. In the present work, we have not only calculated the gas temperature by using the amplitude reduction technique but have also measured the rotational temperature and assumed it to be equal to the gas temperature in the Ar MW discharge. The technique and results will be described and shown for both the TE and the TM mode in Section 3.4.

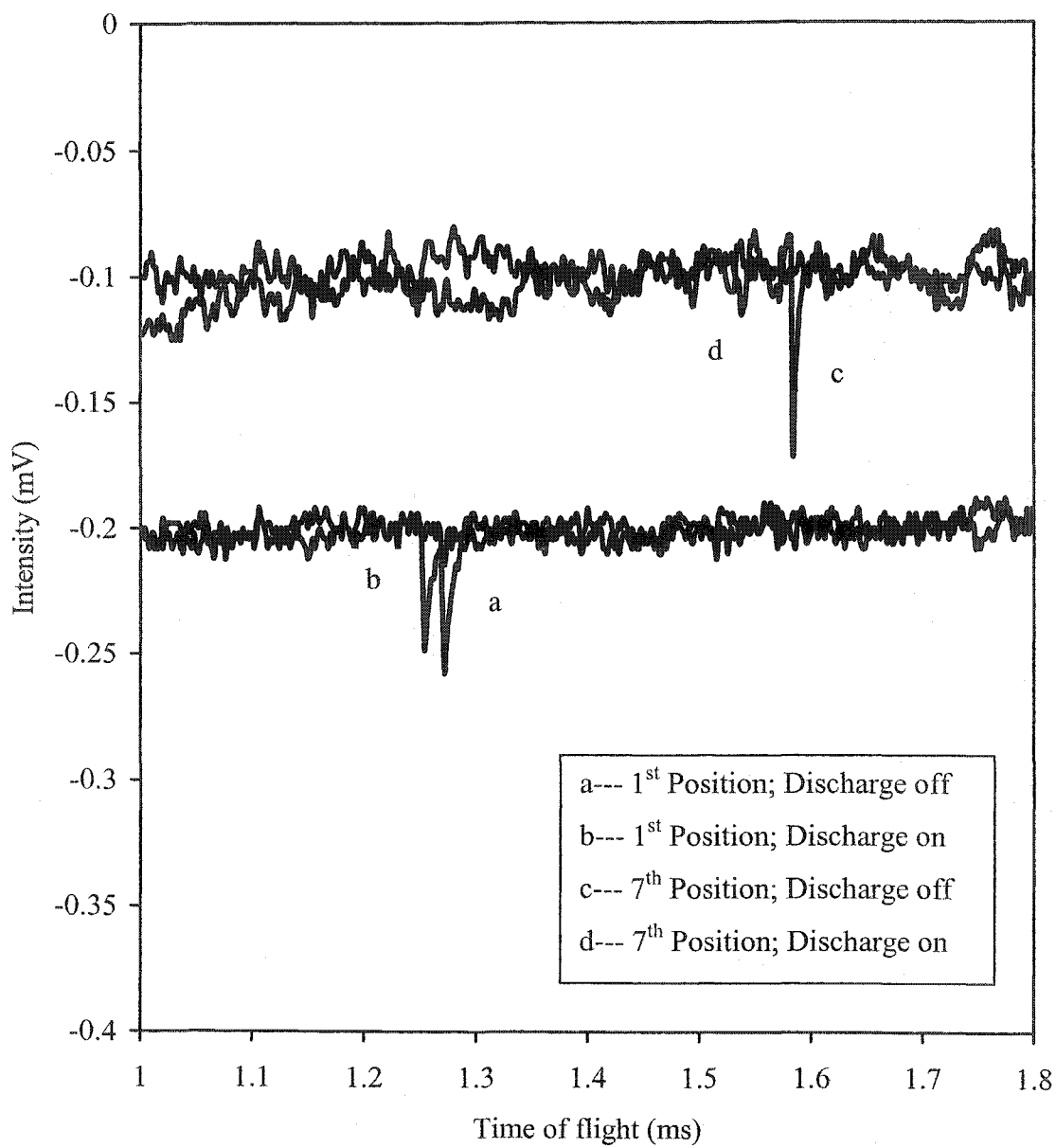


FIG. 50 Shock wave deflection waveform signal in neutral Ar and Ar MW discharge at the 1st position and 7th position (TM mode); Pressure 40Torr; Spark gap voltage 8 kV.

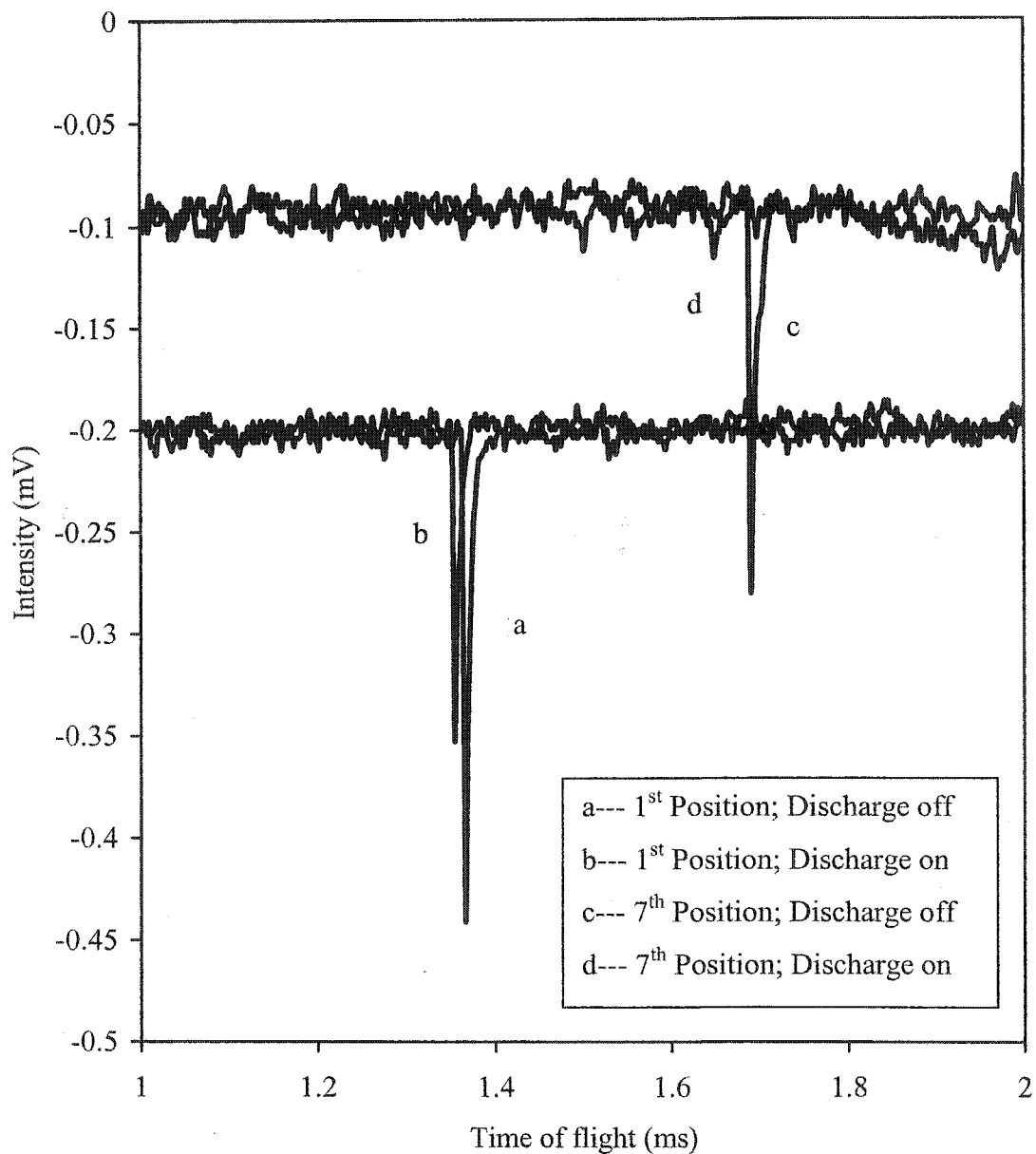


FIG. 51 Shock wave deflection waveform signal in neutral Ar and Ar MW discharge at the 1st position and 7th position (TM mode); Pressure 100 Torr; Spark gap voltage 8 kV.

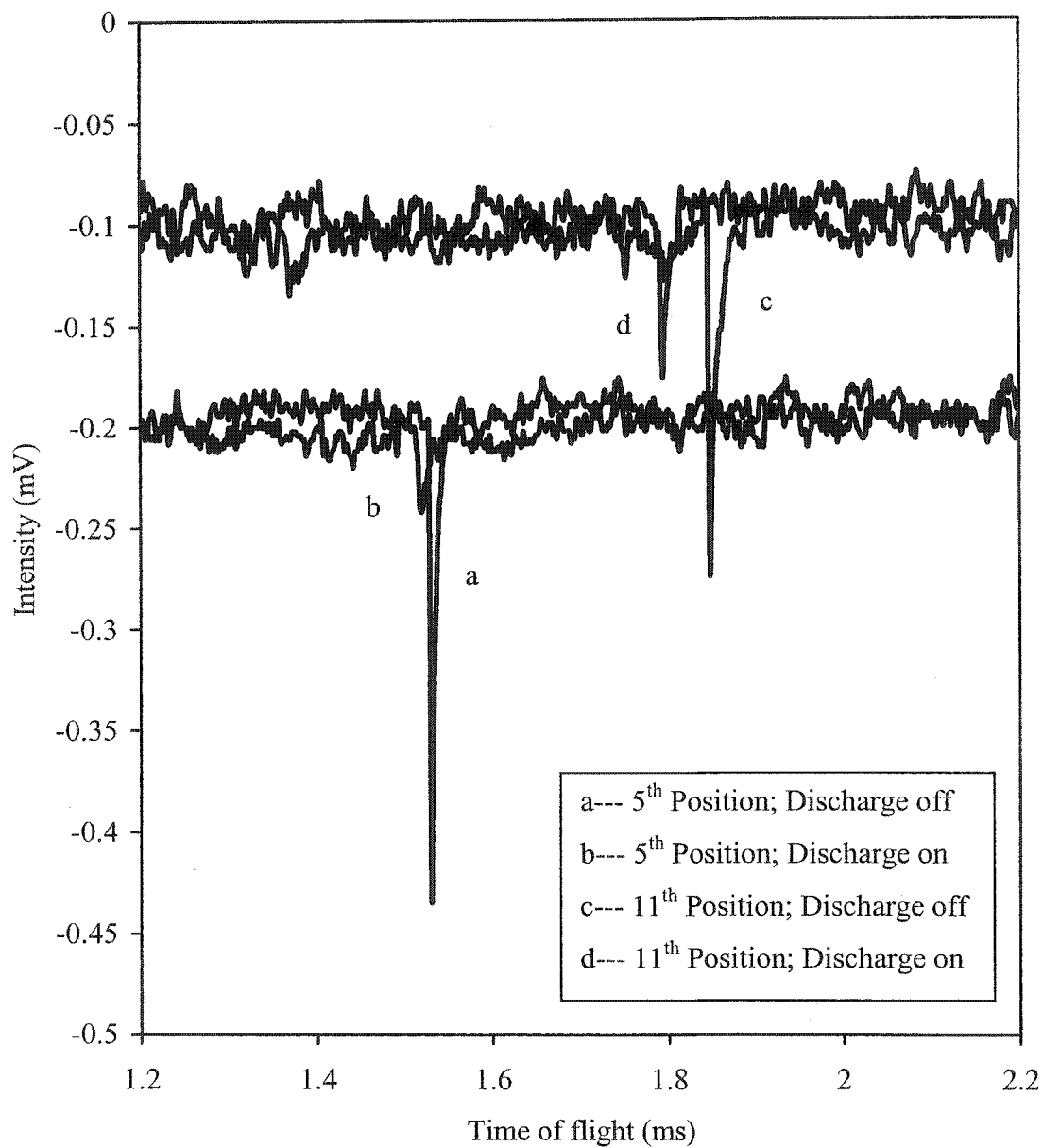


FIG. 52 Shock wave deflection waveform signal in neutral Ar and Ar MW discharge at the 5th position and 11th position (TM mode); Pressure 70Torr; Spark gap voltage 8 kV.

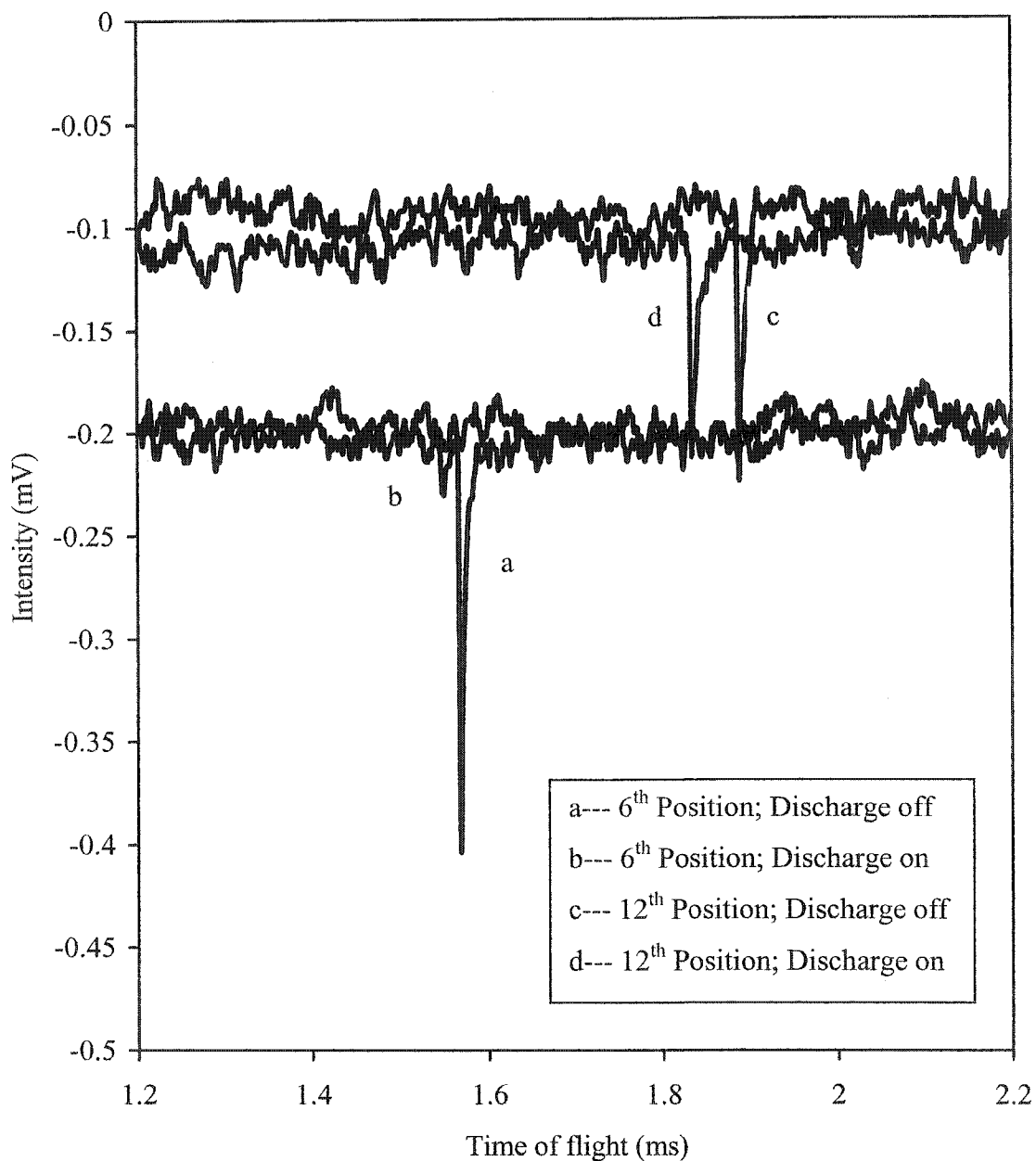


FIG. 53 Shock wave deflection waveform signal in neutral Ar and Ar MW discharge at the 6th position and 12th position (TM mode); Pressure 60Torr; Spark gap voltage 8 kV.

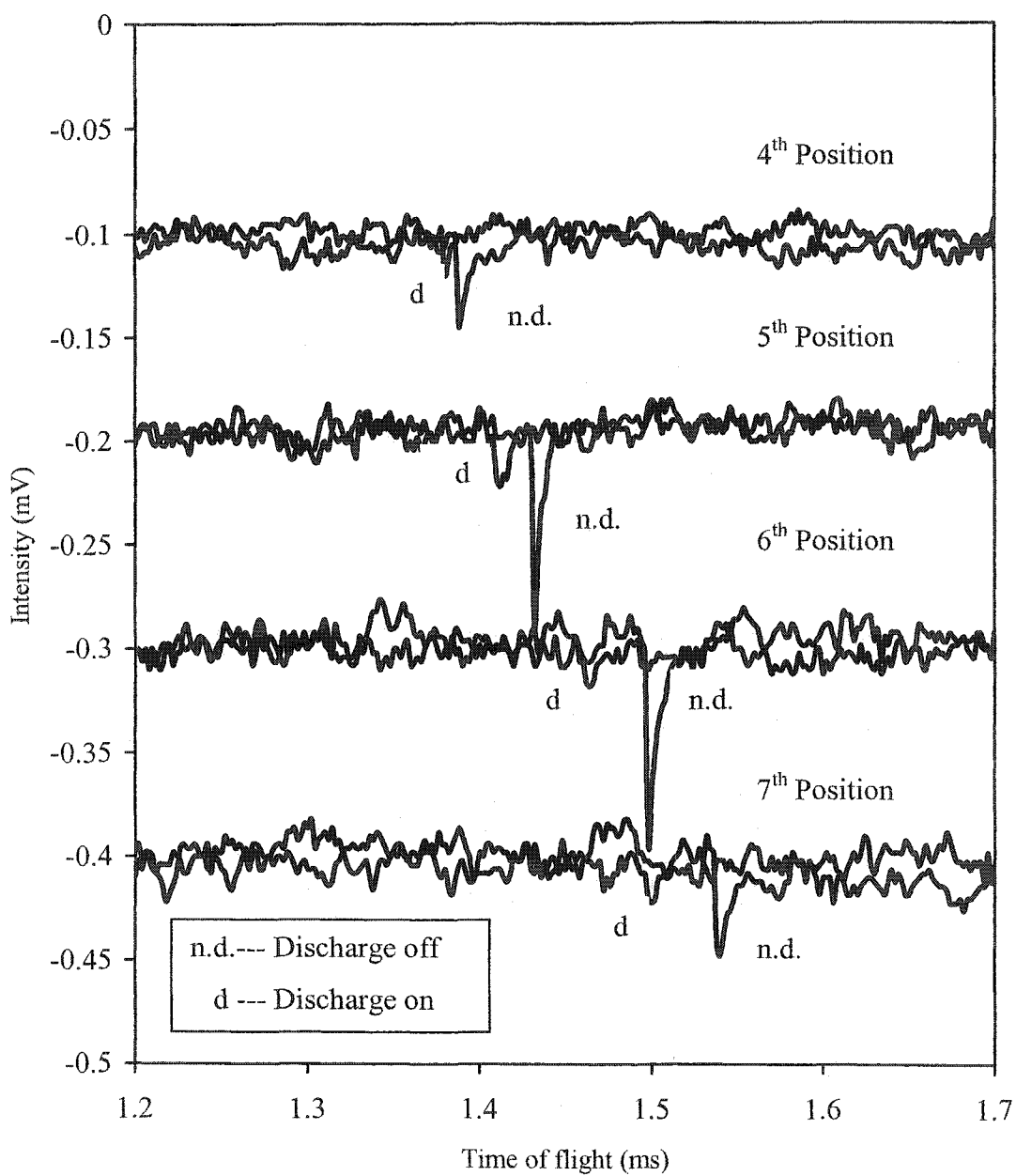


FIG. 54 Shock wave deflection waveform signal in neutral Ar and Ar MW discharge at the 4th, 5th, 6th, and 7th position (TM mode); Pressure 30 Torr; Spark gap voltage 8 kV.

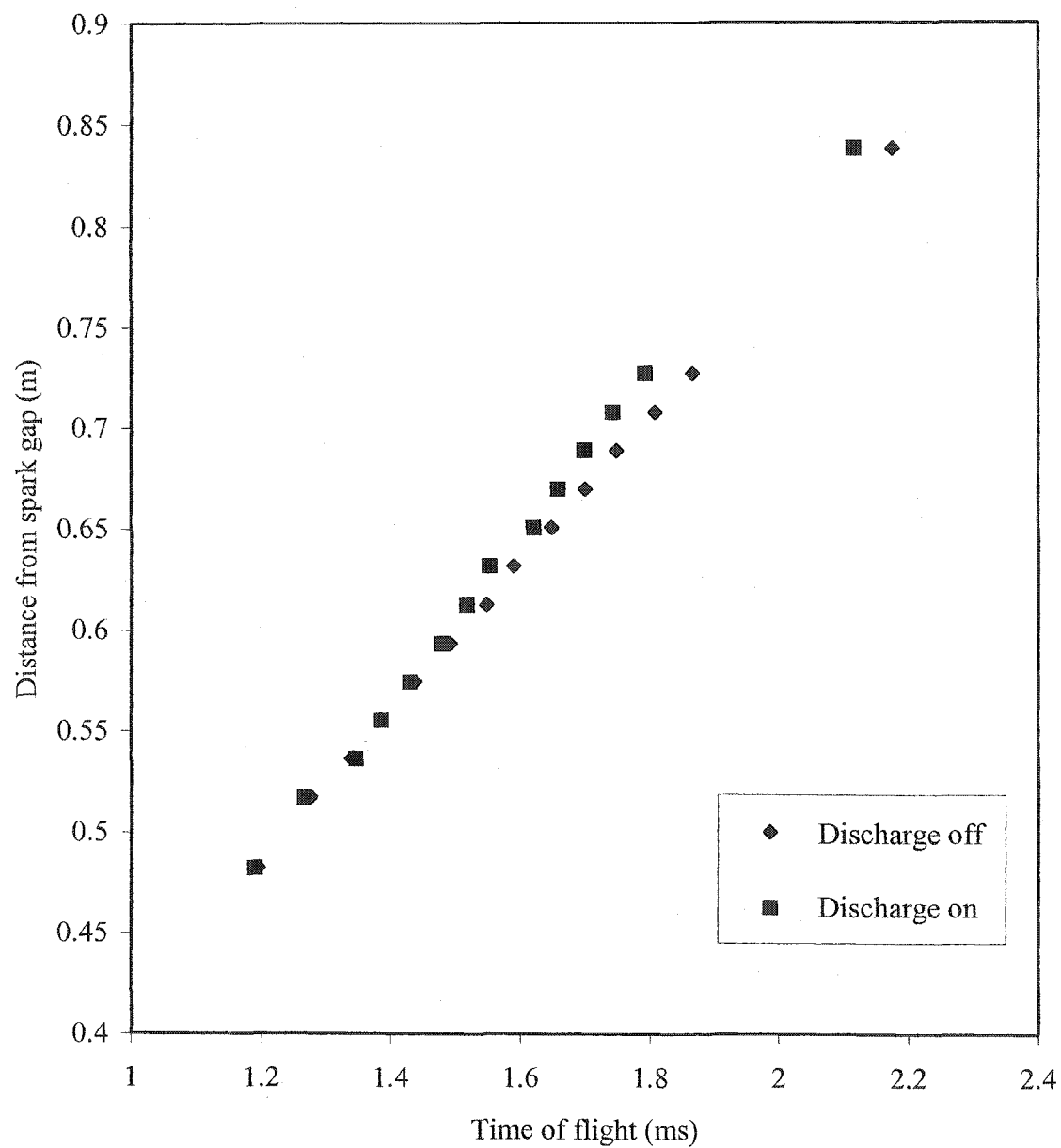


FIG. 55 Propagation of shock wave through neutral Ar and Ar MW discharge at 50 Torr (TM mode); Spark gap voltage 8 kV.

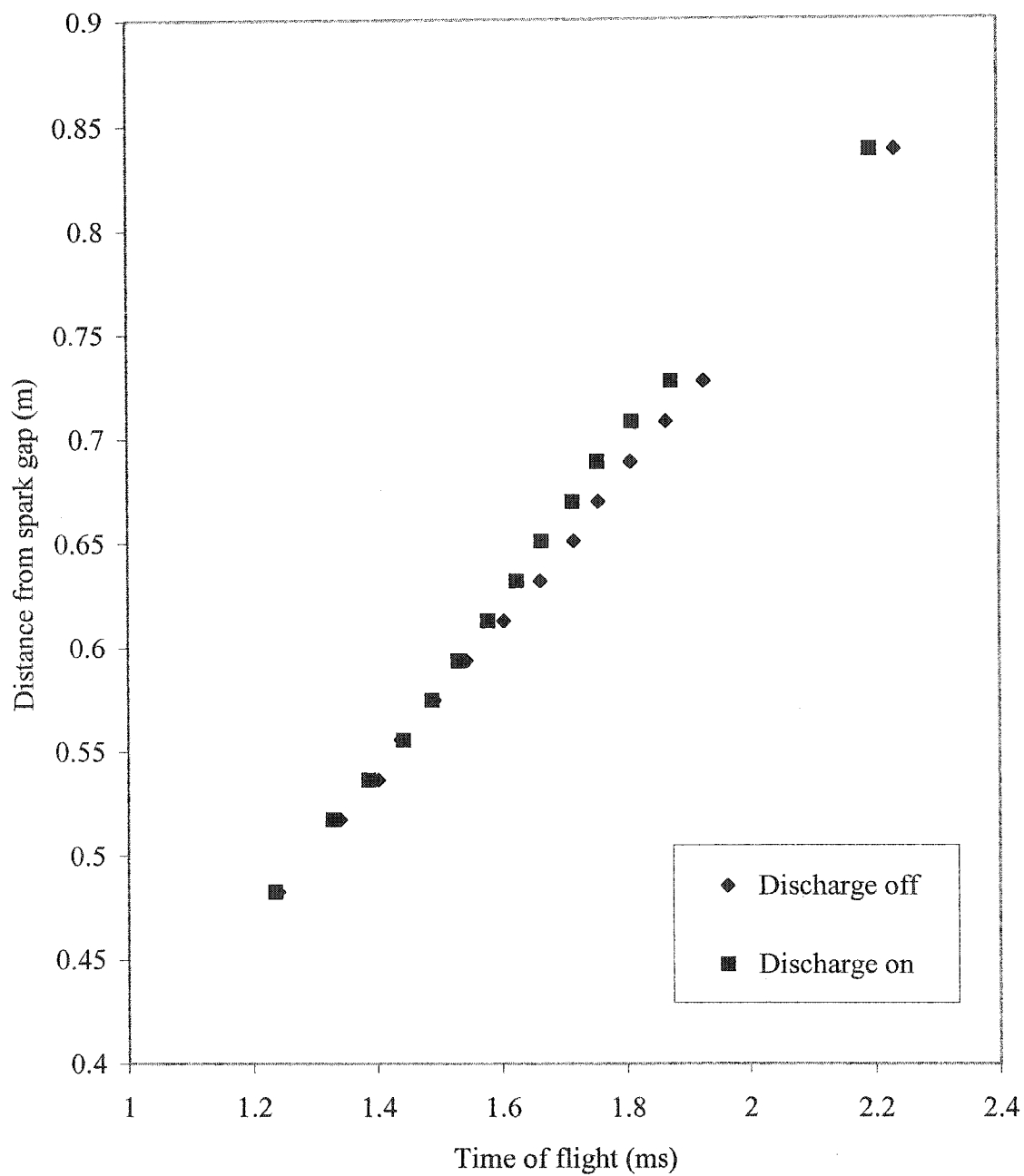


FIG. 56 Propagation of shock wave through neutral Ar and Ar MW discharge at 80 Torr (TM mode); Spark gap voltage 8 kV.

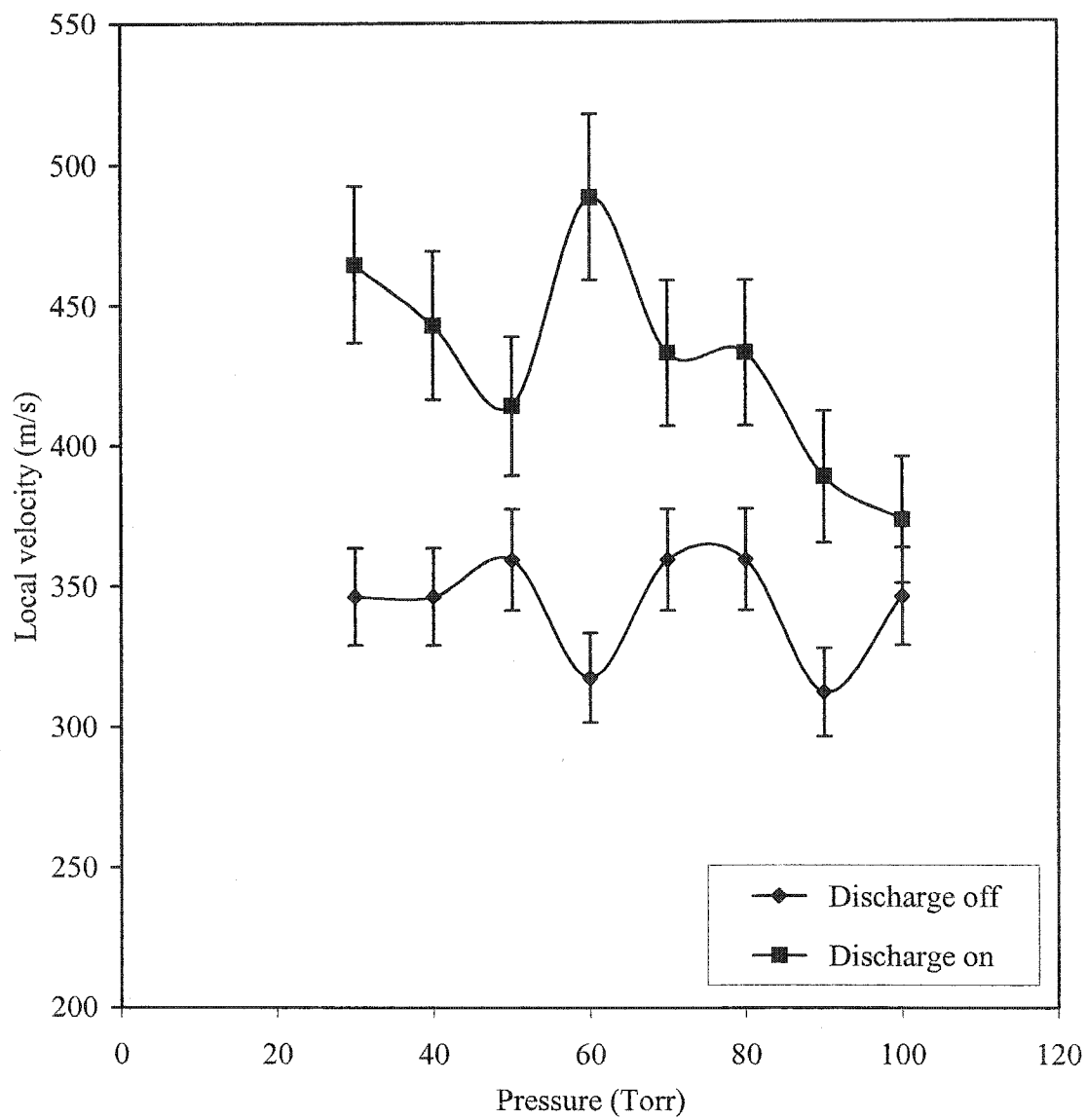


FIG. 57 Shock wave local velocity in neutral Ar and in Ar MW discharge at 4th position in TM mode.

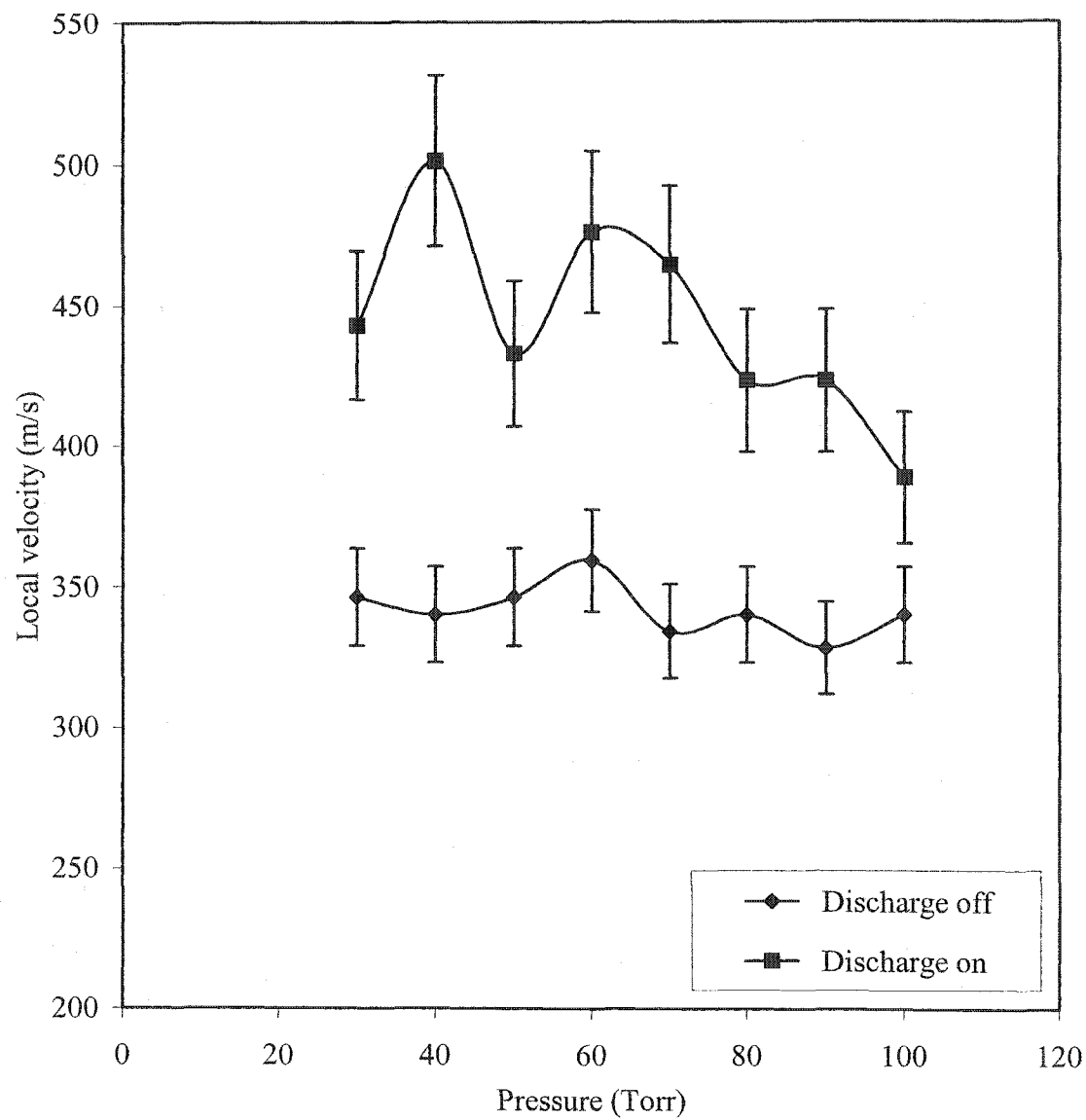


FIG. 58 Shock wave local velocity in neutral Ar and in Ar MW discharge at 5th position in TM mode.

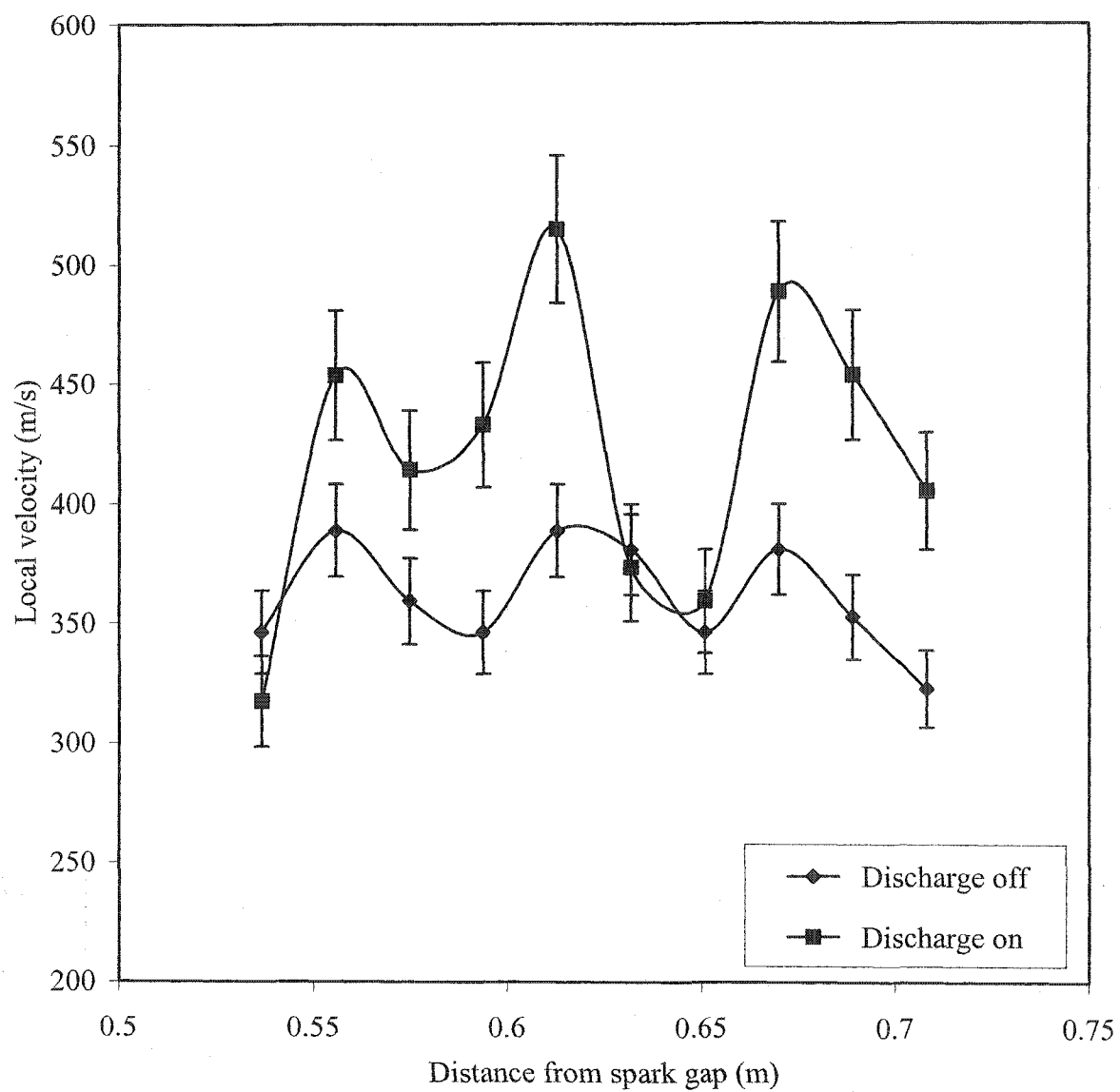


FIG. 59 Shock wave local velocity in neutral Ar and in Ar MW discharge at 50 Torr in TM mode.

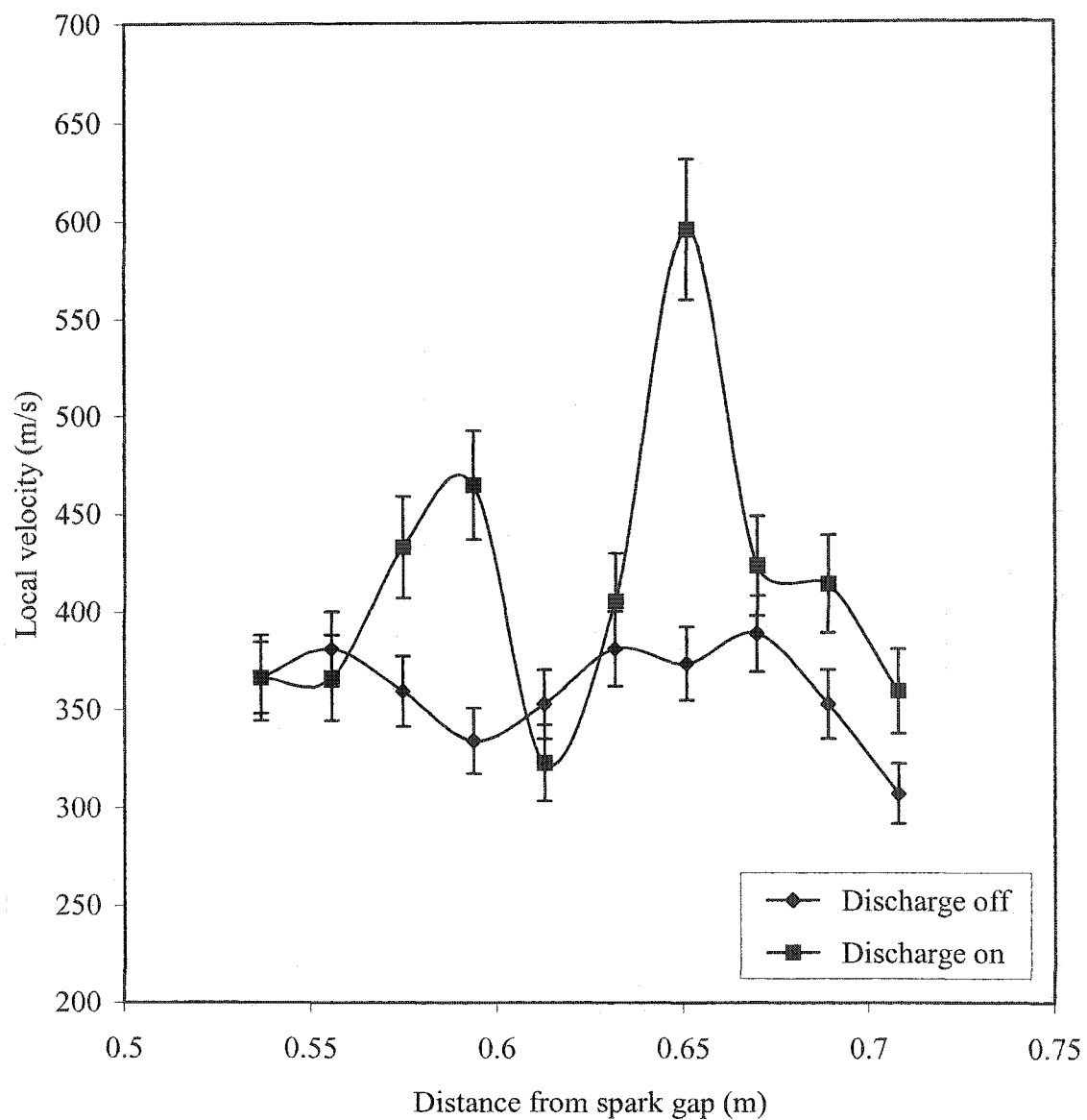


FIG. 60 Shock wave local velocity in neutral Ar and in Ar MW discharge at 70 Torr in TM mode.

3.4 Determination of Gas Temperature

Gas temperature is one of the most important local parameters in a discharge. Local gas temperature effects directly the rates of processes occurring inside the discharge. In the flow tube that we used for our experiment, the gas density decreases with increasing gas kinetic temperature because pressure in the tube is kept constant. Thus the reduced electric field E/N , which is one of the fundamental parameters of the discharge, will be increased when the gas kinetic temperature is increasing. The local and reduced electric field in the discharge will be discussed in Section 3.6. Besides, gas kinetic temperature determination will be used to calculate and predict accurately the electron density inside the discharge (see Section 3.5). Therefore, in the present case, by evaluating the gas kinetic temperature, one actually determines the fundamental parameter of the discharge, providing that the local value of electric field is known.

The determination of rotational temperature from the rotational spectra of the excited molecules is one of the standard diagnostic techniques used in discharges involving molecular gases. By assuming thermodynamic equilibrium of the molecular gases in the discharge, translational temperature and rotational temperature are equal. However, it is well known that rotational temperature may not be identified with gas translational temperature when chemical reactions are involved during the discharge. In order to avoid any error based on the assumption of identity of rotational temperature and translational temperature, we performed two different measurements for determining the gas temperature of the discharge.

In the first method, we used the same set of data from the time-of-flight measurements in both TE and TM mode (see Section 3.3) in order to calculate the gas

temperature using the amplitude reduction technique. We will discuss this technique in detail in the Section 3.4.1. In the second method, we will focus on the gas temperature measurement evaluated from the rotational emission spectrum of N_2 molecules in the discharge. We will describe and show some results from this technique in Section 3.4.2.

3.4.1 Amplitude Reduction Technique

We will use the set of data from time-of-flight measurements in Section 3.3 to calculate the gas temperature in the Ar MW discharge. This technique requires the shock waveform deflection signals that are measured in neutral Ar and in the Ar MW discharge at different distances from the spark gap and at various gas pressures. Shock wave deflection signals were time-integrated to obtain a real-time shock profile. Thus, the shock profile was subtracted from a mean of the background signal. The shock profile can be visualized by the time-dependent intensity, as shown in as Figures 61 and 62. Therefore, we can measure the amplitude of the signal in the presence of (a) the discharge and (b) in neutral gas. The amplitude values a and b depend on the density difference, as shown in Eqs. (34) and (35):

$$a \sim \rho_{2h} - \rho_{1h} \quad (34)$$

and

$$b \sim \rho_{2c} - \rho_{1c}, \quad (35)$$

where ρ_{1h} and ρ_{2h} are the densities of the Ar gas in front of and behind the shock front when the discharge is on, ρ_{1c} and ρ_{2c} are the densities of the Ar neutral gas in front of and behind the shock front when the discharge is off.

We can calculate the ratio of these amplitudes for the shock wave (a/b), as shown in Eq. (36):

$$\frac{a}{b} = \left(\frac{\rho_{1h}}{\rho_{1c}} \right) \left[\frac{\frac{\rho_{2h}}{\rho_{1h}} - 1}{\frac{\rho_{2c}}{\rho_{1c}} - 1} \right]. \quad (36)$$

By assuming that the gas in the Ar MW discharge is ideal, we can use Eqs. (6) and (11) in Section 2.2.2 and to rewrite Eq. (36) in term of the Mach number, pressure and temperature, as in Eq. (37):

$$\frac{a}{b} = \left(\frac{T_{1c}}{T_{1h}} \right) \left(\frac{p_{1h}}{p_{1c}} \right) \left[\frac{\frac{(\gamma+1)M_{1h}^2}{2+(\gamma-1)M_{1h}^2} - 1}{\frac{(\gamma+1)M_{1c}^2}{2+(\gamma-1)M_{1c}^2} - 1} \right]. \quad (37)$$

In the present experiment, the gas pressure in front of the shock wave was the same when the discharge was on (p_{1h}) as when it was off (p_{1c}). Therefore, we can calculate the value of (a/b) in terms of the Mach number and temperature, as shown in Eq. (38):

$$\frac{a}{b} = \left(\frac{T_{1c}}{T_{1h}} \right) \left[\frac{\frac{(\gamma+1)M_{1h}^2}{2+(\gamma-1)M_{1h}^2} - 1}{\frac{(\gamma+1)M_{1c}^2}{2+(\gamma-1)M_{1c}^2} - 1} \right], \quad (38)$$

where M_{1c} and M_{1h} are the Mach numbers in front of a shock wave when the discharge is off and then on, respectively, T_{1c} is the gas temperature in front of shock wave when the discharge is off (~ 293 K), and T_{1h} is the gas temperature in front of shock wave

when the discharge is on. The dominant species in our discharge was Ar, which is an atom. Therefore, the specific heat ratio for the Ar atom roughly corresponds to the γ value of monatomic gases. In the present case, we have $\gamma = 1.658$ at 293 K, and it does not change substantially with temperature.

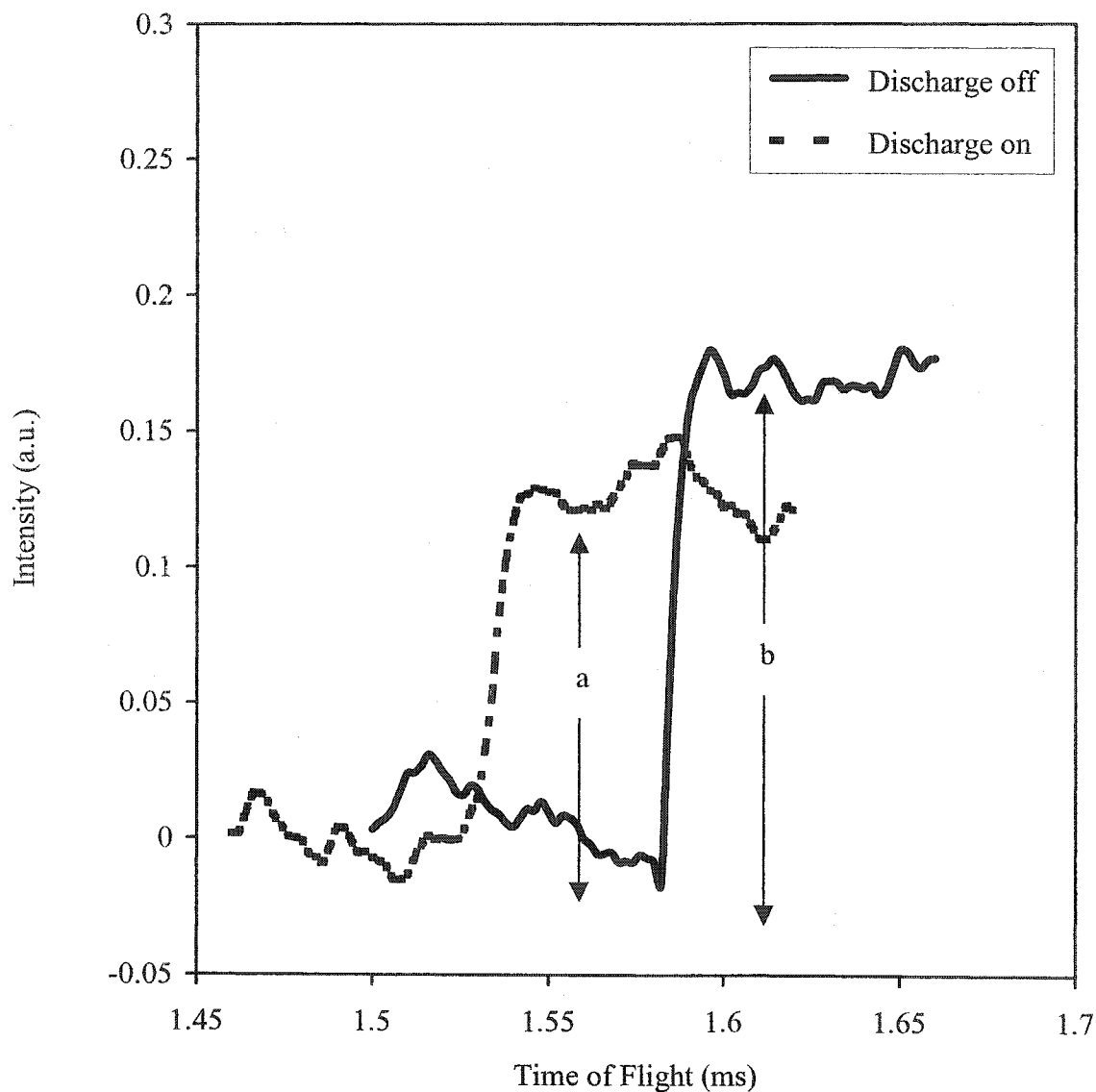


FIG. 61. Amplitude reduction of shock wave in neutral Ar and Ar MW discharge at 8th position, 30 Torr and TE Mode.

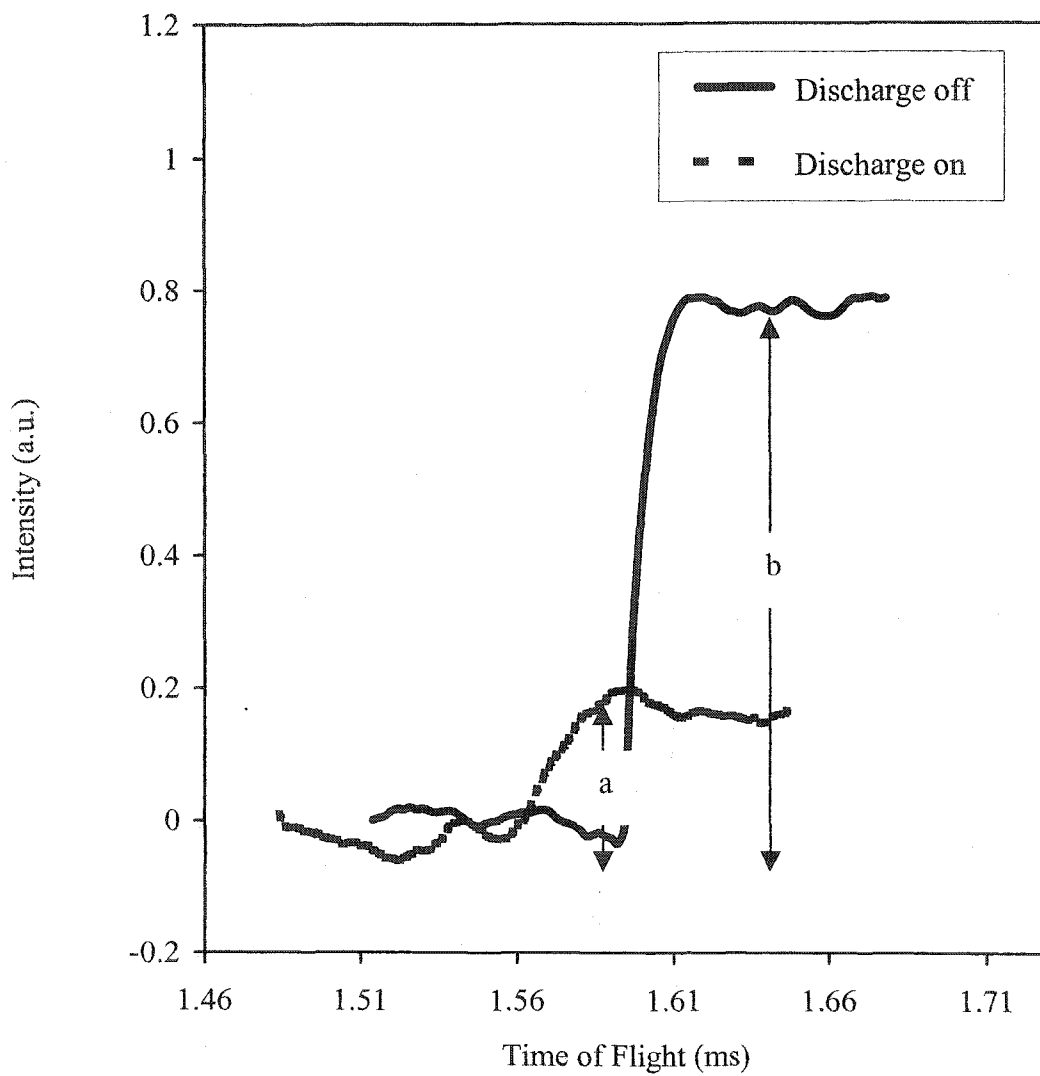


FIG. 62. Amplitude reduction of shock wave in neutral Ar and Ar MW discharge at 6th position, 70 Torr and TM Mode.

The left hand side of Eq. (38) can be evaluated from the data of the time-of-flight measurements described in Section 3.3 by using the technique described above. We can also calculate the Mach number in front of a shock wave for the discharge-off and discharge-on situations by measuring the shock wave velocity and by applying Eqs. (14) and (15). The gas temperature (T_{Ih}) in front of a shock wave when propagating through the discharge could be evaluated numerically to fit Eq. (38). The value of T_{Ih} obtained from Eq. (38) depends on the distance from the spark gap along the resonant cavity in both TE and TM mode, as shown in Figures 63, 64, 65, 66, 67, and 68.

The set of error bars shown in Figures 63 to 68, can be obtained by applying the average measurement uncertainty of a , b , M_{Ic} and M_{Ih} in Eq. (38). The average measurement uncertainties of a and b are about 2.5% and 1.4%, respectively. For M_{Ic} and M_{Ih} , the average measurement uncertainty is between 1.0% and 4.0%, depending on the gas pressure. Thus, the average measurement uncertainties of the gas temperature in TE mode are 7.6%, 10.3%, and 5.9% at the gas pressures of 30, 50, and 70 Torr, respectively (see Figures 63 to 65). For TM mode, the average measurement uncertainties in the gas temperature are 12.3%, 7.6%, and 6.4% at the gas pressures of 40, 50, and 70 Torr, respectively (see Figures 66 to 67).

From all of the data and from Figures 63, 64, and 65, the gas temperature in TE mode can be obtained. All maximum values of the gas temperature at any pressure are always at a distance from a spark gap of about 0.60 to 0.65 m (5th position to 8th position). The gas temperature maximum values are between 700 K to 1100 K. By considering all the data and Figures 66, 67, and 68, we conclude that the gas temperature in TM mode was distributed along the resonant cavity with a wider range

than for TE mode. All maximum values of the gas temperature at any pressure in TM mode were always at 0.57 to 0.68 m (4th position to 8th position) from a spark gap, and the maximum value of the gas temperature in this mode was between 500 K and 1000 K.

In order to compare these results with another technique, the rotational emission spectrum of N₂ molecules measurement was measured, and the gas temperature inside the discharge was determined at any distance from the spark gap (especially between the 4th to the 8th position) along the resonant cavity in both TE and TM modes. This is discussed in the next section.

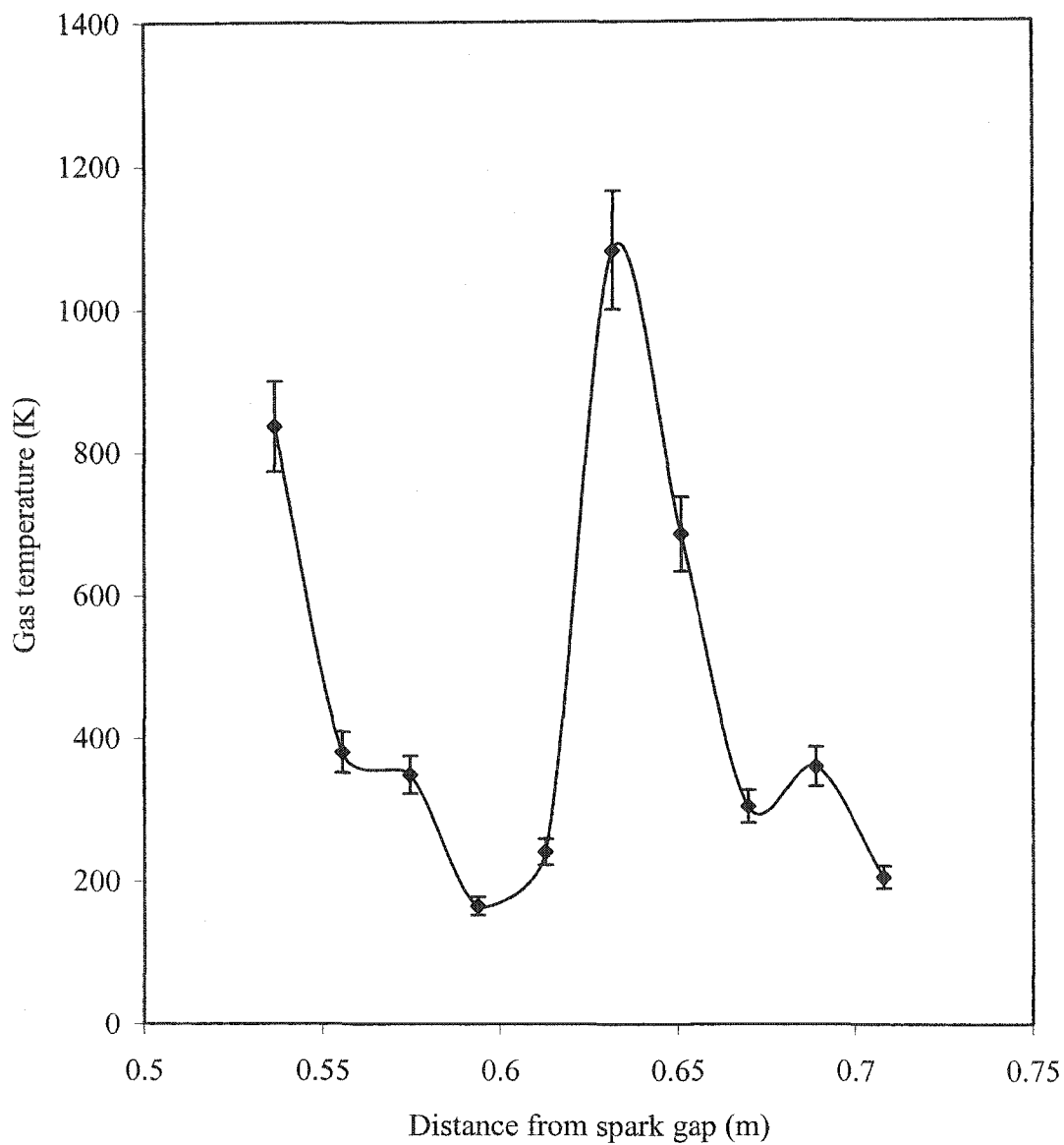


FIG. 63. Gas temperature distribution in Ar MW discharge at 30 Torr in TE mode.

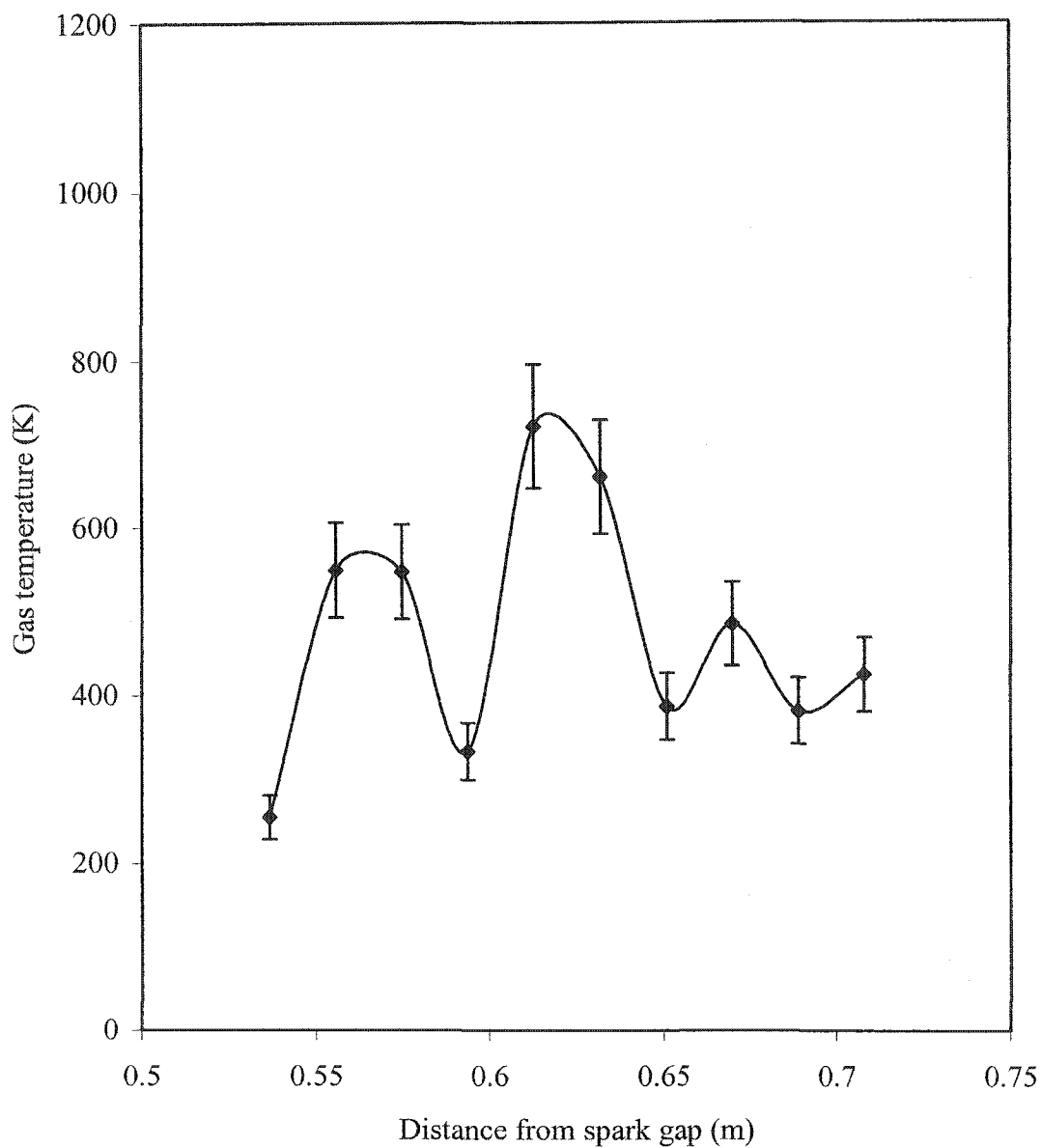


FIG. 64. Gas temperature Distribution in Ar MW discharge at 50 Torr in TE mode.

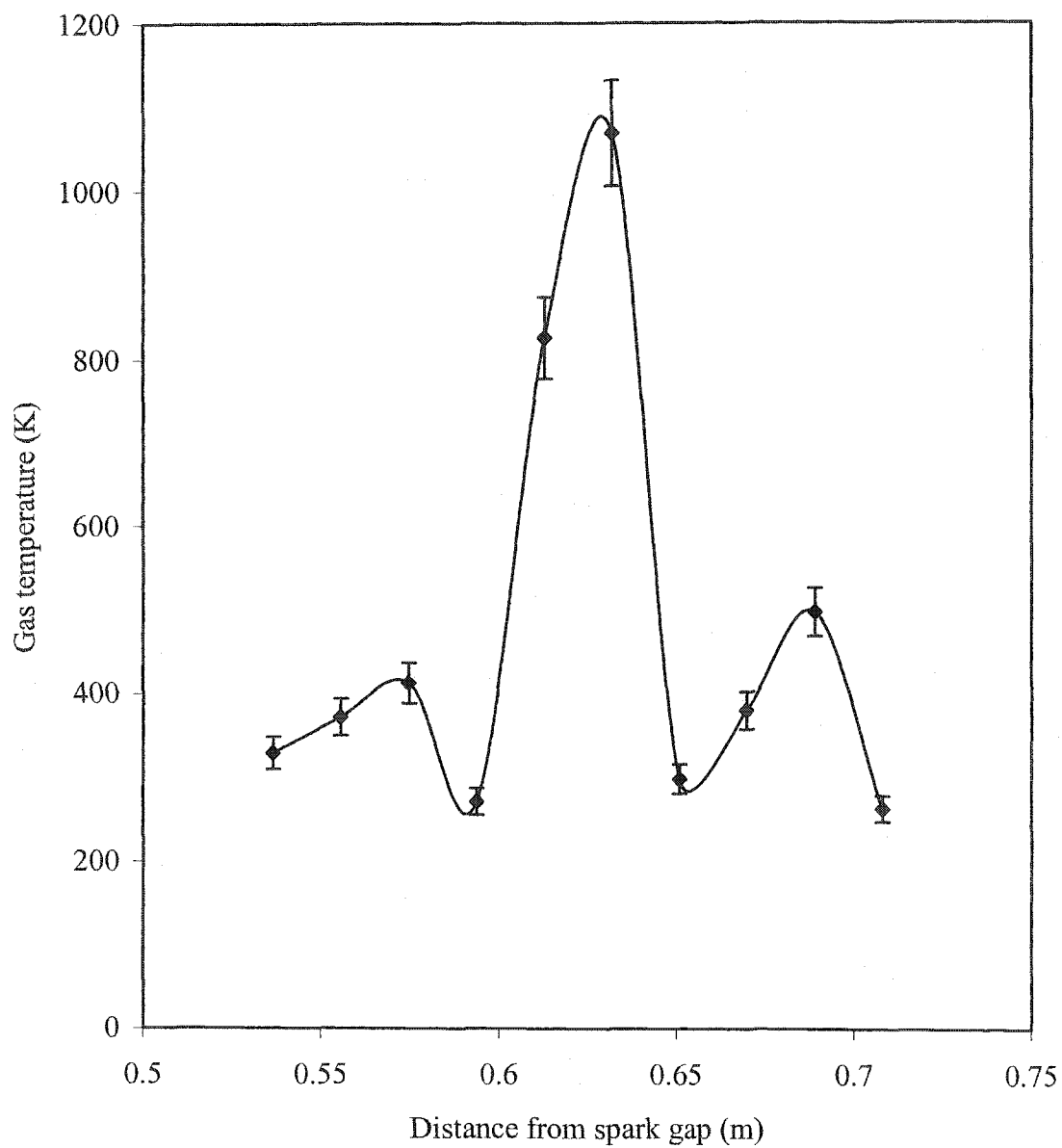


FIG. 65. Gas temperature Distribution in Ar MW discharge at 70 Torr in TE mode.

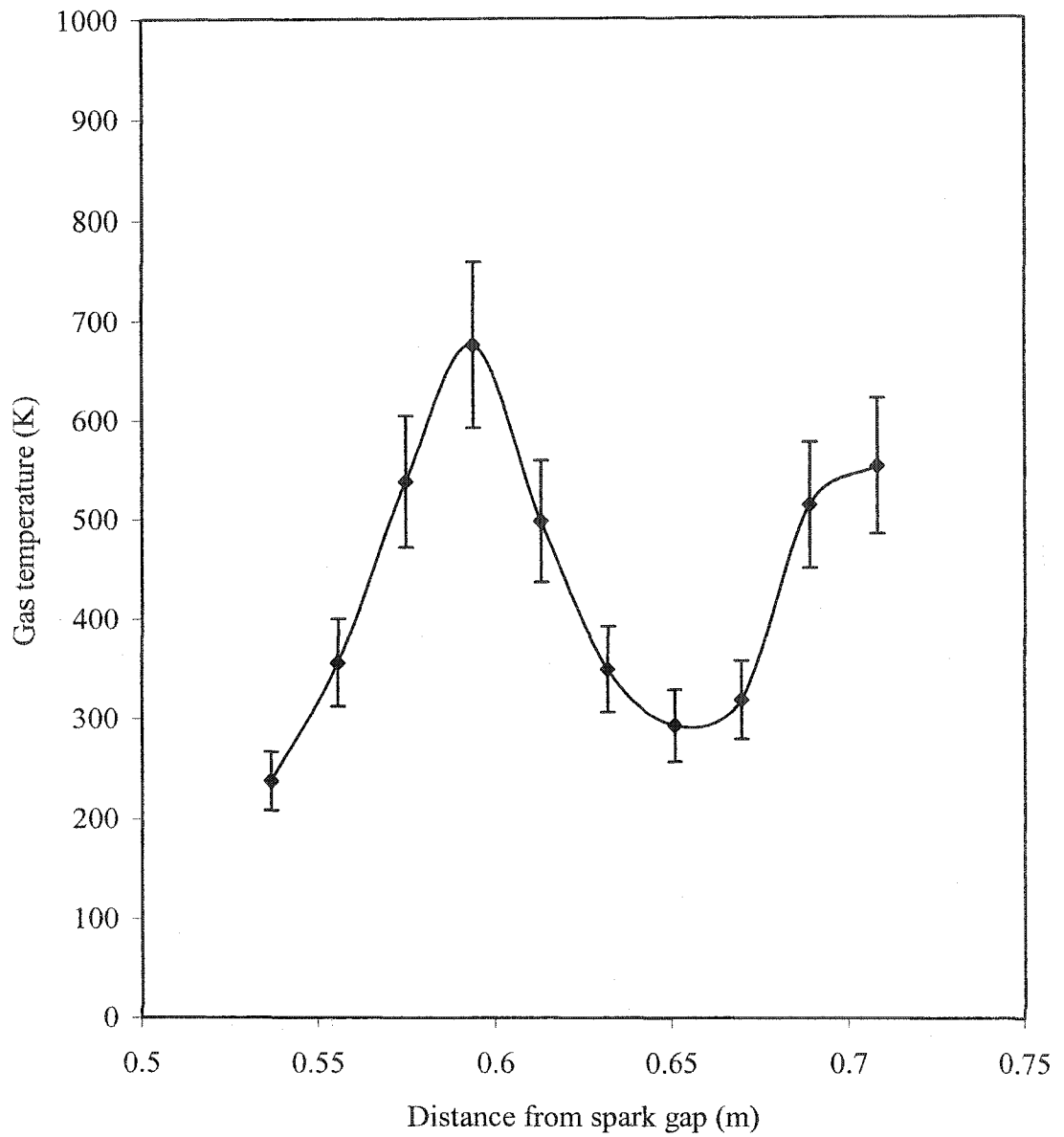


FIG. 66. Gas temperature Distribution in Ar MW discharge at 40 Torr in TM mode.

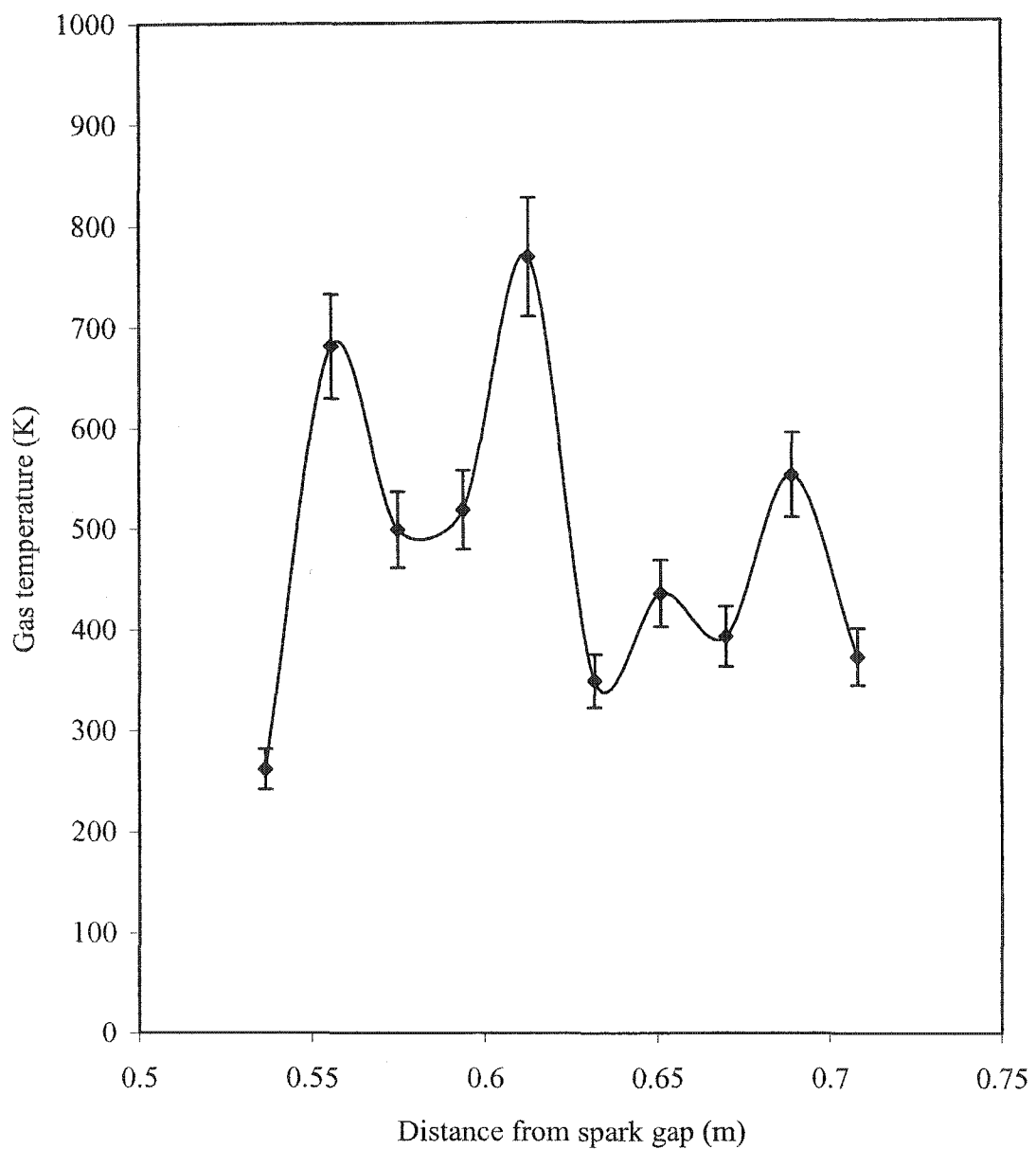


FIG. 67. Gas temperature Distribution in Ar MW discharge at 50 Torr in TM mode.

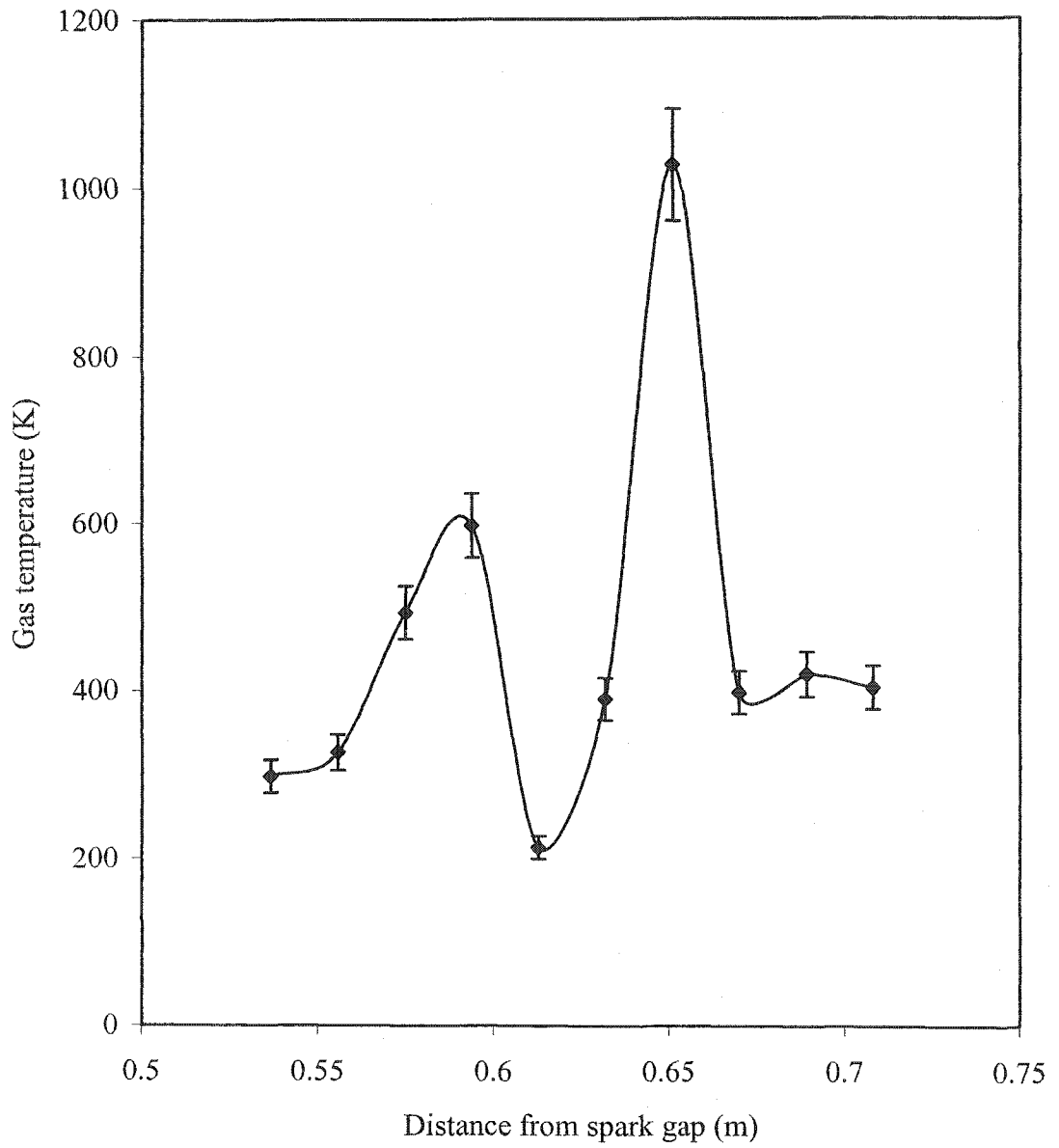


FIG. 68. Gas temperature Distribution in Ar MW discharge at 70 Torr in TM mode.

3.4.2. Emission Spectroscopy of Nitrogen

Optical emission spectroscopy (OES) is one of several highly accurate diagnostic techniques used to observe the gas temperature of a discharge. Since the diagnostic techniques based on OES involve nondestructive measurements and are very simple to set up, they are rather popular in discharge physics. OES can be used to determine the rotational temperature from the spectra of diatomic molecules by measuring the intensity of light emitted from excited molecules. The rotational temperature is approximately equal to translational temperature when the gas molecules are in a state of thermodynamic equilibrium in the discharge. Although the electron and gas temperatures are far from equilibrium, heavy particles in a weakly ionized discharge can attain thermodynamic equilibrium when the rotational and translational temperatures are practically equal during the steady state. For this reason, the rotational temperature can be correlated with the gas temperature of a weakly ionized discharge [43].

During the MW discharge, electrons gain energy from an electric field and excite the molecules by electron impact excitation. The intensity of light emitted by those excited molecules can be measured. However, only a small fraction of the molecules, are excited in a weakly ionized discharge, while most of them remain in the ground state. As their masses are large in comparison with the mass of an electron, those excited molecules preserve the same angular momentum and rotational energies as in their ground states. Furthermore, the distribution of rotational levels for these excited molecules is almost the same as those in the ground state. By using the equivalence of the rotational energy distribution of excited state molecules to that of the

ground state molecules and by carefully examining the spontaneous emission spectra from the de-excitation process of the molecules, we can identify the rotational structure of the excited molecules. We can also measure the rotational temperature of the excited molecules, which we assumed to be the gas temperature of the MW discharge.

In our work, we will use OES to measure the rotational temperature from the spectra of Nitrogen gas, which is the impurity inside the Ar MW discharge. The results of the rotational temperature by use of this technique will be compared with the gas temperature measured by the shock wave amplitude reduction technique in Section 3.4.1.

The spectral experimental setup for the rotational temperature measurement of the Nitrogen gas in the Ar MW discharge is shown in Figure 75. The imaging spectrograph (Acton SpectraPro-500i: Model SP-556 Spectrograph) has a focal length of 0.5 m and is equipped with a triple grating turret for gratings 1, 2, or 3 (grating 1 : 3600 grooves per millimeter; grating 2 : 1800 grooves per millimeter; and grating 3 : 600 grooves per millimeter). The spectral range is 200 to 1400 nm. The resolutions of this spectrograph are 0.005 nm , 0.02285 nm, and 0.07 nm at 435.8 nm for gratings 1, 2, and 3, respectively. The CCD camera (Apogee: Model SPH5-Hamamatsu S7030-1007: Back-Illum, with a pixel array of 1024x122 and a pixel size of 24 micron) is connected to the spectrograph to record the intensity of the emitted light from the Ar MW discharge. A mercury lamp was used to calibrate the wavelengths of absorbed spectra.

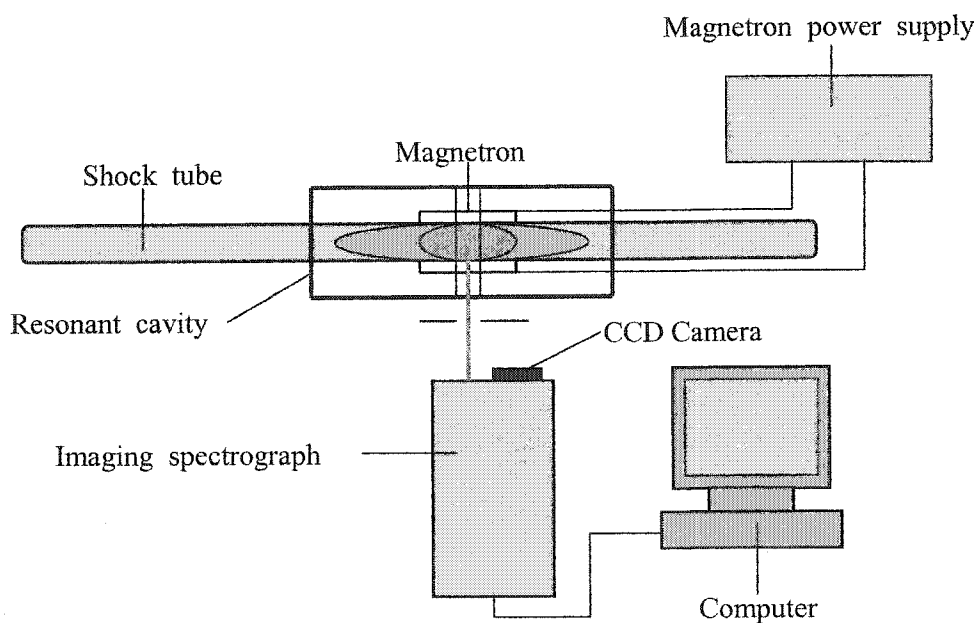


FIG. 69. Schematic of the experimental set-up for N₂ emission spectroscopy.

In the Ar MW discharge, we used the Ar + H₂ (95/5 %) and N₂ (~ 0.01 %) gas mixture. The most abundant constituents inside the discharge were Ar, H₂, and N₂. According to its relatively strong band emission intensity and its well-defined rotational term values, as shown in Table III, the N₂ molecule is the best species for the rotational spectrum analysis. In our experiment setup, we chose the Second Positive System (Figure 70) with the electronic transition from $C^3\Pi_u - B^3\Pi_g$ (492.0 – 280.0 nm) in the ultraviolet and visible ranges of the emission spectra of N₂ [44]. We observed the most intense emission bands in the Second Positive System ($C^3\Pi_u - B^3\Pi_g$) with band origins starting at 466.7 nm, 434.3 nm, 405.9 nm, 380.5 nm, 357.7 nm, and 337.1 nm. These band origins correspond to the (0 – 5), (0 – 4), (0 – 3), (0 – 2), (0 – 1), and (0 – 0) vibrational transitions, respectively [45]. Because of its small value of self absorption

and because there is no contamination of rotational spectra with Ar lines, we selected the rotational spectrum of the (0 - 2) vibrational transitions, which correspond to the band origins 380.5 nm for the rotational temperature analysis.

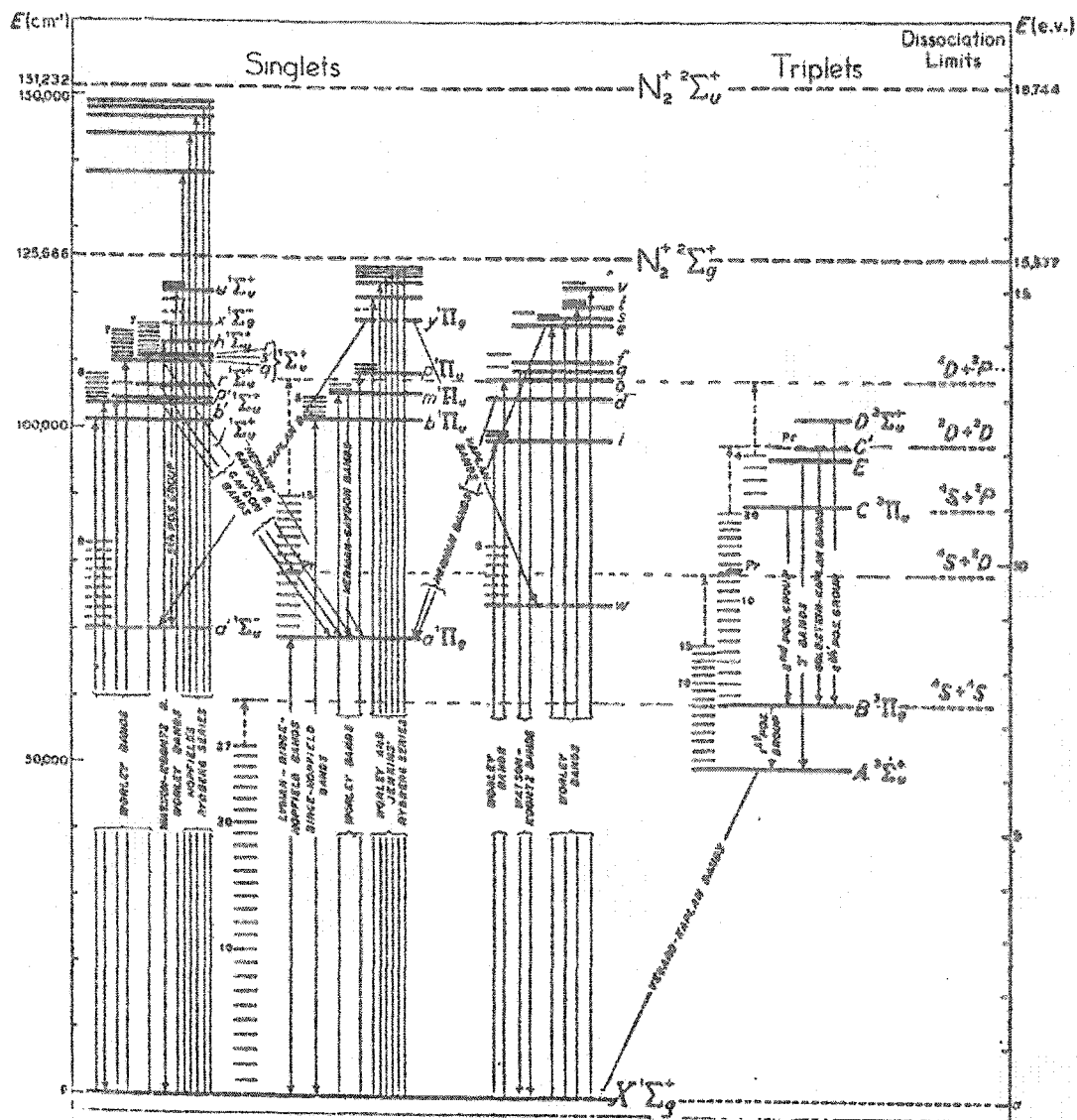


FIG. 70. Energy level diagram of the N₂ molecule reproduced from Ref. [44].

From Figure 70, we have many rotational transitions in each vibrational band or transition in the fine structure. Vibrational bands in the Nitrogen Second Positive System consist of strong P and R branches and weak Q branches. The structure is further complicated by the triplet splitting of the rotational quantum number J in both states, giving three separate P and R sub-branches and two Q sub-branches that correspond to the J selection rules for multiplet components with the same spin (Ω). Therefore, we can write three sub-bands, which are ${}^3\Pi_0 - {}^3\Pi_0$, ${}^3\Pi_1 - {}^3\Pi_1$, and ${}^3\Pi_2 - {}^3\Pi_2$ from the ${}^3\Pi - {}^3\Pi$ band. An example of the ${}^3\Pi_1 - {}^3\Pi_1$ transition belonging to the P , Q , or R branches in the $(0 - 2)$ vibrational band of the $C^3\Pi_u - B^3\Pi_g$ electronic excitation transition is shown in Figure 71, where C and B are spectroscopic notation. In the example, five rotational transitions are from an excited state with a rotational number $J' = 6, 5, 2,$ or 1 to the lower states with rotational quantum numbers $J'' = 6, 5, 2,$ or 1 that correspond to $\Delta J = J' - J'' = +1, 0, -1$. Generally, in a particular excited vibrational band, there are many rotational transitions that are classified into P , Q , or R branches corresponding to the selection rules $\Delta J = J' - J'' = -1, 0, +1$, respectively, where J' and J'' are the upper and lower rotational quantum numbers.

The wavelength [cm^{-1} , the number of wavelengths per centimeter] of the lines of each P , Q , or R branch, can be obtained by following the procedure directed by Herzberg [44] and Hartmann and Johnson [45], as shown in Eq. (39) for the band $\nu' - \nu''$.

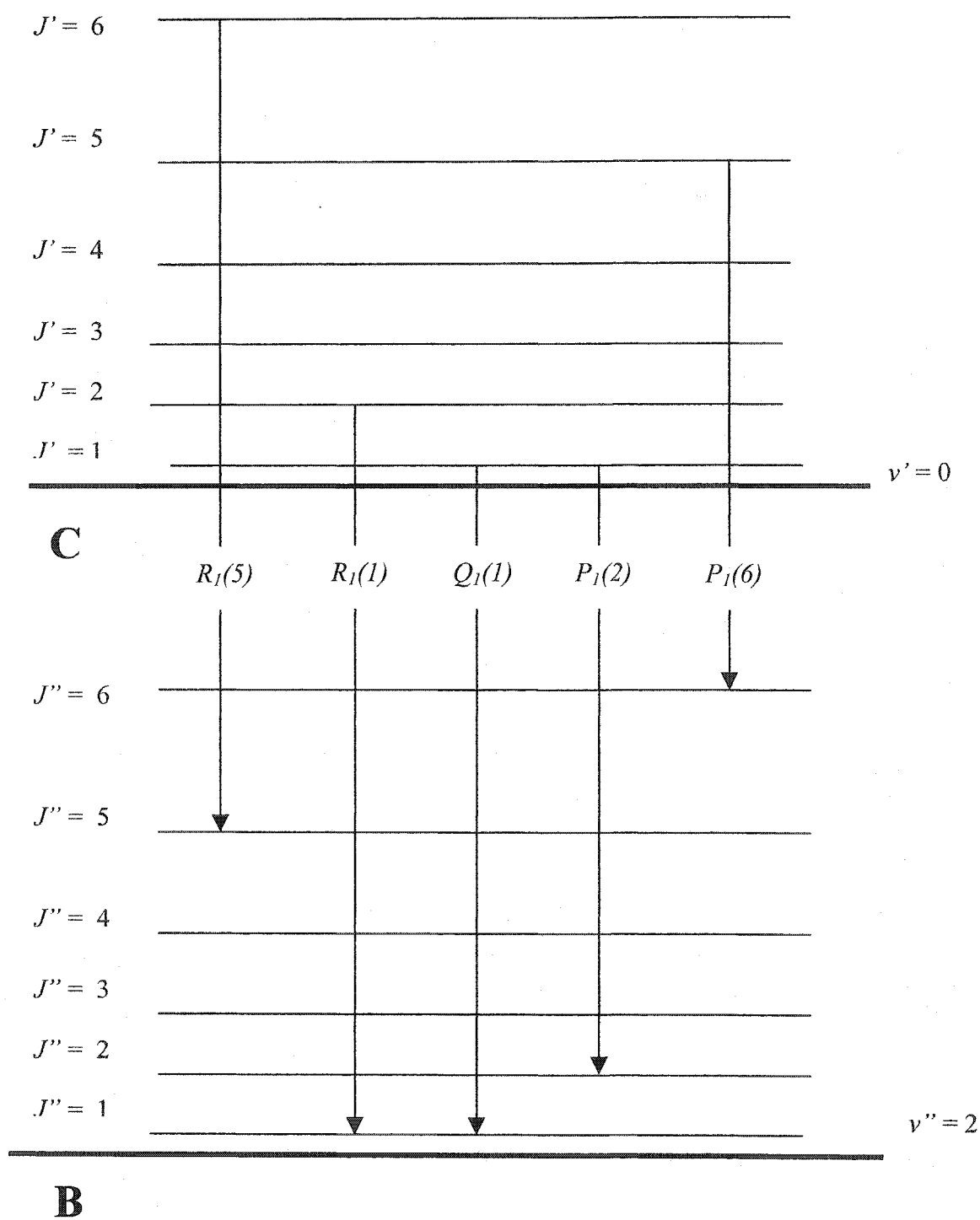


FIG. 71. Example of five rotational transitions of the ${}^3\Pi_1 - {}^3\Pi_1$ transition belonging to the P , Q , or R branches in the $(0-2)$ vibrational band of the $C^3\Pi_u - B^3\Pi_g$ electronic excitation system.

$$\begin{aligned}
P \text{ branches : } & \nu_{\Omega:J}^P = \nu_0 + F'_{\Omega:J-1} - F''_{\Omega:J}; \quad \Omega = 0, 1, 2. \\
Q \text{ branches : } & \nu_{\Omega:J}^Q = \nu_0 + F'_{\Omega:J} - F''_{\Omega:J}; \quad \Omega = 0, 1. \\
R \text{ branches : } & \nu_{\Omega:J}^R = \nu_0 + F'_{\Omega:J+1} - F''_{\Omega:J}; \quad \Omega = 0, 1, 2.
\end{aligned} \tag{39}$$

Here, ν_0 is the band head of the electric vibrational transition, F' and F'' are the term values for the multiplet rotational components of the upper and lower levels, respectively and J is the rotational quantum of the lower level $\nu''(J = J'')$. The subscripts on F' and F'' represent the application of J selection rules.

The term values $F_{\Omega:J}$ ($\Omega = 0, 1, 2$) for the multiplet of any vibrational level ν can be expressed by the semi-empirical formulae given in Ref. [45]:

$$\begin{aligned}
F_{0:J} &= B_v [J(J+1) - Z_1^{1/2} - 2Z_2] - D_v \left(J - \frac{1}{2} \right)^4, \\
F_{1:J} &= B_v [J(J+1) - 4Z_2] - D_v \left(J + \frac{1}{2} \right)^4,
\end{aligned} \tag{40}$$

and

$$F_{2:J} = B_v [J(J+1) + Z_1^{1/2} - 2Z_2] - D_v \left(J + \frac{1}{2} \right)^4,$$

where

$$Z_1 = Y_v(Y_v - 4) + \frac{4}{3} + 4J(J+1),$$

and

$$Z_2 = \frac{1}{3Z_1} \left[Y_v(Y_v - 1) - \frac{4}{9} - 2J(J+1) \right].$$

B_v and D_v are rotational constants and Y_v a spin-axis coupling constant. The values used in the present work for $C^3\Pi_u$ and $B^3\Pi_g$ are given in table III.

TABLE III. Values of constants for the evaluation of rotational term values of the Nitrogen Positive System, $C^3\Pi_u$ and $B^3\Pi_g$, from Ref. [45].

ν	$C^3\Pi_u$			$B^3\Pi_g$		
	B_ν	Y_ν	$D_\nu \times 10^6$	B_ν	Y_ν	$D_\nu \times 10^6$
0	1.8149	21.5	6.7	1.62849	25.9	6.4
1	1.7933	21.5	6.8	1.61047	26.2	6.5
2	1.7694	21.4	7.3	1.59218	26.4	6.7
3	1.7404	21.1	8.5	1.57365	26.8	6.8
4	1.6999	20.3	12.5	1.55509	27.0	6.9
5	-	-	-	1.53676	27.3	7.0

All B_ν , D_ν , and Y_ν values are presented in wavenumber units, cm^{-1} , and they have different values that depend on the specific vibrational level (ν). For the (0 - 2) band of the $C^3\Pi_u - B^3\Pi_g$ transition, the band head (ν_0) is 26281.2 cm^{-1} (or $\lambda_0 \cong 380.5 \text{ nm}$). By using the information from Table III, we constructed the Fortrat diagrams shown in Figure 72. The location of each particular line in the spectrum was calculated from Eqs. (39) and (40). In Figure 73, we show is the actual rotational spectrum for the (0 - 2) band in the Nitrogen Second Positive System that was obtained in the MW discharge with our spectral apparatus.

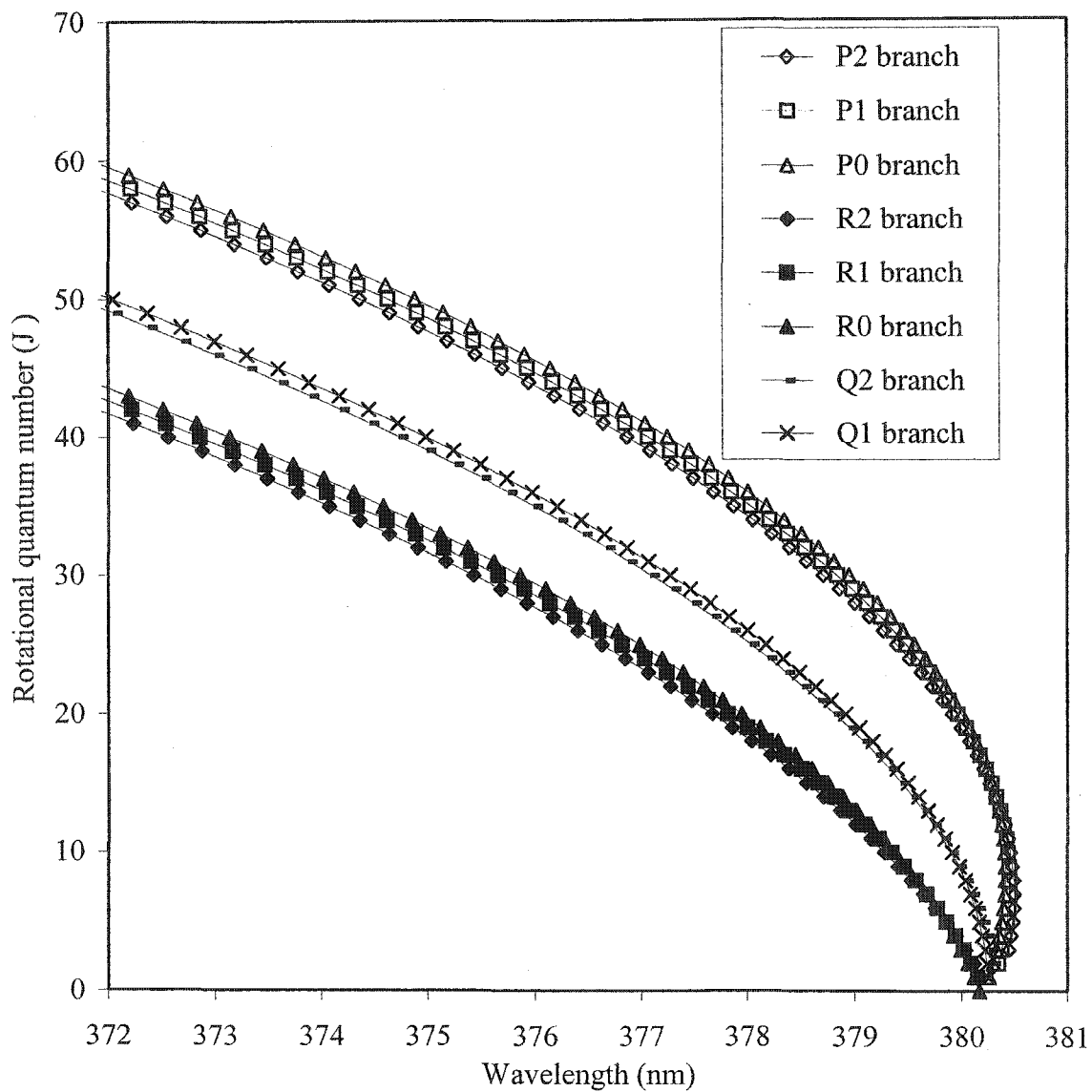


FIG. 72. Fortrat diagram of $N_2(0-2)$ band in $C^3\Pi_u - B^3\Pi_g$ system.

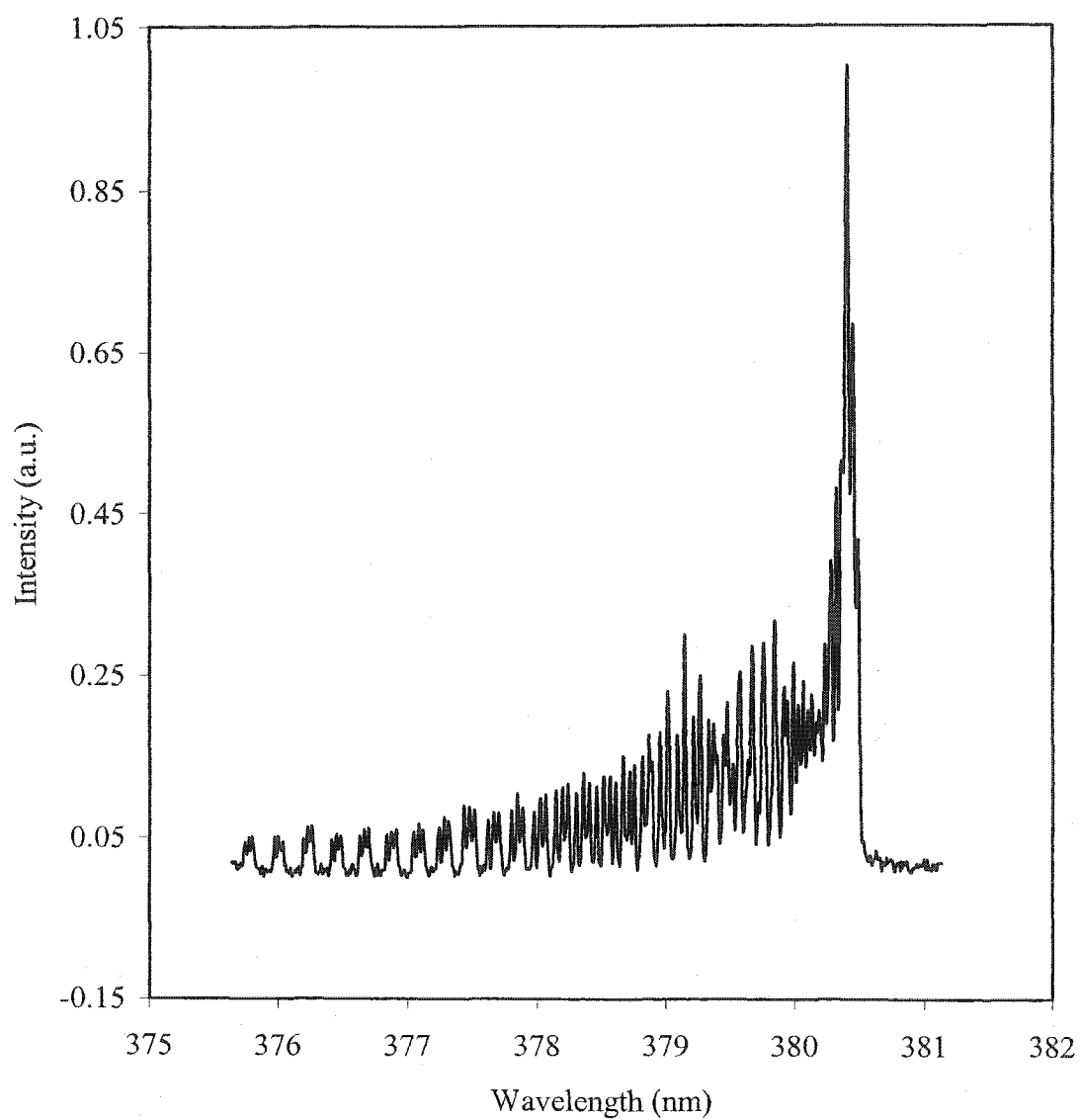


FIG. 73. Rotational spectrum of the (0-2) band at 380.5 nm, of the Nitrogen Second Positive System recorded at 8th position in TM mode discharge at 70 Torr.

From Figures 72 and 73, as well as in all other rotational spectra measured in the experiment, the rotational transition lines corresponding to particular rotational quantum numbers could be identified. However, the calculation of rotational temperature requires more information about the relationship between the relative intensity of rotational lines and the rotational quantum numbers. For this reason, we would like to discuss further the spectral intensity distribution for the $C^3\Pi_u$ state during the excitation process from the ground state $x^1\Sigma_g^+$ ($\nu = 0$) of Nitrogen Second Positive system.

As described in the beginning of this section, the ground state N_2 ($x^1\Sigma_g^+$), principally in the $\nu = 0$ vibrational level, is excited to the upper level of the Nitrogen Second Positive System $C^3\Pi_u$ by electron impact. The rotational distribution is assumed to be unchanged in the excitation process, so it corresponds to the distribution in $x^1\Sigma_g^+$ at its rotational temperature (T_r). We can determine the population distribution term f for any ν' of $C^3\Pi_u$ by application of the Boltzmann law to $x^1\Sigma_g^+$ ($\nu = 0$):

$$f = (2J' + 1) \exp\left(-J'(J' + 1) \frac{hcB_x}{kT_r}\right), \quad (41)$$

where J' is the rotational number of the excited state, B_x is the rotational constant of the ground state ($B_x = 1.9898 \text{ cm}^{-1}$), and c , h , and k are the speed of light, Planck's constant and Boltzmann's constant, respectively. By dividing f by the partition function

$$Q_r = \sum_{J'} f, \quad (42)$$

we obtain the normalised population $P_{J'}$ in the state with the rotational quantum number J' :

$$P_{J'} = \frac{f}{Q_r} = \frac{(2J' + 1)}{Q_r} \exp\left(-J'(J' + 1) \frac{hcB_x}{kT_r}\right). \quad (43)$$

In the de-excitation process from $C^3\Pi_u$ to $B^3\Pi_g$, the population $P_{J'}$ is distributed between the P , Q , and R branches following the line strengths (Hönl-London factors) $S^P_{\Omega:J'}$, $S^Q_{\Omega:J'}$, and $S^R_{\Omega:J'}$. For the Nitrogen second positive system, they are given by

$$\begin{aligned} S^P_{\Omega:J'} &= \frac{(J' + 1 + \Omega)(J' + 1 - \Omega)}{(J' + 1)}, \\ S^Q_{\Omega:J'} &= \frac{(2J' + 1)\Omega^2}{J'(J' + 1)}, \end{aligned} \quad (44)$$

and

$$S^R_{\Omega:J'} = \frac{(J' + \Omega)(J' - \Omega)}{J'}.$$

The line strengths obey the sum rule

$$\sum_{\Omega} \left(S^P_{\Omega:J'} + S^Q_{\Omega:J'} + S^R_{\Omega:J'} \right) = 2J' + 1. \quad (45)$$

Combining Eqs. (41), (43), (44), and (45) gives the normalised intensity of any line; e.g. in the R branch,

$$I_E = S^R_{\Omega:J'} \frac{I}{Q_r} \exp\left(-J'(J' + 1) \frac{hcB_x}{kT_r}\right). \quad (46)$$

We can write identical formulae for the P and Q branches.

In the Nitrogen Second Positive System $C^3\Pi_u - B^3\Pi_g$, the difference of the total angular momentum is $\Delta A = 0$ ($A = 1$ for Π). By using the Hönl-London factors in Eq. (44), we found that the strong value of the line strengths are in the P and R branches. In order to clarify this, we use Eq. (46) with a given rotational temperature $T_r = 1200$ K to calculate the relative intensity distributions for the P , Q , and R branches as functions of J' . The result shows that the peak intensities of the P and R branches, which occur around a J' value of 20, have almost the same value. Therefore, it is very difficult to choose a the particular sub-branch (e.g., P_0 , R_0 , or R_1) from the P and R branches to calculate the rotational temperature. For this reason, we use this information and the Fortrat diagram (Figure 72) to plot the relative intensity distributions of the P , Q , and R branches as functions of wavelength variation from the band head (Figure 74). It is clear that the R branch at high J' is the best choice to use to calculate the rotational temperature, since the lines corresponding to a small J' are closely packed for all three branches. The possibility of overlapping produces difficulties in identifying the rotational transition out of the P , Q , and R branches at low rotational quantum numbers. Furthermore, the resolution of our imaging spectrograph is not sufficient (~ 0.005 nm). Therefore, in order to avoid those problems, we have chosen the rotational transitions at the large rotational quantum numbers of the R branch. By careful examination of Figures 72, 73, and 74, the R_0 sub-branch of the R branch was chosen to use to calculate the rotational temperature in the present experiment.

Eq. (46) can be rewritten in the following form:

$$\ln\left(\frac{I_E}{J'}\right) = -\frac{hcB_x}{kT_r} J'(J'+1) + \text{constant}, \quad (47)$$

where $S^R_{\Omega:J'}$ was replaced with the factor J' obtained from the Hönl-London factors for the R_0 sub-branch of the $C^3\Pi_u - B^3\Pi_g$ transition. All other coefficients and their logarithms were considered constant with respect to J' . Hence, the slope of the linear plot of the logarithm of normalized rotational line intensity, $\ln[I_E/J']$, with respect to $J'(J'+1)$ is inversely proportional to the rotational temperature of the Nitrogen molecules.

The rotational temperature calculated from the slope of the fitting line is shown in Figures 75 and 76 at two different gas pressures (30 and 75 Torr) at the same position of measurement (8th position) in TE mode, while the other discharge parameters were kept constant. In order to reduce the systematic error in measuring the rotational temperature, we have to keep the chemical reactions inside a discharge at a minimum level. Therefore, we tried to take the $N_2(0-2)$ band spectrum from the discharge after the discharge had been operating for a long enough period to allow conditions in the discharge to reach equilibrium. At the same gas pressure, the power applied to the resonant cavity to generate the discharge was kept constant during the data taking process. The discharge volume was maintained inside the resonant cavity throughout all measurements (with the discharge on) by tuning the adjustable wall of the cavity (see Section 2.4.4). Figures 77 and 78 show the rotational temperature of N_2 obtained with the resonant cavity in TM mode at the same power as in Figures 75 and 76 and at two different gas pressures (50 and 70 Torr) and at two different positions of

measurement (7th and 9th position). Error bars in Figures 75, 76, 77, and 78 indicate the uncertainties in the intensity measurements. The errors for rotational temperatures calculated from the slope differences are also shown in the diagrams.

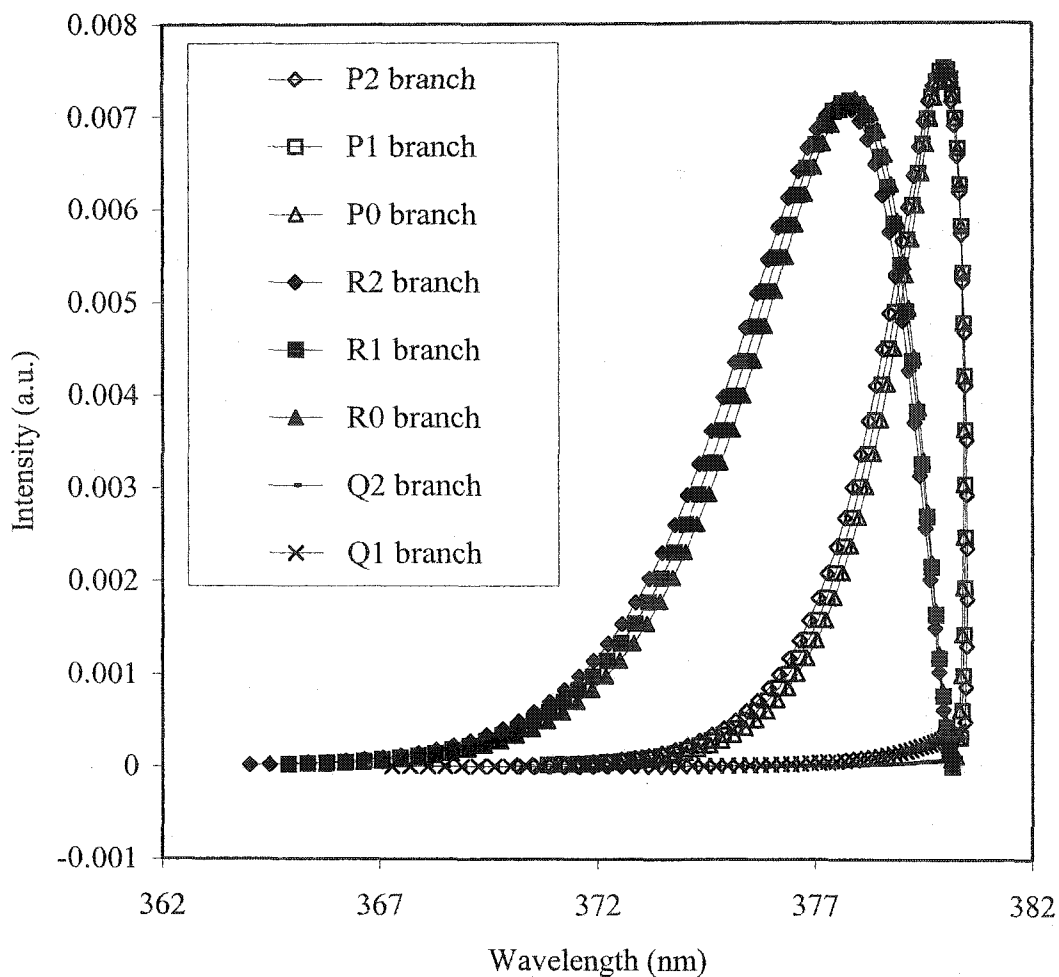


FIG. 74. Intensity distribution of rotational branches in $(0-2)$ band of the second positive system, $C^3\Pi_u - B^3\Pi_g$ in Nitrogen emission spectrum as a function of wavelength variation from the band head (380.5 nm) at $T_r = 1200$ K. Note that the intensity of R branch around 377.0 nm is much higher than the intensities of P and Q branches.

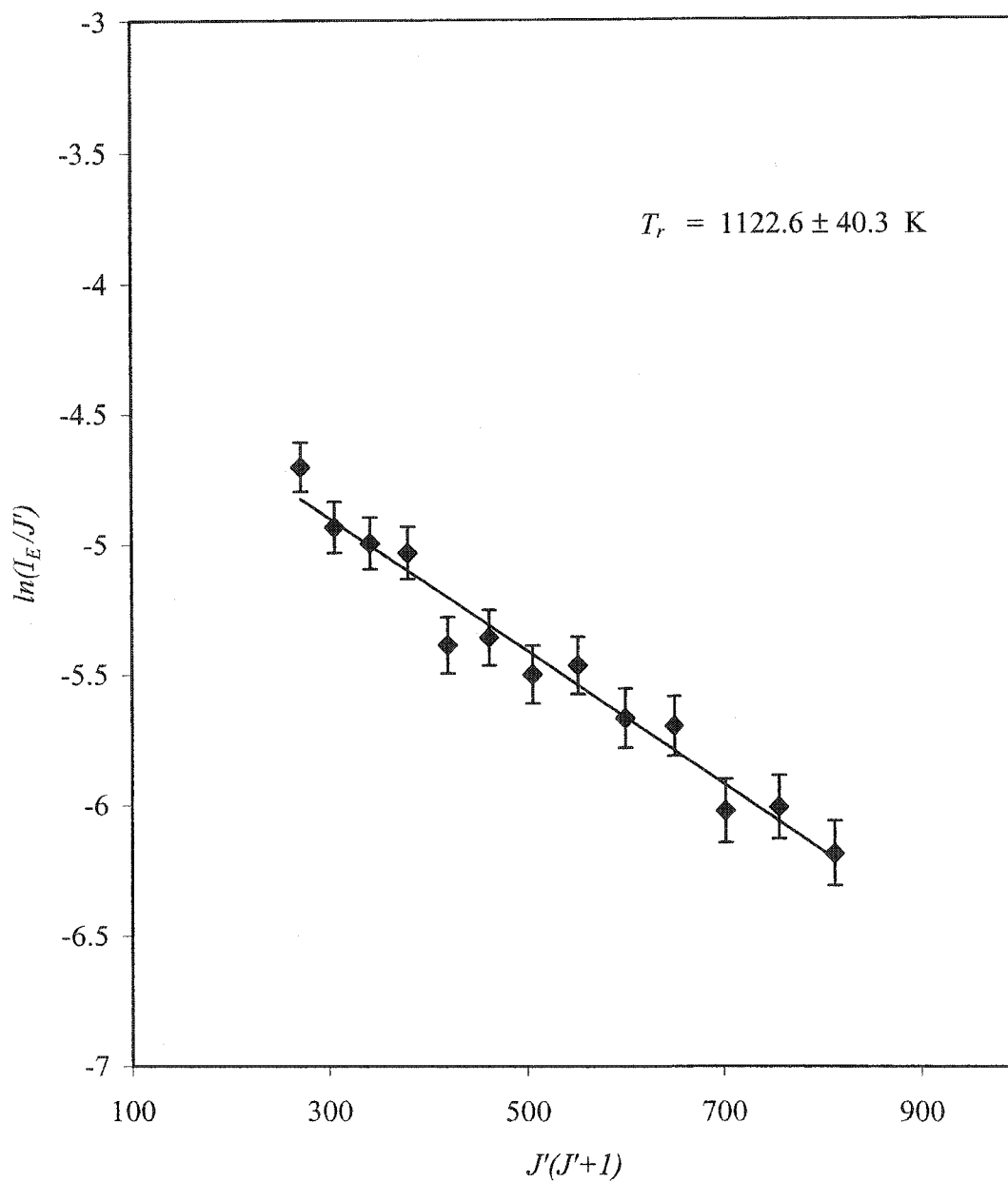


FIG. 75. Rotational temperature from the R_0 branch of the N_2 ($0-2$) band in Second Positive System from TE mode at 8th position and 30 Torr.

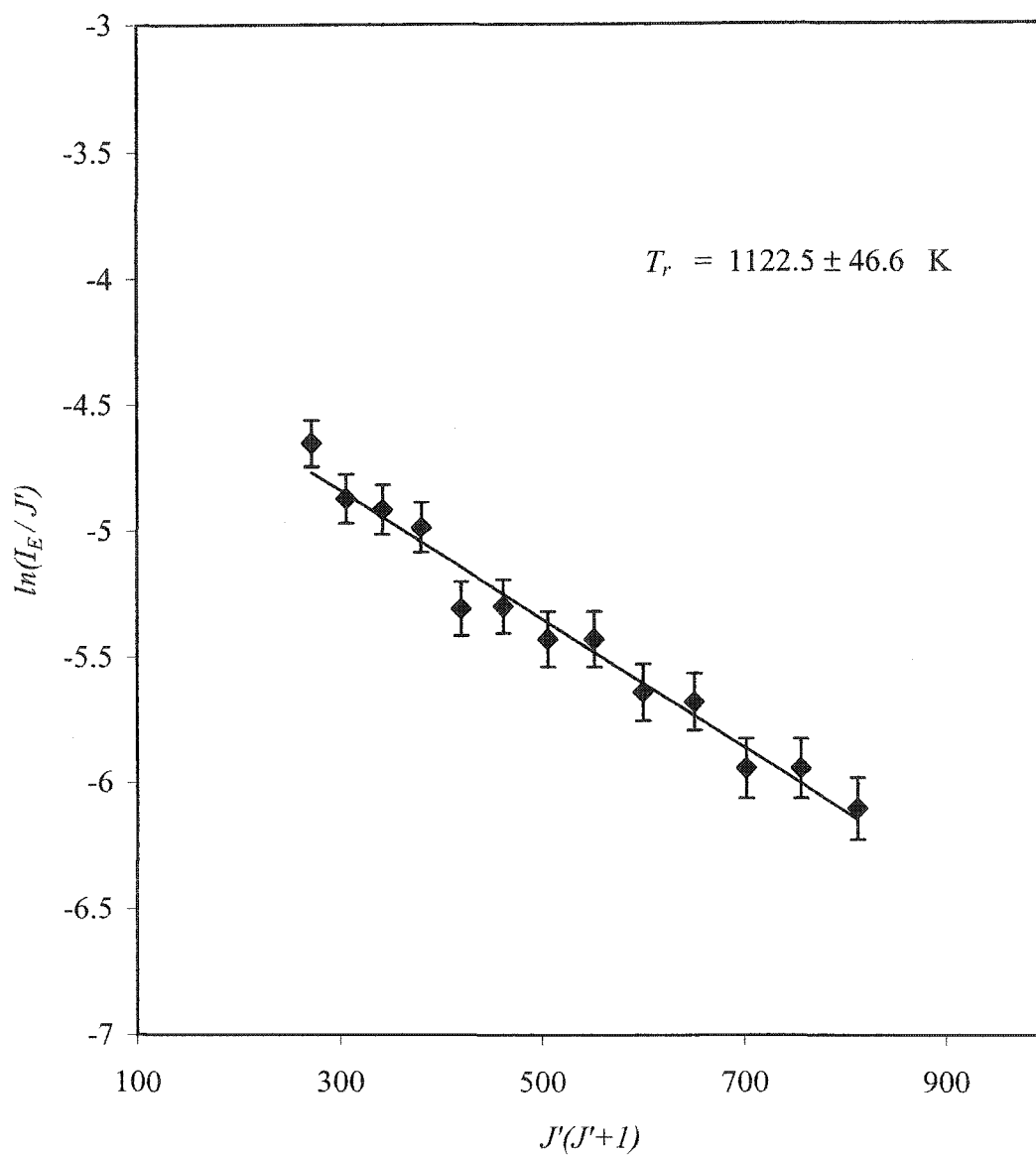


FIG. 76. Rotational temperature from the R_0 branch of the N_2 ($0-2$) band in Second Positive System from TE mode at 8th position and 75 Torr.

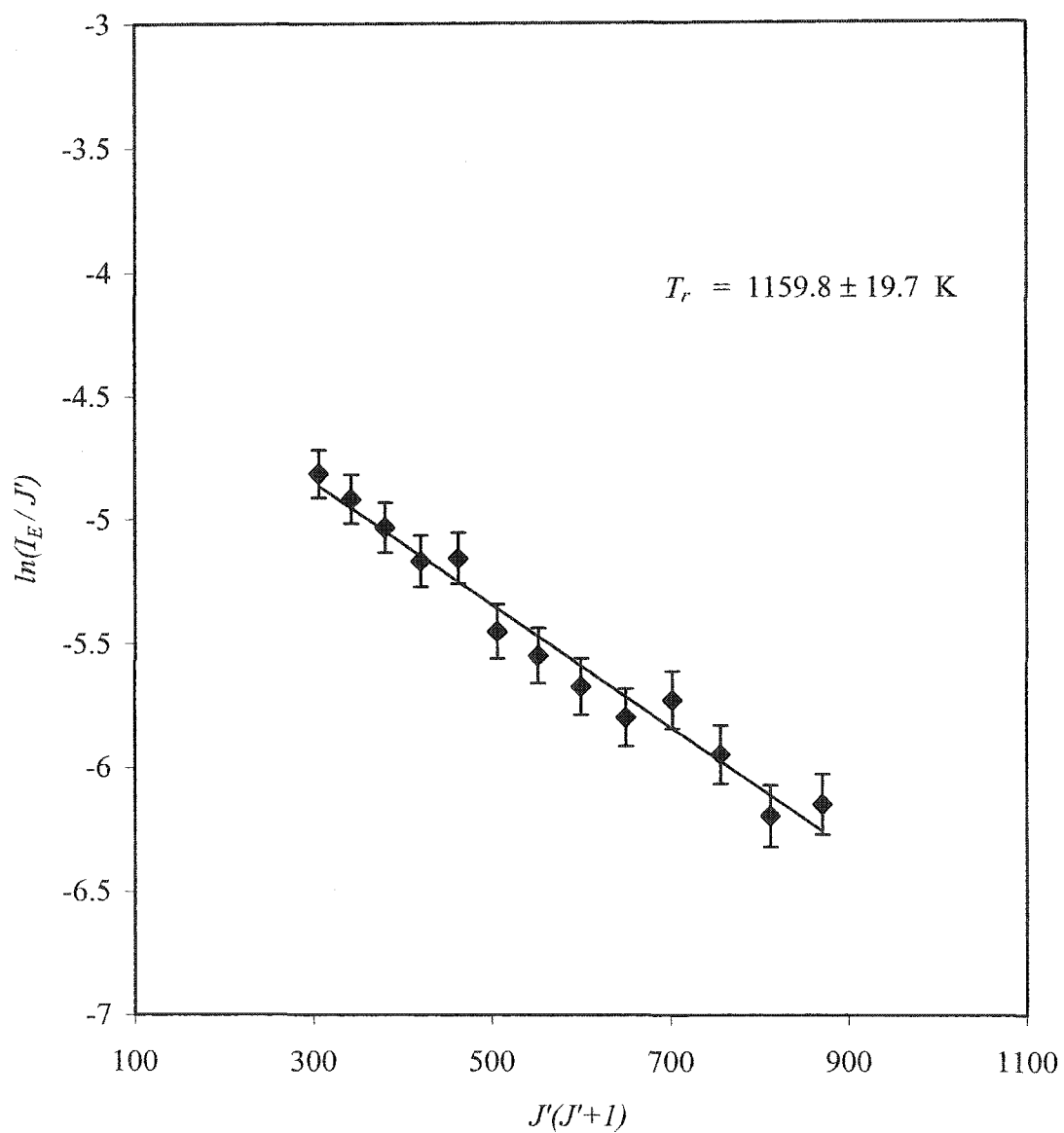


FIG. 77. Rotational temperature from the R_0 branch of the N_2 ($0 - 2$) band in Second Positive System from TM mode at 7th position and 50 Torr.

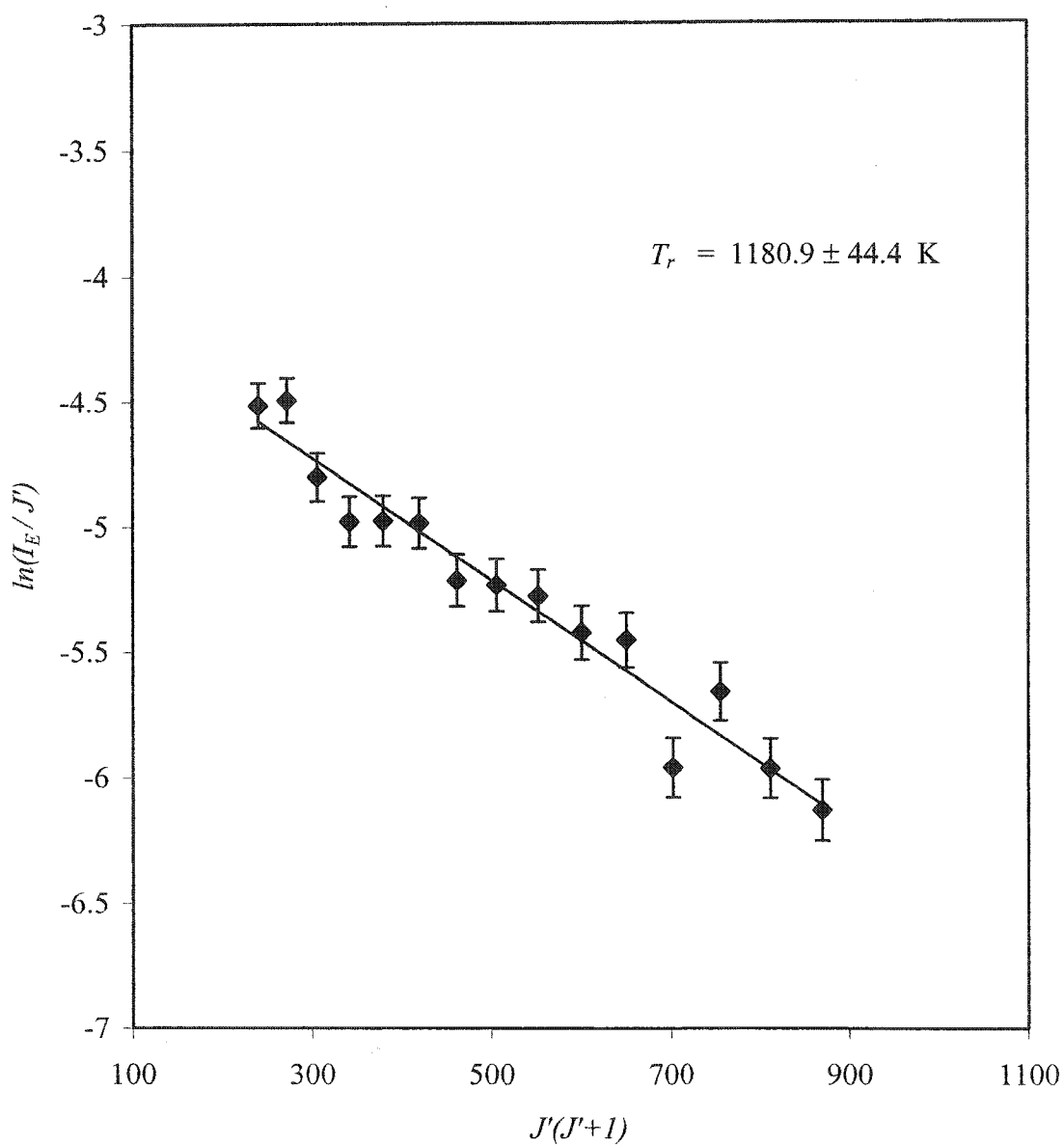


FIG. 78. Rotational temperature from the R_0 branch of the $N_2 (0-2)$ band in Second Positive System from TM mode at 9th position and 70 Torr.

The rotational temperature distribution in the Ar MW discharge at the 7th position measured using the N₂ (0-2) band rotational emission spectrum technique in TE and TM modes are shown in Figures 79 and 80, respectively. We conclude that the rotational temperature in TE mode is slightly higher than in TM mode. The average value of the rotational temperature in TE mode is 1220.82 K and in TM mode is 1199.67 K for a pressure range of 20 to 100 Torr. Therefore, we measured approximately only a two percent difference for the rotational temperature measurements in TE and TM modes. The pressure dependence of the rotational temperature in TE and TM modes is essentially the same. The rotational temperature in TE and TM modes decreases at low pressure to a minimum value in the pressure range from 30 to 50 Torr and then increases again at higher pressure (see Figures 79 and 80).

Error bars in Figures 79 and 80 are the average values of the errors in rotational temperature calculated from the slope differences. One of the important sources of error is the departure from the equilibrium rotational distribution. This issue requires more study in future work. Another source of error indicated in the literature is self-absorption. In order to verify the possibility of self-absorption in our case, we performed a separate analysis of rotational temperature evaluated from the (0-2) and (0-3) bands in TM mode. The two values of temperature were different by 16.1% (as shown in Figure 81). Therefore, we conclude that self-absorption can be neglected in the present work.

The comparison between the gas temperature evaluated from the amplitude reduction technique and the rotational temperature measured by using N₂ (0-2) band rotational emission spectrum technique will be shown and discussed in Section 4.

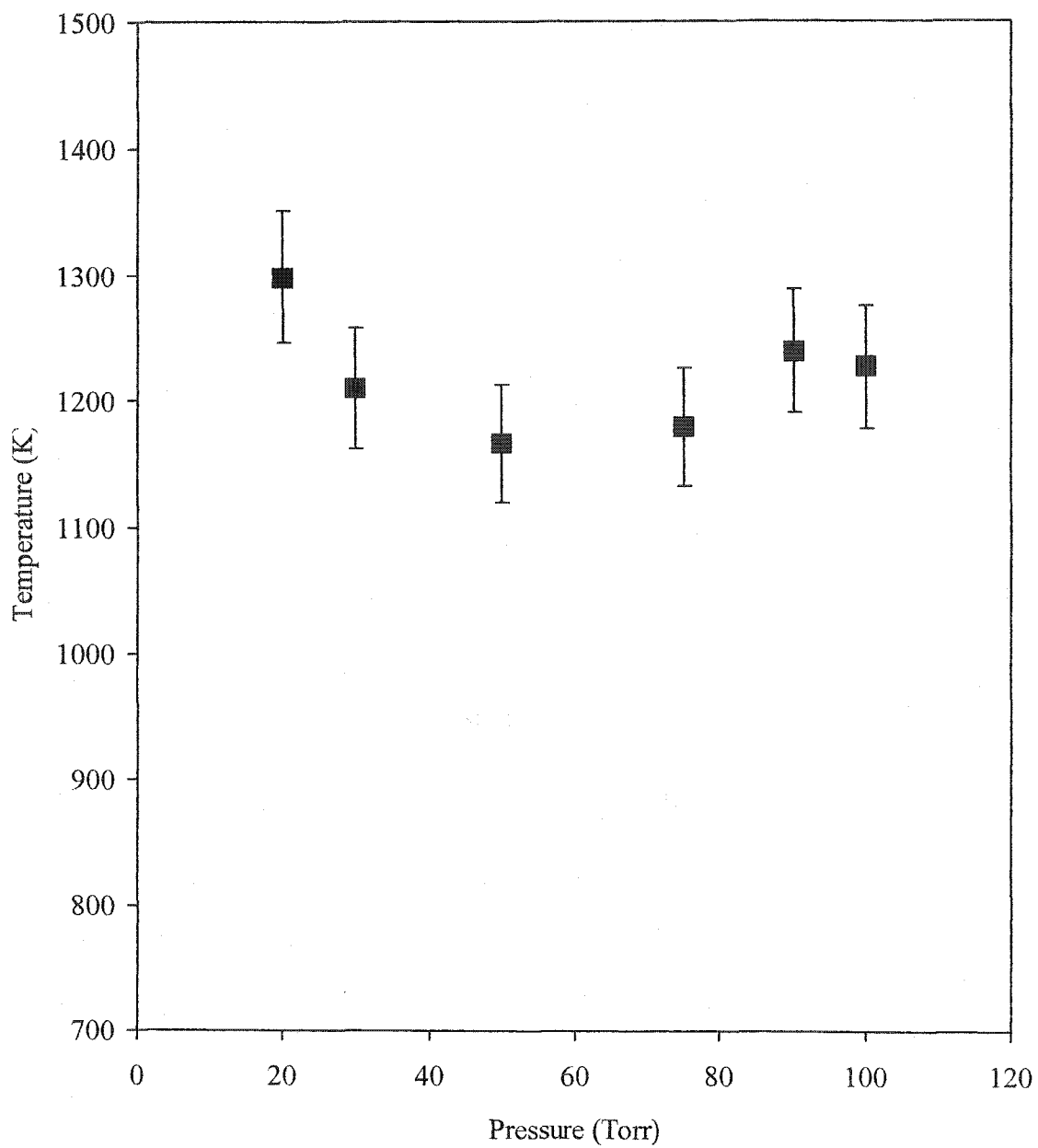


FIG. 79. Rotational temperature in TE mode.

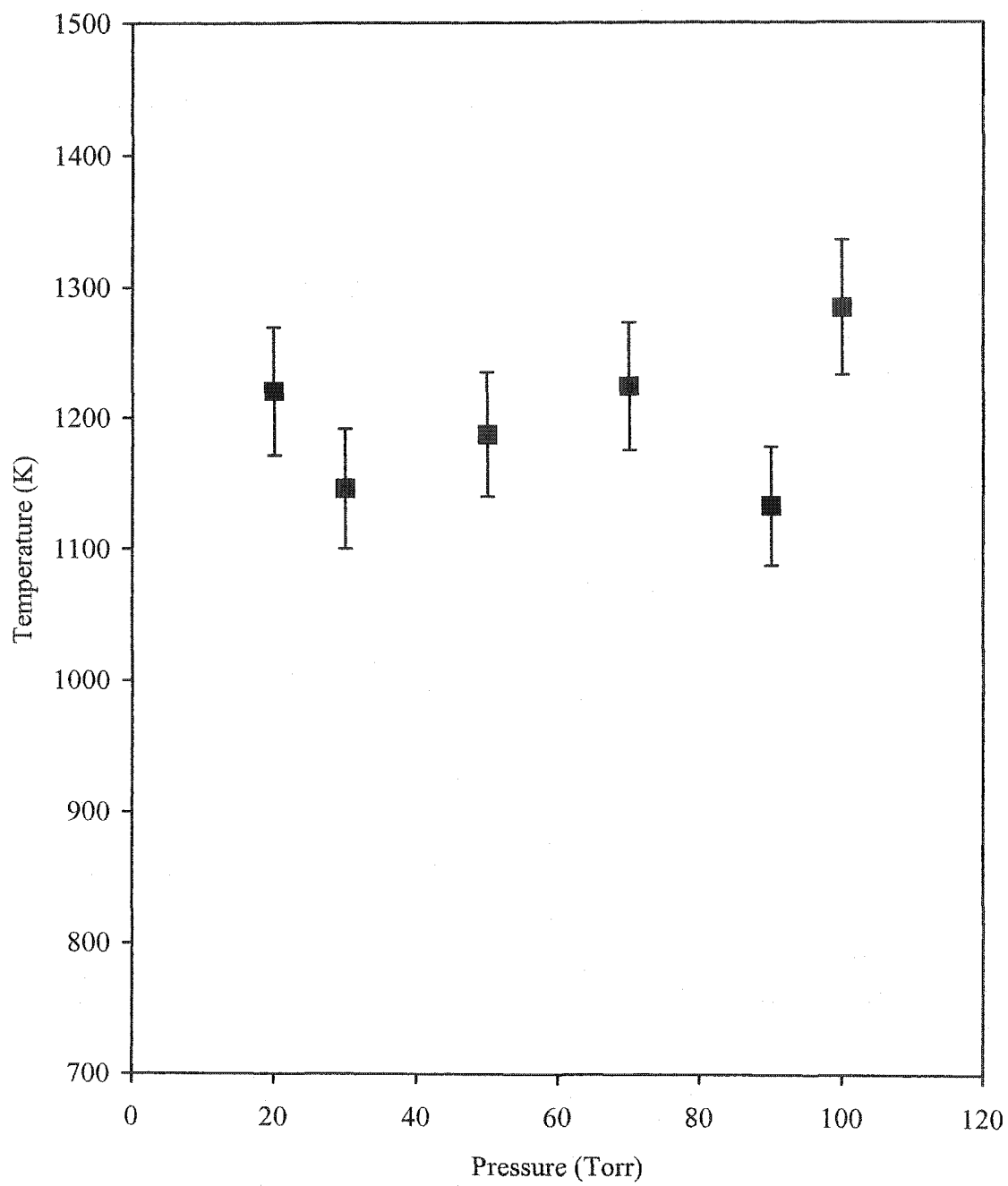


FIG. 80. Rotational temperature in TM mode.

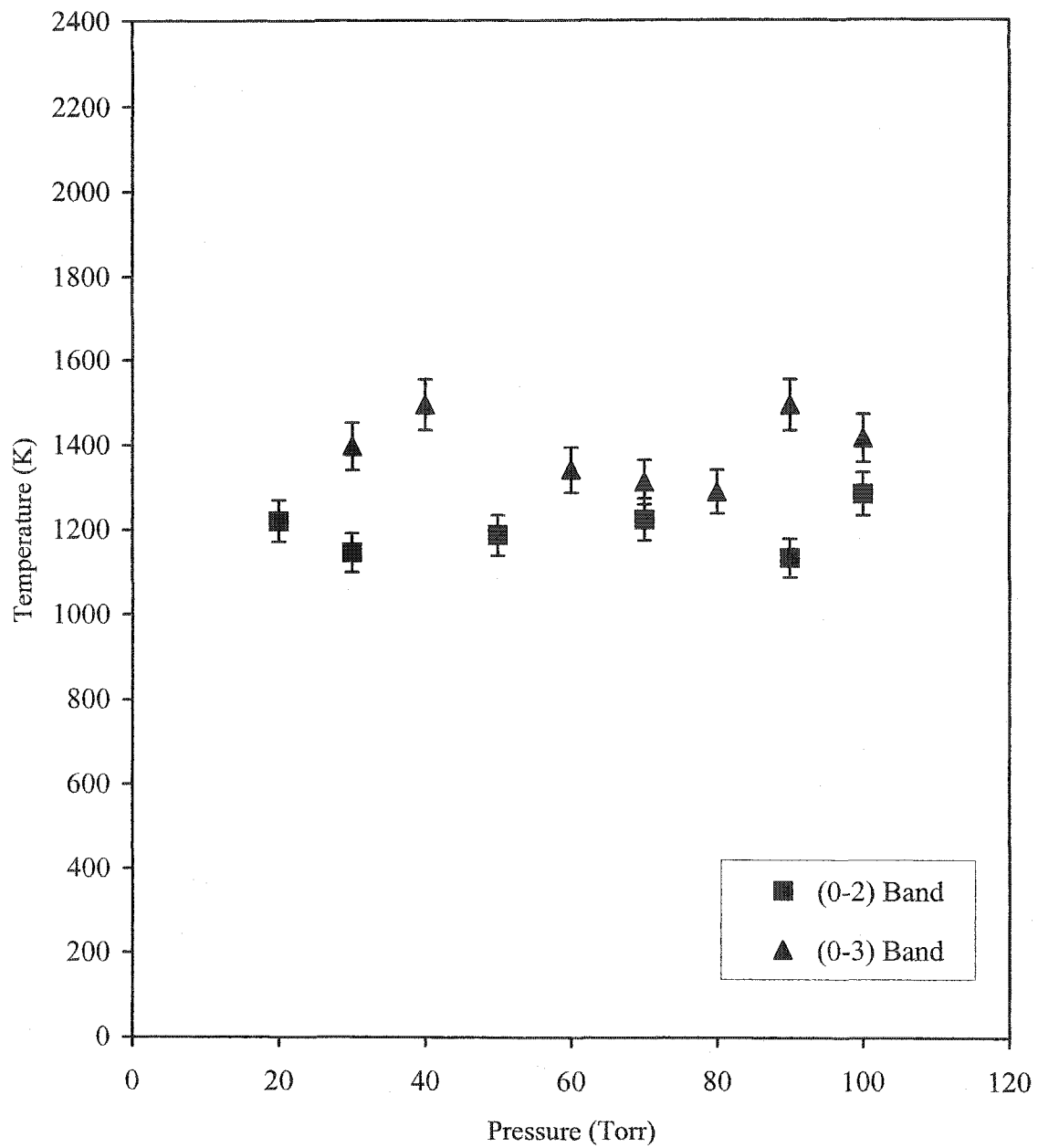


FIG. 81. Comparison of the rotational temperature evaluated from (0-2) and (0-3) bands in TM mode.

3.5 Determination of Electron Density

The electron density, N_e , is one of the most significant fundamental parameters in many types of discharges. Electron density can be obtained from the lineshape of the Balmer lines of atomic hydrogen where the Stark broadening mechanism is dominant over Doppler broadening (usually, H_β at 486.13 nm) in discharges with electron densities greater than 10^{13} cm^{-3} [46]. The hydrogen Balmer β line is the most frequently used spectral line for plasma diagnostic purposes. This technique can be applied to determine the electron density by addition to the discharge of a small amount of hydrogen (typically >1% mole fraction). In our experiment, 5% of hydrogen was mixed with Ar gas in a tank and used to produce a MW discharge.

The shape of the H_β transition is influenced not only by several broadening mechanisms that include Stark and Doppler broadening, but also by instrumental broadening due to the resolution of spectral equipment. The shape of the H_β line has been extensively studied both theoretically as well as experimentally. Basically, the electron density was determined from the half-width at half-maximum (HWHM) of the H_β profiles. As a result of these studies, well-established methods for N_e diagnostics from H_β line profiles have been developed. Simplified techniques for evaluating electron density from Stark broadening of H_β lines have been described in the literature [47,48]. One of them was used in the present work.

The Stark broadening is due to the Coulomb interactions between the outer electron of the hydrogen atom and the charged particles present in the discharge. Because of the relatively higher velocities of electrons in the discharge as compared to

ions, the broadening due to the positive ions is negligible. The electron density is a function of Stark broadening of the H_β line, as shown in Eq. (48).

The Doppler broadening occurs when the emitting hydrogen atom moves with respect to the detection system. As a consequence of the Doppler effect, the wavelength of the detected photon is shifted from $\lambda_0 = 486.13$ nm. Since the radiating hydrogen atoms are in thermodynamic equilibrium at gas temperature T_g , the Doppler broadening can be expressed in term of the mass of the radiating atom (M), the wavelength λ , and the temperature of the radiating atom (T_g), as shown in Eq. (51).

The instrumental broadening due to the resolution of the diffraction grating and the finite dimension of a single pixel in the CCD camera of our imaging spectrograph also add to the H_β lineshape, as shown in Eq. (50).

The experimental set-up for measuring electron density will be described in Section 3.5.1, and the calculation method and results will be discussed and shown in Section 3.5.2.

3.5.1 Experimental Set-up

The experimental set-up for the H_β profile measurement was the same as shown in Figure 69. According to the wavelength of the H_β transition line, the grating of the imaging spectrograph was changed so that 468.13 nm is the central wavelength of the detector frame. The experimental H_β profiles (e.g. in Figure 82) were recorded by the CCD camera, and all experimental H_β profile measurements were performed at the 7th position at difference values of gas pressure from 20–100 Torr in TM mode.

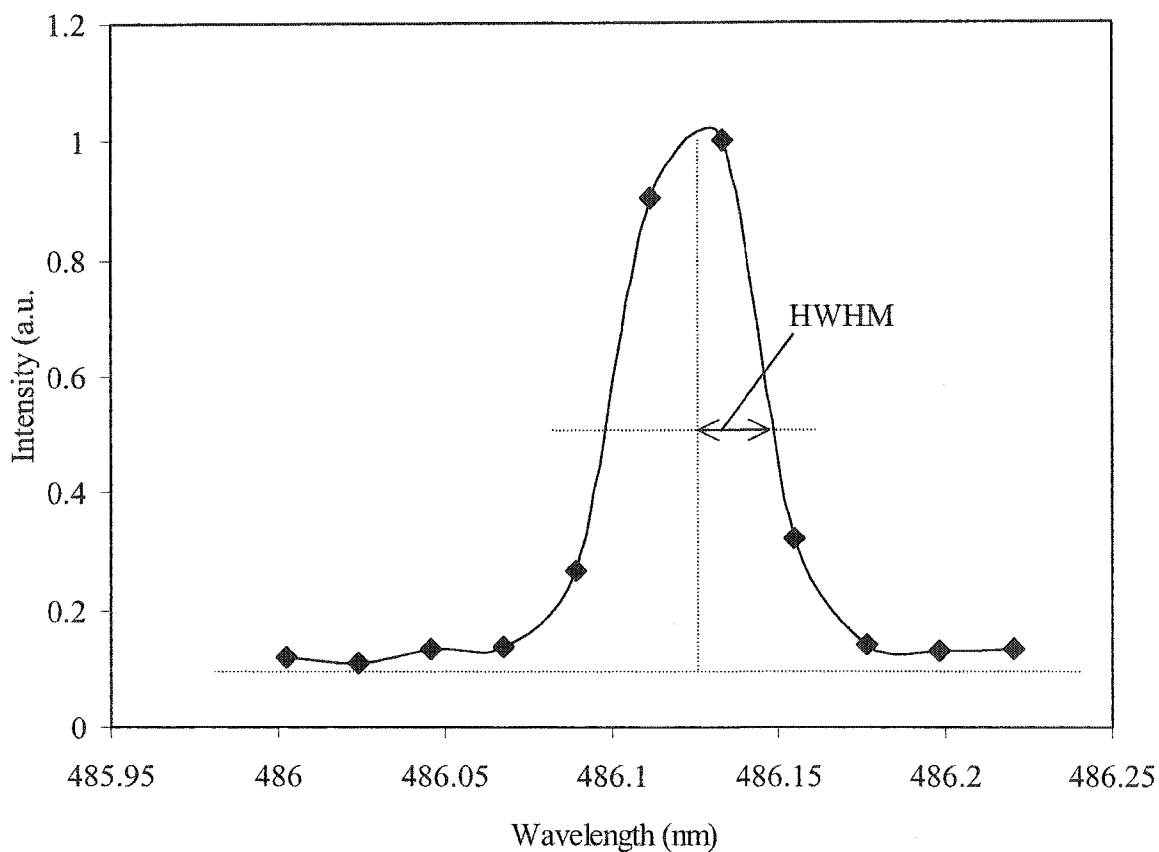


FIG. 82. H_{β} profiles in Ar (5% of hydrogen) MW discharge (TM mode) at 7th position; 30 Torr.

3.5.2 Electron Density Evaluation

In order to simplify and make the determination of N_e from the experimental H_{β} profiles much faster, the well-tested approximate formulae in Eqs. (48) to (51) by Jovićević et al. [47] and Kelleher [48] will be used to calculate N_e from the experimental H_{β} profile data in section 3.5.1:

$$N_e [cm^{-3}] = 10^{16} \cdot \left(\frac{W_s}{4.7333} \right)^{1.49}, \quad (48)$$

$$W_s = \left(W_m^{1.4} - W_{DI}^{1.4} \right)^{1/1.4}, \quad (49)$$

$$W_{DI} = \left(W_D^2 + W_I^2 \right)^{0.5}, \quad (50)$$

and

$$W_D = 3.58 \times 10^{-7} \lambda \left(\frac{T_g}{M} \right)^{0.5}. \quad (51)$$

Here, W_s , W_m , W_D , and W_I are the Stark HWHM, the measured HWHM, the Doppler HWHM, and the instrumental HWHM of the H_β profile, respectively. All of these HWHM are given in Å (10^{-10} m). T_g is the gas temperature of the discharge (in K), M is the mass of the hydrogen atom in amu, and λ is the wavelength of H_β transition line (4861.3 Å).

For all evaluations of the instrumental HWHM, W_I was determined by the grating resolution and the pixel size of the CCD camera in the imaging spectrograph, and its value was 0.02258 nm. For the gas temperature, the results from Section 3.4.2, were used. The electron density in the Ar MW discharge in TM mode can be evaluated using Eqs. (48) to (51) and is shown in Figure 83. The electron density in the Ar MW discharge in TM mode shown in Figure 83 rises for pressures between 4.0×10^{13} and $7.0 \times 10^{13} \text{ cm}^{-3}$. The uncertainties shown in Figure 83 (3%), can be obtained by applying the average measurement uncertainty of T_g (4%) and W_m (0.4%) in Eqs. (48) to (51). Since we used the same value of input power to the magnetron tube in the Ar MW discharge, we also assumed that the electron density in TE mode would not be much different from

the electron density in TM mode. In conclusion, the electron density in the Ar MW discharge in both TE and TM modes should be on the order of 10^{13} cm⁻³ for pressures between 20 and 100 Torr during the experiment.

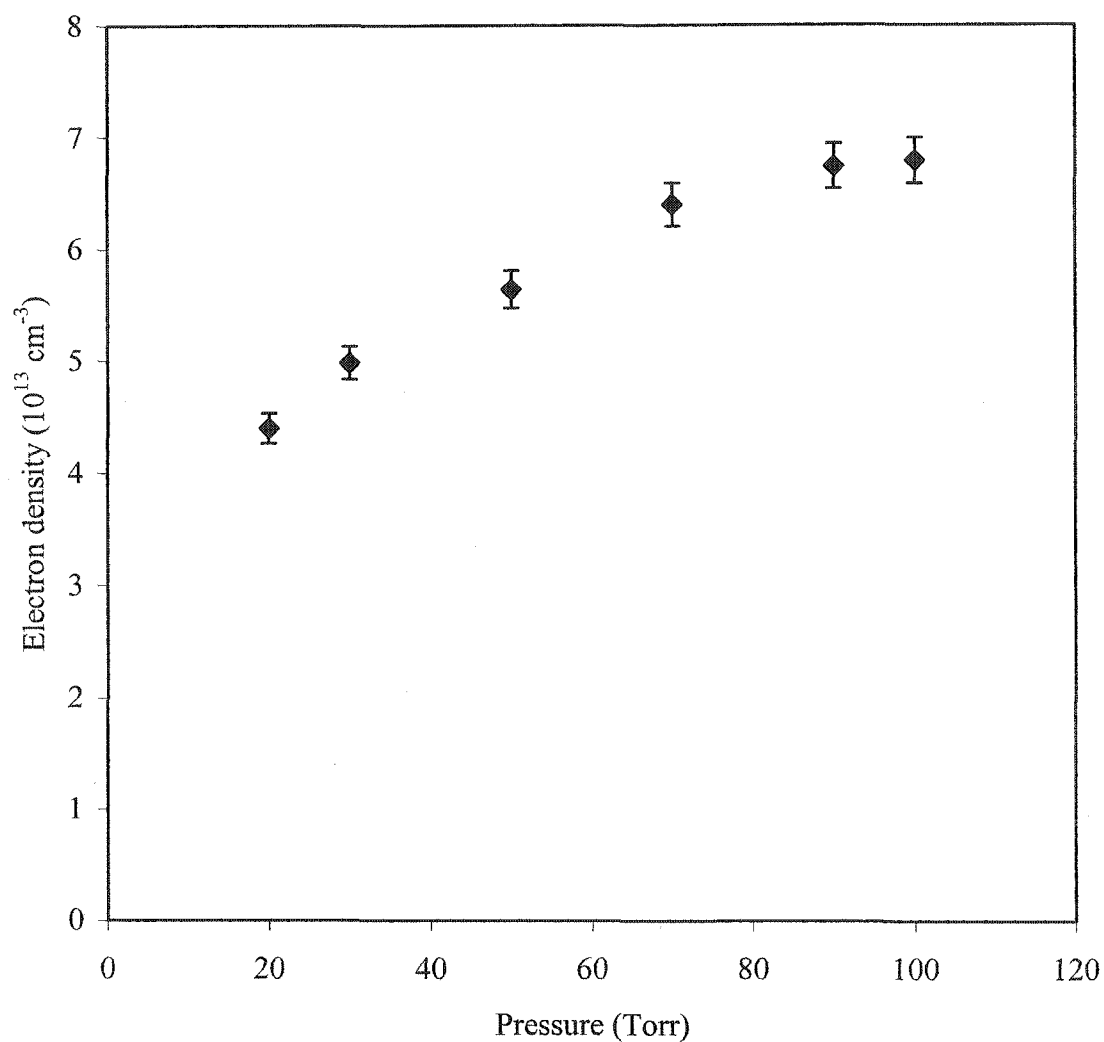


FIG. 83. Electron density in Ar MW discharge (TM mode).

3.6 Evaluation of the Local Electric Field

The local electric field is one of the parameters that characterize conditions in a MW discharge. The local electric field in the Ar MW discharge with impurities was evaluated on the basis of variation of the (0-0) band head intensity ($\lambda_0 = 337.1$ nm) for the Second Positive System of Nitrogen [49]. By assumption, the band head intensity is proportional to the population of the upper electronic state of the Second Positive System:

$$I_{337.1}(t) \sim N_C(t). \quad (52)$$

Here, $I_{337.1}(t)$ is the time dependence of the (0-0) band head intensity and $N_C(t)$ is the time dependence of the population of the upper electronic state of the Second Positive System.

By applying a simplified model for the kinetics of state C , involving only the populating process of direct electron excitation from the ground state and depopulating process of radiative decay to the lower state B shown in Figure 84, the $N_C(t)$ in this model is given by

$$dN_C(t)/dt = k_C(t) N_e(t) N_o - N_C(t)/\tau \quad (53)$$

and

$$k_C(t) = k_C[E(t)/N_o, T_v], \quad (54)$$

where $k_C(t)$ is the rate coefficient for the electron-impact excitation of the state C from the ground state, $E(t)/N_o$ is the time-dependent reduced electric field, T_v is the vibrational

temperature of the system during the discharge, $N_e(t)$ is the time-dependent electron density, N_0 is the ground state concentration, and τ is the average lifetime of the state C.

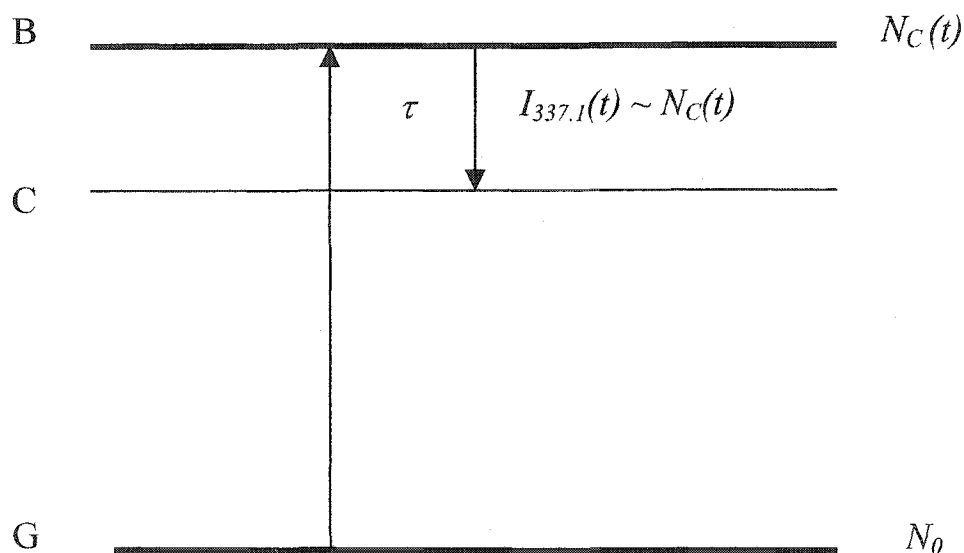


FIG. 84. Simplified kinetic scheme in calculating balance of the excited state C of the Second Positive System of Nitrogen.

The initial electric field (E_0) can be estimated from the observed initial discharge conditions. This electric field amplitude decreases, however, as the MW discharge is established. That happens in the following way: the MW cavity is initially resonant in the $TE_{1,1,1}$ (or $TM_{0,1,2}$) mode with the microwaves generated by the magnetron. As the MW discharge builds up in the shock tube, the dispersive properties of the plasma alter the wavelengths of these standing microwaves, so that the cavity becomes slightly detuned. This slight loss of resonance decreases the stored microwave energy, and the electric field amplitude is thereby reduced to a saturation value (E_{inf}). The unknown

saturation value, E_{inf} , is treated as a free parameter. Therefore, we had to set up an auxiliary experiment to measure E_0 at the central observation point (7th position) by using the microwave breakdown characteristics. We will discuss this topic in detail in Section 3.6.1.

We also assumed that the discharge temperature did not change appreciably during a single pulse of microwave discharge (3 to 6 ms). In this evaluation we used the values of the rate coefficient $k_C [E(t)/N_0, T_v]$ from Refs. [50] and [51].

According to the average electron density given in Section 3.5.2 and the assumption that the time evolution of the electron density is approximated by the time dependence of the intensity of H_β line, we can model the local time-dependent electron density during the discharge $N_e(t)$. The experimental set-up for measuring the time dependence of the intensity of H_β line will be introduced and discussed in Section 3.6.2. The result for the local electric field in the MW discharge calculated from Eq. (53) will be shown in Section 3.6.3.

3.6.1 Measurement of Initial Electric Field

In order to measure the initial electric field E_0 , we used the same basic set up as described in section 3. By adjusting the power supply of the magnetron tube through the variable transformer from 0.75 to 0.85 kW and gradually increasing the pressure in the tube, we could measure the gas pressure at the moment when we got breakdown. By using the microwave breakdown characteristics of Argon from Ref. [52], we could evaluate the breakdown electric field as the initial electric field E_0 in the Ar MW discharge.

The experimental data for breakdown at various diffusion lengths are shown in Ref. [52] for Argon. In our experiment, the microwave frequency was 2.45 GHz. The diffusion length (A) of the cylindrical cavity with flat ends can be evaluated from Ref. [53]:

$$\frac{1}{A^2} = \left(\frac{\pi}{h}\right)^2 + \left(\frac{2.405}{r}\right)^2, \quad (55)$$

where h is the length of a cylinder with flat ends, and r is the radius of the cavity (shock tube). Thus, the diffusion length (A) in our experiment is 0.622 cm in both TE and TM modes. In accord with the microwave frequency and the diffusion length of the cylindrical cavity, the breakdown electric field (initial electric field) at a given pressure can be estimated by extrapolation of data listed in Ref. [53] and assigned to the observed pressure of breakdown. Thus, the initial electric field can be plotted and expressed in term of the input power from the variable transformer of the magnetron tube, as shown in Figure 85.

3.6.2 Measurement of Time Dependence of the Intensity of H_β Line

The scanning monochromator and photomultiplier tube (PMT) were added in the experimental set up in order to measure the time dependence of the intensity of the H_β line (as shown in Figure 86). The monochromator (Jarrell Ash 82-000) has a focal length of 0.5 m and is equipped with a grating of 1180 grooves per millimeter. The spectral range of the monochromator was between 190 nm to 910 nm. The resolution of the monochromator was 0.2 Å. The PMT was a Hamamatsu R928 with a wide spectral response range from 185 nm to 900 nm.

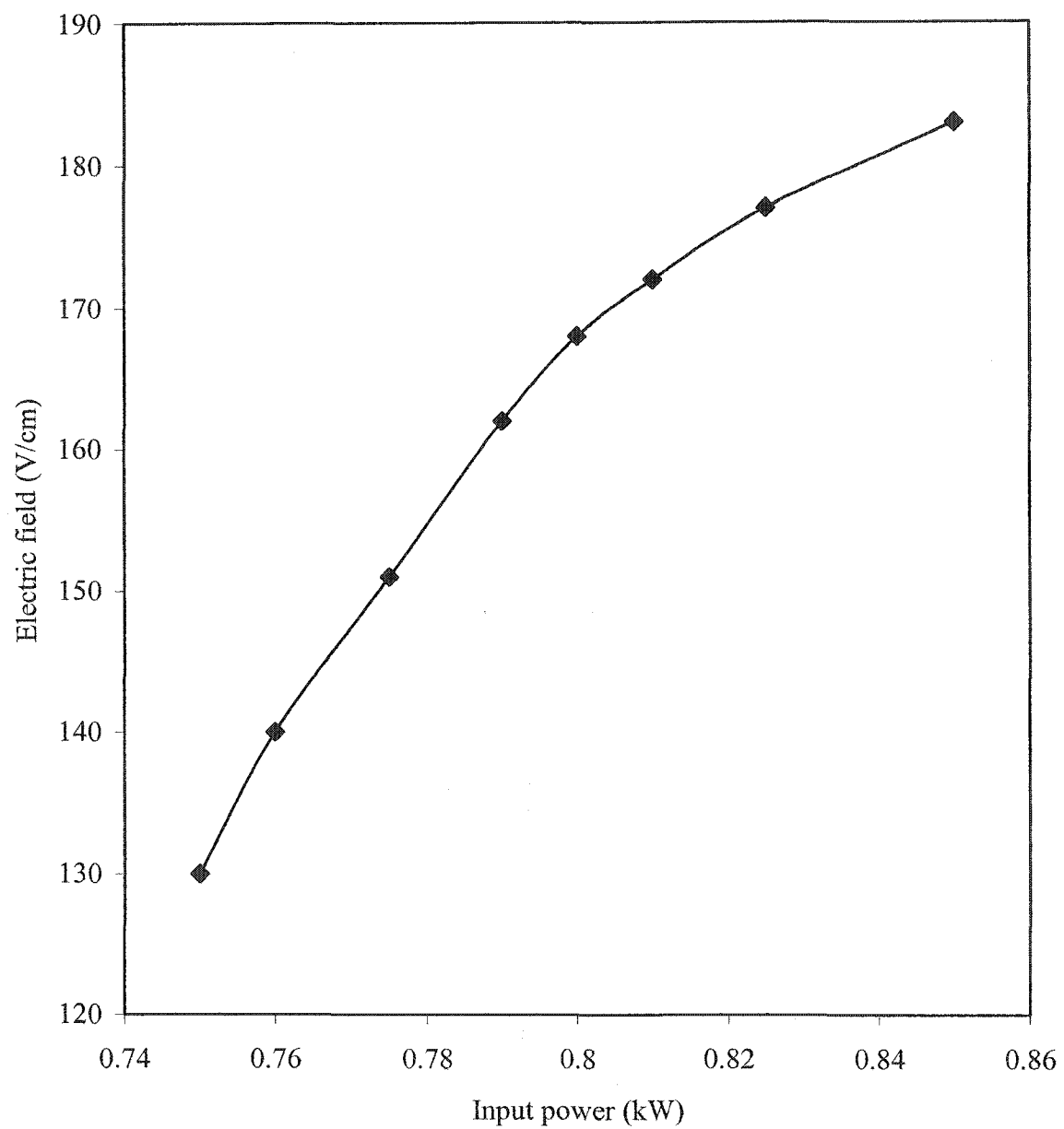


FIG. 85. Initial electric field (E_0) in Ar MW discharge.

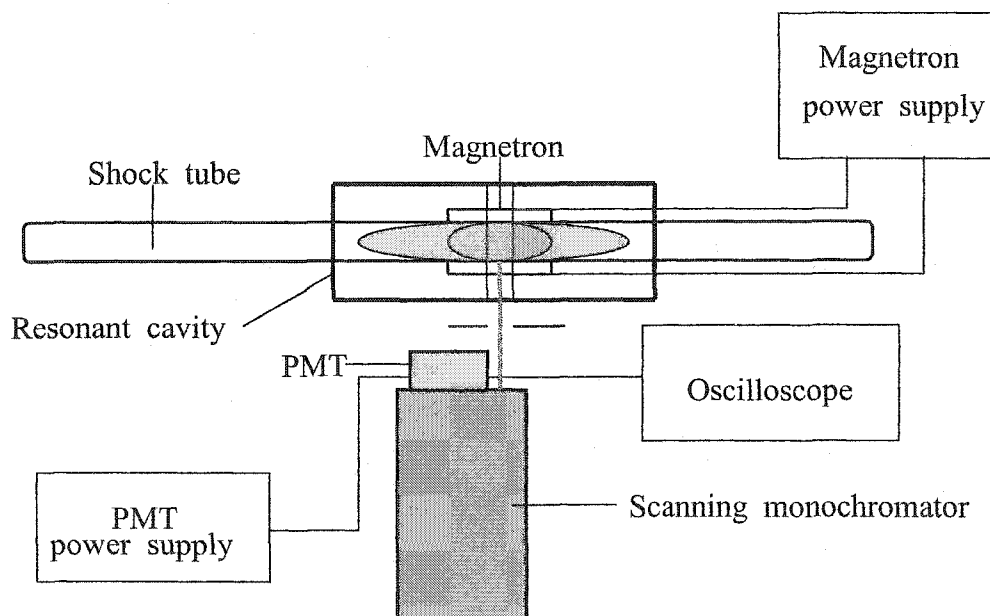


FIG. 86. Schematic of time dependence of the intensity of H_β line measurement.

In the range of the H_β line spectrum ($\lambda = 486.13$ nm), we can scan and measure the time dependence of the intensity of the H_β line, as shown in Figure 87. This experimental data can be fitted using a polynomial regression model for the time-dependent electron density $N_e(t)$, as shown in the same figure. The time-dependent electron density $N_e(t)$ will be used in Eq.(53) for calculating the population of the upper state electronic state of the Second Positive System of the (0-0) band of Nitrogen, $N_C(t)$.

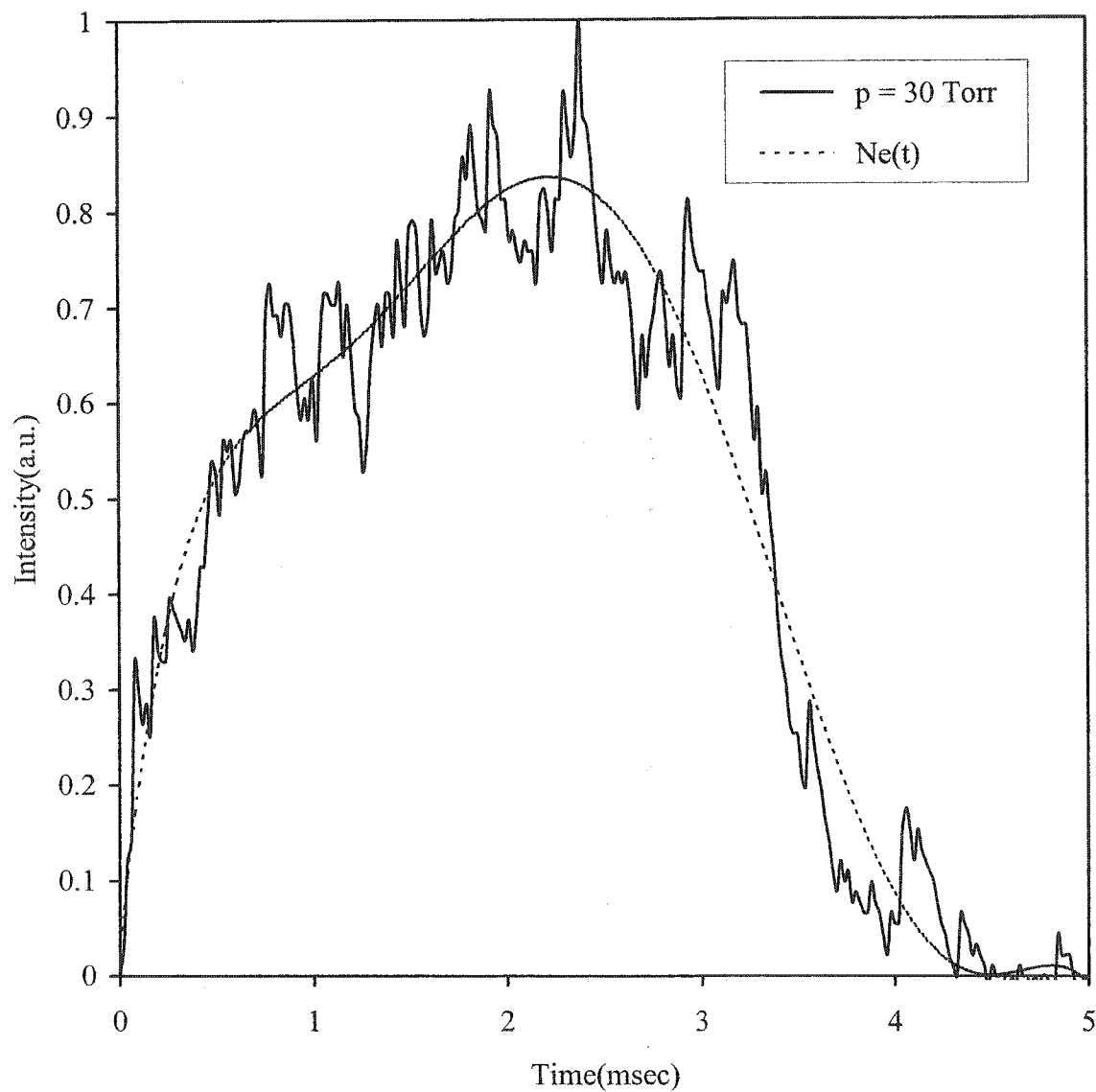


FIG. 87. Time dependence of the intensity of H_{β} line and time- dependent electron density, $N_e(t)$, at 7th position; $p = 30$ Torr.

3.6.3 Evaluation of the Time Evolution of the Local Electric Field

In order to proceed with the time evaluation of the local electric field, we need to measure the variation of the (0-0) band head intensity of the Second Positive System of Nitrogen, $I_{337.1}(t)$. We used the same experimental set-up from Section 3.6.2 tuned to the range of the (0-0) band head wavelength ($\lambda_0 = 337.1$ nm) and obtained the normalized waveform of the time variation of the (0-0) band head intensity of the Second Positive System of Nitrogen, $I_{337.1}(t)/I_{max}$ during the microwave pulse, as shown in Figure 88.

By using the average value electron density given in section 3.5.2, the time-dependent electron density $N_e(t)$ from section 3.6.2, the rate coefficient for the electron-impact excitation of the C state from the ground state $k_C [E(t)/N_0, T_v]$, and all parameters including the assumptions and arguments listed above, we can evaluate the normalized waveform $N_C(t)/N_{Cmax}$ from Eq. (53). This numerical solution of the normalized waveform also should satisfy the Eq. (52). For this reason, the measured normalized waveform $I_{337.1}(t)/I_{max}$ should be fitted with the calculated normalized waveform $N_C(t)/N_{Cmax}$ by adjusting the free parameter E_{inf} . The result of the fitting curve is shown in the Figure 88.

The time evolution of the local electric field was evaluated by use of the adjusted value of E_{inf} and plotted in Figure 89. From this figure, the local electric field inside a resonant cavity in the Ar MW discharge decreased by approximately 60 to 70 percent of the initial electric field supplied from the magnetron tube power supply circuit.

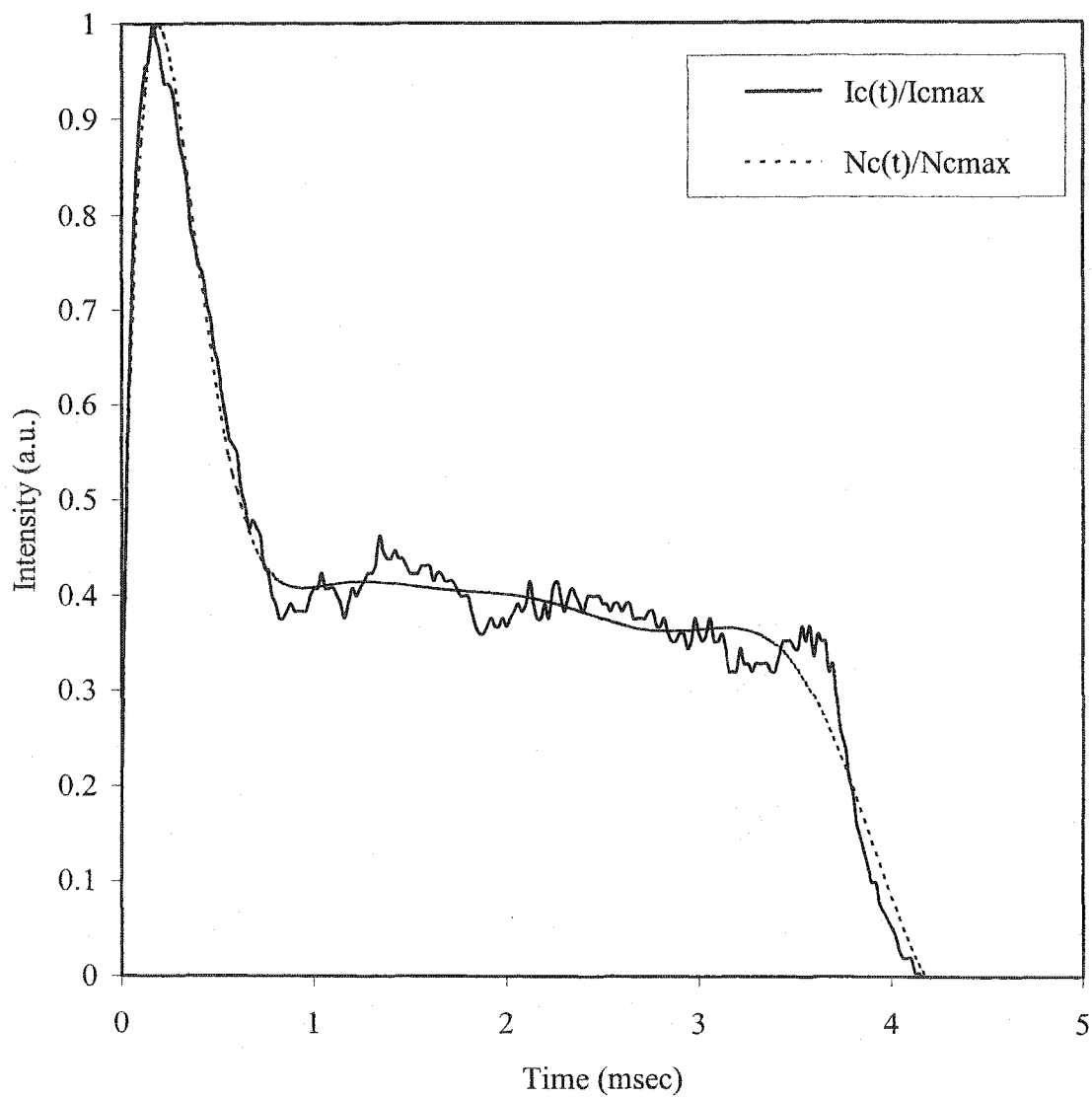


FIG. 88. Measured normalized waveform, $I_C(t)/I_{Cmax}$, at 7th position; $p = 30$ Torr and calculated normalized waveform, $N_C(t)/N_{Cmax}$.

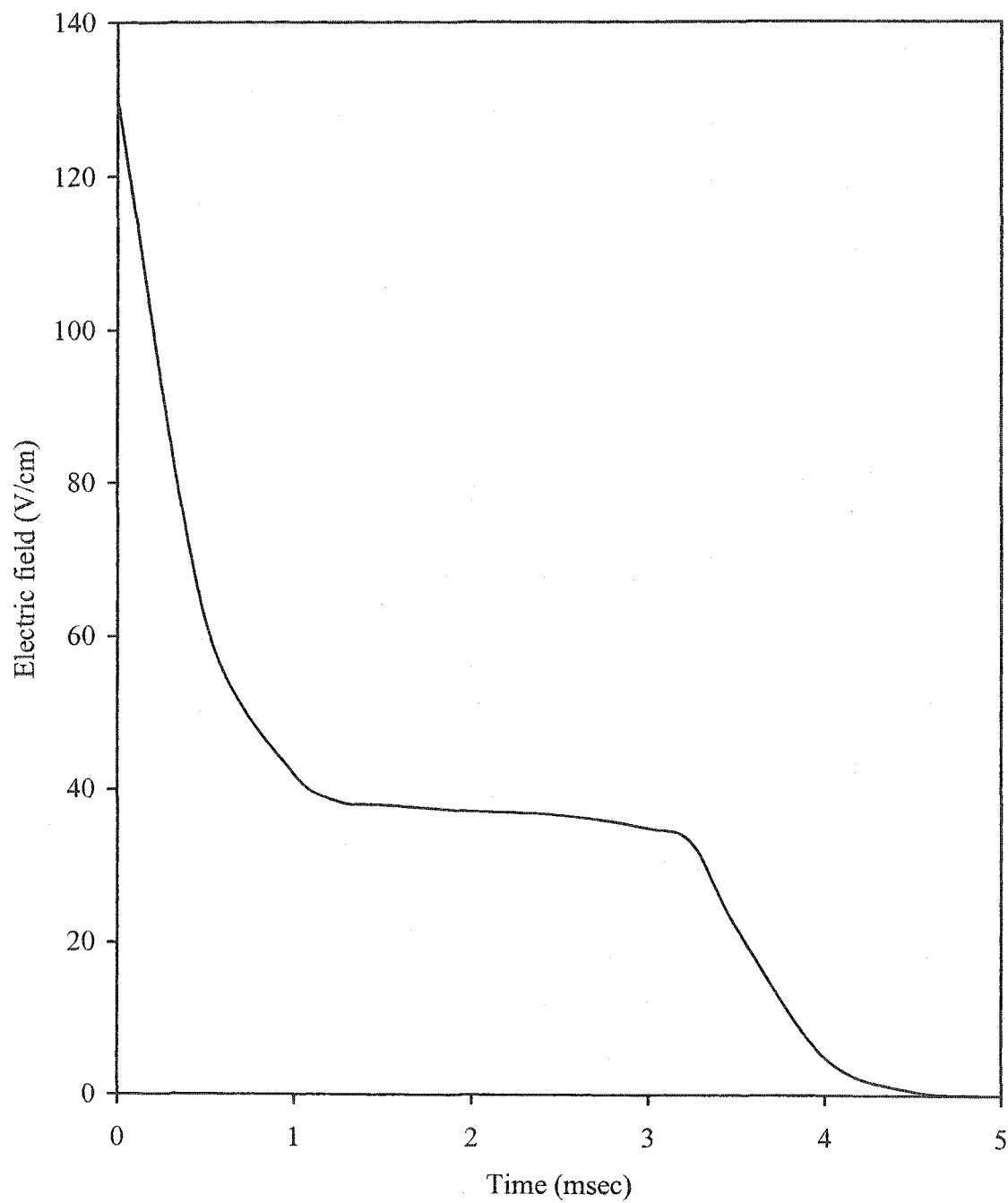


FIG. 89. Time evolution of the local electric field at 7th position; $p = 30$ Torr.

3.7 Evaluation of the average power density

Using the local electric field in the Ar MW discharge, we can estimate the power loss inside the resonant cavity during the experiment. In this case, the shape of our resonant cavity is the cylindrical coaxial cavity shown in Figure 90.

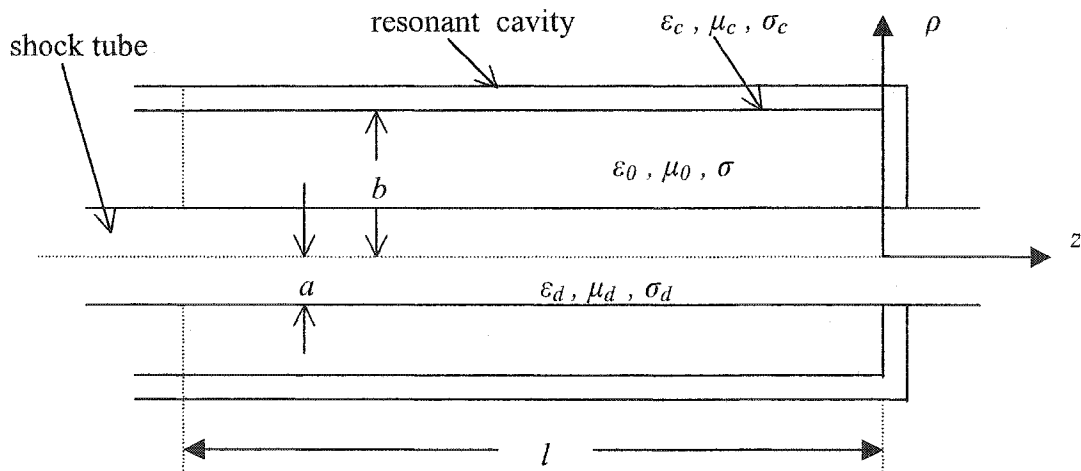


FIG. 90. A cylindrical coaxial cavity in Ar MW discharge.

The average power loss at resonance in the outer cylinder can be obtained by using Eq. (56), as shown below (see also Ref. [40]):

$$P_{out,av} = \frac{V_0^2 l}{2\pi \sigma_c b \delta_c Z_0^2}, \quad (56)$$

where V_0 is the voltage between conductors of a coaxial cavity [that is calculated from the local electric field of Figure 89, as shown in Eq. (57)], l is the length of the outer (or inner) cavity at resonance ($l = \lambda/4$), σ_c is the conductivity of the outer conductor

(Aluminium) [equal to $3.82 \times 10^7 (\Omega \cdot \text{m})^{-1}$], b is the radius of the outer cavity, δ_c is the skin depth of the outer cavity [shown in Eq. (58)], and Z_0 is the characteristic impedance of the resonant coaxial cavity calculated from Eq. (59).

$$E = \frac{2V_0}{\rho \ln(b/a)}, \quad (57)$$

where ρ is radial distance in the range from the radius of the inner cavity (a) to the radius of the outer cavity (b), or $a < \rho < b$.

$$\delta_c = \frac{1}{\sqrt{\pi f \mu_c \sigma_c}}, \quad (58)$$

where f is the microwave frequency (2.45 GHz) and μ_c is the aluminium permeability, which is nearly equal to the permeability of free space (μ_0).

$$Z_0 = \frac{1}{2\pi} \sqrt{\frac{\mu_0}{\epsilon_0}} \ln \frac{b}{a}, \quad (59)$$

where ϵ_0 is the permittivity of free space. A similar calculation for the average power loss in the inner cavity (filled with the Ar MW discharge) gives

$$P_{in,av} = \frac{V_0^2 l}{2\pi \sigma_d a \delta_d Z_0^2}, \quad (60)$$

where σ_d is the conductivity of the Ar MW discharge obtained from Ref. [53] and δ_d is the skin depth of the inner cavity of the Ar MW discharge, which can be obtained from Eq. (58).

Furthermore, the average power loss in the outer cavity walls can be calculated using Eq. (61) as shown below:

$$P_{wall,av} = \frac{V_0^2}{\pi \sigma_c \delta_c Z_0^2} \ln \frac{b}{a}. \quad (61)$$

Since $\rho_d \ll \rho_c$, the average power loss in the inner cavity is much more than in the outer cavity. For this reason, we can estimate the average power loss in this experiment as being approximately equal to the average power loss in the inner cavity or in the Ar MW discharge, shown in Eq. (62):

$$P_{TL,av} \approx P_{in,av} = \frac{V_0^2 l}{2\pi \sigma_d a \delta_d Z_0^2}. \quad (62)$$

Therefore, the average power loss in TM mode can be obtained from Eq. (62), which yields 18.92 Watts.

The input power (750 Watts) supplied to the TM mode cavity by the magnetron circuit was kept constant at all times during the experiment. By use of the dimensions of the TM mode cavity, the average power density in TM modes can be calculated, as shown below.

For TM mode,

$$P_{av} = \frac{750 - P_{TL,av}}{\pi b_{TM}^2 l}, \quad (63)$$

where b_{TM} is the radius of the outer resonant cavity for TM mode.

From Eq. (63), the average power density in the TM mode is approximately 2.61 Watts/cm³.

For the TE mode, a similar calculation for the average power loss and the average power density can be performed. According to the difference in the dimensions for the TE and TM modes, we believe that the average power loss in TE mode should be less than in TM mode and that the average power density in TE mode should be higher than in TM mode when the strengths of the electric fields inside those two cavities are equal.

Section 4

RESULTS AND DISCUSSION

4.1 Introduction

During the last two decades several studies have been published on experimental investigations of shock waves propagating in non-equilibrium weakly ionized gases, especially in d.c. glow discharge [3, 5]. The most important observed effects of non-equilibrium weakly ionized gases on the shock wave are a decrease of shock amplitude combined with a widening of the shock width (dispersion) and an increase of the shock wave velocity.

A simultaneous multi-point laser beam deflection technique was applied to study the local shock wave propagation velocity and shock wave dispersion in a low pressure Nitrogen d.c. glow discharge [3]. The results show that the observed increase in shock wave propagation velocity inside a uniformly diffuse discharge positive column can be explained by thermal gradient effects. The shock wave propagation velocity increase is also dependent on the direction of the applied electric field. Shock wave propagation characteristics in the shock tube have also been measured in low pressure non-equilibrium Argon d.c. glow discharge using the same technique [5]. Since this measurement technique relies on the reflective index modulation, an accurate multi-point measurement of the gas density profiles can be obtained with this technique. Moreover, the shock velocity change in the discharge due to non-equilibrium “*plasma effect*” versus gas heating can be measured. Simultaneous multi-point measurements

also permit estimates of the amplitude-dependent shock wave interactions with the discharge under identical operating conditions.

Spark-generated shock waves were studied in d.c. glow discharges in Argon and Argon-Nitrogen mixtures [18, 54]. The laser Schlieren method was used to measure shock wave arrival times and axial density gradients. The changes in shock wave structure (splitting for instance) and velocity in weakly ionized gases are explained by classical gas dynamics, with the critical role of thermal and multi-dimensional effects (transverse gradients, shock curvature, etc.). Experiments with pulsed discharges allowed us to separate thermal effects from those due to electric fields and charged particles. It was proposed that gas heating is necessary for shock velocity and Schlieren signal parameters to attain their steady-state values. This provides a direct proof that a thermal mechanism is responsible for the effects of a weakly ionized gas on shock wave propagation.

Recent experiments involving shock waves propagation through weakly ionized gases have raised questions regarding interpretation of the experimental results [23]. To aid in analyzing these experimental results, shock waves that were initiated by a simulated spark and that subsequently propagated in a cylindrical tube containing Argon initially at 30 Torr and 300 K have been analyzed numerically. Although discharge processes have not been simulated, it was proposed that the effects of wall shear and thermal gradients alone are sufficient to explain most of the experimental observation.

In the present work an electrodeless MW discharge in TE or TM mode was introduced to study a shock wave dispersion in non-equilibrium weakly ionized gases in order to eliminate a possible influence of the electrodes on shock wave modification that

was present in other experimental work [5, 18, 23]. A simultaneous multi-point laser Schlieren technique was also applied to this study. The results from the present work will be shown and discussed in detail in the next section.

4.2 Shock Wave Dispersion in Weakly Ionized Gas

The present study of shock wave dispersion in weakly ionized gas was performed by using the laser Schlieren technique to measure a time of flight of a shock wave propagating through a neutral Ar and an Ar MW discharge (see Section 3.2). Laser deflection signals were obtained at all available observation points (13 points) along the resonant cavity envelope both in the absence and in the presence of the discharge for a pressure range between 20 and 100 Torr. The discharge operated at constant input power 0.75 kW. Typical waveforms of the laser deflection signals are given in Figures 39 - 43 for the TE mode and Figures 50 - 54 for the TM mode. All results can be plotted in the form of the time-of-flight versus distance from the shock wave generator (see Figures 44 - 45 for TE mode and Figures 55 - 56 for TM mode). It is obvious that the shock wave propagation velocities in the Ar MW discharge are always greater than the shock wave propagation velocities in neutral Ar. Furthermore, the shock wave deflection signal amplitudes were always smaller when the shock wave propagated through the discharge than when it propagated through neutral Ar gas. These two results, as mentioned above, are the same as obtained in a d.c. glow discharge [3, 5]. However, some other effects differ considerably from those obtained in a d.c. glow discharge. In the present experiment, there is no apparent evidence of the multiple shock structure or widening of the shock wave deflection signal that are observed in the

d.c. glow discharge (see Figure 91). The shock wave always retained a more compact structure, even in the case of strong dispersion for both TE and TM modes.

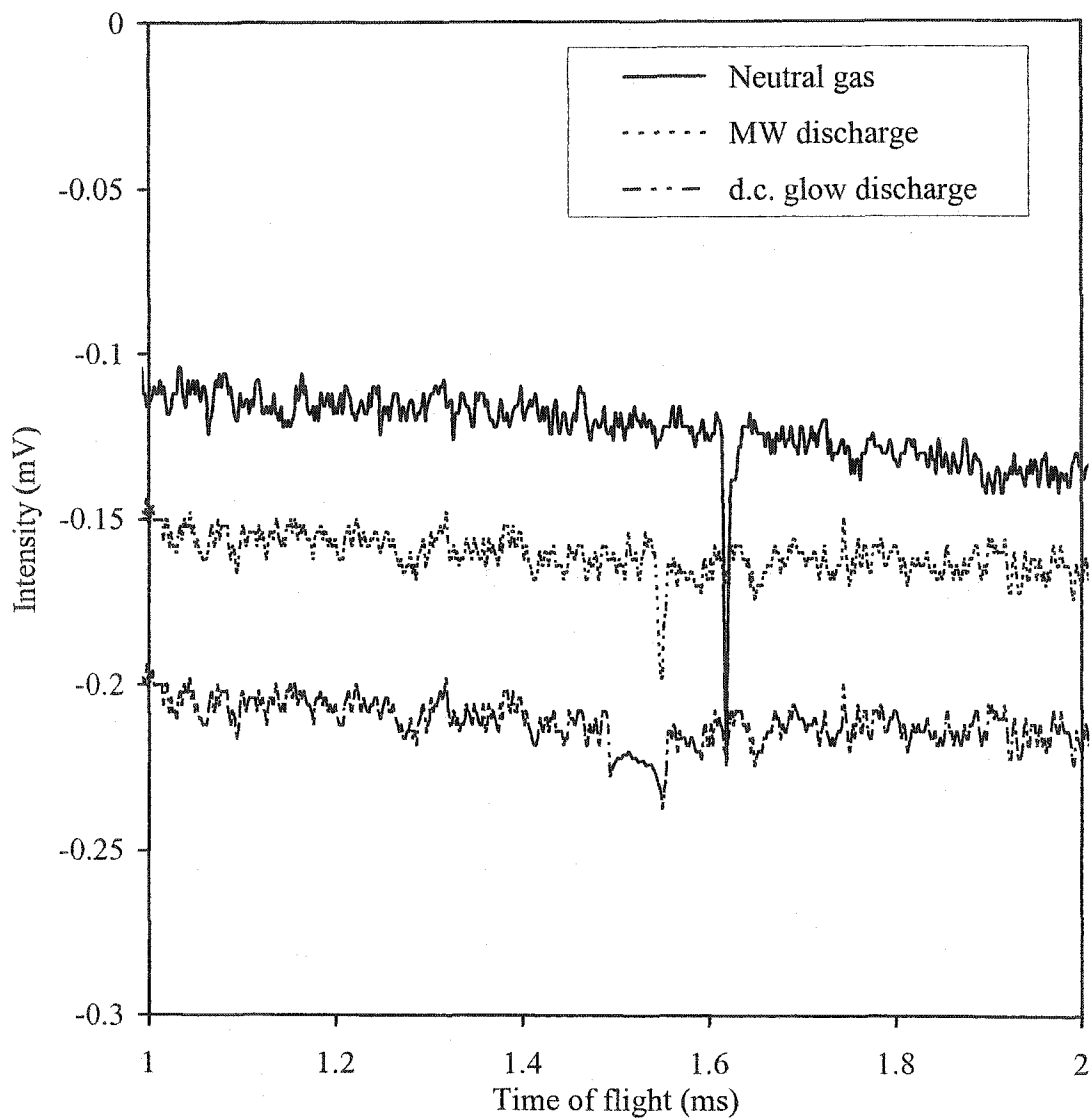


Fig. 91. Comparison of shock wave deflection signal in neutral gas, MW discharge and d.c. glow discharge.

We believe that the primary reason for the observed compact dispersion pattern is the radial distribution of the plasma parameters in the microwave cavity discharge. The electric field and plasma density increase gradually toward the center of the cavity. Therefore, there is no sharp boundary between the cold neutral gas and the hot rarefied medium of discharge plasma as in the case of the electrode region of the d.c. glow discharge. Furthermore, the radial distribution of the rotational temperature in the MW discharge did not change very much, contrary to the radial distribution of the rotational temperature in a d.c. glow discharge. In other words, the radial distribution of rotational temperature in a d.c. glow discharge decreased from the middle position much faster than in the MW discharge, for which it is relatively constant. For this reason, the incoming shock wave is propagating against relatively small gradients in plasma density and gas temperature.

The local propagation velocity of the shock wave in neutral Ar and in the Ar MW discharge was evaluated by using the data obtained from the time-of-flight measurement (see Section 3.3). The local velocity of the shock wave propagating both in the absence and in the presence of the discharge is shown in Figures 46 - 49 for TE mode and in Figures 57 - 60 for TM mode. The local propagation velocity increased in the discharge at all observation points, and in most cases the increase can be attributed to thermal effects, only. Furthermore, in the central region of the cavity (4th to 9th position), the local propagation velocity increased sharply to a level that could also be explained by the increase of gas temperature alone. Beyond the central region, the shock wave local propagation velocity was reduced again to the expected thermal level. This result was consistent in the whole pressure range that we observed. The

comparison between the gas temperature calculated from the observed velocity, on the assumption that the gas is an ideal [see Eqs.(6) and (15) and also Sections 3.3.1 and 3.3.2] and the gas temperature measured from the shock wave amplitude reduction technique in TE and TM mode (see Section 3.4.1) is shown in Figures 92 - 93.

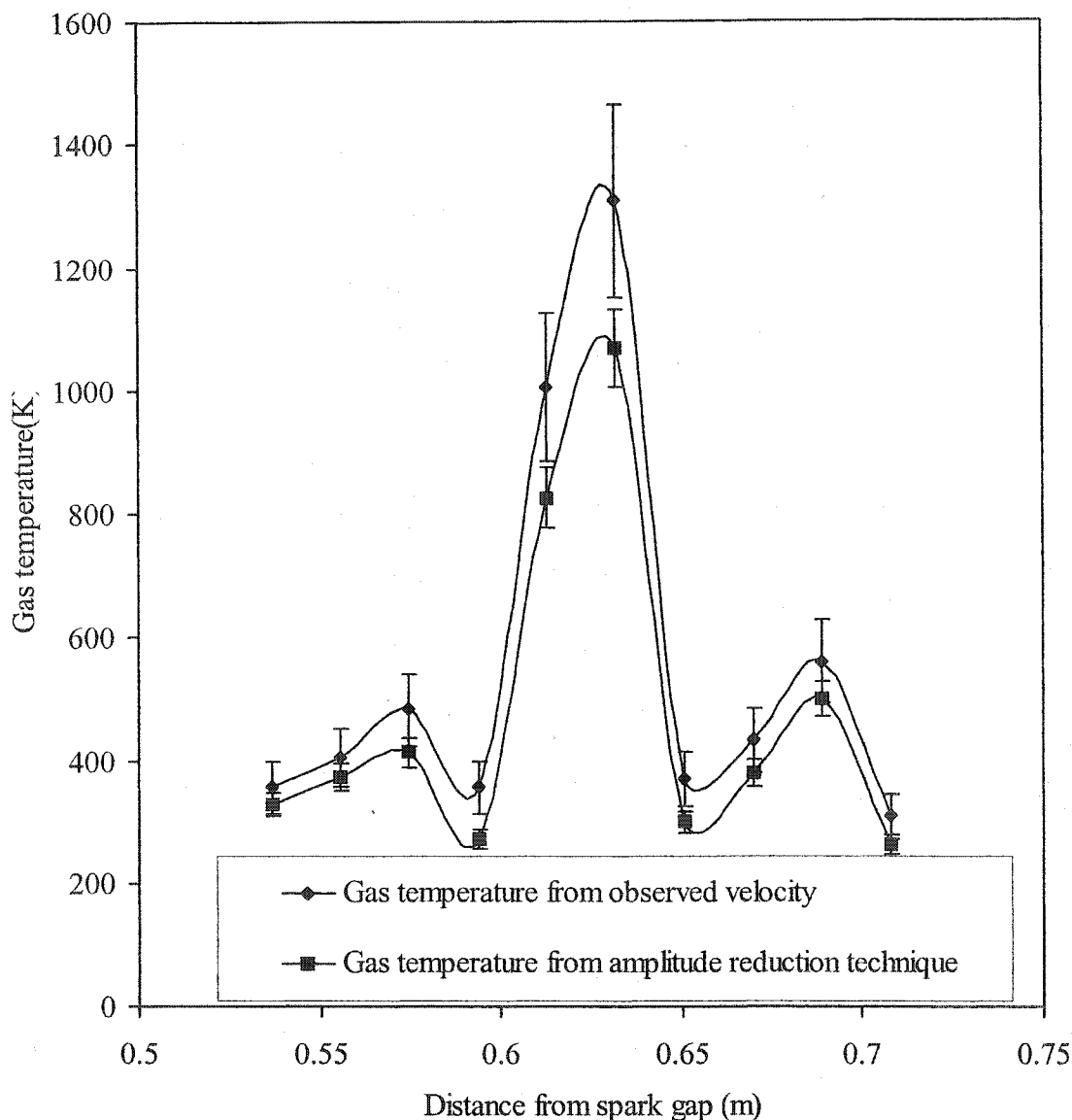


FIG. 92. Comparison between the gas temperature corresponding to the observed local propagation velocity and the measured gas temperature evaluated from shock wave amplitude reduction technique at 70 Torr in TE mode.

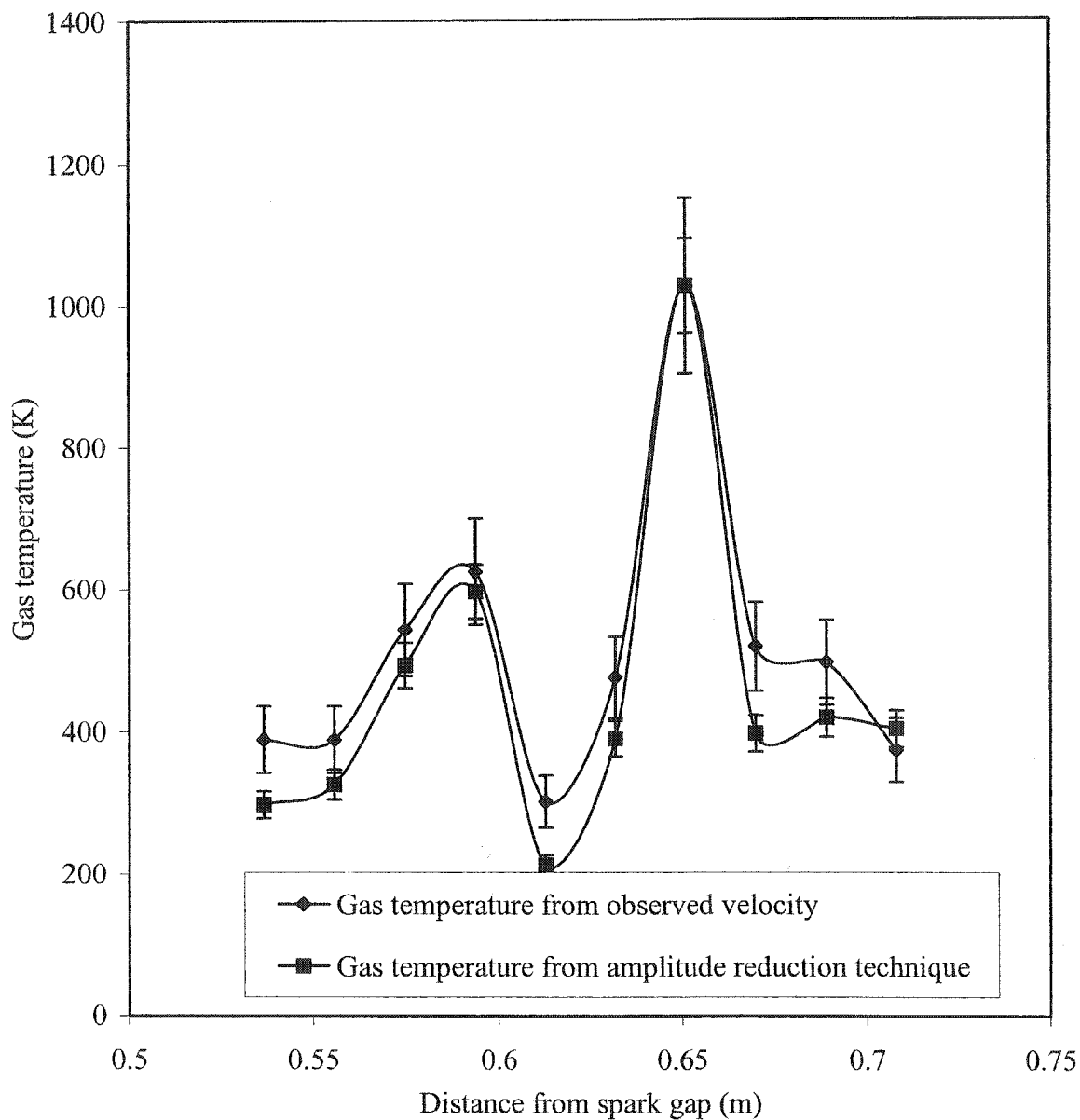


FIG. 93. Comparison between the gas temperature corresponding to the observed local propagation velocity and the measured gas temperature evaluated from shock wave amplitude reduction technique at 70 Torr in TM mode.

4.3 Characterization of MW Discharge

4.3.1 Gas Temperature

The gas temperature distribution along the resonant cavity axis can be evaluated by using the amplitude reduction technique and the data taken from the time-of-flight measurements (see Section 3.4.1). At all pressures, the gas temperature distribution in TE mode had a maximum value between 700 K and 1100 K, and those maximum values were located at the central region of the cavity at distances from a spark gap that are in the range from 0.60 to 0.65 m (5th position to 8th position). In TM mode, the gas temperature maximum values were scattered along the cavity axis in a wider range than in TE mode. All maximum values of the gas temperature at every pressure in TM mode were located at the central region from 0.57 to 0.68 m (4th position to 9th position) from the spark gap, and the maximum values of the gas temperature in this mode were between 500 K and 1000 K. The gas temperature distribution in the Ar MW discharge at selected pressures were shown in Figures 63 – 65 for TE mode and Figures 66 – 68 for TM mode.

The gas temperature distribution along the axis of the resonant cavity at all observation points corresponded with the local propagation velocity of the shock wave. The sharp increase of gas temperature in the central region of the cavity could explain the increase of the observed local propagation velocity in TE mode shown in Figure 92. For TM mode, the gas temperature evaluated from the amplitude reduction technique could apparently be fitted to the sharp increase of the observed local velocity shown in Figure 93. On the other hand, we could explain the increase of shock wave local

propagation velocity at the central region of the cavity in TE and TM modes by using the thermal effect only. The gas temperature calculated from the amplitude reduction technique and observed local velocity at the central region of the cavity, satisfy the necessary relationship $V \sim \sqrt{T}$. We can conclude that this present work is sufficiently precise to show that the thermal effect is dominant.

The result from the amplitude reduction technique was compared with the gas temperature evaluated from the rotational temperature of the spectra of molecular Nitrogen. (Nitrogen was the impurity in the discharge.) Assuming thermodynamic equilibrium of heavy particles in the discharge, the rotational temperature was evaluated and treated like a gas temperature (see Section 3.4.2).

The comparison between the gas temperature measured by using the shock wave amplitude reduction technique and the rotational temperature measured by using N_2 (0-2) band rotational emission spectrum technique in TE and TM mode are shown in Figures 94 and 95, respectively. From both figures, the maximum value of gas temperature calculated using the shock wave amplitude reduction technique at any position was plotted with respect to gas pressure and compared with the rotational temperature evaluated from N_2 (0-2) band rotational emission spectrum at the same observation point. The discharge power was kept constant in all measurements, and the gas pressure varied between 20 and 100 Torr. For TE mode, the relative difference between the two temperature measurements was approximately between 10% and 33%, except at the gas pressure of 80 Torr for which the relative agreement increased to 45%. In TM mode, the relative difference between the two temperature measurements was between 35% and 58%, except for the gas pressure of 70 Torr for which the relative

agreement decreased to 25%. We note a relatively large difference between the two measurements.

From this result, we can see that the shock wave amplitude reduction technique can be used to calculate the real gas temperature distribution inside the Ar MW discharge along the axis of the resonant cavity in both TE and TM mode. On the other hand, the rotational temperature measured from the N_2 (0-2) band rotational emission spectrum can only be used to estimate the upper limit of the discharge temperature.

The rotational temperature in the Ar MW discharge for both TE and TM modes was calculated from the N_2 (0-2) band rotational emission spectroscopy technique based on the assumption of thermodynamic and chemical equilibrium of excited state molecules and ground state molecules in the discharge. According to the result of temperature measurement by two different techniques (see Figures 94 and 95), this assumption may not be satisfied at any time during the experimental process. During the discharge, the electron impact may not only be the major reaction, but also other inelastic collisions may occur (e.g., ground-excited or excited-excited collisions). Furthermore, some chemical reactions may not be in the minimum level, and some of them can occur and evolve toward chemical equilibrium of the discharge. All of these situations can increase the rotational temperature of the excited state molecules. For this reason, the rotational temperature is always higher than the real gas temperature. We observed better agreement for temperature measurements in TE mode than in TM mode. This result requires more study based on detailed spectroscopic data for the TE and TM modes.

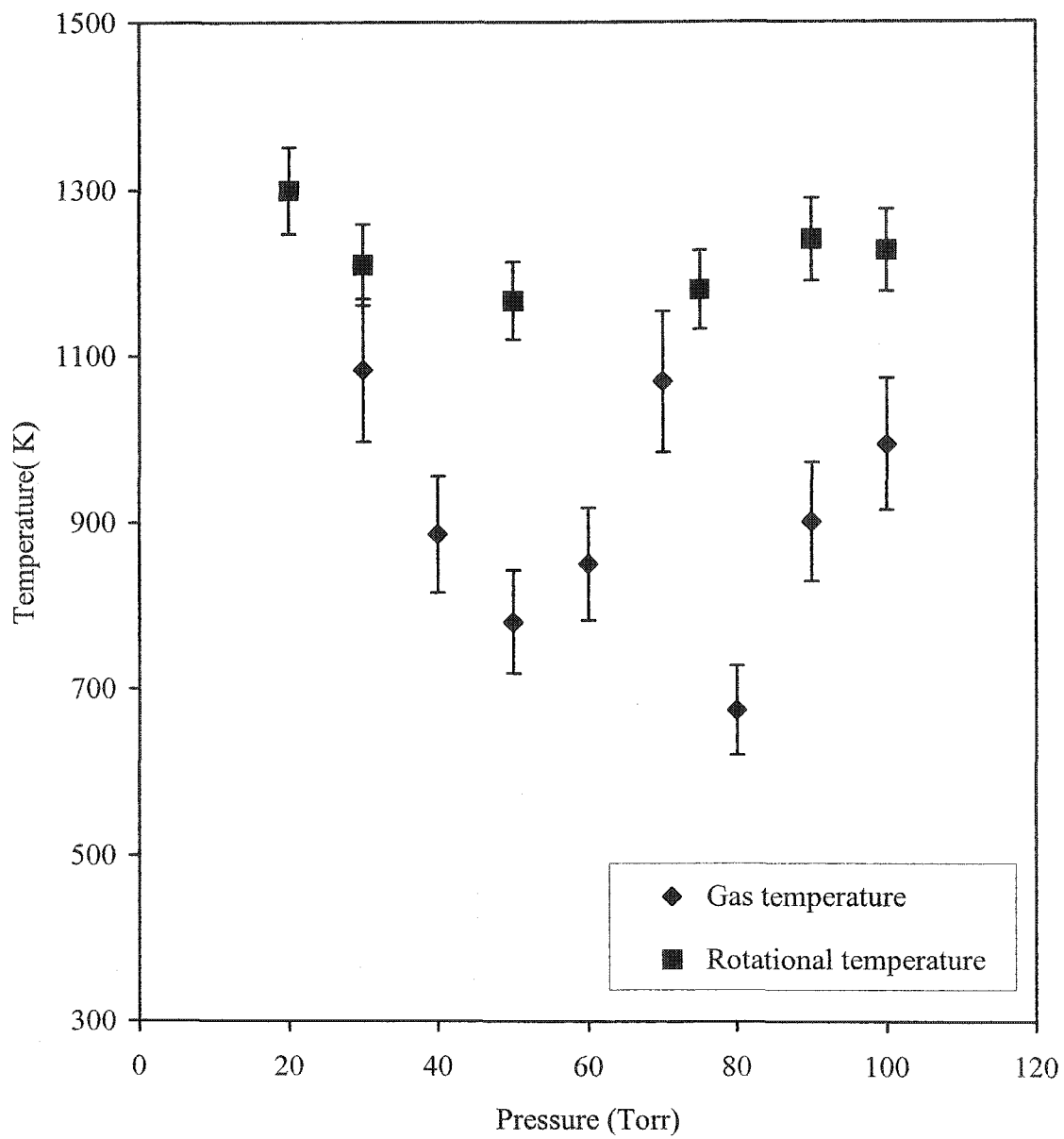


FIG. 94. Gas temperature and rotational temperature in TE mode.

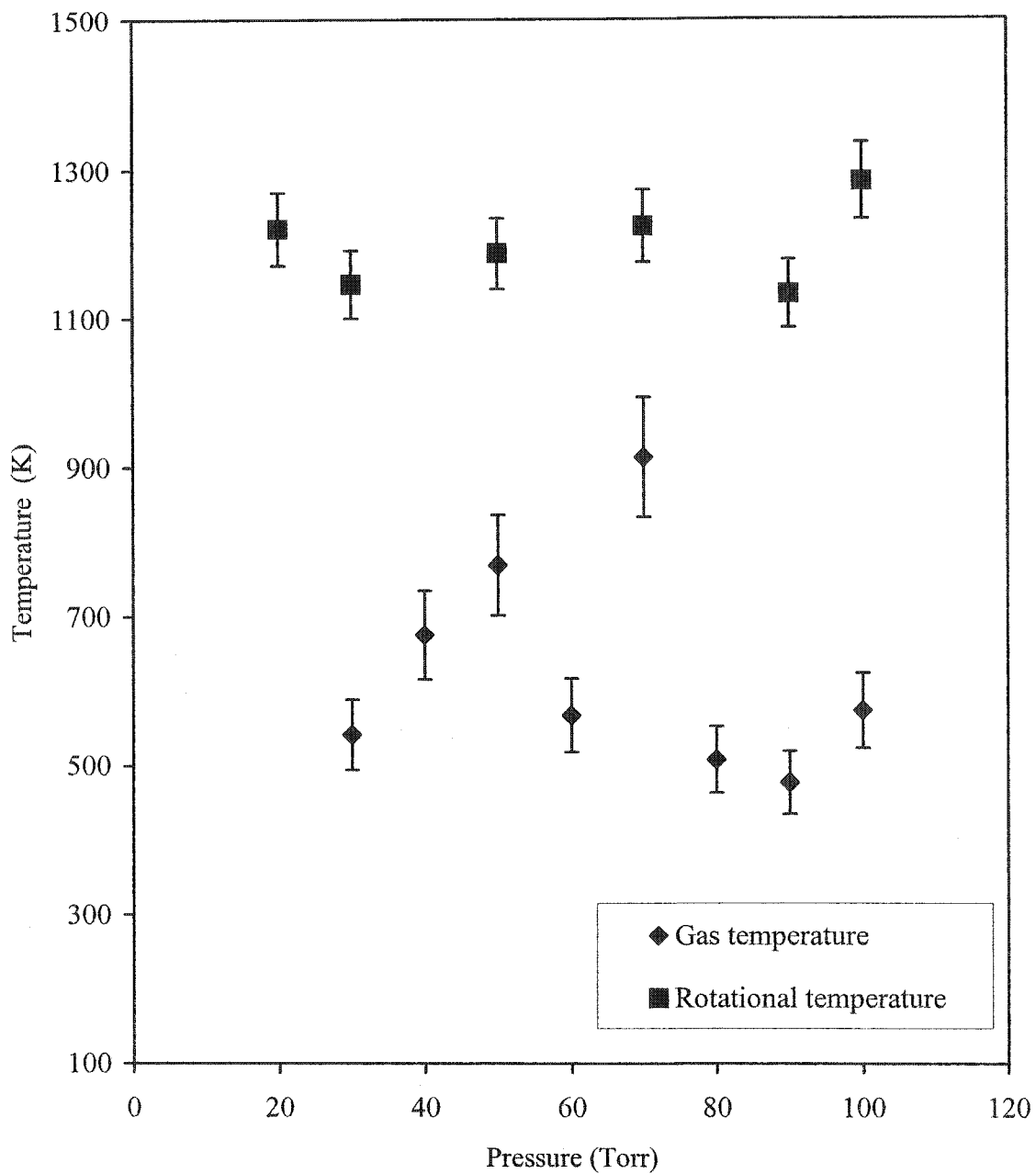


FIG. 95. Gas temperature and rotational temperature in TM mode.

4.3.2 Electron Density

The electron density was evaluated from the Stark broadening of Hydrogen Balmer lines, corrected for Doppler broadening, by use of the gas temperature from Section 3.4 and the well-tested procedure discussed in Section 3.5. The value of electron density in our experiment varied between 4.4×10^{13} and $6.8 \times 10^{13} \text{ cm}^{-3}$ for the gas pressure range between 20 and 100 Torr (see Figure 83). According to this value of electron density, the degree of ionization in the Ar MW discharge was between 10^{-5} and 10^{-4} , compared to the d.c. glow discharge where the degree of ionization is between 10^{-8} and 10^{-6} . Therefore, the present microwave discharge has a higher electron density and a higher degree of ionization than the d.c. glow discharge.

4.3.3 Local Electric Field

The local electric field in the Ar MW discharge can be considered on the basis of the variation of the (0-0) band head intensity ($\lambda_0 = 337.1 \text{ nm}$) of the Second Positive System of Nitrogen. By using a simplified model, based on the assumptions and arguments discussed in Section 3.6, the time evolution of the local electric field could be obtained, as shown in Figure 89. The local electric field inside the resonant cavity in the Ar MW discharge decreased to 40 V/cm from the initial electric field of 130 V/cm generated by the magnetron. Since the magnetron power supply was kept constant in each experiment, we assume that the decrease of the local electric field inside a resonant cavity at any pressure in both TE and TM mode was approximately the same. Due to the detuning effect of the plasma column, the local electric field inside the resonant

cavity decreased by approximately 70% from the initial electric field during a single pulse (3 to 6 ms) in the Ar MW discharge in both TE and TM modes.

4.3.4 Power Density

The average power density inside the discharge was evaluated by calculating the power loss inside the resonant cavity, as discussed in Section 3.7. The power loss during the discharge in TM mode can be determined from the local electric field inside the resonant cavity and the dimension of the cavity. By use of the local electric field evaluated in Section 3.6, the average power density inside the resonant cavity for TM mode during the discharge can be estimated to be about 2.61 Watts/cm³. This value of average power density was a *low power density* used for operating the discharge in the present work. Since the strength of the local electric field inside the resonant cavity for the TE and TM modes is approximately the same, the average power loss in TE mode should be less than in TM mode, but the average power density in TE mode should be higher than in TM mode due to the difference in dimension between the TE and TM mode. We believe that the value of the average power density in TE mode was still in the low power density range (< 10 Watts/cm³) for this work.

4.4 Conclusion

We can conclude that shock wave dispersion in the Ar MW discharge differs considerably from that obtained in a d.c. glow discharge. Multiple shock wave structure or widening of the shock wave deflection signal did not appear in the microwave discharge. In the microwave discharge, we can use the observed gas temperature

(thermal effect) to explain the shock wave local propagation velocity in the central region of the resonant cavity. The rotational temperature was evaluated and used to estimate the upper limit of the gas temperature of the microwave discharge. The degree of ionization of the microwave discharge is about 10^{-5} to 10^{-4} , which is in the range of a weakly ionized gas ($< 10^{-3}$). The local electric field inside the microwave discharge decreased by at least 70% from the initial electric field. The average power density inside resonant cavities during the discharge was in the low power density range (< 10 Watts/cm³) for this study. There are some interesting differences between TE and TM modes for the shock wave local propagation velocity and the gas temperature. We found that the range of the local propagation velocity distribution for a shock wave in TM mode is wider than in TE mode. Furthermore, the difference between the rotational temperature and the gas temperature in TM mode is more than in TE mode. This result will lead us in the future to develop new ways to study in more detail the effect of various modes of the resonant cavity on a microwave discharge.

Section 5

CONCLUSION

Shock wave dispersion in weakly ionized gas was studied in the range of pressure from 20 to 100 Torr at low power density. Weakly ionized gas was generated by a cavity microwave discharge in Argon. This study is complementary to the experiment of Bletzinger, Gunguly, and Garscadden [3,5] on propagation of weak shock waves through weakly ionized gas. Here, the propagation is studied in a microwave cavity discharge instead of in a d.c. glow discharge. The microwave discharge is electrodeless, and shock wave propagation in weakly ionized gas is not affected by the presence of electrodes in the flow. We can conclude that the result of shock wave dispersion in the Ar MW discharge differs considerably from that obtained in a d.c. glow discharge. Multiple shock wave structure, or widening of shock wave deflection signal, did not appear in the microwave discharge. However, the increase of the shock wave local propagation velocity and the decrease of the shock wave deflection signal amplitude were still observed in the microwave discharge. The local propagation velocity of the shock wave was obtained at all observation points along the resonant cavity envelope by using the time-of-flight measurements. The velocity increased sharply in the central region of the cavity (TE and TM modes).

Correlation of local velocity and the gas temperature between the TE mode and the TM mode reveals some interesting aspects of the interaction between the shock wave and the microwave discharge. We found that the range of the local propagation velocity distribution of shock waves in TM mode is wider than in TE mode. Furthermore, the

difference between the rotational temperature and the gas temperature in TM mode is larger than in TE mode. This effect indicates that properties of external fields produce an observable effect on the shock wave. This evidence of the electrodynamic nature of the interaction is analogous to findings in a d.c. glow discharge. In the latter case, the shock wave dispersion is modified by the polarity of the electric field. In the present case, we have evidence that the direction of the electric field (vertical in TE mode and parallel in TM mode) affects a shock wave propagation velocity.

In this study, the fundamental discharge parameters such as the gas temperature, T_g , electron density, N_e , and local electric field, E were evaluated in order to characterize the Ar MW discharge.

The gas temperature in both TE and TM modes were obtained at all observation points along the resonant cavity envelope by using the shock wave amplitude reduction technique. The value of the gas temperature was compared to the rotational temperature calculated from the rotational spectra of Nitrogen gas. We found that the rotational temperature could only be used to estimate the upper limit of the gas temperature of the microwave discharge in both TE and TM modes. The temperatures obtained by these two techniques differs less in TE mode than in TM mode. This result was used to describe the mechanism responsible for changing the shock wave local propagation velocity at the central region of resonant cavity. It was found that the thermal effect was the dominant effect needed to explain the distribution of the shock wave local propagation velocity in the central region of the resonant cavity.

Electron density was evaluated by deconvolution of the Stark and Doppler broadened line shape of H_β using the gas temperature of the discharge and the well-tested

approximate formula [47,48]. The value of electron density can be used to evaluate the degree of ionization of the microwave discharge, which is about 10^{-5} to 10^{-4} . This degree of ionization for the microwave discharge is in the range of a weakly ionized gas ($< 10^{-3}$) but a few orders of magnitude higher than for a d.c. glow discharge.

The time evolution of the local electric field inside the microwave discharge was evaluated on the basis of the variation of the ($0-0$) band head intensity ($\lambda_0 = 337.1$ nm) of the Second Positive System of Nitrogen, time dependence of the electron density, and a simplified model. The local electric field inside the microwave discharge decreased by at least 70% from the initial electric field.

In conclusion, shock wave dispersion in the Ar MW discharge was not the same as that observed in a d.c. glow discharge. We could not observe the multiple shock wave structure or widening of the shock wave deflection signal in the microwave discharge. Most observed effects could be explained by the thermal effect in this study. However, there is a difference between the same effects observed in TE and TM modes. The present study provides an experimental analysis of shock wave dispersion in microwave discharges. As such, it provides basic knowledge for future studies of shock wave dispersion in microwave discharge at atmospheric pressures and higher power densities. Since microwave discharge is one of the methods chosen to produce weakly ionized gas media for shock modification around the hypersonic aircraft of the future, the data collected in this work will hopefully provide a stepping stone for future work in that direction.

REFERENCES

- [1] A.I. Kilmov, A.N. Koblev, G.I. Mishin, Yu. L. Serov, and I.P. Yavor, *Sov. Tech. Phys. Lett.* **8**, 192 (1982).
- [2] P.A. Voinovich, A.P. Ershov, S.E. Ponomareva, and V.M. Shibkov, *High Temp.* **29**, 468 (1990).
- [3] P. Bletzinger and B.N. Ganguly, *Phys. Lett. A* **258**, 342 (1999).
- [4] V.A. Gorshkov, A.I. Klimov, G.I. Mishin, A.B. Fedotov, and I.P. Yavor, *Sov. Phys. Tech. Phys.* **32**, 1138 (1987).
- [5] B.N. Ganguly, P. Bletzinger, and A. Garscadden, *Phys. Lett. A* **230**, 218 (1997).
- [6] S. Popović and L. Vušković, *Phys. Plasmas*. **6**, 1448 (1999).
- [7] D.A. Tidman and N.A. Krall, *Shock Waves in Collisionless Plasmas* (Wiley-Interscience, New York, 1971).
- [8] M.A. Liberman and A.L. Velikovich, *Physics of Shock Waves in Gases and Plasma* (Springer, New York, 1985).
- [9] M. Casanova and O. Larrochi, *Phys. Rev. Lett.* **67**, 2143 (1991).
- [10] A.I. Kilmov, A.N. Koblev, G.I. Mishin, Yu. L. Serov, K.V. Khodataev, and I.P. Yavor, *Sov. Tech. Phys. Lett.* **8**, 240 (1982).
- [11] I.V. Basargin and G.I. Mishin, *Sov. Tech. Phys. Lett.* **15**, 311 (1989).
- [12] G.I. Mishin, Yu. L. Serov, and I.P. Yavor, *Sov. Tech. Phys. Lett.* **17**, 413 (1991).
- [13] G.I. Mishin, A.I. Klimov, and A.Yu. Gridin, *Sov. Tech. Phys. Lett.* **17**, 602 (1992).
- [14] A.P. Bedin and G.I. Mishin, *Tech. Phys. Lett.* **21**, 5 (1995).
- [15] S.O. Macheret, L. Martinelli, and R.B. Miles, *AIAA Paper 99-0598, 37th AIAA Aerospace Sciences Meeting and Exhibit*, Reno, Nevada, January 1999.
- [16] S. Popović, L. Vušković, and A. Chow, *AIAA Paper 2001-3049, 32nd AIAA Plasmadynamics and Lasers Conference and 4th Weakly Ionized Gases Workshop*, Anaheim, California, June 2001.
- [17] P. Bletzinger, B.N. Ganguly and A. Garscadden, *AIAA Paper 2001-3050, 4th Weakly Ionized Gases Workshop*, Anaheim, California, June 2001.
- [18] S.O. Macheret, Y.Z. Ionikh, N.V. Cherhysheva, A.P. Yalin, L. Martinelli, and R.B. Miles, *Phys. Fluids*, **13**, 2693 (2001).

- [19] R.F. Avramenko, A.A. Rukhadze, and S.F. Teselkin, *Sov. Phys. ZHETP Lett.* **34**, 463 (1981).
- [20] G.V. Vstovskii and G.I. Kozlov, *Sov. Tech. Phys.* **31**, 911 (1986).
- [21] V. Soloviev, V. Krivtsov, A. Konchakov, and N.D. Malmuth, *AIAA Paper 99-4908, 30th Plasmadynamics and Lasers Conference*, Norfolk, Virginia, November 1999.
- [22] V. Bychkov and N. Malmuth, *AIAA Paper 99-4938, 30th Plasmadynamics and Lasers Conference*, Norfolk, Virginia, November 1999.
- [23] S. M. Aithal and V. V. Subramaniam, *Phys. Fluids* **12**, 924 (2000).
- [24] A. H. Auslender and R. Rubinstein, *Proceedings of the 2nd Weakly Ionized Gases Workshop*, pp. 119-121, Norfolk, Virginia, April 1998.
- [25] M. Moisan and Z. Zakrzewski, *J. Phys. D: Appl. Phys.* **24**, 1025 (1991).
- [26] H. Matusiewicz, *Spectrochim. Acta* **31B**, 1221 (1992).
- [27] T. Czerwicz, J. Gavillet, T. Belmonte, H. Michel, and A. Ricard, *Surf. Coat. Technol.* **98**, 1411 (1998).
- [28] V. Guerra, E. Tatarova, and C.M. Ferreira, *Vacuum* **69**, 171 (2002).
- [29] J. Henriques, E. Tatarova, V. Guerra, and C.M. Ferreira, *Vacuum* **69**, 177 (2002).
- [30] J.E.A. John, *Gas Dynamics* (Allyn and Bacon, Boston, 1969).
- [31] M.J. Zucrow and J.D. Hoffman, *Gas Dynamics Volume I* (John Wiley & Sons, New York, 1976).
- [32] J.D. Anderson Jr., *Hypersonic and High Temperature Gas Dynamics* (McGraw-Hill, New York, 1989).
- [33] M. Akram and E. Lundgren, *J. Phys. D: Appl. Phys.* **29**, 2129 (1996).
- [34] M. Akram and E. Lundgren, *J. Phys. D: Appl. Phys.* **29**, 2137 (1996).
- [35] R. Reinmann and M. Akram, *J. Phys. D: Appl. Phys.* **30**, 1125 (1997).
- [36] M. N. Hirsh and H.J. Oskam, *Gaseous Electronics: Volume I Electrical Discharge* (Academic Press, New York, 1978).
- [37] R. Dendy, *Plasma Physics: An Introductory Course* (Cambridge University Press, Cambridge, 1993).
- [38] L.G. Meiners and D.B. Alford, *Rev. Sci. Instrum.* **57**, 164 (1986).
- [39] J.D. Jackson, *Classical Electrodynamics* (John Wiley & Sons, New York, 1975).

- [40] W.H. Hayt Jr., *Engineering Electromagnetics* (McGraw-Hill, New York, 1989).
- [41] R.H. Huddlestone and S.L. Leonard, *Plasma Diagnostic Techniques* (Academic Press, New York, 1965).
- [42] R.H. Lovberg and H.R. Griem, *Methods of Experimental Physics: volume 9-part B: Plasma Physics* (Academic Press, New York, 1971).
- [43] T.H. Dinh, Ph.D. Dissertation, "Decomposition of Carbon Dioxide in a Capacitively Coupled Radio Frequency Discharge," Old Dominion University, May 2002.
- [44] G. Herzberg, *Molecular Spectra and Molecular Structure: Spectra of Diatomic Molecules* (D. Van Nostrand Company New York, 1950).
- [45] G. Hartmann and P.C. Johnson, *J. Phys. B: At. Mol. Phys.* **11**, 1597 (1978).
- [46] L. Yu, Ph.D. Dissertation, "Nonequilibrium Effect in Two-Temperature Atmospheric Pressure Air and Nitrogen Plasma," Stanford University, August 2001.
- [47] S. Jovičević, M. Ivković, Z. Pavlović, and N. Konjević, *Spectrochim. Acta* **55B**, 1879 (2002).
- [48] D.E. Kelleher, *JQSRT* **25**, 191 (1981).
- [49] S. Popović, P. Kessaratikoon, A. Markhotok, G. Brooke IV, and L. Vušković, *AIAA Paper 2002-2279, 33rd AIAA Plasmadynamics and Lasers Conference*, Maui, Hawaii, May 2002.
- [50] J. Loureiro and C.M. Ferreira, *J. Phys. D: Appl. Phys.* **22**, 67 (1989).
- [51] S.D. Popa, *J. Phys. D: Appl. Phys.* **29**, 416 (1996).
- [52] A.D. MacDonald, *Microwave Breakdown in Gases* (John Wiley & Sons, Inc., New York, 1966).
- [53] S. C. Brown, *Introduction to Electrical Discharges in Gases* (John Wiley & Sons, Inc., New York, 1966).
- [54] Y.Z. Ionikh, N.V. Chernysheva, A.V. Meshchanov, A.P. Yalin, and R.B. Miles, *Phys. Lett. A* **259**, 387 (1996).

APPENDIX**TABLE OF LASER POSITIONS IN TIME-OF-FLIGHT MEASUREMENT**

Position	Distance from spark gap (m)
1	0.517
2	0.536
3	0.556
4	0.575
5	0.594
6	0.613
7	0.632
8	0.651
9	0.669
10	0.689
11	0.708
12	0.727
13	0.746

VITA

NAME Prasong Kessaratikoon
ADDRESS Department of Physics, Old Dominion University, 4600 Elkhorn Ave,
 Norfolk, VA 23529

EDUCATION

December 2003 **Ph.D.**, Applied Physics, Old Dominion University
 Dissertation: *Shock Wave Dispersion in Weakly Ionized Gas*
 May 1999 **M.S.**, Physics, Old Dominion University
 September 1987 **M.S.**, Physics, Chulalongkorn University, Bangkok, Thailand
 Thesis: *Neutron Measurement by Using Thermoluminescent Technique*
 March 1983 **B.Ed.**, Physics Education, Burapha University, Chonburi, Thailand

HONORS AND AWARDS

1997–2001 Thailand Government Scholarship, Faculty of Science, Department of
 Physics, Thaksin University, Songkhla, Thailand
 1983-1986 UDC Scholarship, Faculty of Science, Department of Physics, Thaksin
 University, Songkhla, Thailand
 1980-1983 Honor student, Burapha University, Chonburi, Thailand, 1983

RECENT PUBLICATIONS AND PRESENTATIONS

May 2003 *Energy Pooling Processes in Partially Ionized Argon*, L. Vušković, P.
 Kessaratikoon, S. Popović, presented in the 2003 Meeting of the
 Division of Atomic, Molecular, and Optical Physics, Boulder, 20-24
 May, 2003.
 October 2002 *Shock Wave Dispersion in Microwave Discharge*, P. Kessaratikoon, A.
 Markhotok, G. Brooke IV, S. Popović, L. Vušković, presented in the
 55th Annual Gaseous Electronics Conference, Minneapolis, 15-18
 October, 2002.